

Charge Transport Processes in Quantum Dot Sensitized Solar Cells

REMYA NARAYANAN

A Dissertation Submitted to the
Indian Institute of Technology Hyderabad
In Partial Fulfillment of the Requirements for
The Degree of Doctor of Philosophy



भारतीय प्रौद्योगिकी संस्थान हैदराबाद
Indian Institute of Technology Hyderabad

Department of Chemistry

July, 2014

Declaration

I declare that this written submission represents my ideas in my own words, and where others' ideas or words have been included, I have adequately cited and referenced the original sources. I also declare that I have adhered to all principles of academic honesty and integrity and have not misrepresented or fabricated or falsified any idea/data/fact/source in my submission. I understand that any violation of the above will be a cause for disciplinary action by the Institute and can also evoke penal action from the sources that have thus not been properly cited, or from whom proper permission has not been taken when needed.



(Signature)

(Remya Narayanan)

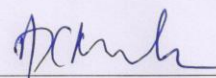
(CY10P011)

Approval Sheet

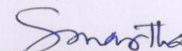
This thesis entitled “**Charge Transport Processes in Quantum Dot Sensitized Solar Cells**” by Remya Narayanan is approved for the degree of Doctor of Philosophy from the Indian Institute of Technology Hyderabad.



External Examiner
Prof. A.Q. Contractor
Department of Chemistry
Indian Institute of Technology Bombay
Mumbai - 400076, India



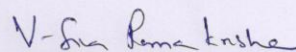
External Examiner
Prof. Ashok Kumar Mishra
Department of Chemistry
Indian Institute of Technology Madras
Chennai- 600036, India



Internal Examiner
Dr. Surendra K. Martha
Department of Chemistry
Indian Institute of Technology Hyderabad
Yeddumailaram - 502205, India



Adviser
Dr. M. Deepa
Assistant Professor
Department of Chemistry
Indian Institute of Technology Hyderabad
Yeddumailaram - 502205, India



Chairman
Dr. V. Siva Rama Krishna
Department of Electrical Engineering
Indian Institute of Technology Hyderabad
Yeddumailaram - 502205, India

Acknowledgements

I would like to take this opportunity to express my thanks to those who helped me with various aspects of conducting research and the writing of this thesis.

First and foremost, Dr. M. Deepa, my supervisor, for her academic advice and guidance, patience and support throughout the research work and the writing of this thesis. I have learned a lot from her; without her help, I could not have finished my dissertation successfully.

I would also like to appreciate advices of the doctoral committee members, Dr. Ch. Subrahmanyam and Dr. G. Prabusankar for their critical comments, which enabled me to recognize the weaknesses of my dissertation and make the necessary improvements according to their comments.

I would especially like to thank the Head of the Department, Prof. Faiz Ahmed Khan and all other faculty members in the Department of Chemistry for their encouragement and support.

I thank Prof. U. B. Desai, Director, for academic support and the facilities, which enabled me to carry out the research work at the Institute.

I am grateful to Dr. Avanish Kumar Srivastava, CSIR-National Physical Laboratory, New Delhi for HRTEM analysis. I acknowledge Dr. Manoj A. G. Namboothiri, IISER Trivandrum for his valuable suggestions in photoelectrochemical measurements.

I would like to convey my heartfelt thanks to the Indian Institute of Technology Hyderabad, for offering me an ideal environment, so that I could pursue my research work.

My labmates, Bhaskar, Rambabu, Narsimha Reddy, Naresh, Radha and Ramesh extended their support in a very special way and I gained a lot from them through personal and scholarly interactions; and their suggestions at various points of my research program helped me a lot. I also acknowledge my dear friends, Dayamani, Jancy, Faby, Ranjeesh, Akhila, Parvathi, Sumi, Anand, Asok, Arya, Arun, Aravind and Snehal for their support and good wishes.

I owe a lot to my parents and my brother who encouraged and helped me at every stage of my personal and academic life. I am greatly indebted to my beloved husband, Sandeep for supporting me for everything.

Above all, I owe it all to God Almighty for granting me wisdom, health and strength, to undertake this research task and enabling me to take it to its completion.

**Dedicated to
My Parents and Husband**

Abstract

Colloidal nanocrystals or quantum dots (QDs) have attained immense scientific interest as light sensitive materials due to band gap tunability by size control, ease of preparation, multiple exciton generation and low cost. In the last decade, although reasonably high power conversion efficiencies (PCEs) of 5% have been realized in quantum dot sensitized solar cells (QDSSCs), the efficiencies of QDSSCs continue to lag behind that of dye sensitized solar cells or DSSCs. To address the issue of improving overall PCE values in QDSSCs, new strategies such as Forster resonance energy transfer or FRET, plasmonic effects, and blending the photosensitizer dots with carbon nanostructures etc., were implemented in this thesis.

Since photovoltaic performance parameters are closely linked to the energetics of the components which, in turn dictates electron transfer dynamics, in this work, we fabricated hitherto unexplored photoanode architectures and charge transfer and transport mechanisms were studied by detailed fluorescence quenching, and lifetime analyses. The effect of a carbon nanostructure, ionic liquid functionalized graphene oxide (FGO) and metal nanoparticles (Au) in promoting electron transport in a QDSSC with TiO_2/CdSe as the photoactive electrode was studied and a PCE of $\sim 1\%$ (under 1 sun) was realized for this assembly relative to other configurations. Taking this further, the effect of another carbon nanostructure, C_{60} nanowhiskers, on a CdS QD solar cell performance was discerned by comparing the charge propagation dynamics of CdS/ C_{60} nanowhiskers with that of an assembly containing conventional C_{60} clusters (i.e., CdS/ C_{60}) and the advantage of the whiskers was clearly brought out. Apart from the use of carbon nanostructures, another concept, FRET, was also exploited in this work to realize improved efficiencies in QDSSCs. An electrode tethered QD assembly of ZnS/CdS/ZnS was used as the donor and copper phthalocyanine (CuPc) molecules dissolved in the electrolyte were used as the acceptors. Luminescent and conductive carbon dots or C-dots were also included in this cell to improve electron transfer and transport. Incident photon to current conversion efficiency or IPCE measurements revealed an optimal coverage of the visible spectrum due to FRET. A quasi-solid state FRET enabled QDSSC was demonstrated. Extending this further, another FRET cell was fabricated, with reversed roles, wherein CdS/CdSe QDs served as acceptors and a Lucifer yellow dye dissolved in electrolyte functioned as the donor. Vis-à-vis FRET, an enhanced solar cell performance and a PCE of 1.8% was obtained. Further, the hole transporting ability of the conventional $\text{S}_n^{2-}/\text{S}^{2-}$ layer was also improved by use of poly(3,4-ethylenedioxythiophene) microfibers. Plasmonic effects were tapped for improving solar cell responses, by integrating Au microfibers with CdS/ TiO_2 electrodes. This work was further extended by combining this plasmonic photoanode with an electrical double layer capacitor based on multiwalled carbon nanotubes (MWCNTs). A new design for a solar powered supercapacitor was implemented wherein the photocurrent generated by the plasmonic electrode was channelized to charge the MWCNT supercapacitor. The benefit of plasmonics in improving solar cell parameters was also demonstrated by using Au encapsulated C-dots in a ZnO based DSSC and a PCE of 4.1% was achieved. Another practical application was illustrated by using electrochromic MoO_3 as a counter electrode in the ZnO/Dye/Au@C-dots based cell and photoelectrochromism was shown.

Overall, in this thesis, the charge transport mechanisms that prevail in QDSSCs and how they control photovoltaic parameters is demonstrated.

Nomenclature

Contents

Declaration	ii
Approval Sheet	Error! Bookmark not defined.
Acknowledgements	iv
Abstract	vi
Nomenclature	vii
1 Introduction.....	11
1.1 Solution processed quantum dot sensitized solar cells: An overview	1
1.2 History	1
1.3 Structure and mechanism of the dye sensitized solar cells	2
1.4 Quantum dot sensitized solar cells.....	5
1.4.1 Why quantum dots.....	5
1.4.2 Quantum confinement	5
1.4.3 Size-dependent effects	6
1.4.4 Multiple exciton generation	7
1.4.5 QDs in solution processed cells	7
1.4.6 Working principle of QDSSCs	8
1.4.7 Size morphology dependence on PEC response	12
1.4.8 Role of carbon nanostructures in QDSSCs	14
1.4.8.1 Fullerene.....	15
1.4.8.2 Carbon nanotube	16
1.4.8.3 Graphene	17
1.4.9 Improving PCE by surface plasmon resonance	20
1.4.10 Incorporation of FRET	23
1.5 Objective of the present work.....	27
1.5 References.....	29
2 Materials and characterization techniques.....	32
2.1 Materials	32
2.2 Characterization techniques.....	36
2.2.1 Scanning electron microscopy.....	36
2.2.2 Transmission electron microscopy	37
2.2.3 Atomic force microscopy	39
2.2.4 Conductive atomic force microscopy.....	40
2.2.5 Kelvin Probe Force Microscopy.....	41

2.2.6	UV Visible spectrophotometry.....	41
2.2.7	Photoluminescence spectroscopy	43
2.2.8	Lifetime analysis	45
2.2.9	X- ray Powder Diffraction.....	46
2.2.10	Raman spectrophotometer	47
2.2.11	Current-voltage characteristics.....	48
2.2.12	Incident photon current conversion efficiency	49
2.2.13	Cyclic voltammetry	50
2.2.14	Linear sweep voltammetry	52
2.2.15	Chronoamperometry.....	53
2.2.16	Chronopotentiometry	53
2.2.17	Electrochemical impedance spectroscopy	54
2.3	References.....	55
3 Influence of functionalized graphene oxide and Au nanoparticles on the photoelectrochemical response of a TiO₂/CdSe QDs assembly.....		
3.1	Introduction.....	56
3.2	Experimental.....	56
3.2.1	Synthesis of CdSe QDs	56
3.2.2	Synthesis of gold nanoparticle dispersion	57
3.2.3	Synthesis of functionalized graphene oxide from graphite rods	57
3.2.4	Fabrication of the QD sensitized electrodes.....	58
3.3	Results and discussion	58
3.3.1	High resolution transmission electron microscopy studies	58
3.3.2	Structural characterizations of FGO.....	61
3.3.3	Absorption and fluorescence quenching studies	61
3.3.4	Emission decay analyses	66
3.3.5	Energetics	69
3.3.6	C-AFM studies	70
3.3.7	Photoelectrochemistry of cells	73
3.4	Summary.....	76
3.5	References.....	77
4 Impact of C₆₀ nanowhiskers on the photovoltaic performance of a CdS based QDSSC		
4.1	Introduction.....	78
4.2	Experimental.....	79
4.2.1	C ₆₀ nanowhiskers and C ₆₀ based films.....	79
4.2.2	CdS sensitized electrodes	79

4.2.3	MWCNT/PDDA electrode by LbL assembly	79
4.3	Results and discussion	80
4.3.1	Optical microscopy analysis.....	80
4.3.2	TEM analysis.....	82
4.3.3	Structural analysis of nanowhiskers	83
4.3.4	Fluorescence quenching and lifetime	85
4.3.5	C-AFM and surface potential analysis	88
4.3.6	Photoelectrochemistry of Cells	94
4.3.7	Electrochemical impedance spectroscopy of cells	97
4.4	Summary.....	101
4.5	References.....	101
5 Effect of FRET and carbon dots on light harvesting capability of CdS QDs		
based photoanode.....		103
5.1	Introduction.....	103
5.2	Experimental.....	104
5.2.1	Synthesis of C-dots.....	104
5.2.2	Fabrication of the photoanode.....	104
5.2.3	Preparation of the MWCNT electrode	105
5.2.4	Preparation of the gel electrolyte.....	105
5.3	Results and discussion	107
5.3.1	Energetics and donor-acceptor distances by HRTEM.....	107
5.3.2	Characterization of C-dots.....	111
5.3.3	SEM images of MWCNTs	112
5.3.4	Fluorescence and lifetime studies.....	113
5.3.5	Forster radius calculation	118
5.3.6	Performance of solid-state FRET cells.....	121
5.3.7	EIS analysis.....	127
5.4	Summary.....	128
5.5	References.....	129
6 FRET from a Lucifer yellow dye to CdS/CdSe QDs leads to enhanced solar		
cell performance		130
6.1	Introduction.....	130
6.2	Experimental.....	131
6.2.1	Fabrication of photoanode.....	131
6.2.2	Synthesis of PEDOT microfibers	132
6.2.3	Synthesis gel electrolyte.....	132
6.3	Results and discussion	133

6.3.1	Characterizations of TiO ₂	133
6.3.2	HRTEM analyses	134
6.3.3	Energetics of the FRET cell.	136
6.3.4	Structure and CV of LY dye.....	137
6.3.5	Emission analysis	138
6.3.6	Time-resolved emission decay	140
6.3.7	Electrolyte modification	144
6.3.8	Forster radius and energy transfer rate	145
6.3.9	Conduction via PEDOT microfibers	146
6.3.10	Solar Cell Performance	148
6.3.11	EIS analysis.....	153
6.4	Summary.....	154
6.5	References.....	155
7 A plasmonic solar cell integrated with a carbon nanotubes supercapacitor		
in a single device: Unifying energy conversion and storage.....		157
7.1	Introduction.....	157
7.2	Experimental.....	157
7.2.1	Preparation of Au fibers	157
7.2.2	Fabrication of photoanode.....	158
7.2.3	Fabrication of MWCNT electrodes	159
7.2.4	Synthesis of electrolytes and cells.....	160
7.3	Results and discussion	160
7.3.1	HRTEM analyses	160
7.3.2	Optical characterization.....	162
7.3.3	Emission and lifetime studies.....	164
7.3.4	Photoelectrochemical response	167
7.3.5	Photovoltaic supercapacitor performance	170
7.3.6	EIS analysis	176
7.4	Summary.....	177
7.5	References.....	178
8 Plasmonic effects of Au encapsulated carbon dots increase the efficiency of		
a ZnO based DSSC		180
8.1	Introduction.....	180
8.2	Experimental.....	181
8.2.1	Au@C-dots and photoanode fabrication	181
8.2.2	MWCNT electrode and DSSC construction	182
8.3	Results and discussion	182

8.3.1	Structural features of Au@C-dots and ZnO nanorods	182
8.3.2	SEM and TEM analysis.....	184
8.3.3	Structural characterizations of ZnO and Au@C-dot	186
8.3.4	Plasmonic and interactive effects of Au@C-dots	186
8.3.5	Emission and lifetime studies.....	187
8.3.6	Energy transfer between ZnO and N719 dye	189
8.3.7	Plasmonic and FRET enabled DSSCs.....	193
8.3.8	Photoelectrochromic cells with MoO ₃ as coloring counter electrode.....	195
8.3.9	Fabrication of the MoO ₃ electrode	196
8.3.10	SEM analysis.....	196
8.3.11	Structural characterization of MoO ₃	196
8.3.12	Photoelectrochromic response.....	197
8.4	Summary.....	201
8.5	References.....	201
9	Summary and conclusions	203
	List of Publications	206

List of Figures

Figure 1.1: (a) Schematic and (b) working principle of a DSSC.....	3
Figure 1.2: The density of energy states of materials from bulk to quantum dots.....	6
Figure 1.3: Schematics of size dependent energy level alignments of QDs.....	6
Figure 1.4: Schematic of multiple exciton generation in a QD.....	7
Figure 1.5: Schematic of a QDSSC.....	9
Figure 1.6: Different technique used for QD film deposition.....	11
Figure 1.7: Dependency of electron transfer rate on particle size of CdSe QDs.....	12
Figure 1.8: (a) CdSe QDs / TiO ₂ nanoparticles, CdSe QDs / TiO ₂ nanotubes and (b) CdSe solution and films prepared using QDs of different sizes.....	13
Figure 1.9: IPCE response of CdSe QDs with different diameters (a) on the TiO ₂ nanoparticles (b) on TiO ₂ nanotubes.....	13
Figure 1.10: (a) Schematic of a Mn doped CdS/TiO ₂ based solar cell and (b) J-V characteristics of different photoanodes.....	14
Figure 1.11: Electron transport dynamics in a CdSe-C ₆₀ system.....	15
Figure 1.12: (a)IPCE and (b) the photocurrent response of the electrodes to on-off cycles of illumination of C ₆₀ , CdSe quantum dots and CdSe-C ₆₀ clusters on SnO ₂ :F electrode.....	16
Figure 1.13: (a) Illustration of SWNTs and (b) stacked cup carbon nanotubes based solar cells.....	17
Figure 1.14: (a) Emission decay measurements and (b) photocurrent response of the electrodes to on-off cycles of illumination.....	17
Figure 1.15: Schematic of graphene based solar cells.....	18
Figure 1.16: (a) IPCE and (b) energy band diagram of bilayer system.....	18
Figure 1.17: (a) IPCE and (b) photocurrent <i>versus</i> time responses of (i) CdSe, (ii) CdSe/GO and (iii) CdSe/rGO.....	19
Figure 1.18: Schematic representation of the interplay between the LSPR and excitons.....	20
Figure 1.19: J-V spectra for Au@TiO ₂ and Au@SiO ₂ based DSSC.....	21
Figure 1.20: (a) Absorption and (b) J-V spectra of the device with and without plasmons.....	22
Figure 1.21: (a) Schematic of a plasmon enhanced DSSC, (b) plasmon enhanced DSSC avoid electron-hole recombination due to thinner photoanode layer and (c) mechanism of plasmon enhanced DSSC and (d) IPCE spectra of the DSSC with and without the Ag@TiO ₂	23

Figure 1.22: (a) Schematic representation of FRET and (b) overlap between the emission of donor and absorbance of acceptor.....	24
Figure 1.23: (a) Schematic representation of the system based on FRET and (b) energy level alignment of each component relative to vacuum.....	25
Figure 1.24: (a) Schematic of a FRET based photovoltaic device and (b) J-V plots for mercaptopropionic acid/CdSe, SQSH and CdSe/SQSH photoanodes.....	25
Figure 1.25: (a) Schematic representation of the cell structure (b) energy level alignment and (c) IPCE spectra of the devices.....	26
Figure 2.1: (a) Schematic of SEM and (b) photograph of SEM Instrument used herein.....	37
Figure 2.2: (a) A schematic of TEM and (b) photograph of TEM instrument used herein.....	38
Figure 2.3: (a) A schematic of AFM and (b) photograph of AFM instrument used herein.....	40
Figure 2.4: Schematic diagram of UV-Vis spectrophotometer.....	42
Figure 2.5: Photograph of UV-Vis spectrophotometer used herein.....	43
Figure 2.6: Jablonski diagram.....	44
Figure 2.7: (a) A schematic of a fluorescence spectrophotometer and (b) photograph of fluorescence spectrometer used herein.....	45
Figure 2.8: (a) Schematics of XRD, b) Photograph of XRD used herein.....	47
Figure 2.9: (a) A schematic of Raman Spectrometer and (b) photograph of Raman Spectrometer used herein.....	48
Figure 2.10: (a) A typical J-V scan and its components. (b) Photograph of the solar simulator used for the solar cell characteristics.....	49
Figure 2.11: Schematics of the IPCE measurement system and (b) photograph of the IPCE equipment used herein.....	50
Figure 2.12: (a) cyclic voltammogram of 5 mM ferro-ferricyanide redox couple in phosphate buffer saline (PBS) (pH 7.0, 50 mM, 0.9% NaCl) and (b) A photograph of Autolab PSTAT system used herein.....	52
Figure 2.13: (a) Nyquist plot with impedance vector and Bode plots showing (b) log Z and (c) phase angle <i>versus</i> frequency.....	55
Figure 3.1: Schematic showing fabrication of TiO ₂ /CdSe/FGO/Au electrode.....	58
Figure 3.2: HRTEM images of components of photoanode TiO ₂ /CdSe/FGO/Au.....	60
Figure 3.3: (a) EDS plot and (b) Raman spectrum of FGO.....	61
Figure 3.4: (a) Digital photographs of solutions of components of photoanode and (b) absorbance of different components of photoanode TiO ₂ /CdSe/FGO/Au.....	62
Figure 3.5: Main edge absorption spectra plotted as (a) $(\alpha h\nu)^2$ and (b) $(\alpha h\nu)^{1/2}$ vs. photon energy (h ν) for CdSe QDs and TiO ₂ respectively.....	63
Figure 3.6: Photoluminescence spectra of colloids. (a) CdSe +Au (b) CdSe+FGO (c) FGO + Au and (d) CdSe + (FGO + Au).....	65

Figure 3.7: Time resolved fluorescence decay profiles of different components of photoanode.....	68
Figure 3.8: Schematics of the energy band diagram of TiO ₂ /CdSe/FGO/Au composite and possible mode of electron transfer.....	70
Figure 3.9: a schematic of the configuration employed for C-AFM measurements. Representative current and topography images of TiO ₂ /CdSe/FGO/Au composite film.....	72
Figure 3.10: a) Photovoltage and b) photocurrent on-off cycles for photoelectrochemical cells based on TiO ₂ /CdSe/FGO/Au. Measurements were performed under zero applied current or bias.....	74
Figure 3.11: (a) J-V characteristics and (b) IPCE spectra of TiO ₂ /CdSe/FGO/Au composite based photoelectrochemical cells.....	76
Figure 4.1: Optical micrographs of (a) neat C ₆₀ (b) C ₆₀ nanowhiskers (c) enlarged view of the tubular C ₆₀ nanowhiskers (d) CdS/C ₆₀ electrode (e) CdS/C ₆₀ (NW) electrode showing the nanowhiskers embedded in CdS and (f) MWCNT/PPDA electrode.....	82
Figure 4.2: TEM images of C ₆₀ NW of different magnifications.....	83
Figure 4.3: Raman spectra of (a) C ₆₀ (i) and C ₆₀ (NW) (ii) (b) and (c) show the deconvoluted peaks (d) X-ray diffractograms of neat C ₆₀ and C ₆₀ (NW); the hkl values are shown in parenthese.....	84
Figure 4.4: (a) Emission spectra (b) Time resolved fluorescence decay traces of neat CdS, CdS/C ₆₀ and CdS/C ₆₀ (NW) electrodes.....	87
Figure 4.5: Concurrent topography and current images of neat CdS, CdS/C ₆₀ , and CdS/C ₆₀ (NW) electrodes and resultant I-V curves obtained after averaging 15 I-V curves recorded at 15 equidistant spots.....	90
Figure 4.6: Topography and surface potential maps of neat CdS, pristine C ₆₀ , and C ₆₀ (NW) electrodes.....	92
Figure 4.7: Energy band diagram showing the possible modes of electrons transfer.....	93
Figure 4.8: (a) I-V characteristics of photoelectrochemical cells based on CdS/C ₆₀ (NW), CdS/C ₆₀ and neat CdS electrodes as the photoanodes with (a) MWCNT/PPDA film as the counter electrode and (b) Pt as the counter electrode.....	95
Figure 4.9: IPCE measurements of three photoelectrochemical cells based on CdS/C ₆₀ (NW), CdS/C ₆₀ and neat CdS electrodes as the photoanodes with (a) MWCNT/PPDA film as the counter electrode and (b) Pt as the counter electrode.....	97
Figure 4.10: (a) Nyquist plots recorded under an ac amplitude of 10 mV for cells based CdS/C ₆₀ (NW) electrode with MWCNT/PPDA and Pt as the counter electrode under an open circuit bias of +0.550 V (b) bode plots of and phase angle versus log frequency of the different counter electrodes.....	100
Figure 5.1: Digital photographs of the polymeric gel with and without CuPc, C-dot suspension and the device configuration.....	106
Figure 5.2: Energy band diagram of the FRET cell.....	108

Figure 5.3: HRTEM images of (a) ZnS/CdS/ZnS QDs, (b) C-dots, (c), (d) and (e) overlapping lattice fringes co-exist with an amorphous phase in a CdS/C-dot/CuPc co-assembly.....	111
Figure 5.4: (a) Absorption spectrum of the C-dots dispersed in the deionized water, (b) cyclic voltammogram of the C-dot solution and (c) Raman spectrum of an electrophoretically deposited C-dot film.....	112
Figure 5.5: SEM images of MWCNTs.....	112
Figure 5.6: (a) Absorption spectrum of CuPc solution and the emission spectrum of the ZnS/CdS/ZnS electrode, (b) quenching of emission profile of the ZnS/CdS/ZnS electrode upon exposure to different concentrations of CuPc solutions (c) emission spectra of ZnS/CdS/ZnS, C-dot, CdS/C-dot and ZnS/CdS/ZnS/C-dot electrodes (d) Time resolved fluorescence decay traces of different components of photoanodes and in presence and absence of CuPc solution.....	116
Figure 5.7: (a) PL decay trace of ZnS/CdS/ZnS/C-dot (b) Mott-Schottky plot of a C-dot dispersion.....	117
Figure 5.8: Integrated fluorescence intensity <i>versus</i> absorbance of donor.....	119
Figure 5.9: IPCE spectra of quasi solid-state solar cells with various components of photoanode ZnS/CdS/ZnS/C-dot in the presence and absence of CuPc solution.....	123
Figure 5.10: J-V characteristics of quasi solid-state solar cells with various components of photoanode ZnS/CdS/ZnS/C-dot in the presence and absence of CuPc solution.....	126
Figure 5.11: J-V characteristics of control cells with either donor or acceptor as photoanodes.....	126
Figure 5.12: Nyquist plots recorded under an ac amplitude of 10 mV and a zero dc bias for quasi solid-state solar cells based on photoanodes with and without C-dot.....	128
Figure 6.1: (a) X-ray diffractograms and (b) Lattice scale image of TiO ₂	133
Figure 6.2: HRTEM images of CdS/CdSe QDs and CdS/CdSe/LY assembly.....	135
Figure 6.3: (a) Energy levels of a TiO ₂ /CdS/CdSe/ZnS–LY/PEDOT/S ²⁻ assembly (b) schematic of a FRET cell and (c) photographs of different components of FRET cell.....	137
Figure 6.4: (a) Structure of LY dye and (b) Cyclic voltammogram of an aqueous solution of a LY dye.....	138
Figure 6.5: (a) Absorption and fluorescence spectra of the LY donor dye (b) overlap of absorption of the TiO ₂ /CdS/CdSe/ZnS electrode and emission of the LY dye (c) fluorescence quenching of LY dye in the presence of TiO ₂ /CdS/CdSe/ZnS electrode (d) emission of pristine TiO ₂ /CdS/CdSe/ZnS electrode and for the same electrode in the presence LY dye.....	140
Figure 6.6: Time resolved fluorescence decay traces of Lucifer yellow dye in the presence and absence of TiO ₂ /CdS/CdSe/ZnS electrode, (b) CdS/CdSe/ZnS electrode in the presence and absence of LY dye solution (c) TiO ₂ /CdS/CdSe/ZnS electrode in the presence of an aqueous solution of PEDOT microfibers.....	143

Figure 6.7: (a) SEM micrograph of PEDOT microfibers, (b) cyclic voltammograms of a PEDOT microfibers/S ²⁻ solution and (c) Nyquist plots of a PEDOT microfibers/S ²⁻ solution.....	148
Figure 6.8: IPCE spectra of quasi solid-state solar cells (a) the TiO ₂ /CdS/CdSe/ZnS–LY/S ²⁻ cell with different concentrations of LY dye and (b) the donor-acceptor TiO ₂ /CdS/CdSe/ZnS–LY/S ²⁻ cell the acceptor only TiO ₂ /CdS/CdSe/ZnS–S ²⁻ cell.....	150
Figure 6.9: J-V characteristics of quasi solid-state solar cells with the following photoanode architectures: (a) donor-acceptor TiO ₂ /CdS/CdSe/ZnS–LY/ S ²⁻ and acceptor only TiO ₂ /CdS/CdSe/ZnS– S ²⁻ cells and (b)TiO ₂ /CdS/CdSe/ZnS–LY/PEDOT/S ²⁻ and TiO ₂ /CdS/CdSe/ZnS–PEDOT/S ²⁻ cells.....	152
Figure 6.10: Nyquist plots recorded under an ac amplitude of 10 mV and a zero dc bias for quasi solid-state cells (a) with PEDOT and without PEDOT (b) donor-acceptor solar cell, and acceptor only cell.....	154
Figure 7.1: Electron microscopy images of Au fibers and TiO ₂ /CdS/Au film.....	162
Figure 7.2: (a) Absorption spectra of a (i) TiO ₂ /CdS and (ii) a TiO ₂ /CdS/Au film, (b) absorption spectra of a TiO ₂ /CdS/Au film under white LED irradiation at different intervals and (c) absorption spectra of the Au colloid with various concentrations of CdS QDs.....	164
Figure 7.3: (a) Emission and (b) lifetime analysis of a TiO ₂ /CdS film, a TiO ₂ /CdS/Au film.....	166
Figure 7.4: (a) Energy band diagram of a plasmonic solar cell showing the possible electron transfer modes and (b) a schematic of the solar powerd supercapacitor.....	167
Figure 7.5: (a) J-V charactristics of the cell (b) IPCE spectra and (c) photocurrent on-off cycles of a cell based on TiO ₂ /CdS and TiO ₂ /CdS/Au as photoanode.....	169
Figure 7.6: Schematics of (a) the photovoltaic supercapacitor configuration.....	173
Figure 7.7: Charge-discharge characteristics of the solar powered supercapacitor.....	174
Figure 7.8: (a) Cyclic voltammogram of the MWCNT supercapacitor (b) specific capacitance change as a function of the number of cycles under light on-off conditions.....	176
Figure 7.8: Nyquist plots recorded under an ac amplitude of 10 mV for (a) photoanodes based on TiO ₂ /CdS and TiO ₂ /CdS/Au and (b) the MWCNT.....	177
Figure 8.1: XPS survey spectrum of Au@C-dots.....	183
Figure 8.2: Electron microscopy images of Au@C-dot and ZnO nanorods.....	185
Figure 8.3: (a) XRD pattern of ZnO nanorods (b) Raman spectrum of Au@C-dots.....	186
Figure 8.4 Absorption spectra of N719, Au@C-dot, ZnO/N719 and ZnO/N719/Au@C-dot.....	187
Figure 8.5: (a) Emission spectra of aqueous solutions of Au@C-dots with different concentrations of N719 and life time decay analysis of Au@C-dot and Au@C-dot/N719.....	189

Figure 8.6: (a) Spectral overlap between the absorption of the N719 dye and the emission of ZnO nanorods (b) emission spectrum and (c) emission decay profiles of ZnO film and the ZnO/N719 electrode.....	192
Figure 8.7: Energy level diagram of (a) the ZnO/N719/Au@C-dots photoanode and (b) electron propagation and FRET in the corresponding DSSC.....	193
Figure 8.8: (a) IPCE spectra and (b) J-V characteristics of DSSCs with the following photoanodes: ZnO/N719 and ZnO/N719/Au@C-dots.....	195
Figure 8.9: SEM images of MoO ₃ film.....	196
Figure 8.10: (a) XRD pattern and (b) Raman spectrum of MoO ₃	195
Figure 8.11: J-V characteristics of solar/photoelectrochromic cells with MoO ₃ as a counter electrode.....	198
Figure 8.12: Photoelectrochromic cell configurations with MoO ₃ as the coloring counter electrode.....	199
Figure 8.13: Transmittance as a function of wavelength of MoO ₃ as the coloring counter electrode of a photoelectrochromic device.....	200

List of Tables

Table 1.1: Performance parameters of quantum dot solar cells.....	26
Table 2.1: List of chemicals used in experimental work.....	32
Table 3.1: Kinetic parameters of emission decay analysis of photoanode electrode films.....	67
Table 3.2: Solar cell parameters of cells.....	75
Table 4.1: Kinetic parameters of emission decay analysis of photoanode electrode films.....	86
Table 4.2: Electrochemical impedance spectroscopy results obtained by fitting.....	99
Table 5.1: Kinetic parameters of emission decay analysis of photoanode films.....	115
Table 5.2: Solar cell parameters of cells.....	125
Table 6.1: Kinetic parameters of emission decay analysis.....	142
Table 6.2: Solar cell parameters of cells.....	152
Table 7.1: Kinetic parameters of emission decay analysis.....	165
Table 7.2: Solar cell parameters of cells.....	169
Table 8.1: Kinetic parameters of emission decay analysis.....	192
Table 8.2: Solar cell parameters of cells.....	195

Chapter 1

Introduction

1.1 Solution processed quantum dot sensitized solar cells: An overview

Global energy utilization is anticipated to increase at the rate of about 2% per year for the next 25 years. Mankind cannot afford to continue to progress by relying on sources of energy that emit greenhouse gases. The best alternative is the maximum utilization of other energy resources such as solar, wind, water, wave etc. Among all, solar power has great potential as a renewable source of energy. Solar energy has the benefit of being stable and abundant; around 130,000TW of solar radiation falls upon the earth surface. If 0.1% of the solar energy were harvested efficiently, the world's energy crisis can be abolished. Ever since the French scientist, Edmond Becquerel, discovered the photoelectric effect, researchers and engineers have been infatuated with the idea of converting light into electric power or chemical fuels, and the present challenge is to develop a system that can convert solar energy into electricity efficiently.

1.2 History

The region between 400-1100 nm has the highest photon density in the A.M 1.5 solar spectrum. Semiconductors are considered as the traditional photovoltaic materials, since they can absorb energy greater than or equal to their band gap. First generation solar cells are based on the single crystalline silicon solar cells. Silicon has a band gap of 1.1 eV, and it can absorb the entire visible as well as a part of the infrared region. The first modern photovoltaic (PV) solar cell, worked on the concept of a p-n junction diode. Silicon (Si) [p/n based] cells were developed by Chapin et al., in 1954. Power conversion efficiencies (PCEs) in single crystalline Si cells, are now quite high, ~ 24 % has been achieved in the lab, but they suffer from high cost of manufacturing.^[1] These high production costs are due to the requirement of

extremely pure starting materials, in addition to sophisticated technical processing procedures.

Thin film solar cells are classified as the second generation solar cells. CdTe is considered to be the best performer in this genre.^[2] The working principle is the same as that of silicon based solar cells. Yet another material, copper indium gallium sulfide, selenide (CIGS) has also aroused considerable research interest; these materials offer high efficiencies. They are less costly but the efficiencies need to be further increased to match with those of the silicon based solar cells.

In 1991, Michael Gratzel introduced the dye sensitized solar cells (DSSCs)^[3] and the era of the third generation solar cells commenced. Thereafter, these solar cells have attracted enormous research effort and interest since they are capable of providing high efficiency at highly reduced costs. Cells utilizing this technology provide an efficiency of about 15 % at the lab level and 10 % at the commercial level.^[4,5] Recently, Quantum Dot Sensitized Solar Cells (QDSSCs) have shown promise as cost-effective but efficient alternates to DSSCs; efficiencies as high as ~ 5% have been achieved in the non-perovskite domain.^[6] This dissertation deals with third generation solar cells, with a strong focus on QDSSCs.

1.3 Structure and mechanism of the dye sensitized solar cells

To date photovoltaics- has been predominantly controlled by solid state junction devices, mainly made of silicon. But this dominance has been countered to some extent by the emergence of the DSSCs. DSSCs comprise of a working electrode which typically consists of a nanosized, mesoporous wideband gap semiconducting material such as TiO₂, ZnO or SnO₂ which is deposited over fluorine doped tin oxide glass substrate (FTO or SnO₂:F), and dye molecules which can act as the light sensitizers.^[7-10] Ruthenium polypyridyl based dyes are regarded as the most efficient dyes. Due to the high surface area of the wide band gap

semiconductor, a large amount of the dye can be absorbed. A thin layer of platinum deposited over FTO is employed as a counter electrode. In a photoelectrochemical cell (PEC), the electrolyte should be a redox couple so that it can function as a hole transport layer. An epoxy is used to seal the edges of the device. The working of a DSSC is shown in **Figure 1.1**.

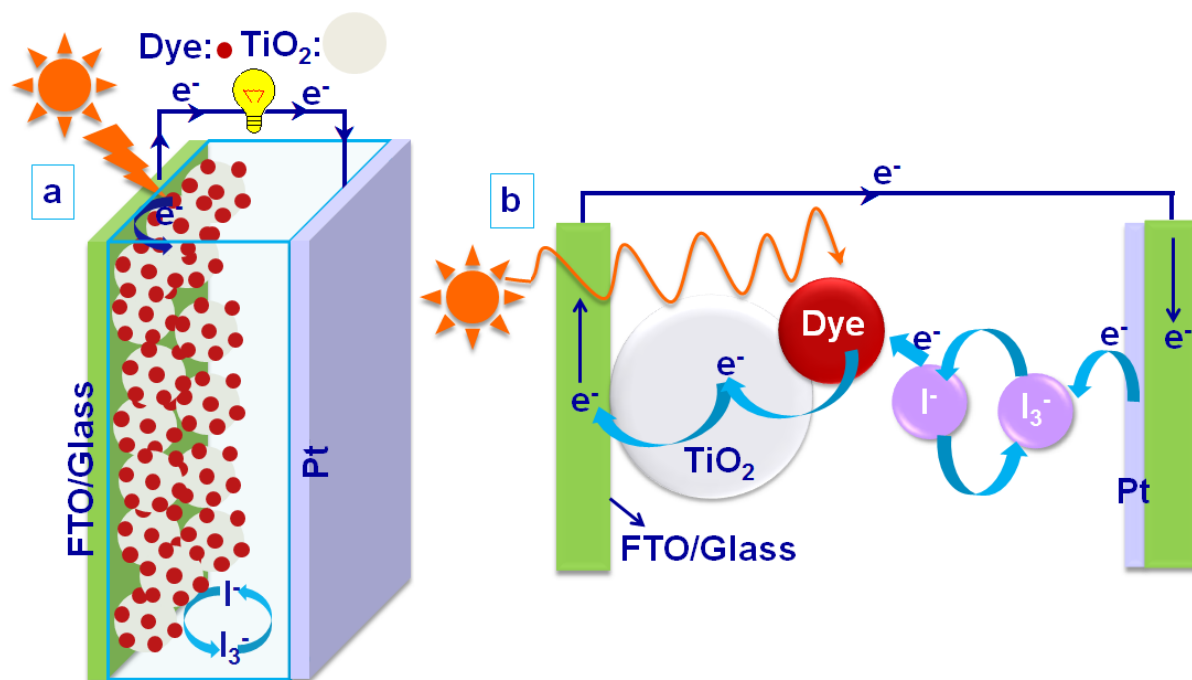


Figure 1.1: (a) Schematic and (b) working principle of a DSSC.

In a typical PEC or a DSSC, the electrons of the dye are excited from the valence band (VB) to the conduction band (CB), by absorption of solar energy. The excited electrons are transferred to the conducting substrate through the CB of the wide band gap semiconductor. The electrons reach the counter electrode through the external circuit. The electrons again return to the photoanode (TiO₂/Dye assembly) by the reduction of the oxidized species of the redox electrolyte. Subsequently, the regeneration of the oxidized dye is accomplished by the acceptance of electrons from the reduced redox component. In this way, solar radiation is converted into electricity.

The initial dye reported in Gratzel's original solar paper had the ruthenium tris(bipyridine) structure and it showed an absorption onset at 700 nm.^[9] Nowadays, dyes ranging from porphyrins, organic, to other metal based pyridyl compounds are being used.^[11,12] The N719 and N3 dyes are the best performing dyes and they are the ruthenium pyridyl based dyes. The electrolyte plays an important role in liquid junction solar cells. An ideal electrolyte must transport reduced and oxidized species across the cell between the working and counter electrodes rapidly in order to complete the circuit. At the cathode, the electrolyte the (I₂/I⁻ redox couple in a DSSC) undergoes reduction by accepting electrons and, I₃⁻ is converted to I⁻. The overall reaction is represented in equation 1.



For the efficient conversion of light into electricity, certain conditions need to be met. The first one is that the lowest unoccupied molecular orbital (LUMO) of the dye should be more negative in potential (*versus* Normal Hydrogen Electrode (NHE)) than that of the conduction band edge of TiO₂. This makes the electron transfer process thermodynamically favorable. The dye should be in intimate electrical as well as the chemical contact with TiO₂, to allow fast injection of the photogenerated electrons. Usually, the dye is chemisorbed to TiO₂ through carboxylic acid or sulfanilic acid or through phosphonic acid groups.^[13,14] The highest occupied molecular orbital (HOMO) of the dye should be more positive than that of the redox potential of the electrolyte. Finally, the band gap determines the spectral range of light that it can absorb. The magnitude of the band gap should be such that the dye is capable of absorbing the visible part of the solar spectrum. Currently, ionic liquids are also being incorporated in the electrolyte due to their high viscosity, high boiling points, low volatility, good electrochemical and thermal stability and high conductivity.^[15]

1.4 Quantum dot sensitized solar cells (QDSSCs)

1.4.1 Why quantum dots?

In recent years, nanomaterials have attained a widespread interest, as they allow the development of solar cells with higher efficiencies, in particular, the size dependent properties such as quantization effect in semiconductor nanoparticles can be exploited herein. Quantum dots (QDs) are crystalline semiconductors with sizes in the range of 1-10 nm, each containing 100-100000 atoms. Due to their unique size dependent optical and electronic properties, especially their tunable optical absorption, QDs are useful for solar cell applications. QDs have been used in a wide range of applications such as photovoltaics, light emitting diodes, fluorescent tags for biological imaging etc.^[16,17]

1.4.2 Quantum confinement

Quantum confinement is known as the spatial dimension reduced below the exciton radius.^[18,19] Charge carriers become spatially confined and their energy bands will split into discrete energy levels like that of a molecule. The energy of the bulk material is continuous in three dimensional space. When the system is transformed from bulk to QD, the density of states (DOS) will be gradually reduced. This DOS confinement is shown in the **Figure 1.2**. In case of quantum wells, free charge carriers are confined in one dimension, in quantum wires, charge carriers are confined in two dimensions, whereas in QDs, the charge carriers are confined in all the three directions (**Figure 1.2**).

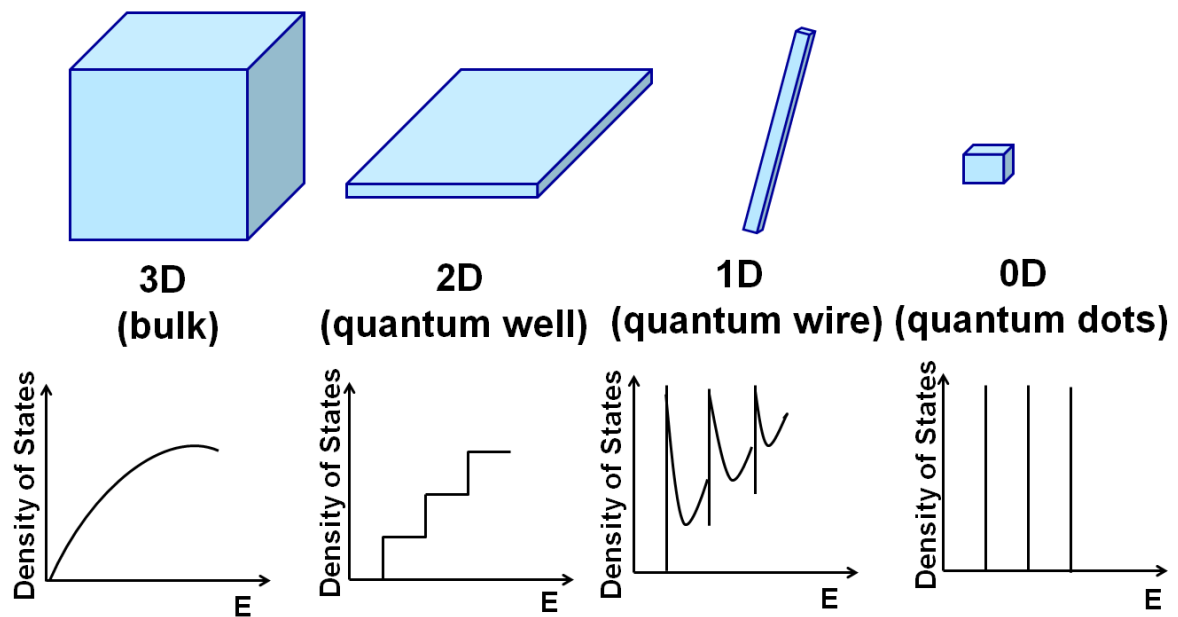


Figure 1.2: The density of energy states of materials from bulk to QDs.

1.4.3 Size-dependent effects

Optical properties of the QDs are merely size dependent. One of the specific advantage of using QDs in solar cells, is the size quantization which allows the tuning of the band gap and hence the visible response.^[20-22] **Figure 1.3** shows the modulation of energy levels by size control.

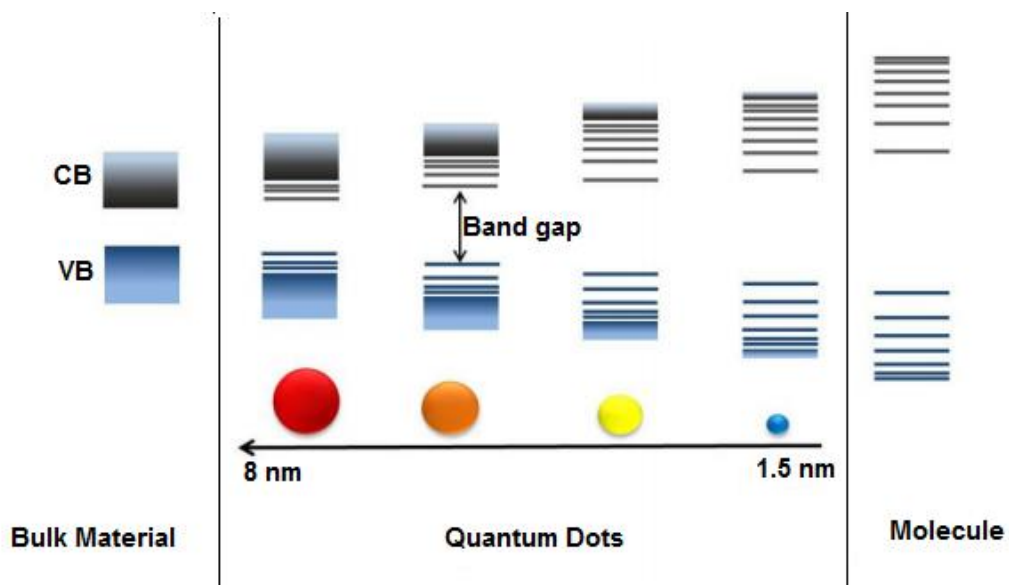


Figure 1.3: Schematic of size dependent energy level alignments in QDs.

With the gradual increase of size, both absorption and fluorescence red shift continuously. The decrease in size of the QDs leads to an increase in band gap.

1.4.4 Multiple exciton generation

QDs can also undergo multiple exciton generation (MEG). Multiple charge carrier generation in semiconductor nano-crystals is also advantageous, when used in a solar cell. Upon illumination, an electron gets excited from the VB to the CB of the QDs by high energy photons and an electron-hole pair (exciton) is generated. If the excitation energy of the photons is at least twice as high as the band gap of the QD, the excess kinetic energy can be utilized to excite another electron from the VB through impact ionization. As a result, by impinging one photon, 2 excitons are generated. The quantum efficiency can therefore exceed 100%. MEG was first demonstrated in PbSe QDs.^[23] Later it was illustrated in PbS^[24] and CdSe/ZnS (core/shell)^[25] architectures. MEG, can in principle, lead to higher overall efficiencies (**Figure 1.4**).

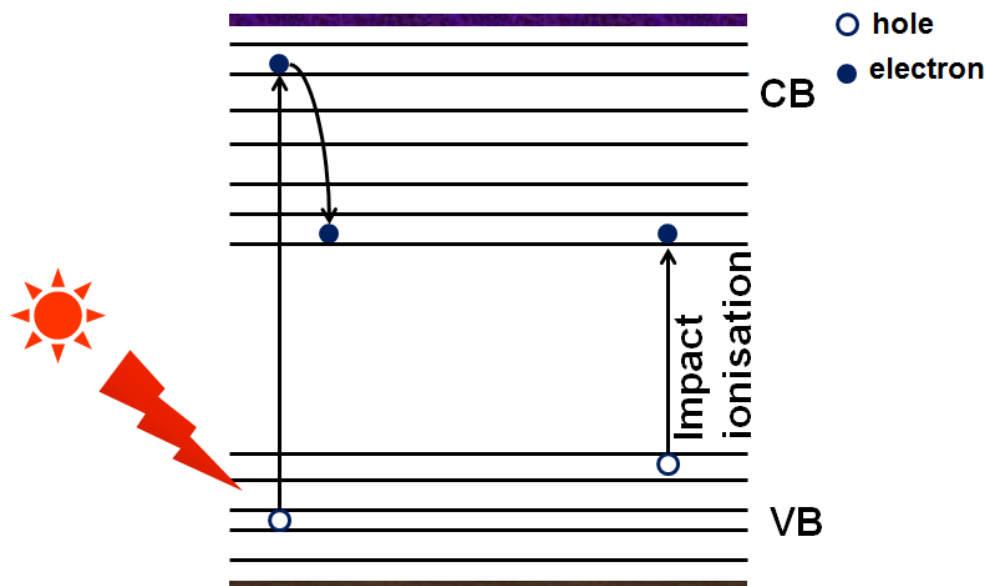


Figure 1.4: Schematic of multiple exciton generation in a QD.

1.4.5 QDs in solution processed cells

Various geometric shapes of semiconductor nanocrystals such as spheres, tubes, wires, rods etc., have been used in the past in PV devices in order to improve the efficiency of solar cells.^[26] QDSSCs are promising, as they can be fabricated by inexpensive means and can offer reasonably high efficiencies. There also exists an exciting possibility of increasing efficiency beyond the traditional Shockley and Queisser limit of 32%.^[27] Moreover, by tuning the size of the dots, the optical properties can also be tuned. To date, mesoporous metal oxides sensitized with various QDs such as CdS,^[28] CdSe,^[29] PbS,^[30] InP,^[31] ZnSe,^[32] PbSe,^[33] and InAs^[34] have been widely explored; as these QDs absorb the visible light radiation of solar spectrum. Even though, a QDSSC, according to theory, can offer higher efficiency, the reported efficiencies are still low, typically, in the range of 3-6%.^[35] But the ease of processing QDs by wet colloid chemistry, adjustable band gap and their capability to generate more electron-hole pairs from a single photon impingement, render them to be suitable candidates for practical use. Quantum confinement, mini band and Auger recombination effects, are cumulatively known to boost exciton concentration, quantum yield, hot electron lifetime and therefore, the overall efficiency of QDSSCs.^[36,37] Typically, lower band gap semiconductors will absorb visible light radiation, and since the band gap is small, electron-hole recombination is faster which results in a lower efficiency. Along with QDs, incorporation of a large band gap semiconductor such as TiO₂, ZnO, SnO₂ can improve charge transport by restricting electron hole recombination to a great extent. In this regard, researchers have extensively investigated CdS-TiO₂,^[38,39] TiO₂-CdSe,^[40] SnO₂-CdSe,^[41] based photoanodes in the past.

1.4.6 Working principle of a QDSSC

The working principle of a QDSSC is similar to that of a DSSC. It consists of three components: a working electrode, a counter electrode and an electrolyte. The working

electrode is the photoanode which consists of QDs anchored to the wide band gap semiconductor such as TiO₂, ZnO etc., which, in turn are tethered to a conductive electrode. The electrolyte is usually a S_n²⁻/S²⁻ based redox couple.^[42,43] The schematic shown below displays electron transfer and the current generation. The electron gets excited from the VB of the QD to the CB of the QD, upon illumination of light. The excited electrons are injected from the CB of QD to the CB of TiO₂. Electrons travel through the external circuit and reach the counter electrode, where they are used for the reduction of the electrolyte. The reduced electrolyte then travels through the electrolyte to reach the photoanode. Finally the regeneration of the QDs occurs at the photoanode through the oxidation of the electrolyte species.

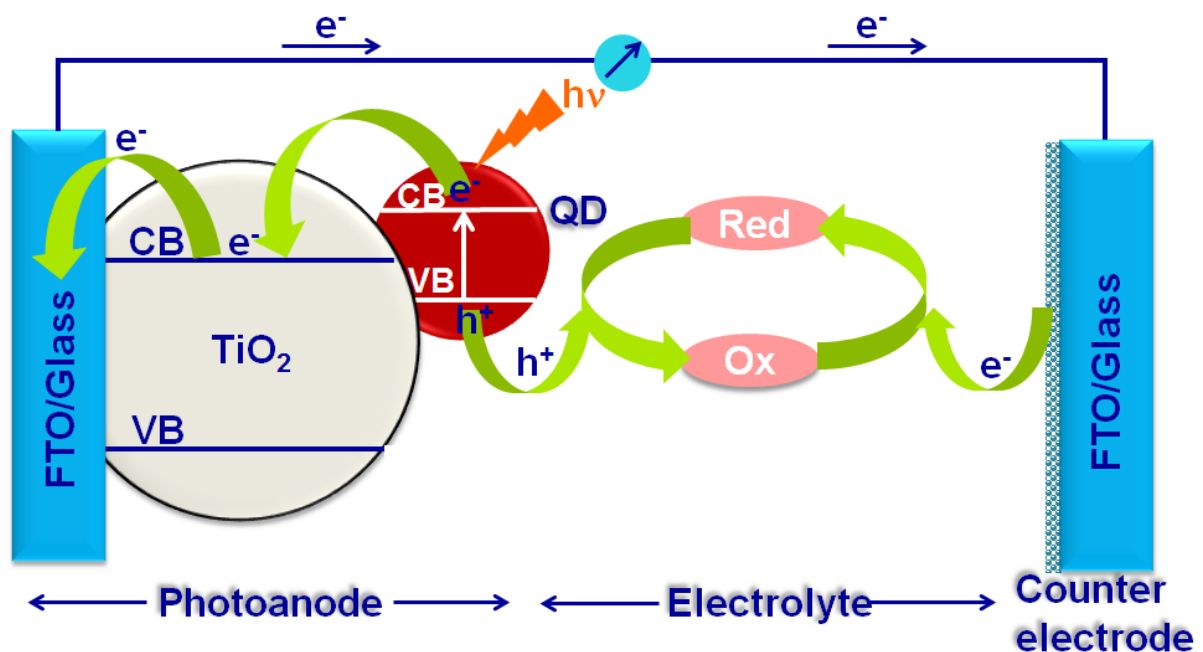
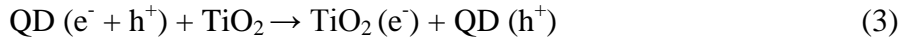


Figure 1.5: Schematic of a QDSSC.

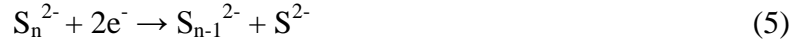
The following phenomena occur in a QDSSC.

At the photoanode:





At the counter electrode:



When a dye is used, the adsorption is limited to a monolayer, whereas in the case of QDs, multilayer sensitization is possible by successive ion layer absorption and reaction (SILAR), which involves the immersion of the electrode in the desired precursor and the species is absorbed by the electrode. The excess ions are removed by rinsing it with the blank solvent. This is followed by immersion in the second precursor solution. The SILAR method, is nowadays, widely being used in the QDSSCs.^[44]

The second commonly used deposition method is the bi-functional linker assisted one. Here, the pre-synthesized QDs are deposited over the wide band gap semiconductor by using a linker molecule in between. The linker typically has a carboxylic group at one end to bind the TiO₂ molecules and the other end has a thiol group to bind the metal ions typically Cd²⁺. Alternatively, pre-synthesized QDs can be deposited over the wide band gap semiconductor, by electrophoresis from their colloid.^[45] Different techniques, generally, used for QD film deposition is shown in **Figure 1.6**.

When the QDs are anchored over the wide band gap semiconductor, a significant quenching of photoluminescence is observed, (for QDs, generally, are luminescent) which indicates a non radiative charge transfer. The decrease in the average lifetime values also supports the non radiative charge transfer mechanism.

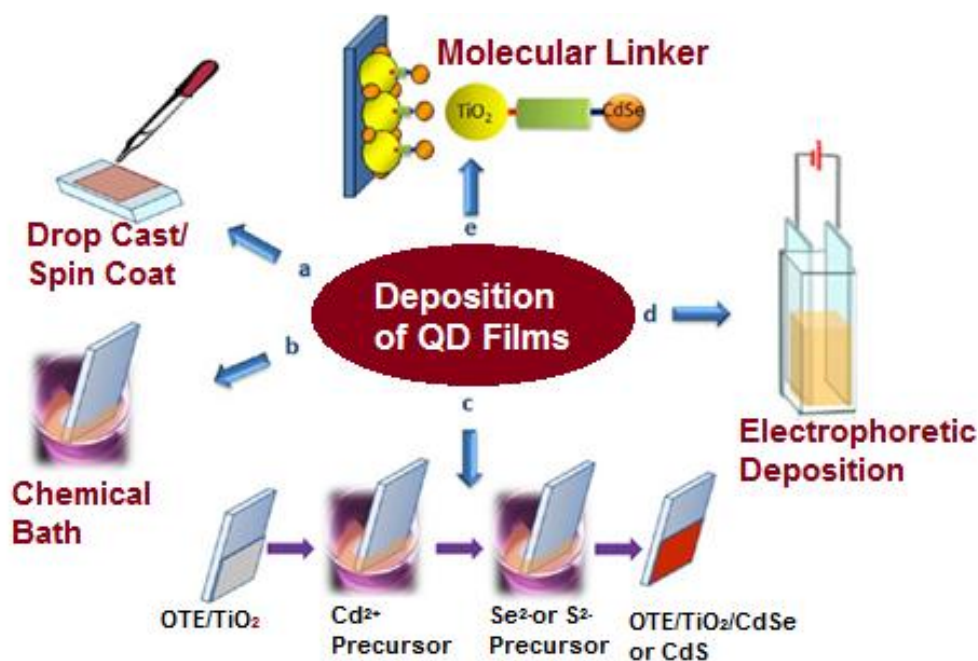


Figure 1.6: Different techniques uses for QD film deposition.^[45] Reprinted with permission from (P. V. Kamat, *J. Phys. Chem. Lett.* **4** (2013) 908-918) Copyright (2014) American Chemical Society.

In a DSSC, the I_2/I^- redox species is generally employed as the electrolyte, but due to the oxidative properties of iodine on QDs, the I_2/I^- couple cannot be used in a QDSSC. An aqueous solution of sodium sulfide (Na_2S) is therefore employed as the electrolyte. This results in the formation of the sulfide/polysulfide redox species (S_n^{2-}/S^{2-}) which is not as effective as the I_2/I^- redox couple in preventing the back electron transfer between the photogenerated electrons and the oxidized species of the electrolyte. However, the good stability QDs in the sulfide electrolytes enables their use in QDSSCs. Equation 6 represents the reaction of S^{2-} and water.



Apart from the sulfide redox couple, other redox species have also been used in QDSSCs, such as the cobalt redox couple, iron redox couple etc.

1.4.7 Size morphology dependence on PEC response

The optical properties of the QD can be tailored by tuning the dot size. Several recent investigations on charge transfer rate from QDs to TiO_2 , reveal that it is a size dependant mechanism. It was found, that as the size of the QD decreases, the electron transfer rate from QD to TiO_2 increases, which is due to the increased energy difference between the CB of the QD and that of TiO_2 . In case of the CdSe/TiO_2 system, faster electron transfer was observed in the 2.4 nm sized CdSe QDs compared to 7.5 nm sized QDs (**Figure 1.7**).^[46] In an earlier report, CdSe QDs of four different particle sizes of 2.3, 2.6, 3.0, 3.7 nm were synthesized. The photocurrent response varied with the particle size. The maximum photocurrent was observed with CdSe QDs of 3.0 nm diameter. As the particle size of QD decreases, photocurrent increases, the CB of the QD shifts to more negative potentials, thus increasing the driving force for the charge transfer, when the particle size is small, the photocurrent density decreases, due to a poor absorption of the incident visible photons.^[44]

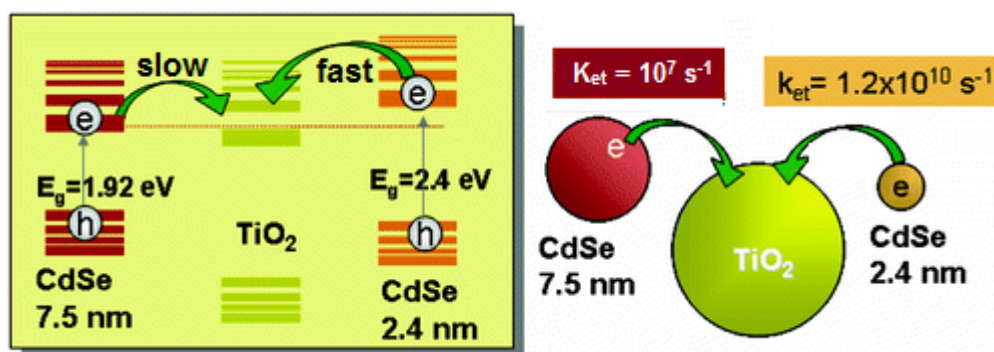


Figure 1.7: Dependence of electron transfer rate on particle size of CdSe QDs.^[46] Reprinted with permission from (A. Kongkanand, K. Tvrdy, K. Takechi, M. K. Kuno, P. V. Kamat, *J. Am. Chem. Soc.* **130** (2008) 4007-4015). Copyright (2014) American Chemical Society.

In the same study, authors showed the effect of same sized CdSe QDs assembled on TiO_2 films: of (a) particle and (b) nanotube morphologies using bifunctional linker molecules (**Figure 1.8**). An improvement in the photoconversion efficiencies (PCEs) was achieved as

charge transport is promoted through the TiO₂ nanotube architecture. Due to the higher surface area of the tubular morphology, there is an increase in the loading of the QDs over the metal oxide which, too improves current collection and hence the efficiency (**Figure 1.9**).

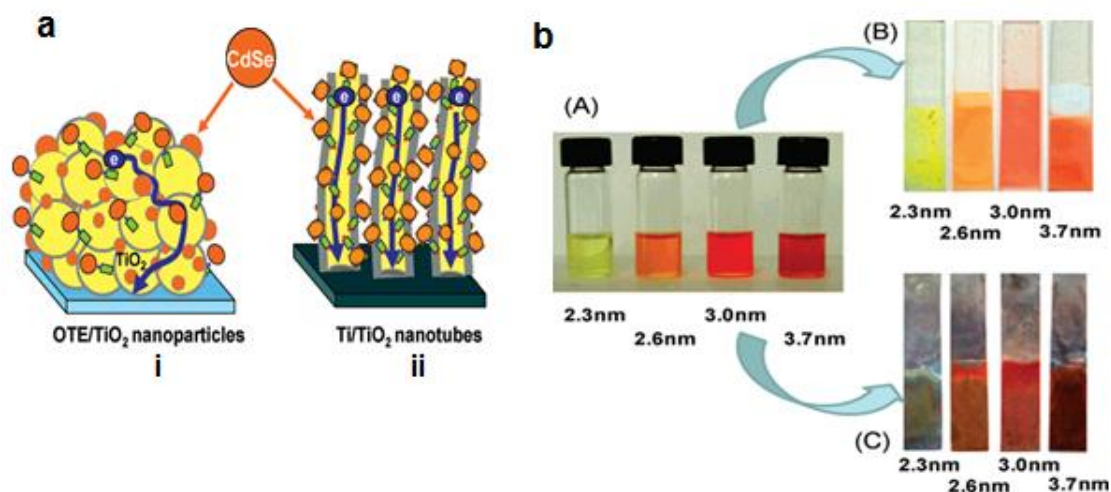


Figure 1.8: (a) CdSe QDs / TiO₂ nanoparticles, CdSe QDs / TiO₂ nanotubes and (b) CdSe solutions and films prepared using QDs of different sizes.^[46] Reprinted with permission from (A. Kongkanand, K. Tvrđy, K. Takechi, M. K. Kuno, P. V. Kamat, *J. Am. Chem. Soc.* **130** (2008) 4007-4015) Copyright (2014) American Chemical Society.

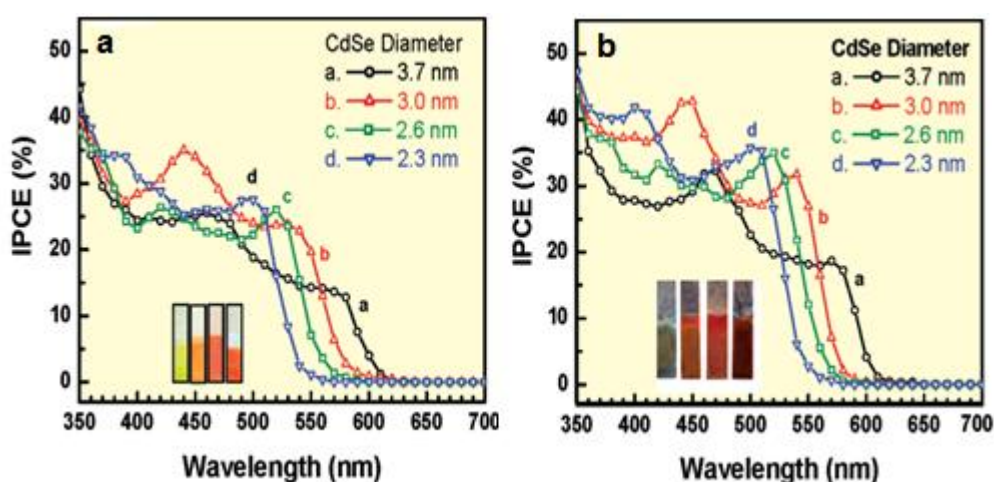


Figure 1.9: IPCE response of CdSe QDs with different diameters (a) on the TiO₂ nanoparticles (b) on TiO₂ nanotubes.^[46] Reprinted with permission from (A. Kongkanand, K. Tvrđy, K. Takechi, M. K. Kuno, P. V. Kamat, *J. Am. Chem. Soc.* **130** (2008) 4007-4015) Copyright (2014) American Chemical Society.

While TiO_2 is the most commonly used wide band gap semiconductor, other semiconductors such as ZnO , SnO_2 have also been studied and some examples are summarized here. QD sensitized ZnO nanowire arrays were reported and oxygen plasma treatment was found to activate the ZnO surface, resulting in an increased anchoring of QDs. Upon photoexcitation, excitons were generated in CdSe QDs and subsequently injected from CdSe QDs to ZnO nanowires.^[47] ZnO nanorods and CdSe assembly showed higher incident photon conversion efficiency (IPCE) maximum of 25% in the visible light region (450 nm).^[48] Hossain et al., reported PbS sensitized SnO_2 QDSSCs, which can presented a PCE of 2.23% and a high photocurrent density of 17.3 mA cm^{-2} .^[49]

Kamat's group demonstrated that by employing Mn^{2+} doping of CdS , midgap states are created by Mn doping, and these states trap electrons and screen them from electron hole recombination. As a consequence, PCE increased significantly. Mn doped CdS/CdSe QDs deposited on mesoporous TiO_2 film, as the photoanode assembly, delivered a PCE of 5.4 %, wherein a $\text{Cu}_2\text{S}/\text{graphene}$ composite was employed as the counter electrode and sulfide/polysulfide as the electrolyte (**Figure 1.10**).^[50]

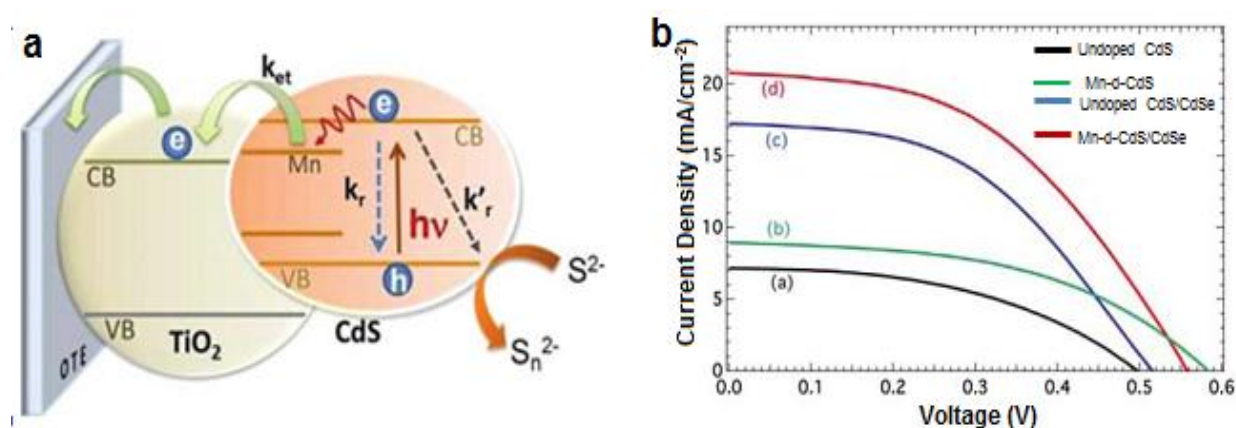


Figure 1.10: (a) Schematic of a Mn doped CdS/TiO_2 based solar cell and (b) J-V characteristics of different photoanodes.^[50] Reprinted with permission from (P. K. Santra, P. V. Kamat, *J. Am. Chem. Soc.* **134** (2012) 2508-2511) Copyright (2014) American Chemical Society.

1.4.8 Role of carbon nanostructures in QDSSCs

The major challenge in a QDSSC is to ensure an efficient transfer of the photogenerated electrons as soon as they are generated upon illumination. This can be achieved by use of carbon nanostructures. High conductivity and electron accepting properties of carbon nanostructures make them promising for solar cells. Employing carbon nanostructures in a QDSSC permits faster charge and transport and this can result in a higher PCE.

1.4.8.1 Fullerene

Fullerene is known to be a good electron acceptor, and it has been widely used in organic photovoltaics.^[51] Utilization of electron accepting properties of fullerene in QDSSCs has been implemented by Brown et al., in a CdSe based device.^[52] An enhancement in photocurrent was observed, due to effective harvesting of excited electrons from CdSe QDs. CdSe QDs and C₆₀ clusters were directly deposited over the SnO₂:F/Glass by electrophoresis.

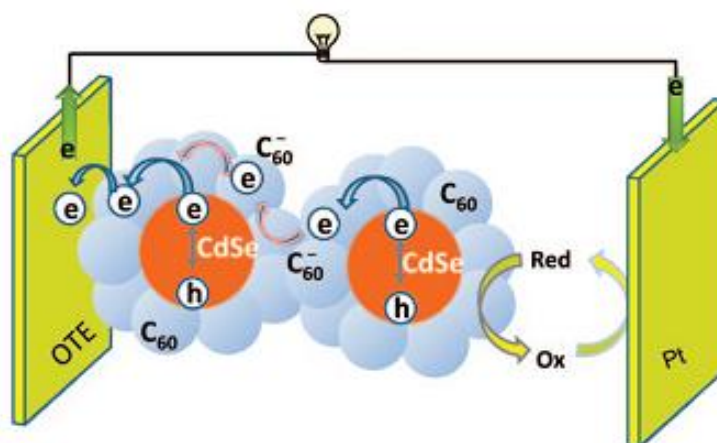


Figure 1.11: Electron transport dynamics in a CdSe-C₆₀ system.^[52] Reprinted with permission from (P. Brown, P. V. Kamat, *J. Am. Chem. Soc.* **130** (2008) 8890-8891). Copyright (2014) American Chemical Society.

Due to the good electron accepting properties of C₆₀, the excited electrons from the CdSe can be transferred to the Fermi level to the C₆₀, which lies at -0.2 V with respect to the NHE

which is less negative with respect to the CB of CdSe (**Figure 1.11**). The CdSe-C₆₀ composite showed a five times enhancement in photocurrent compared to the device without C₆₀ (**Figure 1.12**).

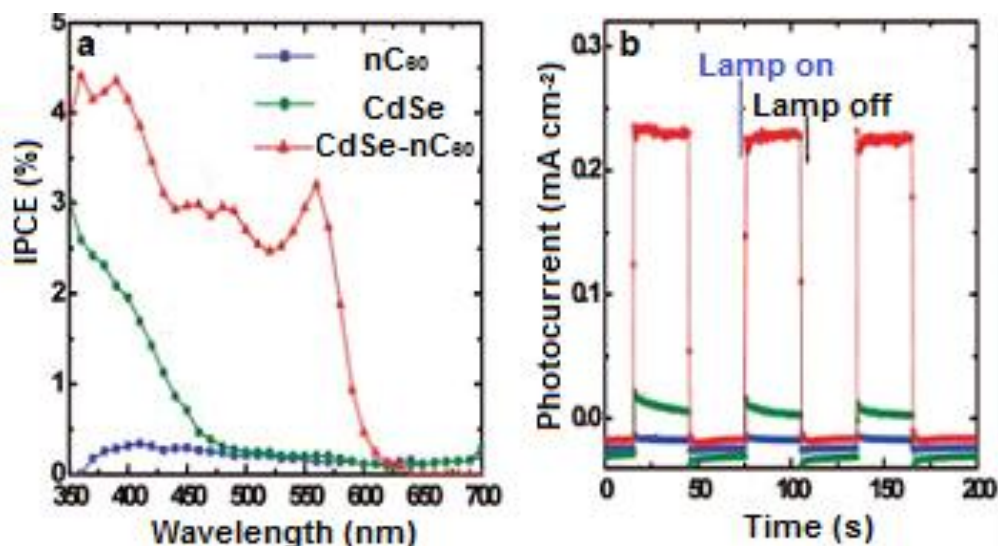


Figure 1.12: (a) IPCE and (b) the photocurrent response of the electrodes to on-off cycles of illumination of C₆₀, CdSe quantum dots and CdSe-C₆₀ clusters on SnO₂:F electrode. A 0.1 M Na₂S aqueous solution was employed as the electrolyte.^[52] Reprinted with permission from (P. Brown, P. V. Kamat, *J. Am. Chem. Soc.* **130** (2008) 8890-8891). Copyright (2014) American Chemical Society.

1.4.8.2 Carbon nanotubes

Carbon nanostructures due to their unique structure and high surface area, have been extensively employed in energy conversion devices. The electron accepting ability of carbon nanotubes (CNTs) facilitates both electron transfer and transport, thus minimizing the electron-hole recombination and enhances the overall PCE. In previous reports, based on various CNT assemblies such as stacked cup carbon nanotubes (SCCNTs)- SnO₂ and TiO₂-SWNT, the enhanced photo-response with the incorporation of the CNTs was probed. The charge separation between excited CdSe QDs and SCCNTs was successfully tapped to generate photocurrent in a QDSSC. A CdSe-SCCNTs based device showed a significant

enhancement in photocurrent compared to the blank CdSe device (**Figure 1.14**). The quenching of CdSe emission, as well as transient absorption measurements, confirmed the ultrafast electron transfer to SCCNTs.^[53]

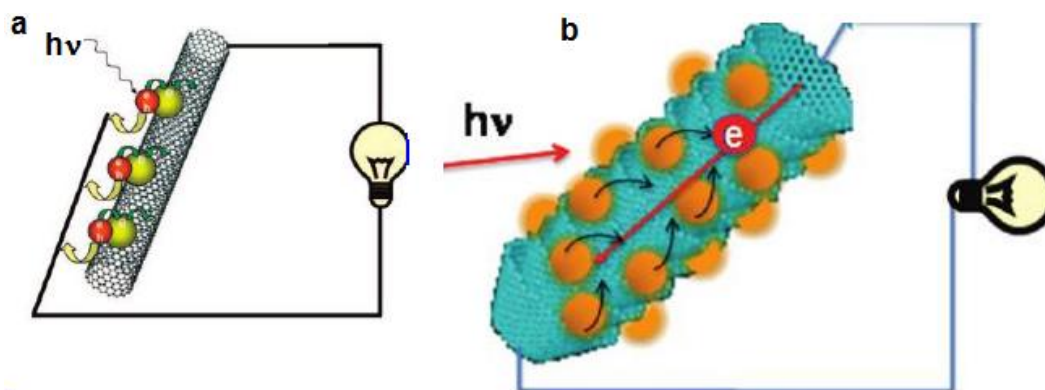


Figure 1.13: (a) Illustration of SWNTs and (b) SCCNTs - based solar cells. Copyright (2014) American Chemical Society.

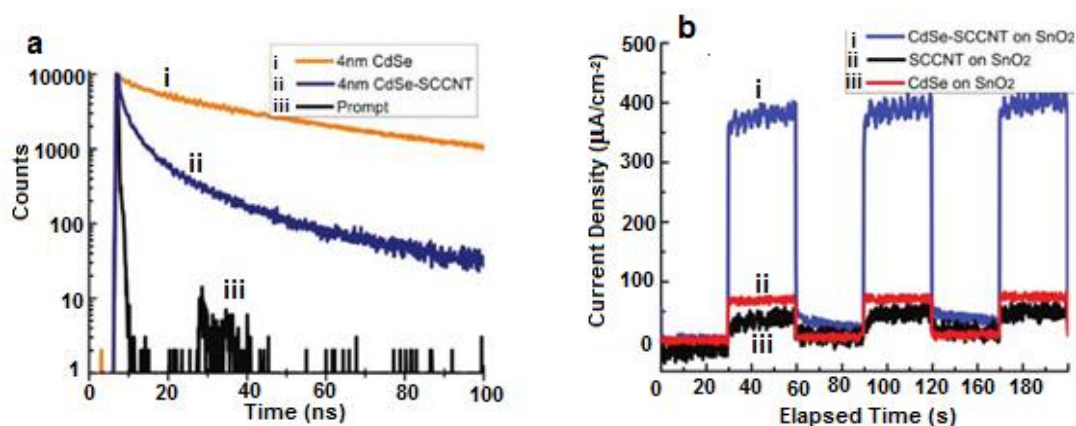


Figure 1.14: (a) Emission decay measurements ($\lambda_{\text{ex}} = 373 \text{ nm}$) and ($\lambda_{\text{em}} = 547 \text{ nm}$) and (b) photocurrent response of SCCNT based electrodes to on-off cycles of illumination.^[53] Reprinted with permission from (B. Farrow, P.V. Kamat, *J. Am. Chem. Soc.* **131** (2009) 11124-11131). Copyright (2014) American Chemical Society.

1.4.8.3 Graphene

Graphene has also been extensively used in photovoltaics and photocatalysis. Due to its high surface area (which results in a large interface), high mobility of $10000 \text{ cm}^2 \text{ V}^{-1} \text{ s}^{-1}$ and

its tunable band gap, graphene is an excellent electron acceptor in photovoltaics (**Figure 1.15**).

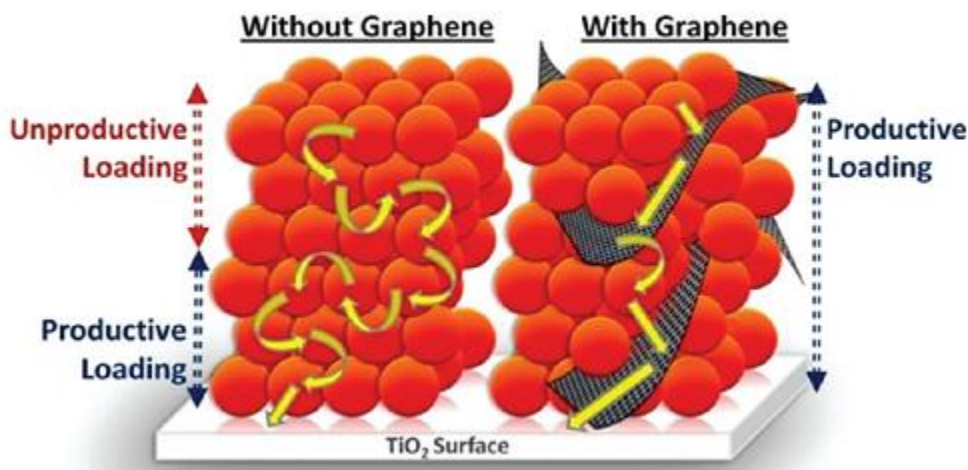


Figure 1.15: Schematic of a graphene based solar cell.^[54] Reprinted with permission from (I. V. Lightcap, P. V. Kamat, *J. Am. Chem. Soc.* **134** (2012) 7109-7116). Copyright (2014) American Chemical Society.

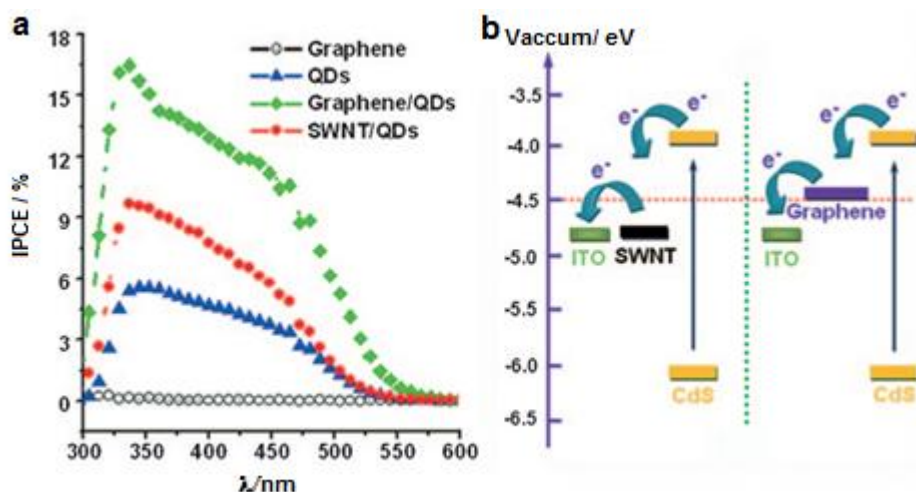


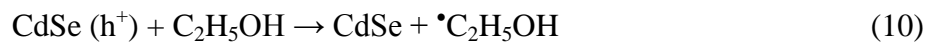
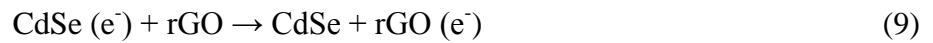
Figure 1.16: (a) IPCE and (b) energy band diagram of CdS and Graphene or SWNT based systems.^[55] Copyright (2014) Wiley-VCH, Germany.

CdS QDs can be distributed uniformly on graphene, whereas in cases of SWNTs, the beneficial distribution of CdS is difficult. The favorable work function of graphene makes it

effective for the separation of the photogenerated electron-hole pairs and transfer of electrons to the electrode surface, thus resulting in high performance graphene/QD solar cells.^[54]

Very recently, Lightcap et al., reported a CdSe-graphene composite based photoanode and it displayed improved photocurrent response of ~ 150% compared to those prepared without GO (**Figure 1.15**). IPCE spectra of the different photoelectrodes and the energy level alignment of the bilayer system are shown in **Figure 1.16**.

Lightcap et al., examined the kinetics of the excited state interaction between colloid QDs and graphene, and found that the overall performance enhanced. In a CdSe/GO assembly, due to the excited electron transfer from CdSe QDs, GO undergoes reduction and forms reduced graphene oxide (rGO). The electron transfer mechanism is summarized below.^[54]



Electrons are injected into rGO and shuttled to the electrode while holes are used to oxidize sulfide to polysulfide. Electrons travel through an external circuit to the rGO/Cu₂S counter electrode. In the absence of the rGO, the loss of electrons through recombination rate is very high, which is evident from the IPCE and photocurrent spectra (**Figure 1.17**). A CuO/rGO composite was employed as the counter electrode.

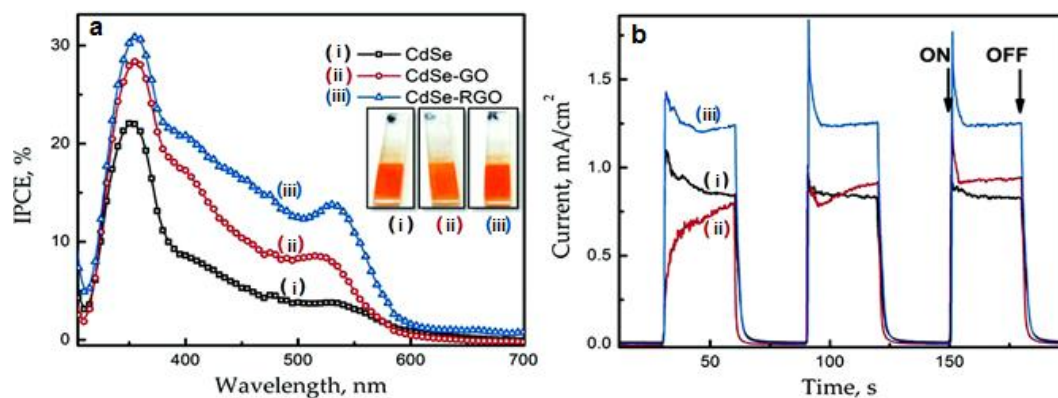


Figure 1.17: (a) IPCE and (b) photocurrent *versus* time responses of (i) CdSe, (ii) CdSe/GO and (iii) CdSe/rGO. Photographs of the three electrodes are shown in the inset of (a).^[54] Reprinted with permission from (I. V. Lightcap, P. V. Kamat, *J. Am. Chem. Soc.* **134** (2012) 7109-7116). Copyright (2014) American Chemical Society.

1.4.9 Improving PCE by surface plasmon resonance (SPR effects)

To achieve maximum efficiency, it is important to utilize most of the solar spectrum. The optical properties of the nanostructures have been already implemented in photovoltaics in order to enhance the PCEs. The light harvesting properties can be amplified by employing surface plasmon resonance (SPR). SPR is the collective oscillation of electrons in solid or liquid stimulated by incident light. The resonance conditions are established when the frequency of the photon matches the natural frequency of surface electrons oscillating against the restoring force of positive nuclei. SPR, in nanometer sized particles, is called the localized SPR (LSPR) (**Figure 1.18**). It has been shown that in the presence of the metal nanoparticles, the absorption of the sensitizer gets enhanced via near field effects, whereas the path length increases via far-field scattering. The fast electron transfer capability of the metal nanoparticles can improve the photovoltaic performance. Electron storage properties leads to a shift in Fermi level to more negative potentials *versus* NHE.^[56]

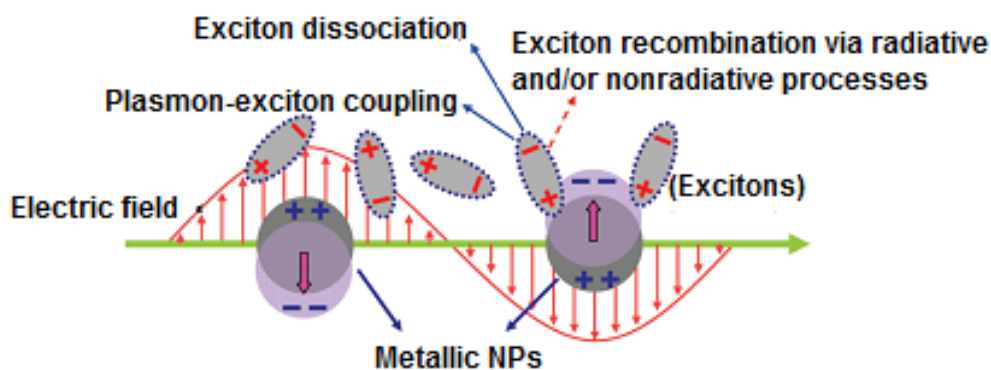


Figure 1.18: Schematic representation of the interplay between the LSPR and excitons.^[56] Reprinted with permission from (J-L. Wu, F-C. Chen, Y-S. Hsiao, F-C. Chien, P. Chen, C-H. Kuo, M. H. Huang, C-S. Hsu, *ACS Nano* **5** (2011) 959-967). Copyright (2014) American Chemical Society.

At higher temperatures, however, metal nanoparticles act as recombination centers. In order to alleviate this effect, a thin layer of an insulating materials is applied. An effective strategy to increase efficiencies of DSSCs or hybrid solar cells involves the incorporation of metal nanoparticles which can either induce plasmonic enhancements to the photoanode's absorption via LSPR or they can promote charge transfer by accepting electrons from the CB of the photoactive semiconductor, via Fermi level equilibration upon illumination. In the latter scenario, the open circuit voltage (V_{OC}) increases as the Fermi level of the wide gap semiconductor is pushed to more negative potentials (with respect to NHE) and as a consequence, the zero current potential increases. The roles of charge transfer and plasmonic effects in enhancing the PCEs of an Au@TiO₂ and an Au@SiO₂ assembly have been distinguished in an earlier report by Choi et al. (**Figure 1.19**).^[57]

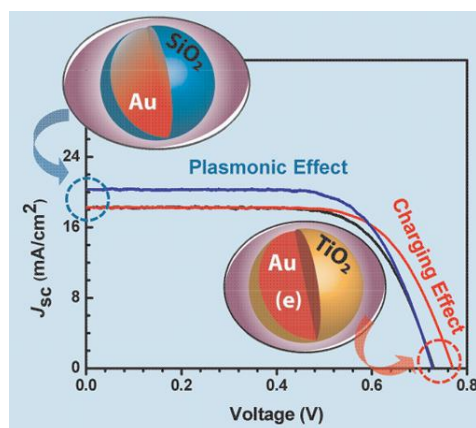


Figure 1.19: J-V spectra for an Au@TiO₂ and an Au@SiO₂ based DSSC.^[57] Reprinted with permission from (H. Choi, W. T. Chen, P. V. Kamat, *ACS Nano* **6** (2012) 4418-4427). Copyright (2014) American Chemical Society.

In another study, for a solar cell with a photoanode composed of PbS QDs and Au plasmons, the relative enhancements expected from an array of nanoshells at various vertical locations, within the colloidal QD film (CQD) was shown.

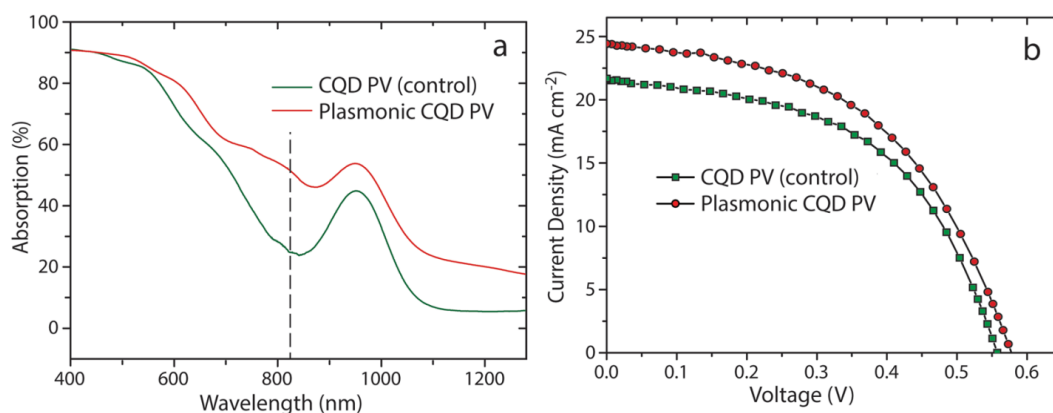


Figure 1.20: (a) Absorption and (b) J-V spectra of the device with and without plasmons.^[58] Reprinted with permission from (D. Paz-Soldan, A. Lee, S. M. Thon, M. M. Adachi, H. Dong, P. Maraghechi, M. Yuan, A. J. Labelle, S. Hoogland, K. Liu, E. Kumacheva and E. H. Sargent, *Nano Lett.* **13** (2013) 1502-1508). Copyright (2014) American Chemical Society.

Fixing them close to the illumination side of the film led to considerable parasitic absorption in the visible range (400-600 nm), restricting the optical improvement (**Figure 1.19**). Both short circuit current density (J_{sc}) and V_{oc} were higher than that of solar cells

without Au plasmons; J_{SC} increased by 13% and the overall PCE increased by 11% in the plasmonic device.^[58] In yet another study, in order to demonstrate the effect of the plasmonic antenna, gold nanorods decorated over TiO_2 has been employed as the photoanode.^[59] When the LSPs are excited by light of wavelengths shorter than 700 nm an interband transition from d-bands to the sp CB may be promoted, and pairs of excited electrons and electron holes should form around the interface between the gold nanorods and TiO_2 , whereas the holes will be trapped at the TiO_2 surface states.

In yet another report, a DSSC with sole TiO_2 - only showed a PCE of 3.1%, whereas the plasmon-enhanced DSSC with $Ag@TiO_2$ nanoparticles showed a PCE of 4.4%. The enhancement in PCE is mainly due to the increased photocurrent due to enhanced dye absorption by LSPR.^[60] Schematic and IPCE performance of the cell is shown in **Figure 1.21**.

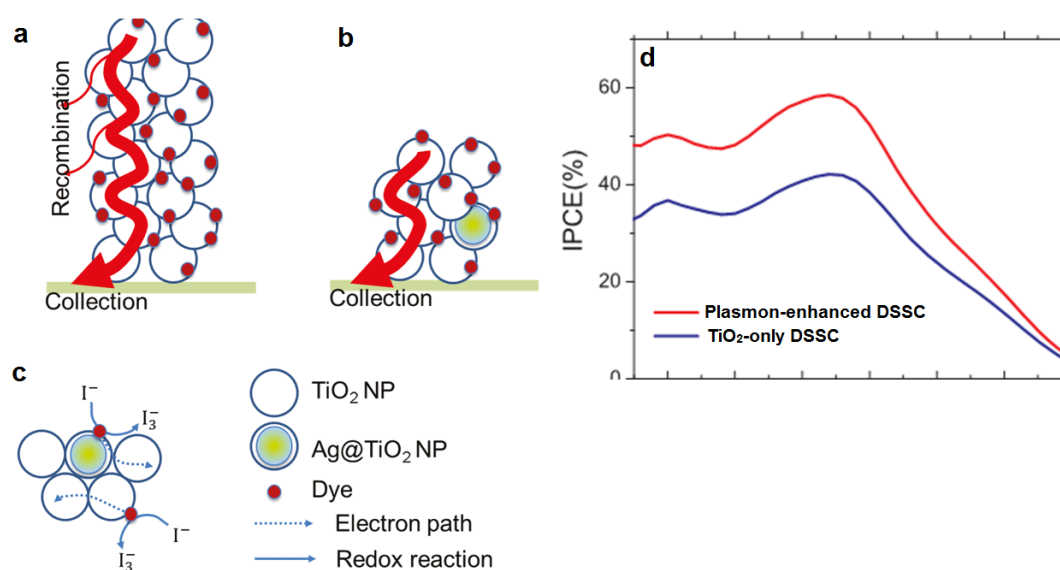


Figure 1.21: Schematics of (a) Plasmon enhanced DSSC, (b) plasmon enhanced DSSC avoid electron-hole recombination due to thinner photoanode layer and (c) mechanism of plasmon enhanced DSSC and (d) IPCE spectra of the DSSC with and without $Ag@TiO_2$.^[60] Reprinted with permission from (J. Qi, X. Dang, P. T. Hammond, A. M. Belcher, *ACS Nano* **5** (2011) 7108-7116.). Copyright (2014) American Chemical Society.

1.4.10 Incorporation of FRET

In order to improve the PCE, a novel strategy namely, Forster resonance energy transfer (FRET) was recently proposed in QDSSCs. In this mechanism, the donor in an excited state can transfer its excitation energy to a nearby acceptor through non radiative fashion (Figure 1.22a). It is a distance dependant interaction. The donor and acceptor should be in close proximity (typically in between 1-10 nm) for FRET interaction. The absorption spectrum of the acceptor should overlap with the fluorescence spectrum of the donor (Figure 1.22b). The transition dipole orientation of the donor and acceptor should be approximately parallel. These are the primary criteria for FRET to occur.

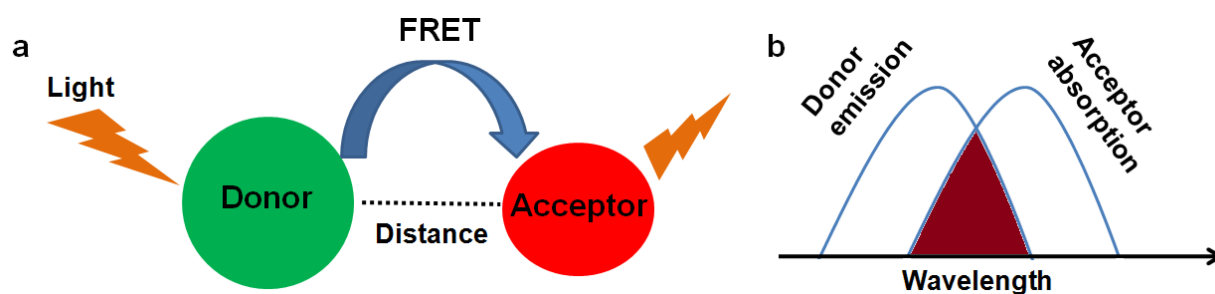


Figure 1.22: (a) Schematic representation of FRET and (b) overlap between the emission of the donor and absorbance of acceptor.

Earlier, FRET was predominately used in biological applications such as automated DNA sequencing, immunoassays, structural confirmation of proteins etc. Of late, it's application was extended to QDSSCs as well. One of the most striking advantages of FRET is that the entire spectral region can be utilized by using photoactive components which do not have favorable energy level offsets. In most of the earlier reports, QDs were employed as the donors while dyes were used as the acceptor moieties. In an earlier report, Buhbut et al., fabricated a CdSe/CdS/ZnS/TiO₂/SQ2 dye assembly (**Figure 1.23a**), wherein the QDs functioned as antennas for funneling energy to the dye molecules and as a result, complete coverage of the visible spectrum was realized as both processes occurred in tandem (**Figure**

1.23b): light absorption in the blue/green region by the dot and exciton generation in the red absorbing dye because of FRET interaction. High IPCE was achieved for the FRET cell in the entire visible range, as opposed to narrow IPCE peaks observed for cells with either the sole donor or the sole acceptor.^[61]

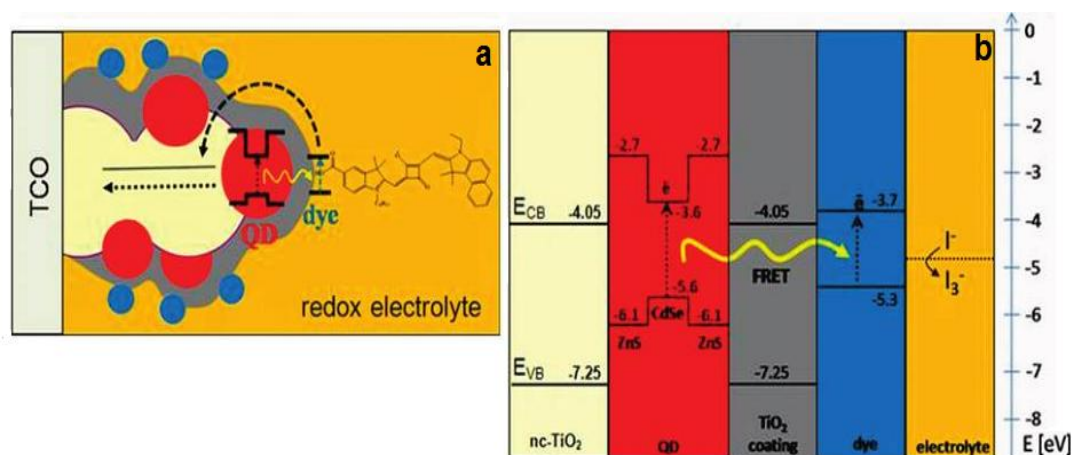


Figure 1.23: (a) Schematic representation of the system based on FRET in which QDs are donors, and dye molecules are acceptors and (b) energy level alignment of each component relative to vacuum.^[61] Reprinted with permission from (S. Buhbut, S. Itzhakov, E. Tauber, M. Shalom, I. Hod, T. Geiger, Y. Garini, D. Oron, A. Zaban, *ACS Nano* **4** (2010) 1293-1298). Copyright (2014) American Chemical Society.

Kamat's group coupled energy transfer and electron transfer in a QD-dye assembly. CdSe QDs functioned as donors, whereas a squaraine dye (SQSH) worked as the acceptor.^[62] The TiO₂/SQSH/CdSe assembly exhibited an overall PCE of 3.65% (**Figure 1.24**). From transient absorption measurements, it was shown that the energy transfer between excited CdSe QDs and SQSH occurs via FRET and electron transfer occurs from SQSH to TiO₂. The synergy of covalently linked QDs and the near IR absorbing squaraine dye provides new opportunities to harvest photon from selective regions of the solar spectrum.

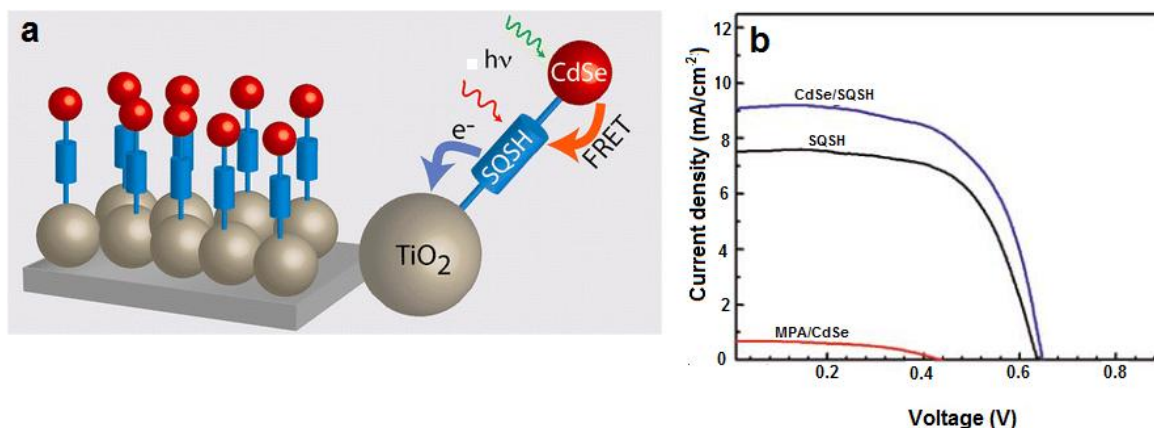


Figure 1.24: (a) Schematic of a FRET based photovoltaic device and (b) J-V plots for mercaptopropionic acid/CdSe, SQSH and CdSe/SQSH photoanodes.^[62] Reprinted with permission from (H. Choi, R. Nicolaescu, S. Paek, J. Ko, P. V. Kamat, *ACS Nano* **5** (2011) 9238-9245). Copyright (2014) American Chemical Society.

Etgar et al. also demonstrated increased PCE due to FRET in a system with CdSe QDs as the donor moiety and a newly designed squaraine dye as the acceptor unit. The IPCE spectrum showed the full coverage of the visible region (**Figure 1.25**).^[63]

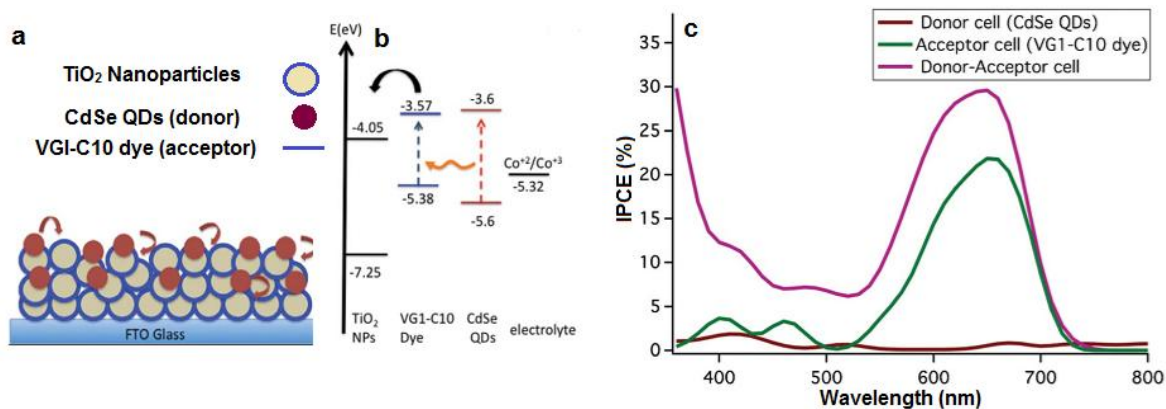


Figure 1.25: (a) Schematic representation of the cell structure, (b) energy level alignment and (c) IPCE spectra of the donor alone cell, acceptor alone cell and donor-acceptor cell.^[63] Copyright (2014) Wiley-VCH, Germany.

Table 1.1 gives the performance parameters of QDSSCs, reported in literature.

Table 1.1: Performance parameters of QDSSCs (data from literature)

Photoanode, counter electrode (CE) configurations	V_{OC} (V)	J_{SC} (mA cm ⁻²)	FF	η (%)	Reference
Mn-doped-CdS/TiO ₂ CE: Cu ₂ S/RGO	0.583	8.9	49	2.53	[50]
CdSe/TiO ₂ (Linker assisted deposition of capped CdSe) CE: Pt/FTO	0.61	3.15	61	1.17	[64]
TiO ₂ /CdS/PbS (varying cationic baths, using SILAR) CE:Pt/FTO	0.41	2.64	57	0.62	[65]
CdS-TiO ₂ /CdSe-TiO ₂ (in paint form), CE: Cu ₂ S/reduced graphene oxide	0.585	3.1	59	1.08	[38]
Orange and red CdSeS/TiO ₂ (Electrophoretic deposition of capped CdSeS) CE: Cu ₂ S/reduced graphene oxide	0.557	11.2	51	3.20	[66]
TiO ₂ /CdS/CdSe (Chemical bath deposition, CBD) CE: CuS/CoS	0.45	17.11	55.4	4.1	[67]
TiO ₂ /CdS/CdSe (Flexible solar cells, CBD) CE: Cu ₂ S	0.511	12.3	54.9	3.45	[68]
TiO ₂ /CdS/CdSe/ZnS (By SILAR) CE: Cu ₂ S/Brass	0.48	13.52	53	3.44	[69]
TiO ₂ /SQSH/CdSe FRET Cell CE: Pt/FTO	0.647	9.077	62	3.65	[62]
TiO ₂ /Au@SiO ₂ /N719 CE: Pt	0.727	20.31	69	10.21	[59]

FF (fill factor), V_{OC} (open circuit voltage), J_{SC} (short circuit current density) and η (efficiency)

1.5 Objectives of the present work

Although the above described strategies, that have been employed for enhancing solar cell parameters, have been successful to some extent, but there is enough scope for further improving photovoltaic performances in solution processed QDSSCs. In the present thesis, these lacunae have been addressed, by constructing hitherto unreported photoanode architectures, and by unraveling the charge transport mechanism therein, we correlate these phenomena with their solar cell performance characteristics.

The main objectives of the present work are summarized below.

- i. To study the effect of carbon nanostructures on the photovoltaic performance of QDSSCs and link the same with electron transfer and transport mechanisms.
- ii. To analyze the influence of FRET in QDSSCs by using some unique donor-acceptor combinations.
- iii. To tap the potential of plasmonic effects by using Au nanoparticles in photovoltaics.
- iv. To extend the applicability of solution processed solar cells developed herein to dual function devices such as a) a solar powered supercapacitor and b) a photoelectrochromic cell.

In **Chapter 3** the roles of a carbon nanostructure, namely, ionic liquid functionalized graphene oxide and metal nanoparticles, i.e., Au nanoparticles in controlling electron transfer and transport mechanisms were studied and they were linked to the solar cell performance of a CdSe/TiO₂ based cell. Taking this further, the beneficial influence of yet another novel carbon nanostructure, fullerene nanowhiskers relative to pristine fullerene clusters on photovoltaic performance of CdS based QDSSCs was analyzed and demonstrated in **Chapter 4**. Another powerful strategy, i.e., FRET was implemented in QDSSCs and energy and electron relay modes were elucidated in FRET enabled QDSSCs in **Chapters 5 and 6**. In both chapters, quasi solid-state devices were fabricated. In **Chapter 5**, CdS QDs were employed as the donors and copper phthalocyanine molecules were used as acceptors. In addition, carbon-dots or C-dots were also included to improve the charge propagation ability of the photoanode. In **Chapter 6**, the roles of QDs and dye were reversed; CdS/CdSe QDs were employed as the acceptors and an unconventional Lucifer yellow dye (traditionally confined to biological applications) served as the donor. Further, the hole transport capability of the sulfide redox couple electrolyte was modified by the use of poly(3,4 ethylenedioxythiophene) or PEDOT microfibers. Besides FRET and use of carbon nanostructures, plasmonic effects were also tapped for improving solar cell responses, by

integrating Au microfibers with a TiO₂/CdS electrode. This work was further extended by combining this plasmonic photoanode with an electrical double layer capacitor based on MWCNTs. **Chapter 7** presents a solar powered supercapacitor wherein a plasmonic QDSSC sources the photocurrent for charging/discharging a conjoined supercapacitor based on MWCNTs was demonstrated.

The benefit of plasmonics in improving solar cell parameters was further reiterated by using Au encapsulated C-dots in a ZnO based DSSC. This is described in **Chapter 8**. In this chapter, we extended the use of plasmonic effect to improve solar cell efficiencies, and constructed cells using Au@C-dots in the photoanode. A simple strategy was employed to improve the efficiency of a ZnO nanorods based DSSC by use of Au encapsulated carbon dots (Au@C-dots) in the photoanode. The localized surface plasmonic resonance of Au in the 500-550 nm range coupled with the ability of C-dots to serve as co-sensitizers increase the energy harvesting efficiency of the DSSC with ZnO/N719/Au@C-dots photoanodes. The use of plasmonic Au@C-dots was further explored by integrating the ZnO/N719/Au@C-dots photoanode with electrochromic MoO₃ as counter electrode for photoelectrochromic applications.

Various techniques such as scanning electron microscopy (SEM), atomic force microscopy (AFM), transmission electron microscopy (TEM), UV–visible spectroscopy (UV-Vis), fluorescence spectroscopy and emission decay analysis, electrochemical techniques [cyclic voltammetry (CV), linear sweep voltammetry (LSV), chronoamperometry and electrochemical impedance spectroscopy (EIS)], instrumentation for determination of solar cell parameters such as J_{SC} , V_{OC} , FF, η and IPCE are described in the next **Chapter 2**. These were used to characterize QDSSCs and their components, in terms of morphological, compositional, optical, photoelectrochemical and electrochemical grounds for their optimization for solar cell applications.

1.6 References

- [1] M. A. Green, *Prog. Photovoltaics* **17** (2009) 183-189.
- [2] R. W. Birkmire, B. E. McCandless, *Curr. Opin. Sol. State & Mater. Sci.* **14** (2010) 139-142.
- [3] B. O'Regan, M. Gratzel, *Nature* **353** (1991) 737-740.
- [4] http://techon.nikkeibp.co.jp/english/NEWS_EN/20130716/292380/.
- [5] http://en.wikipedia.org/wiki/Dye-sensitized_solar_cell.
- [4] B. Fang, M. Kim, S-Q. Fan, J. H. Kim, D. P. Wilkinson, J. Ko, J-S. Yu. *J. Mater. Chem.* **21** (2011) 8742-8748.
- [5] J. J. Wu, S. C. Liu, *Adv. Mater.* **14** (2002) 215-218.
- [6] J. A. Anta, E. Guillen, R. T. Zaera, *J. Phys. Chem. C* **116** (2012) 11413-11425.
- [7] H. J. Snaith, C. Ducati, *Nano Lett.* **10** (2010) 1259-1265.
- [8] N. Romeo, A. Bosio, R. Tedeschi, A. Romeo, V. Canevari, *Sol. Energy. Mat. Sol. Cells* **58** (1999) 209-218.
- [9] M. K. Nazeeruddin, P. Pechy, T. Renouard, S. M. Zakeeruddin, R. Humphry-Baker, P. Comte, P. Liska, L. Cevey, E. Costa, V. Shklover, L. Spiccia, G. B. Deacon, C. A. Bignozzi, M. Grätzel, *J. Am. Chem. Soc.* **123** (2001) 1613-1624.
- [10] R. B. M. Koehorst, G. K. Boschloo, T. J. Savenije, A. Goossens, T. J. Schaafsma, *J. Phys. Chem. B* **104** (2000) 2371-2377.
- [11] E. Galoppini, *Coord. Chem. Rev.* **248** (2004) 1283-1297.
- [12] P. Pechy, F. P. Rotzinger, M. K. Nazeeruddin, O. Kohle, S. M. Zakeeruddin, R. Humphrybaker, M. Gratzel, *J. Chem. Soc., Chem. Commun.* **10** (1995) 1093-1093. [13] O. Schwarz, D. van Loyen, S. Jockusch, N. J. Turro, H. J. Durr, *Photochem. Photobiol. A-Chem.* **132** (2000) 91-98.
- [14] A. J. Nozik, *Ann. Rev. Phys. Chem.* **9** (1978) 189-222.
- [15] P. Wang, S. M. Zakeeruddin, I. Exnar, M. Gratzel, *Chem. Commun.* (2002) 2972-2973.
- [16] A. B. Ellis, S. W. Kaiser, J. M. Bolts, M. S. Wrighton, *J. Am. Chem. Soc.* **99** (1977) 2839-2848.
- [17] Y. Zheng, S. Gao, J. Y. Ying, *Adv. Mater.* **19** (2007) 376-380.
- [18] A. J. Nozik, M. C. Beard, J. M. Luther, M. Law, R. J. Ellingson, J. C. Johnson, *Chem. Rev.* **110** (2010) 6873-6890.
- [19] G. Meyer, *Inorg. Chem.* **44** (2005) 6852-6864.
- [20] P. V. Kamat, *J. Phys. Chem. C* **112** (2008) 18737-18753.
- [21] V. I. Klimov, *J. Phys. Chem. B* **110** (2006) 16827-16845.
- [22] R. E. Bailey, S. Nie, *J. Am. Chem. Soc.* **125** (2003) 7100-7106.
- [23] R. J. Ellingson, M. C. Beard, J. C. Johnson, P. R. Yu, O. I. Micic, A. J. Nozik, A. Shabaev, *Nano Lett.* **5** (2005) 865-871.
- [24] J. B. Sambur, T. Novet, B. A. Parkinson, *Science* **330** (2010) 63-66.
- [25] B. Fisher, J. M. Caruge, D. Zehnder, M. Bawendi, *Phys. Rev. Lett.* **94** (2005) 087403-087407.
- [26] M. Seol, H. Kim, Y. Tak, K. Yong, *Chem. Commun.* **46** (2010) 5521-5523.
- [27] W. Shockley, H. J. Queisser, *J. Appl. Phys.* **32** (1961) 510-519.
- [28] Z. Ali, I. Shakir, D. J. Kang, *J. Mater. Chem. A* **2** (2014) 6474-6479.
- [29] M. A. Becker, J. G. Radich, B. A. Bunker, P. V. Kamat, *J. Phys. Chem. Lett.* **5** (2014) 1575-1582.
- [30] H. Wang, T. Kubo, J. Nakazaki, T. Kinoshita, H. Segawa, *J. Phys. Chem. Lett.* **4** (2013) 2455-2460.
- [31] A. Zaban, O. I. Micic, B. A. Gregg, A. J. Nozik, *Langmuir* **14** (1998) 3153-3156.
- [32] L- C. Chen, C- C Wang, B- S. Tseng, *J. Optoelect. Biomed. Mater.* **1** (2009) 249-254.

- [33] H. M. Choi, I. A. Ji, J. H. Bang, *ACS Appl. Mater. Interfaces* **6** (2014) 2335-2343.
- [34] D. Hu, C. C. McPheeters, E. T. Yu, D. M. Schaadt, *Nanoscale Res. Lett.* **6** (2011) 83-87.
- [35] X-Y. Yu, J-Y. Liao, K-Q, Qiu, D-B. Kuang, C-Y. Su, *ACS Nano* **5** (2011) 9494-9500.
- [36] A. V. Firth, Y. Tao, D. Wang, J. Ding, F. Bensebaa, *J. Mater. Chem.* **15** (2005) 4367-4372.
- [37] P. Yu, K. Zhu, A. G. Norman, S. Ferrere, A. J. Frank, A. J. Nozik, *J. Phys. Chem. B* **110** (2006) 25451-25454.
- [38] M. P. Genovese, I. V. Lightcap, P. V. Kamat, *ACS Nano* **6** (2012) 865-872.
- [39] K-H. Lin, C-Y. Chuang, Y-Y. Lee, F-C. Li, Y-M. Chang, I-P. Liu, S-C. Chou, Y-L. Lee, *J. Phys. Chem. C* **116** (2012) 1550-1555.
- [40] S. Ding, X. Yin, X. Lu, Y. Wang, F. Huang, D. Wan, *ACS Appl. Mater. Interfaces* **4** (2012) 306-311.
- [41] J. Xiao, Q. Huang, J. Xu, C. Li, G. Chen, Y. Luo, D. Li, Q. Meng, *J. Phys. Chem. C* **118** (2014) 4007-4015.
- [42] G. Hodes, J. Manassen, D. Cahen, *Nature* **261** (1976) 403-404.
- [43] A. B. Ellis, S. W. Kaiser, M. S. Wrighton, *J. Am. Chem. Soc.* **98** (1976) 1635-1637.
- [44] A. M. E. Raj, S. M. Delphine, C. Sanjeeviraja, M. Jayachandran, *Physica B* **405** (2010) 2485-2491.
- [45] P. V. Kamat, *J. Phys. Chem. Lett.* **4** (2013) 908-918.
- [46] A. Kongkanand, K. Tvrdy, K. Takechi, M. K. Kuno, P. V. Kamat, *J. Am. Chem. Soc.* **130** (2008) 4007-4015.
- [47] K. S. Leschkies, R. Divakar, J. Basu, E. Enache-Pommer, J. E. Boercker, C. Barry Carter, U. R. Kortshagen, D. J. Norris, E. S. Aydil, *Nano Lett.* **7** (2007) 1793-1798.
- [48] J. Chen, C. Li, G. Eda, Y. Zhang, W. Lei, M. Chhowalla, W. I. Milne, W. Q. Deng, *Chem. Commun.* **47** (2011) 6084-6086.
- [49] M. A. Hossain, Z. Y. Koh, Q. Wang, *Phys. Chem. Chem. Phys.* **14** (2012) 7367-7374.
- [50] P. K. Santra, P. V. Kamat, *J. Am. Chem. Soc.* **134** (2012) 2508-2511.
- [51] C-Z. Li, H-L. Yip, A. K-Y. Jen, *J. Mater. Chem.* **22** (2012) 4161-4177.
- [52] P. Brown, P. V. Kamat, *J. Am. Chem. Soc.* **130** (2008) 8890-8891.
- [53] B. Farrow, P.V. Kamat, *J. Am. Chem. Soc.* **131** (2009) 11124-11131.
- [54] I. V. Lightcap, P. V. Kamat, *J. Am. Chem. Soc.* **134** (2012) 7109-7116.
- [55] C. X. Guo, H. B. Yang, Z. M. Sheng, Z. S. Lu, Q. L. Song, C. M. Li, *Angew. Chem. Int. Ed.* **49** (2010) 3014-3017.
- [56] J-L. Wu, F-C. Chen, Y-S. Hsiao, F-C. Chien, P. Chen, C-H. Kuo, M. H. Huang, C-S. Hsu, *ACS Nano* **5** (2011) 959-967.
- [57] H. Choi, W. T. Chen, P. V. Kamat, *ACS Nano* **6** (2012) 4418-4427.
- [58] D. Paz-Soldan, A. Lee, S. M. Thon, M. M. Adachi, H. Dong, P. Maraghechi, M. Yuan, A. J. Labelle, S. Hoogland, K. Liu, E. Kumacheva and E. H. Sargent, *Nano Lett.* **13** (2013) 1502-1508.
- [59] S. Gao, K. Ueno, H. Misawa, *Acc. Chem. Res.* **44** (2011) 251-260.
- [60] J. Qi, X. Dang, P. T. Hammond, A. M. Belcher, *ACS Nano* **5** (2011) 7108-7116.
- [61] S. Buhbut, S. Itzhakov, E. Tauber, M. Shalom, I. Hod, T. Geiger, Y. Garini, D. Oron, A. Zaban, *ACS Nano* **4** (2010) 1293-1298.
- [62] H. Choi, R. Nicolaescu, S. Paek, J. Ko, P. V. Kamat, *ACS Nano* **5** (2011) 9238-9245.
- [63] L. Etgar, J. Park, C. Barolo, V. Lesnyak, S. K. Panda, P. Quagliotto, S. G. Hickey, Md. K. Nazeeruddin, A. Eychmuller, G. Viscardi, M. Gratzel, *RSC Adv.* **2** (2012) 2748-2752.
- [64] H. J. Lee, J-H. Yum, H. C. Leventis, S. M. Zakeeruddin, S. A. Haque, P. Chen, S. I. Seok, M. Gratzel, Md. K. Nazeeruddin, *J. Phys. Chem. C* **112**, (2008) 11600-11608.

- [65] H. J. Lee, P. Chen, S-J. Moon, F. Sauvage, K. Sivula, T. Bessho, D. R. Gamelin, P. Comte, S. M. Zakeeruddin, S. I. Seok, M. Gratzel, Md. K. Nazeeruddin, *Langmuir* **25**, (2009) 7602-7608.
- [66] P. K. Santra, P. V. Kamat, *J. Am. Chem. Soc.* **135** (2013) 877-885.
- [67] Z. Yang, C-Y. Chen, C-W. Liu, H-T. Chang, *Adv. Energy Mater.* **1** (2011) 259-264.
- [68] X. Huang, S. Huang, Q. Zhang, X. Guo, D. Li, Y. Luo, Q. Shen, T. Toyoda, Q. Meng, *Chem. Commun.* **47** (2011) 2664-2666.
- [69] H. J. Lee, J. Bang, J. Park, S. Kim, S-M. Park, *Chem. Mater.* **22** (2010) 5636-5643.

Chapter 2

Materials and characterization techniques

This chapter provides details about the various materials and techniques that were utilized for the syntheses and characterization of QDSSCs.

2.1 Materials

Various chemicals that were used during experiments performed in this thesis with their details are tabulated in **Table 2.1**.

Table 2.1: List of chemicals used in experimental work.

		Chemicals used	Company	Empirical/ Molecular formula
PRECURSORS	1	Cadmium acetate dehydrate (M.W. 230.5 g/mol)	Merck	$\text{Cd}(\text{CH}_3\text{COO})_2 \cdot 2\text{H}_2\text{O}$
	2	Sodium sulfide (M.W. 78.04 g/mol)	Merck	Na_2S
	3	Cadmium nitrate tetrahydrate (M.W. 308.48 g/mol)	Merck	$\text{Cd}(\text{NO}_3)_2 \cdot 4\text{H}_2\text{O}$
	4	Bismuth nitrate pentahydrate (M.W. 485.07 g/mol)	Merck	$\text{Bi}(\text{NO}_3)_3 \cdot 5\text{H}_2\text{O}$
	5	Sodium thiosulfate pentahydrate (M.W. 248.18 g/mol)	Merck	$\text{Na}_2\text{S}_2\text{O}_3 \cdot 5\text{H}_2\text{O}$
	6	Selenium powder (A.W. 78.97 g/mol)	Aldrich	Se powder
	7	Dextrose (M.W. 180.15 g/mol)	Aldrich	$\text{C}_6\text{H}_{12}\text{O}_6$
MONOMERS	8	3,4-Ethylenedioxythiophene (EDOT) (M.W.~142.18 g/mol)	Aldrich	$\text{C}_6\text{H}_6\text{O}_2\text{S}$
	9	Acrylamide(M.W.~71.08 g/mol)	Merck	$\text{C}_3\text{H}_5\text{NO}$
ANIONIC SURFACTANTS	10	Sodiumdodecylsulfate (M.W. ~288.38 g/mol)	Aldrich	$\text{C}_{12}\text{H}_{25}\text{OSO}_3\text{Na}$

IONIC LIQUIDS	11	1-Butyl-3-methylimidazolium trifluoromethanesulfonate (M.W. ~ 288.29 g/mol)	Merck	$C_9H_{15}F_3N_2SO_3$
	12	1-Butyl-3-methyl imidazolium iodide. (M.W.~266.12 g/mol)	Merck	$C_8H_{15}N_2I$
ELECTROACTIVE SALT	13	Lithium perchlorate (M.W.~ 106.39 g/mol)	Aldrich	$LiClO_4$
	14	Lithium trifluoromethanesulfonate (M.W. ~ 156.01 g/mol)	Aldrich	$LiCF_3SO_3$
SOLVENTS	15	Methanol (M.W.~32 g/mol)	Merck	CH_3OH
	16	Propylene carbonate (M.W. ~ 102.09 g/mol)	Merck	$C_4H_6O_3$
	17	Polyethyleneglycol (PEG-400) (M.W.~ 380 g/mol)	Merck	$HO(C_2H_4O)_nH$
	18	Ethanol (M.W.~ 46 g/mol)	Merck	C_2H_5OH
	19	Acetone (M.W.~ 58.08 g/mol)	Merck	CH_3COCH_3
	20	Dimethylformamide (DMF) (M.W.~73.10 g/mol)	Merck	C_3H_7NO
	21	Toluene (M.W.~ 92.14 g/mol)	Merck	$C_6H_5CH_3$
	22	2-Propanol (M.W. 60.1 g/mol)	Merck	C_3H_8O

MISCELLANEOUS	23	Trioctyl phosphine oxide (99.9 % purity) (M.W.~ 386.63 g/mol)	Aldrich	$[\text{CH}_3(\text{CH}_2)_7]_3\text{PO}$
	24	Trioctyl phosphine (90 % purity) (M.W.~ 370.64 g/mol)	Aldrich	$[\text{CH}_3(\text{CH}_2)_7]_3\text{P}$
	25	Hydrogen tetrachloroaurate (M.W.~ 393.83 g/mol)	Aldrich	$\text{HAuCl}_4 \cdot 3\text{H}_2\text{O}$
	26	Potassium hexacyanoferrate (M.W.~ 329.26 g/mol)	Aldrich	$\text{K}_3[\text{Fe}(\text{CN})_6]$
	27	Tetraoctylammoniumbromide (M.W.~ 546.81 g/mol)	Aldrich	$\text{C}_{32}\text{H}_{68}\text{BrN}$
	28	Sodium borohydride (M.W. ~37.83 g/mol)	Merck	NaBH_4
	29	Sodium sulfate (M.W.~ 142.04 g/mol)	Merck	Na_2SO_4
	30	Ferric chloride (M.W.~162.21 g/mol)	Merck	FeCl_3
	31	Sodium nitrite (M.W. ~ g/mol)	Merck	NaNO_2
	32	3- Mercaptopropionic acid (MPA) (M.W. 106.14g/mol)	Merck	$\text{C}_3\text{H}_6\text{SO}_2$
	33	Zinc nitrate (M.W. 189.36g/mol)	Merck	ZnNO_3
	34	Hexamethylenetetramine (M.W. 140.18 g/mol)	Merck	$(\text{CH}_2)_6\text{N}_4$
	35	Iodine (A.W. 126.9 g/mol)	Merck	I_2
	36	Bis(tetrabutylammonium) [cis -di(thiocyanato)bis(2,2' -bipyridyl-4-carboxylate-4'-carboxylic acid)-Ru(II)] (N719) (M.W. 1188.18 g/mol)	Aldrich	$\text{C}_{58}\text{H}_{86}\text{O}_8\text{N}_8\text{S}_2\text{Ru}$
	37	Titanium dioxide (M.W. 79.86 g/mol)	Evonik	TiO_2
	38	Ammonium persulfate (M.W. 228.18 g/mol)	Merck	$(\text{NH}_4)_2\text{S}_2\text{O}_8$
	39	Bis-acrylamide	Merck	$\text{C}_7\text{H}_{10}\text{N}_2\text{O}_2$

		(M.W. 154.17 g/mol)		
40	Titanium isopropoxide (M.W. 79.86 g/mol)		Aldrich	$C_{12}H_{28}O_4Ti$
41	6-amino-2-(hydrazenecarbonyl)- 1,3-dioxobenzo[de]isoquinoline -5,8-disulfonate de lithium (Lucifer yellow) (M.W. 444.25 g/mol)		Aldrich	$C_{13}H_{10}Li_2N_4O_9S_2$
42	Copper phthalocyanine tetra sodium sulfonate (M.W. 988.28g/mol)		Aldrich	$C_{32}H_{16}CuN_8O_{12}S_4Na_4$
43	Multiwalled carbon nanotubes (MWCNTs)		Aldrich	
44	Fullerenes (C_{60})		Aldrich	
45	Graphite rods		Aldrich	

Besides these, deionized water (resistivity~18.2 MΩ cm) obtained through Millipore Direct-Q 3 UV system was used as solvent. Inorganic transparent electrodes of SnO₂:F coated glass (Pilkington, sheet resistance: 14 Ω sq⁻¹) were cleaned in a soap solution, 30% HCl solution, double distilled water and acetone prior to use and these were used as current collector. A spacer (a transparent acrylic tape, 1 mm thick and 5 mm wide) was used between the two electrodes to fill the electrolyte when cells were assembled into quasi solid-state devices.

2.2 Characterization techniques

The work presented in this thesis mainly focuses on the fabrication and characterization of QDSSCs. The cells and their components were characterized by various techniques which are described below.

2.2.1 Scanning electron microscopy (SEM)

SEM is a powerful tool to examine the materials, with a combination of high magnification, larger depth of focus and greater resolution. SEM produces a largely magnified image by using electrons to form an image. A beam of electrons is generated by an electron gun, typically, the tungsten filament. The electron beam is accelerated through high voltage and passes through a system of apertures and electromagnetic lenses to produce a thin beam of electrons.^[1] When the beam hits the sample, secondary electrons (SE), back scattered electrons (BSE) and X-rays are ejected out. SE emerges from the small layer on the surface and generate best resolution which, delivers topographical contrast, whereas BSE emerges from the deeper regions and gives information about composition contrast and material specific characteristics. These electrons are detected by detectors, transformed into a signal which is then projected onto a screen. Energy dispersive X-ray spectroscopy (EDX), an attachment for SEM, is employed for the elemental analysis of the sample. X-ray photons are converted into an electrical signal which is recorded by a multi-channel analyzer. The analyzer records the signal in terms of an energy slot and projects it onto a display screen. The slot position is proportional to the X-ray photon energy which passes into the detector. A histogram of the X-ray energy received by the detector, is obtained on the screen, wherein the heights of the individual peaks, are a direct measure of the amount of a particular element prevalent in the sample.

In the present study, Zeiss FE-SEM has been utilized for recording field emission SEM topographical images. Surface morphologies of the MWCNTs, PEDOT fibers (**Chapter 6**),

Au microfibers (**Chapter 7**) and ZnO nanorods (**Chapter 8**) were analyzed using FESEM. A schematic of a SEM is shown below (**Figure 2.1**).

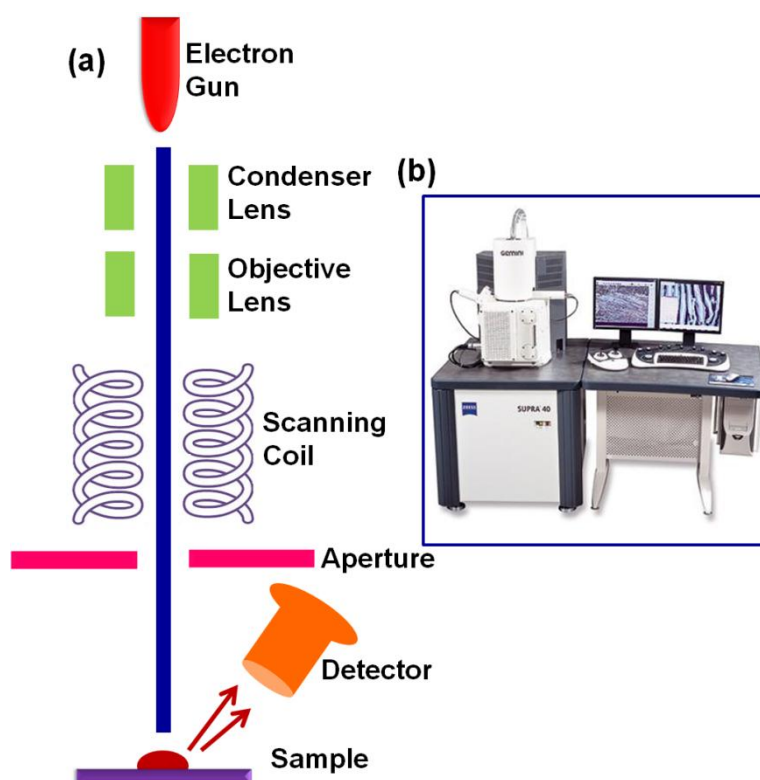


Figure 2.1: (a) Schematic of a SEM and (b) photograph of the FE-SEM Instrument used herein.

2.2.2 Transmission electron microscopy (TEM)

Transmission electron microscopy (TEM) is a familiar technique for imaging materials at an atomic resolution; structural information can be acquired both by imaging and by electron diffraction. High energy electrons (> 100 kV) are used instead of photons and electromagnetic lenses known as condenser lenses are used instead of the glass lenses as in an optical microscope which help to focus the electrons into a very thin beam. The electron beam passes through the sample and magnifies the image using the sets of lenses known as objective lenses, intermediate lenses and projector lenses and are enlarged all the way. This image is projected on a fluorescent screen or a CCD camera. Electrons from the beam are either scattered or lost, subject to the density of the sample under study. At the bottom of the microscope, unscattered electrons hit the fluorescent screen. The darker regions with larger

contrast arise from the portions wherein lesser number of electrons are transmitted owing to a high density or a large thickness of the specimen, whereas the regions of lower contrast reveal those parts of the specimen, corresponding to a lower density or thickness, and as a consequence a greater number of transmitted electrons prevail. The schematic diagram of a TEM is shown below (Figure 2.2).

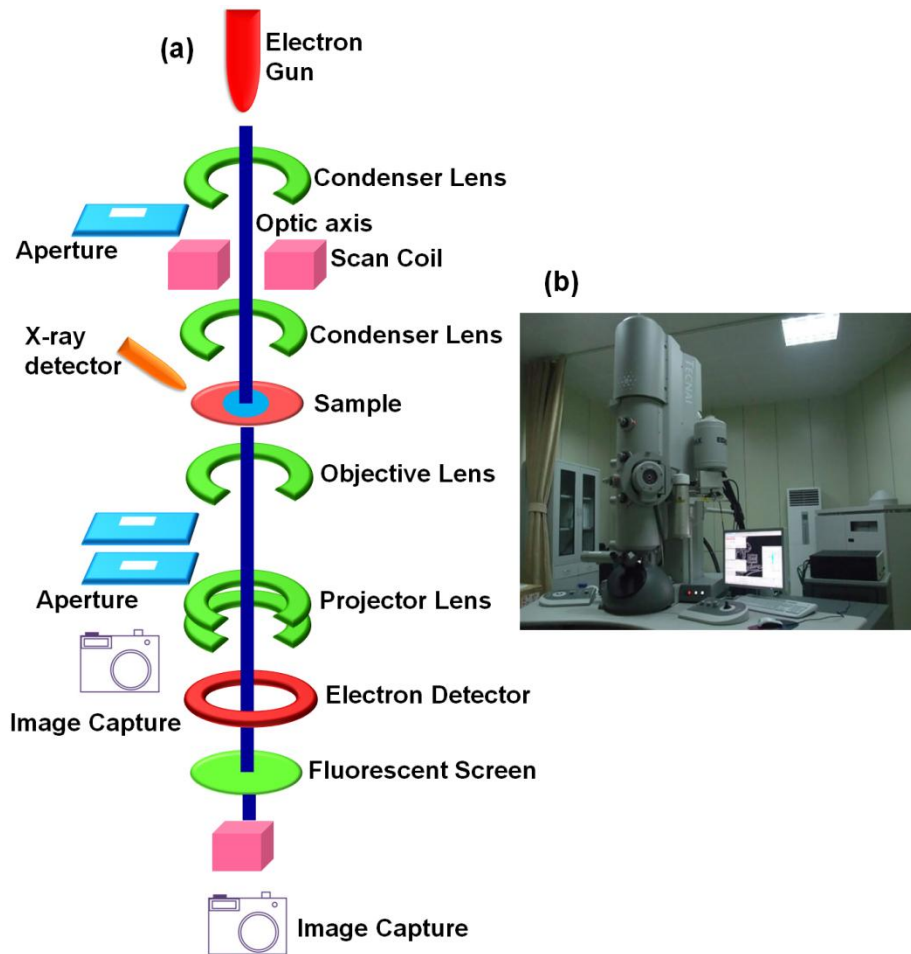


Figure 2.2: (a) A schematic representation of TEM and (b) photograph of the TEM instrument used herein.

TEM can be used as an electron diffraction camera by suitable combination of the microscopic lenses. This is done by inserting a suitable diffraction aperture instead of objective lenses aperture. Here, electrons are used to estimate the orientation of the crystal and the size and shape of the crystallite from the shape and structure of the pattern.

In the present work, TEM and high resolution TEM or HRTEM has been used for the microstructural analysis of QDs and other photoanode components. For this, thin layers of the samples were carefully extracted using forceps into deionized water and then transferred onto a carbon-coated copper grid 3.05 mm in diameter, and the solvent was evaporated at room temperature before use. A HRTEM Tecnai G2 F30 STWIN with a FEG source operating at 300 kV was used.

2.2.3 Atomic force microscopy (AFM)

Atomic force microscopy (AFM) is an advanced technique for topographical characterization of materials. In addition to imaging the surface with nanometre resolution in 3D profile, AFM can also be used to determine surface roughness, surface forces etc. In AFM, a sharp microscale cantilever tip interacts with the sample surface sensing the local forces between the molecules of tip and the sample surfaces. This force can be described by using the Hooke's law.

$$F = -K x \quad (1)$$

In (1) F is the force, K is the spring constant and x is the cantilever deflection.

AFM consists of a probe, a cantilever, a scanner, a laser, a data processor and a photodetector. The imaging modes can be classified into static (contact) and dynamic (non-contact) modes. In contact mode, the force acting between the tip and the specimen surface is held at a fixed value during scanning by preserving a constant deflection.^[2] The interactive force operative between the tip and the specimen falls in the repulsive region of the intermolecular force curve. Tapping mode is usually employed for imaging soft samples. The tip is vacillated at its resonating frequency and is placed above the specimen such that it contacts the sample for a short period of time during the vacillation. In the non-contact mode, which is an ac mode, the instrument relies on the use of an oscillating cantilever. AFM is very useful for imaging samples at the atomic scale on a range of surfaces. The atoms at the

apex of the tip, which is held just above the sample surface, sense the atoms lying on the top surface of the sample. The subsequent chemical interactions between the two, slightly change the tip's vibration frequency, and therefore, these can be detected and mapped.

In this work, we have used AFM to examine the topography, and the thickness of the photoanode. AFM, conductive atomic force microscopy (C-AFM) and Kelvin probe force microscopy (KPFM) data were recorded by using a Veeco, Multimode 8 with ScanAsyst coupled with nanoscope 8.10 software (**Figure 2.3**).

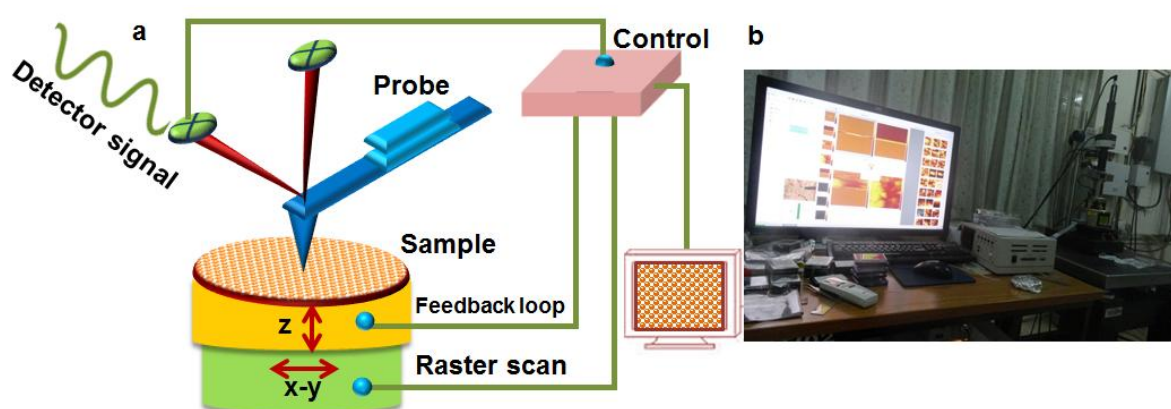


Figure 2.3: (a) Schematic of an AFM and (b) a photograph of the AFM instrument used herein.

2.2.4. Conductive atomic force microscopy (C-AFM)

Conductive atomic force microscopy is an imaging mode of contact AFM, wherein an electronically conducting tip is scanned in contact with the specimen surface, while a dc voltage is applied between the sample and the tip and the sample generates a current image and a topographical image as well. Upon developing an image of the topography, the tip is moved to a definite position on the surface. The potential of the tip is ramped and simultaneously the current produced is measured and local current *versus* voltage (I-V) curves are acquired by the instrument.

For recording C-AFM data, cantilevers made of antimony doped silicon (n-doped; resistivity $\sim 0.01 - 0.025 \Omega \text{ cm}$) and coated with Pt-Ir (20 nm) on the front and backside were used here. The spring constant of tip was 0.2 N cm^{-2} . The current sensitivity was 1 nA V^{-1} and

a load force of 49 nN was maintained between the tip and the sample. The sample deposited on FTO coated glass, (area $\sim 10 \text{ mm}^2$) was attached to a stainless steel support with a conducting carbon tape. The topography, current images and point contact I-V profiles were recorded at room temperature. C-AFM was used to study the distribution of localized currents in photoanodes.

2.2.5 Kelvin Probe Force Microscopy (KPFM)

Kelvin probe force microscopy (KPFM) is a non-contact variant of AFM. The work function of the surface can be measured at atomic or molecular levels. AFM measures the contact potential difference (V_{CPD}) between the sample surface and the tip, which equals the work function difference between the sample and the tip. V_{CPD} was measured by applying an external potential until the surface charges cease. At this point, the external potential is equal to the V_{CPD} . KPFM measures the work function of the material using this principle.

In the present work, the surface potential of composite films were measured by employing cantilevers made of antimony doped silicon and with a metallized apex of Co/Cr on the front and the back side of the tip. The spring constant of tip was $1\text{-}5 \text{ N cm}^{-2}$. The tip height was $14 \text{ }\mu\text{m}$, and the tip radius was $\sim 30 \text{ nm}$. An ac bias is applied to the tip, and as a result of this an electrostatic force is generated between the tip and the sample. This is V_{CPD} . The dc potential which is applied to nullify V_{CPD} , is the work function of the sample.

$$V = V_{\text{dc}} - V_{\text{CPD}} + V_{\text{ac}} \sin\omega t \quad (2)$$

2.2.6 UV-Visible spectrometry

Absorption is an important characteristic of a solar cell. The amount of light that can be absorbed by a photoanode can be determined by using UV-visible spectroscopy. Absorption by a homogeneous transparent sample follows the Beer-Lambert law and which relates the amount of light absorbed by the sample with its concentration, as expressed in equation (3).^[3]

$$A = \log (I_0/I) = \epsilon cl \quad (3)$$

In (3), A is the absorbance and I_0 is the intensity of the incident light impinging on the sample and I is the intensity of the light transmitted through the sample, c is the concentration of the absorbing sample and l is the path length through the sample. ϵ is the molar extinction coefficient. Absorbance of solid samples is measured in the diffuse reflectance mode, wherein an integrating sphere is used to collect photons scattered off the surface of the film. The reflectance data is converted to absorbance by using the Kubulka-Munk relationship (equation 4).

$$f(R) = (1-R)^2/2R = K/s = Ac/s \quad (4)$$

In (4) R is the reflectance, K is the absorption coefficient, s is the scattering coefficient, A is absorbance, and c is the concentration of the absorbing species. This mode was employed herein, to measure the absorbance of TiO_2 , ZnO and other solid photoanode samples.

A UV-Vis spectrometer consists of a light source, sample holder, a diffraction grating, monochromator and a detector. The light source is often a tungsten filament and a deuterium arc lamp. The detector is typically a photodiode or a charged coupled device (CCD). The equipment is calibrated with a reference cell with neat solvent to determine I_0 , whereas in the dual beam mode, I and I_0 of the sample and reference cells are measured simultaneously as shown in **Figure 2.4**.

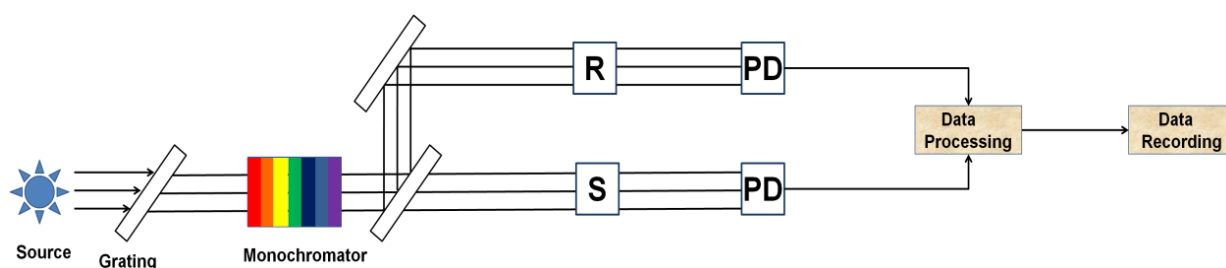


Figure 2.4: Schematic diagram of a UV-Vis spectrometer

The absorption of energy by a sample leads to an electron transfer from ground state to the excited state, and thus the position of the absorption maximum depends upon the energy difference between the valence band (VB) and conduction band (CB). In the present work, UV-Vis spectroscopy was used to measure the absorption of QDs in solution, photoactive films and precursor solutions. In a typical experiment, the absorbance of the material was recorded as a function of the wavelength. It has been foresaid that, optical properties QDs can be tuned by size control, thus correlate size and band gap of the QDs from the absorption analysis. For solid samples diffuse reflectance has been utilized. Absorption was recorded on a Shimadzu UV-Visible-NIR 3600 spectrophotometer (**Figure 2.5**).

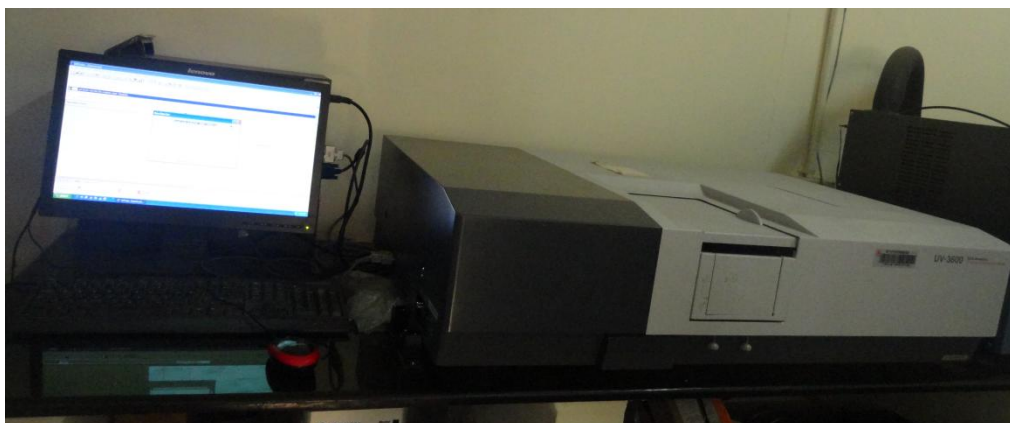


Figure 2.5: Photograph of a UV-Vis spectrophotometer used herein.

2.2.7 Photoluminescence (PL) spectroscopy

Photoluminescence (PL) spectroscopy is a powerful tool for probing the optical and electronic properties of materials in a semiconductor. Upon illumination, electrons are excited from the VB to the CB, which is known as photo-excitation. The electrons return to the ground state eventually, by losing energy. Fluorescence and phosphorescence are the photon emission phenomena that occur during the molecular relaxation from the electronic excited state. These radiative processes involve transitions between the vibrational and electronic states. Subsequent to excitation, the electrons cascade to the lowest vibrational

level of the excited electronic state. Fluorescence occurs, when the electrons relax from the lowest level vibrational state of the excited state to the allowed vibration level of the ground state.^[4] The excited state structure and the relevant electronic transitions can be explained clearly by using the Jablonski diagram (**Figure 2.6**).

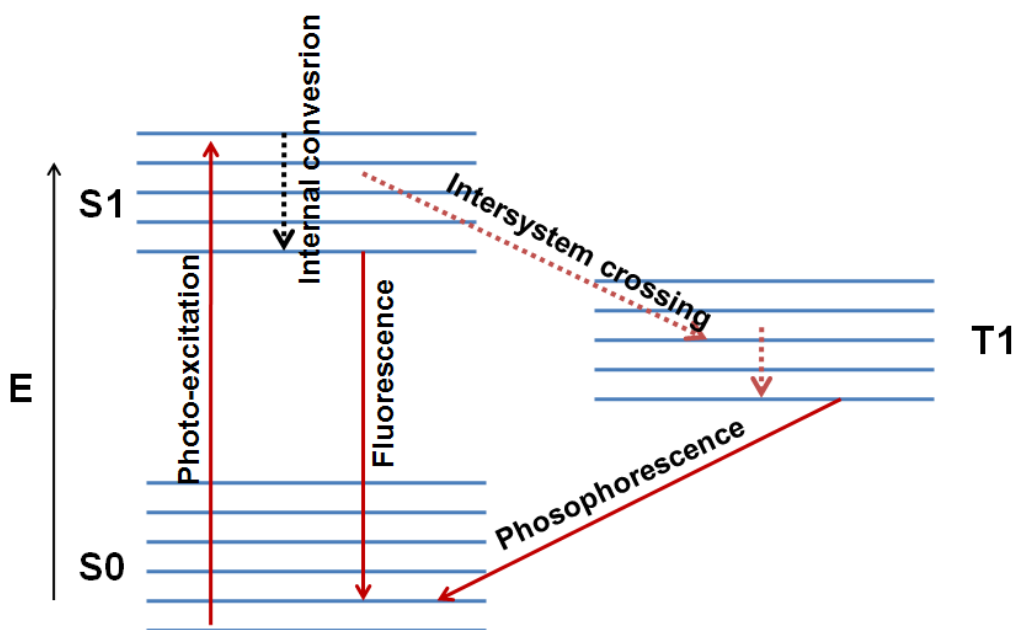


Figure 2.6: Jablonski diagram illustrating fluorescence.

A PL spectroscopy consists of a light source, a sample holder with optical components, a monochromator, and a detector. The most commonly used light source is a Xenon arc lamp. A photomultiplier or a CCD employed as the photodetector. In more sophisticated equipments, monochromators are provided for both the selection of excited light and for the analysis of the sample emission. Sensitivity can be further improved by employing band pass filters. A schematic of a fluorescence spectrophotometer is shown in **Figure 2.7**. A fluorescence spectrum is a plot of emission intensity as function of wavelength measured at a constant excitation wavelength.

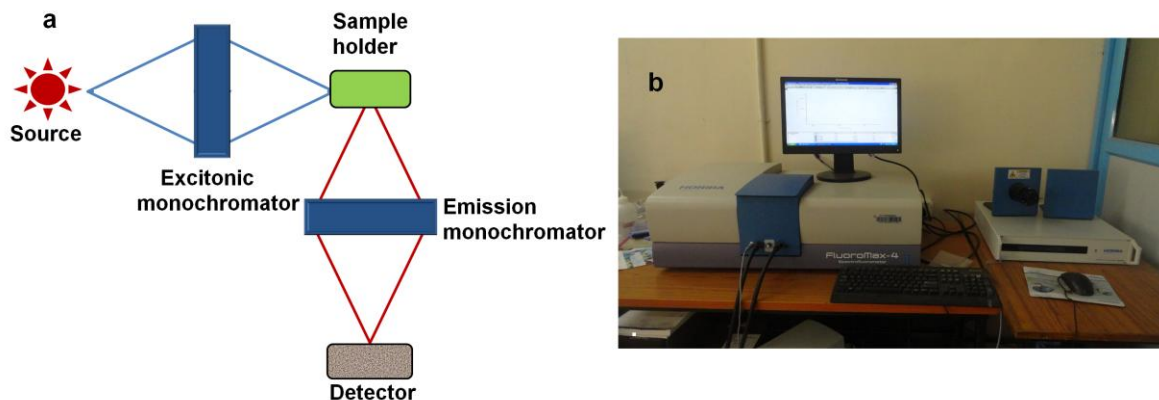


Figure 2.7: (a) A schematic of a fluorescence spectrophotometer and (b) photograph of fluorescence spectrometer (with lifetime analyser) used herein.

QDs are known to be highly luminescent materials. In this thesis, we have used fluorescence spectroscopy to explain the charge transfer as well as the energy transfer mechanisms in QDSSCs. Quantum yield was calculated by use of steady state emission analysis. Fluorescence spectra were measured using a Horiba Fluoromax-4 fluorescence spectrometer.

2.2.8 Lifetime analysis

Once an electron is excited to a higher energy state by absorption of radiation, the duration for which the excited electron resides in the higher energy state is known as the lifetime of the electron. After this time, the system spontaneously reverts to its original state by emission of radiation of appropriate energy or by radiation less decay. Time resolved measurements were performed with a pulsed laser source and the decay of the fluorescence intensity was measured as a function of time. A steady state observation is the average of the time resolved phenomena over the intensity decay of the sample. For a fluorophore which exhibits an exponential fluorescence decay, its intensity decay can be fitted into equation (5).

$$I(t) = I_0 \exp(-t/\tau) \quad (5)$$

In (5) τ is the mono exponential decay time constant.

Time correlated single photon counting (TCSPC) is a popular technique for the lifetime analysis. It measures the time of emission of individual fluorescent photons and it was used herein. The probability distribution of a single photon emission forms the basis of this measurement, which yields the actual intensity against time distribution of the all emitted photon subsequent excitations. The instrument consists of a nano LED diode with 1 MHz as the repetition time and a pulse duration of 1.3 ns was used as the excitation source. Light-scattering Ludox solution (colloidal silica) was utilized to obtain the instrument response function (prompt). In the actual experiment, each photon emitted by the sample as a result of excitation is timed and recorded, whereas in the time to amplitude converter (TAC) requires only the timing of the first photon in a given time interval after excitation. Before the signal reaches the TAC, it passes through the constant function discriminator (CFD) which measures the arrival time of the photoelectron pulse with high time resolution.

A Horiba JobinYvon DAS6 fluorescence decay analysis software was used to fit the function to the experimental data and the average lifetime was calculated by using the following equation. Lifetime analysis is a supporting tool for the emission studies. From lifetime, we can deduce the charge transfer as well as the energy transfer mechanisms in complex systems. Rate of charge transfer kinetics was also calculated from the difference in lifetimes before and after the addition of the quencher by using the following equation.^[5]

$$k_t = 1/\tau_{(QD+ Quencher)} - 1/\tau_{(QD)} \quad (6)$$

2.2.9 X- ray Powder Diffraction (XRD)

XRD is a useful analytical tool for phase identification and unit cell analysis. Crystalline atoms cause the beam of incident X-rays to diffract in many specific directions. Crystal structure information can be deduced from Bragg's law.

$$n\lambda = 2d\sin\theta \quad (7)$$

In (7) n is a small integer, λ is the wavelength of the X-ray beam from X-ray tube usually $\text{CuK}\alpha_1 = 1.5405\text{\AA}$, d is the inter-planar spacing of the crystal, θ is the angle between the incident collimated X-ray beam and an atomic lattice in the crystal.

The instrument consists of a X-ray source, usually, the cathode ray tube, and the X-rays are collimated and directed towards the sample. The interaction leads to constructive interference. The detector detects the diffracted X-rays, which are then counted. By subjecting the specimen to a range of 2θ values, all plausible diffraction lattice directions are obtained owing to the random orientation of the powdered sample (**Figure 2.8a**). From the 2θ values of the diffraction peaks, the d -spacings are obtained using Bragg's law and this permits the identification of the crystalline specimen since each crystal is characterized by a set of unique d -spacings. This is generally accomplished by a comparison of d -spacings with standard reference data.^[6]

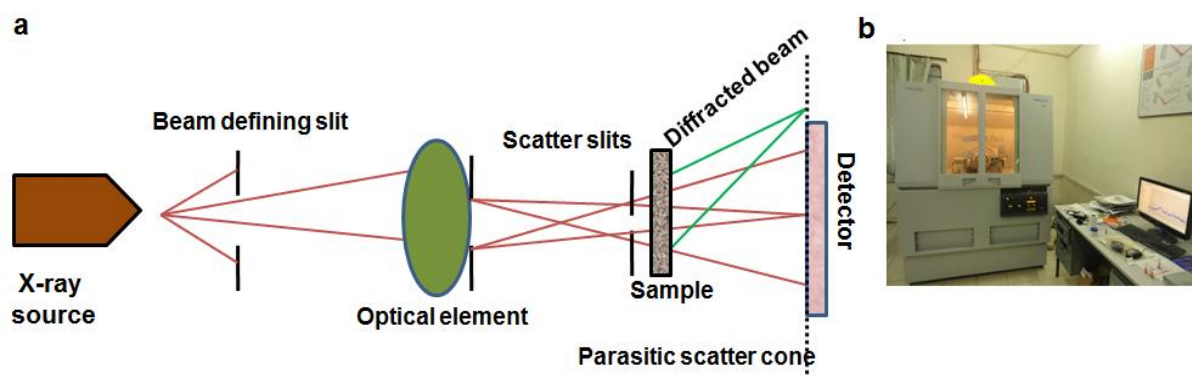


Figure 2.8: (a) Schematics of XRD and (b) photograph of XRD machine used herein.

2.2.10 Raman spectroscopy

Raman spectroscopy is a sophisticated tool to observe rotational, vibrational, and other low frequency modes. It relies on the inelastic scattering of a monochromatic radiation. During this process, there is an energy exchange between the incident photon and the sample, such that the re-emitted photons have higher or lower frequency than that of the incident photons, which is known as Raman effect. This energy difference (Raman shift) can be used for identifying functional groups, lattice modes in a sample.

A Raman spectrometer consists of a laser source, light collection optics, a monochromator and a detector (mainly PMT or CCD). The wavelength corresponding to the elastic Rayleigh scattering are filtered out and the rest of the light is sent to the detector. A Bruker Senterra Dispersive Raman Microscope Spectrometer was used in the present work, and a laser wavelength of 785 nm was used for the measurement (**Figure 2.9**).

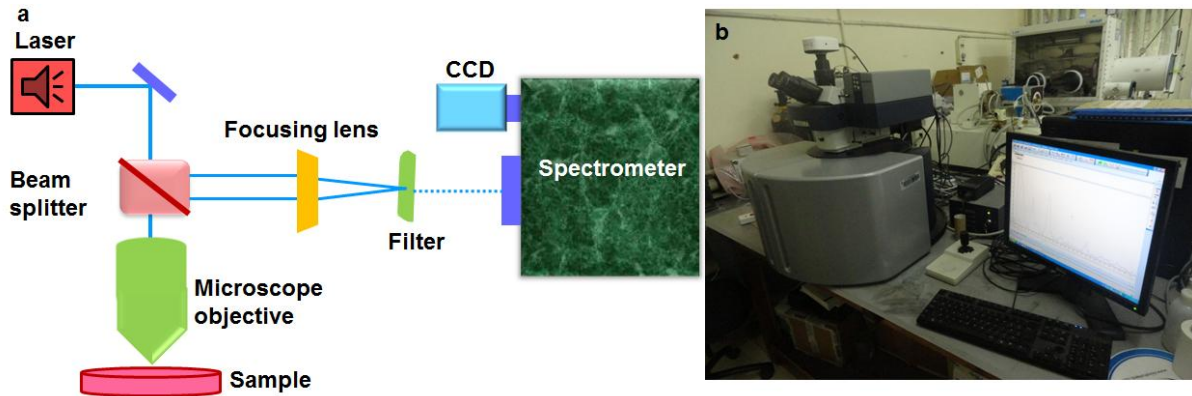


Figure 2.9: (a) Schematic of a Raman spectrometer and (b) a photograph of a Raman microscope spectrometer used herein.

2.2.11. Current-voltage characteristics (J-V)

A solar simulator measures the maximum power output (P_{out}) of a photoelectrochemical cell by sweeping the potential across the cell and measuring the resultant current upon illumination. Thus, the photovoltaic performance can be illustrated using the J-V graph (current per unit area or current density *versus* voltage) (**Figure 2.10**).

The power conversion efficiency (PCE, η) can be calculated by using the following equation.

$$\eta = P_{out}/P_{in} = V_{OC} \times J_{SC} \times FF/ P \quad (8)$$

V_{OC} is the open circuit voltage; this is the maximum potential obtained from a solar cell, and this is obtained at zero current. J_{SC} is the short circuit current density, which is the maximum current produced without applying any bias and is directly related to the maximum

number of carriers generated in the cell upon illumination. FF is the fill factor. The ideal value for the FF is 1. P_{in} is the intensity of the incident light.

A solar simulator consists of a light source, usually a Xenon arc lamp, this lamp offers high intensities and the unfiltered spectrum which matches well with sun's electromagnetic spectrum. Condenser lenses and mirrors are used to fold the optical paths as per requirement. An AM 1.5G filter is located just before the homogenizer to ensure reproducible spectral shaping. Upon illumination, current-voltage is monitored by using a source meter from zero load (short circuit condition) to infinite load (open circuit condition). In the present thesis, current-potential (I-V) data were measured using a Newport Oriel 3A solar simulator with a Keithley model 2420 digital source meter. A 450 W Xenon arc lamp was used as the light source with a light intensity of 100 mW cm^{-2} and of Air Mass (AM) 1.5 illumination; the spatial uniformity of irradiance was confirmed by calibrating with a $2 \text{ cm} \times 2 \text{ cm}$ Si Reference Cell traceable to NREL and re-affirmed with a Newport power meter.

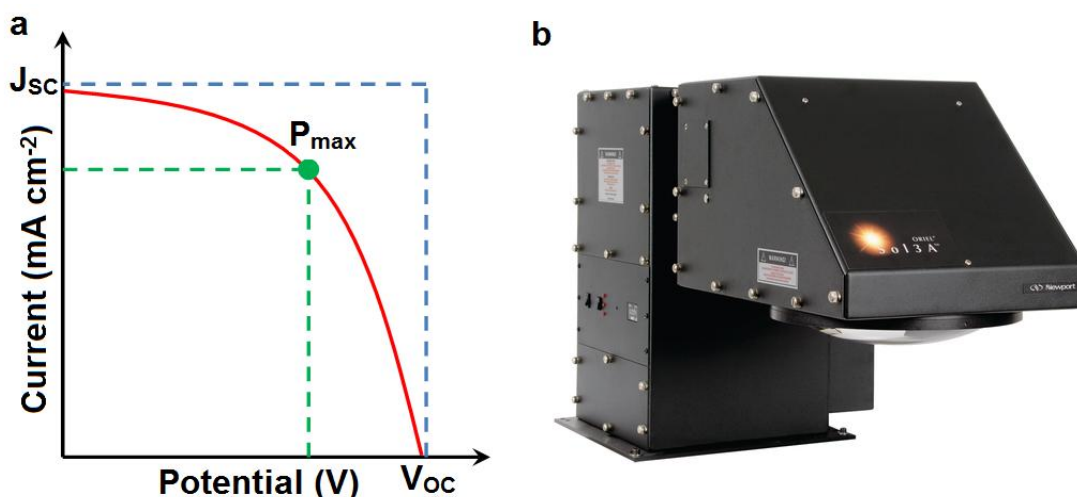


Figure 2.10: (a) A typical J-V scan and (b) a photograph of the solar simulator used herein.

2.2.12 Incident photon to current conversion efficiency (IPCE)

IPCE is an important parameter for the photoelectrochemical cell, which describes how efficiently the impinging photons are converted to electrons at different wavelengths. IPCE was calculated by using the following equation.^[7]

$$\text{IPCE (\%)} = J_{\text{SC}} (\text{A cm}^{-2}) \times 124000 / \lambda (\text{nm}) \times I (\text{W cm}^{-2}) \quad (9)$$

In (9) J_{SC} is the short circuit current density generated under monochromatic light illumination, λ is the wavelength of incident light and I is the incident power.

The basic components of a IPCE system are a light source, usually Xenon lamp or a quartz tungsten halogen (QTH) lamp, a monochromator to split up different wavelengths of light (**Figure 2.11**). The generated current was measured by using a source meter or a multimeter. A Si reference cell was employed for the calibration.

In the present thesis, IPCE data was obtained using a 150 W Xenon arc lamp as a light source coupled with a Horiba monochromator equipped with a 1200 groove / nm grating and a blaze wavelength of 330 nm, over a wavelength span of 350 – 600 nm. Photocurrents were measured under back illumination using a Keithley 2420 digital source meter. The power of the incident beam was measured by using a calibrated Si photodiode having a known response (ThorLabs, FDS100) and also ratified with a radiant power meter from Newport (842-PE).

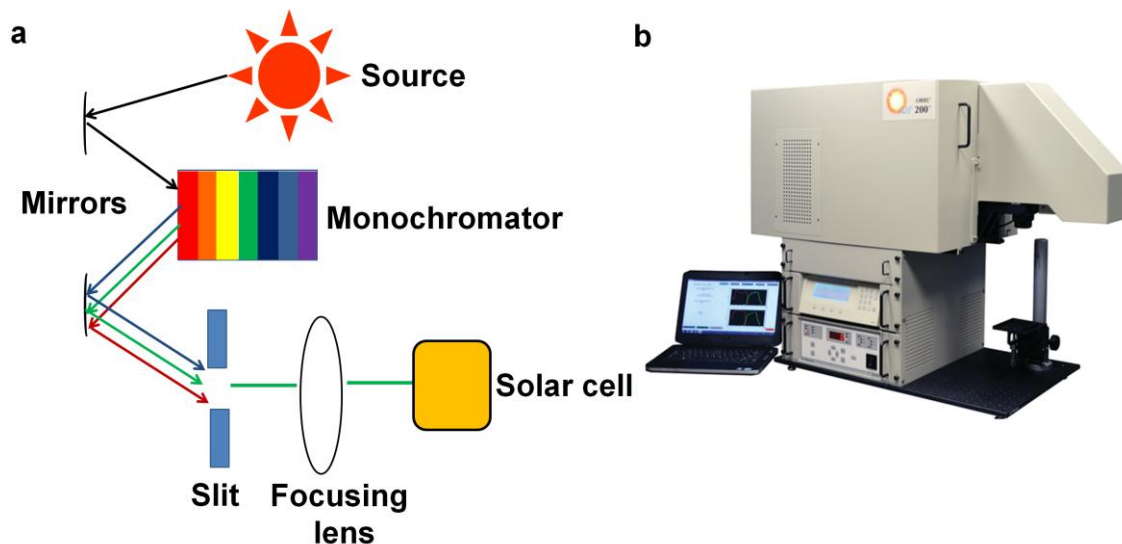


Figure 2.11: (a) Schematic of the IPCE measurement system and (b) a photograph of the IPCE equipment used herein.

2.2.13 Cyclic voltammetry (CV)

CV is an electroanalytical tool which provides the complete electrochemical spectrum of an electroactive material. CV measurements are usually carried out in a three electrode cell. In a three electrode configuration, the potential between the working electrode (WE) and the reference electrode (RE) can be controlled and hence the current flow between the WE and counter electrode (CE) can be analyzed. The potential applied to the WE is continuously swept back and forth at a fixed scan rate. Sweep in the electrodic potential with respect to the time is known as scan rate, which has a triangular wave form. The current measured is monitored as a function of applied potential over a fixed voltage range and the obtained plot is denoted as a cyclic voltammogram. CV can provide important information about the oxidation reduction potential of an electroactive species, extent of reversibility and the electrochemical potential stability window. From CV plots, the magnitudes of peak current (i_p , cathodic and anodic), oxidation/reduction potential (E_p), the number of electrons transferred per molecule of the reactant (n), rate constant and diffusion coefficient (D) can be determined. In this thesis, CV was employed to analyze the redox properties of the QDs, and to characterize the supercapacitor performance. The capacitance was calculated by the following equation.

$$C = dQ/dV = \int I dt / dV = I \Delta t / \Delta V = I / \text{scan rate} \quad (10)$$

In (10) C is the capacitance, Q is the charge.

An Autolab PGSTAT 302N Potentiostat/Galvanostat coupled with a NOVA 1.9 software was used to record CV plots (**Figure 2.12**).

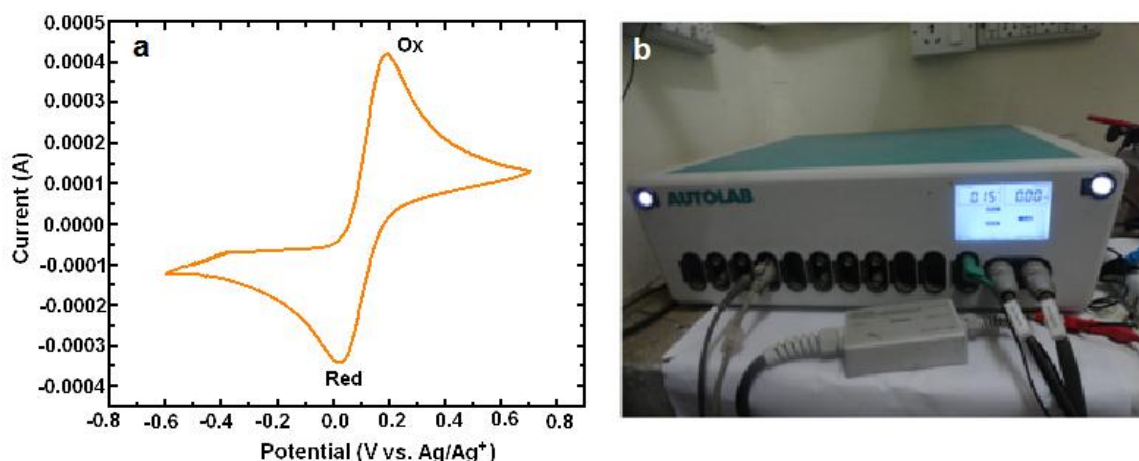


Figure 2.12: (a) A cyclic voltammogram of a 5 mM ferro-ferricyanide redox couple in a phosphate buffer saline (PBS) (pH 7.0, 50 mM, 0.9% NaCl) and (b) a photograph of Autolab PSTAT system used herein.

2.2.14 Linear sweep voltammetry (LSV)

Linear sweep voltammetry (LSV) is another analytical technique, which involves the sweeping of electrode potential only in one direction between the start point and the end point at a fixed scan rate. As potential is ramped, the faradic current increases as a function of scan rate. This is caused by an enhanced flux of the electroactive sample to the electrode at high scan rates. The extent of the increase in the faradic current scales with the square root of scan rate. This implies that by increasing the scan rate in a LSV measurement, an increased analytical signal to noise ratio can be achieved. But at the same time, the capacitive contribution to the total current is found to be directly proportional to scan rate, which leads to a decreased signal to noise ratio, as a function of increasing scan rate.

In this thesis, LSV was used to (a) measure the I-V characteristics and to (b) measure the conductivity of the film of interest. Conductivity was measured by using the following equation.

$$\sigma = (I/V) \times (l/a) \quad (11)$$

In (11) l is the thickness and a is the area of the film. I-V measurements were carried out by using an Autolab PGSTAT 302N Potentiostat/Galvanostat coupled with a NOVA 1.9 software.

2.2.15 Chronoamperometry (CA)

Chronoamperometry is an electroanalytical technique in which the potential of the working electrode is kept constant and the resulting current from the faradaic process is monitored as a function of time. As the current is integrated over relatively longer time intervals, chronoamperometry gives a better signal to noise ratio in comparison to other amperometric techniques.^[8] In this dissertation, CA was used to characterize the photocurrent generation in the photoelectrochemical cell. The plots were recorded under a step time of 60 s. Upon illumination, the cell showed photocurrent, whereas in dark it showed zero current CA was also used for the synthesis of a conducting polymer film. The experiments were performed in both three and two electrode systems by using an Autolab PGSTAT 302N Potentiostat/Galvanostat coupled with a NOVA 1.9 software.

2.2.16 Chronopotentiometry (CP)

Chronopotentiometry is a constant current electroanalytical tool wherein a constant current is applied and the potential response generated is plotted as a function of time. Here this technique was used to measure the photovoltage response of a photoelectrochemical cell. Upon illumination, the device showed the corresponding photovoltage and in dark it showed very less photovoltage. The measurement was carried out at a step time of 60 s. It was also used to measure the galvanostatic charge – discharge characteristics of a photosupercapacitor, which is discussed in detail in **Chapter 7**. The specific capacitance was calculated by using the following equation.

$$SC = I \times \Delta t / \Delta V \times m \quad (12)$$

In (12), SC is the specific capacitance, I is the current applied for charge or discharge, Δt is the time in seconds for charge or discharge, ΔV is voltage window and m is mass of active material of the working electrode. Measurements were carried out on an Autolab PGSTAT 302N Potentiostat/Galvanostat coupled with a NOVA 1.9 software.

2.2.17 Electrochemical impedance spectroscopy (EIS)

EIS measures the impedance of a system, over a range of frequencies and therefore the frequency response of the system is revealed. In EIS, a sinusoidal potential is applied to the working electrode in an electrochemical cell and the resulting sinusoidal current generated as a result of this perturbation is measured. This current signal can be analyzed as the sum of sinusoidal function. The excitation signal can be expressed as a function of time.^[9]

$$E_t = E_0 \sin \omega t \quad (13)$$

In (13), E_t is the potential applied at time t, E_0 is the amplitude of the potential signal, and the radial frequency is denoted by ω . ω (expressed in radians/second) and the frequency f (expressed in Hz) are related by the following equation.

$$\omega = 2\pi f \quad (14)$$

In a linear system, the response signal, I_t , is shifted in phase (Φ) and has a different amplitude than I_0 .

$$I_t = I_0 \sin (\omega t + \phi) \quad (15)$$

Impedance is therefore, a measure of the ac resistance offered by the system to the flow of an alternating current in a complex system. A complex electrical system comprises of a resistance, capacitance and an inductor. In general, the impedance can be represented as shown in equation (16).

$$Z = E_t/I_t = E_0 \sin(\omega t) / I_0 \sin(\omega t + \phi) = Z_0 \sin(\omega t) / \sin(\omega t + \phi) \quad (16)$$

The data obtained by EIS is expressed graphically in a Bode or a Nyquist plot (**Figure 2.13**).

The Bode plot can give information related to applied frequency.

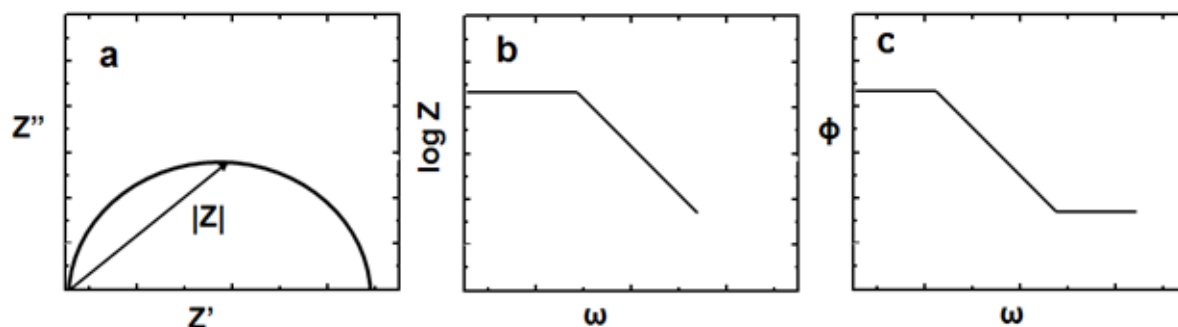


Figure 2.13: (a) Nyquist plot with impedance vector and Bode plots showing (b) log Z and (c) phase angle *versus* frequency.

In this work, EIS was used to analyze charge transfer resistance and diffusion in a photoelectrochemical cell. EIS was used to measure the conductivity of solutions also, which were deduced from Z'' *versus* Z' plot (Nyquist plot). A FRA analyzer connected to a Autolab PGSTAT 302N Potentiostat/Galvanostat was used for recording EIS spectra in this thesis.

2.3 Reference

- [1] <http://www.steve.gb.com/images.science/scanning-electron-microscope.png>.
- [2] www.nrel.gov.
- [3] H. H. Perkampus, *UV-Vis Spectroscopy and its Application*, Springer-Verlag, Berlin, Newyork, (1992).
- [4] J. R. Lakowicz, *Principles of Fluorescence Spectroscopy, 2nd ed.*; Kluwer Academic/Plenum Publishers: New York, (1999).
- [5] P. V. Kamat, K. Tvrdy, D. R. Baker, J. G. Radich, *Chem. Rev.* **110** (2010) 6664-6688.
- [6] http://www.wiley-vch.de/books/sample/3527310525_c01.pdf.
- [7] A. Kongkanand, K. Tvrdy, K. Takechi, M. K. Kuno, P. V. Kamat, *J. Am. Chem. Soc.* **130** (2008) 4007-4015.
- [8] C. G. Zoski, *Handbook of Electrochemistry*, Elsevier Science, (2007).
- [9] E. Barsoukov, J. R. Macdonald, *Impedance Spectroscopy: Theory, Experimental and Applications*, Wiley-Interscience, (2005).

Chapter 3

Influence of functionalized graphene oxide and Au nanoparticles on the photoelectrochemical response of a TiO₂/CdSe QDs assembly

3.1 Introduction

In view of the extensive efforts devoted to maximizing the efficiency of photocurrent generation by use of diverse methodologies for photoanode preparation,^[1-3] which were discussed in **Chapter 1**, in this study, the fabrication and characterization of a novel nanocomposite constituted by CdSe QDs/Au nanoparticles (NPs) tethered to a coating of ionic liquid functionalized graphene oxide (FGO) nanosheets and mesoporous titania (TiO₂) is presented. In particular, much emphasis was laid on characterizing the microstructure of the composite deposit, as morphology is known to have a profound effect on the performance of the photoanode. The excited state interactions involving charge propagation between all the four components of the composite were followed by fluorescence quenching and by studying the ultrafast kinetics of photogenerated charge carrier decay. This work, therefore attempts to furnish an understanding of pertinent factors, which control charge transfer and kinetics in QDSSCs, and thus will be relevant for creating new photoanode architectures for high efficiency cells.

3.2 Experimental

3.2.1 Synthesis of CdSe QDs

CdSe nanocrystal QDs were prepared by using a chemical route procedure reported previously involving the TOPO/TOP capping method.^[4] Briefly, selenium (Se) solution was prepared by mixing 0.40 g of Se powder, 10 mL of TOP, and 0.20 mL of toluene. 20 g of technical-grade TOPO and 0.25 g of cadmium acetate dihydrate were taken in a three-neck, and stirred for 10 minutes at about 150 °C. It was then heated to 300 °C. At this temperature,

the selenium solution was immediately injected to the flask. The solution was heated at 300 °C for only 2 minutes to arrest the QD size, which was accompanied by a color change from yellow to red. The resulting red colored solution was cooled to room temperature and an excess amount of ethanol was added to the solution, to precipitate the QDs. In order to remove the superfluous TOPO, the precipitated QDs were re-dissolved in a small quantity of toluene and re-precipitated in ethanol. The procedure was repeated for two more times, and the precipitate was stored under nitrogen.

3.2.2 Synthesis of gold nanoparticle (Au NP) dispersion

A suspension of Au NPs in toluene was prepared by the method developed by Brust et al.^[5] Two solutions, one containing HAuCl₄ (0.18 g) in 15 mL of deionized water and another composed of tetraoctylammoniumbromide (1.09 g) in 40 mL of toluene were prepared. The two solutions were mixed and stirred continuously for about 10 minutes until the color of the aqueous phase became clear and thereafter, a solution of NaBH₄ (0.4 M) in deionized water was added slowly. The color of the upper organic phase changed from orange to ruby red whereas the lower aqueous phase turned colorless. The mixture was stirred for 30 more minutes. The organic phase containing Au NPs was extracted, washed once with dilute sulfuric acid for neutralization and subsequently five times with distilled water. The strength of the resulting ruby red dispersion was 4 mM, assuming the complete reduction of HAuCl₄ to Au. It was stored in dark at room temperature.

3.2.3 Synthesis of functionalized graphene oxide (FGO) from graphite rods

1-butyl-3-methyl-imidazolium trifluoromethanesulfonate and water were mixed in a 1:1 weight ratio and taken in a rectangular glass cell. Graphite rods were employed as both cathode and anode, and a fixed dc potential of 15 V was applied across the cell for 2 hours at room temperature. Exfoliation of the graphite rod occurred specifically at the anode. The expanded graphite rod was immersed in DMF intermittently. Graphene oxide, functionalized

by the ionic liquid, is transferred to the solvent, each time. It was collected by centrifugation, washed with DMF and ethanol, and dried at 50 °C, in an oven for 12 hours.

3.2.4 Fabrication of the QD sensitized electrodes

A thick slurry of TiO₂ anatase nano-powder and FGO (0.11 mg per ml of solvent) was prepared in ethanol. The resulting slurry was coated on FTO coated glass using a doctor blade method and annealed at 150 °C for 40 minutes to enable evaporation of the solvent and adherence of TiO₂/FGO to the substrate. The QD sensitized film was prepared by first keeping the TiO₂/FGO film immersed in a 0.1 M MPA linker solution in deionized water for 10-12 h. A dispersion of Au NPs (4 mM) and a solution of TOP/TOPO capped CdSe QDs (200 mM) were mixed in a 1:1 volume ratio and the TiO₂/linker coating was submerged in the resulting suspension for 10-12 h for anchoring of the CdSe QDs and Au NPs vis-à-vis sulfur on the linker molecules. The resulting TiO₂/CdSe/FGO/Au electrode was washed with toluene and stored in dark (**Figure 3.1**). The same protocols were employed for fabricating TiO₂/CdSe, TiO₂/CdSe/FGO and TiO₂/CdSe/Au electrodes.

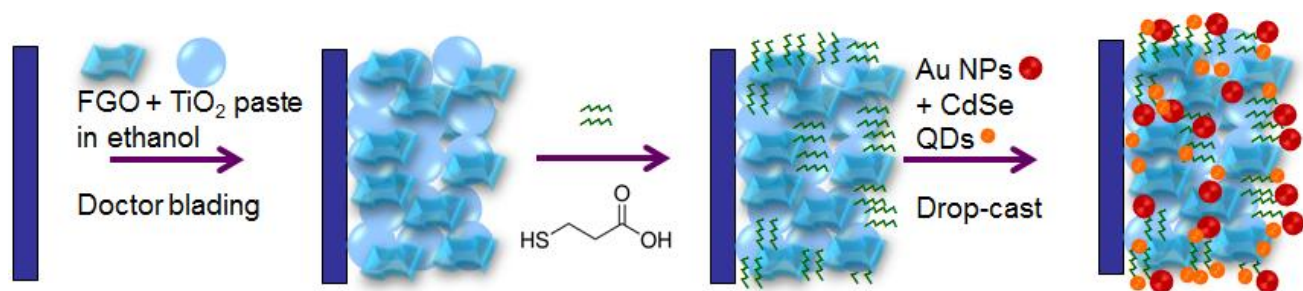


Figure 3.1: Schematic showing the fabrication of a TiO₂/CdSe/FGO/Au electrode.

3.3. Results and discussion

3.3.1 HRTEM studies

Figure 3.2a is a low magnification image of exfoliated graphene oxide functionalized by imidazolium triflate (FGO). The entrapping of the ionic liquid cation and anion in the FGO nanosheets was confirmed by EDX, which showed clear signals due to N, S and F arising from the imidazolium and triflate ions and also by Raman spectroscopy. The nanosheets are

entangled with one another and wrinkles and foldings are observed on the surface as well as edges. The overlapping of nanosheets produces the crisscross lattice fringes, shown in **Figure 3.2b**. The defects in the structure, introduced by the action of the ionic liquid and oxygen containing functionalities, show up in the image in the form of ripples. In some regions (inset of **Figure 3.2c**), the hexagonal lattice on the graphene nanosheet could be identified; a blown up view of the quasi-hexagonal arrangement of carbon atoms is presented in **Figure 3.2c**. The slight difference in contrast for the atom in the center is suggestive of a foreign atom like oxygen. The image of the TiO₂/CdSe/FGO/Au composite reveals layers of crinkled FGO nanosheets (**Figure 3.2d**) and from the fast Fourier transformation (FFT) performed on a small region of the film, the electron diffraction pattern, thus obtained showed a hexagonal array of bright spots, confirming that the high crystalline quality of the FGO nanosheets is preserved in the composite. The CdSe QD size was estimated to be ~3.9 nm, from TEM images (**Figure 3.2i**). A typical image is shown in **Figure 3.2e**; the fringes are fuzzy in some portions probably due to overlapping of the contributions from different moieties, and it appears that CdSe QDs, TiO₂ and Au NPs are flanked to FGO nanosheets. In some regions, distinctive lattice spacings from TiO₂ with a periodicity of 0.127 nm (JCPDS: 89-4921) and dark fringes with a 0.149 nm separation that originate from CdSe, were clearly seen to be embedded in the FGO nanosheets (**Figure 3.2f**). Further evidence affirming the attachment of CdSe QDs with TiO₂, was obtained in the form of a clear interface, shown in **Figure 3.2g**, wherein the bright and dark fringes originate from TiO₂ and CdSe QDs respectively. The change in the contrast of the lattice fringes at the boundary of the two moieties, is due to the molecular level linking of the two, and also could be due to the presence of the bulky TOPO ligands surrounding the CdSe QDs. The edges of the FGO nanosheets are visible in **Figure 3.2h**, and the inset shows an Au crystallite implanted in the FGO nanosheets.

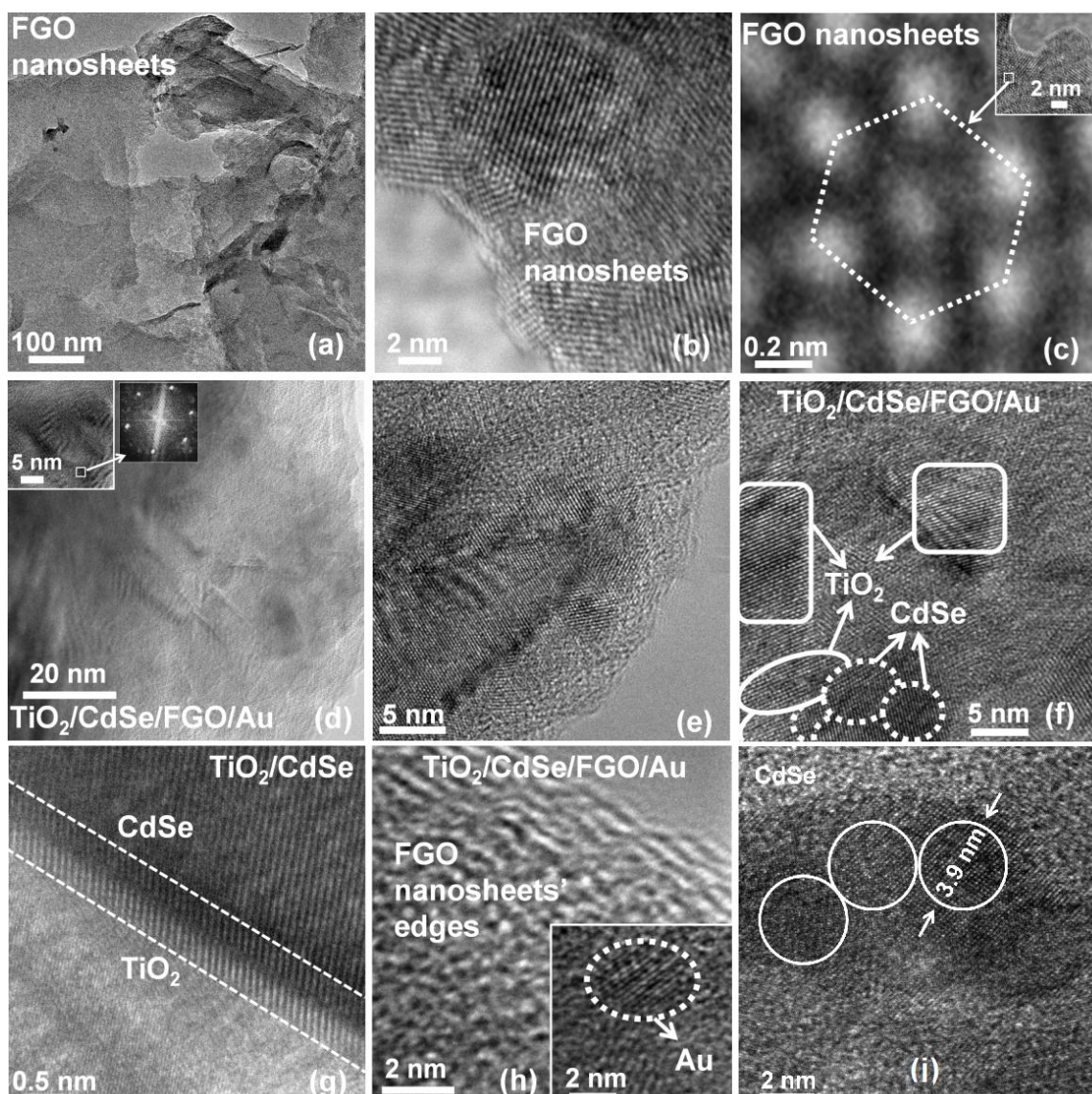


Figure 3.2: (a) Low magnification image of crinkled FGO nanosheets, HRTEM images of (b) overlapping FGO nanosheets, (c) atomic scale image of the hexagonal lattice of carbon atoms obtained from a region shown in the inset, (d) HRTEM image of $\text{TiO}_2/\text{CdSe}/\text{FGO}/\text{Au}$ composite, the inset is the spotty electron diffraction pattern generated by FFT performed on a small region of the composite (shown in the left hand side inset), (e) a blown up view of the $\text{TiO}_2/\text{CdSe}/\text{FGO}/\text{Au}$ composite, with overlapping lattice fringes; contributions from all the components, (f) lattice spacings from TiO_2 and CdSe QDs flanked to FGO nanosheets, (g) magnified view of a TiO_2/CdSe QD interface, (h) Au NPs anchored to FGO nanosheets (inset showcases one Au crystallite) and (i) Neat CdSe QDs of diameter 3.9 nm.

The average Au NP size was ~ 3 nm, and the fringe separation of 0.123 nm, agrees well with the face centered cubic lattice of Au (JCPDS: 65-2870). It is apparent that CdSe QDs, FGO nanosheets, Au NPs and TiO_2 are homogeneously dispersed in the composite, as only a

connection between these nano-moieties at the molecular level can account for the HRTEM observations.

3.3.2 Structural characterizations of FGO

The elemental composition of ionic liquid functionalized graphene oxide (FGO), in terms of atomic percentages is as follows: C: 43.8%, N: 28.2%, O: 14.7%, F: 13.1% and S: 0.3%. It is apparent that the ionic liquid, 1-Butyl-3-methyl imidazolium trifluoromethanesulfonate is incorporated between the graphene oxide nanosheets, for otherwise signals due to N, S and F would not have arisen. The most likely mechanism for sandwiching of the ionic liquid between the GO nanosheets is via π - π interactions enabled by the imidazolium ring on the ionic liquid cation and the aromatic nature of the GO sheets. The Raman spectrum of FGO nanosheets shows broad D and G bands. The G peak is seen at 1582 cm^{-1} and arises from the in-plane vibration of sp^2 hybridized carbon atoms. The D band due to surface defects on graphene sheets, is observed at 1310 cm^{-1} .

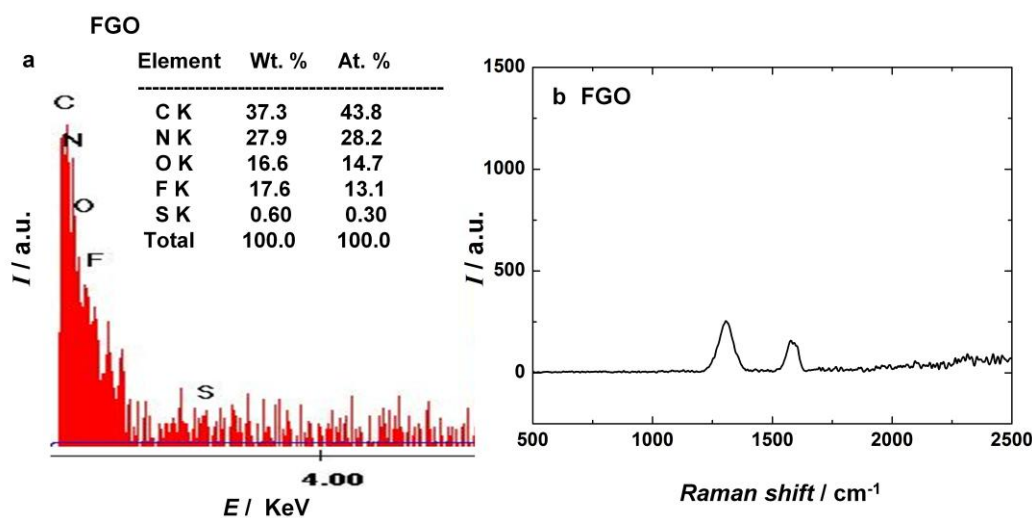


Figure 3.3: (a) EDS plot and (b) Raman spectrum of ionic liquid functionalized graphene oxide.

3.3.3 Absorption and fluorescence quenching studies

The digital photographs of the precursor sols of CdSe QDs, Au NPs, FGO nanosheets and their mixtures are shown in **Figure 3.4a**. **Figure 3.4b** shows the absorption spectra of Au NPs, CdSe QDs, TiO₂ nanopowder and FGO nanosheets. Au NPs show an intense absorption

peak at 525 nm, attributable to surface plasmon resonance and CdSe QDs show a weak band gap excitation peak at 551 nm, corresponding to a HOMO-LUMO gap of 2.02 eV. Both FGO and TiO₂ show a flat absorption in the visible region. Band gaps were determined from Tauc plots shown in **Figure 3.5**.

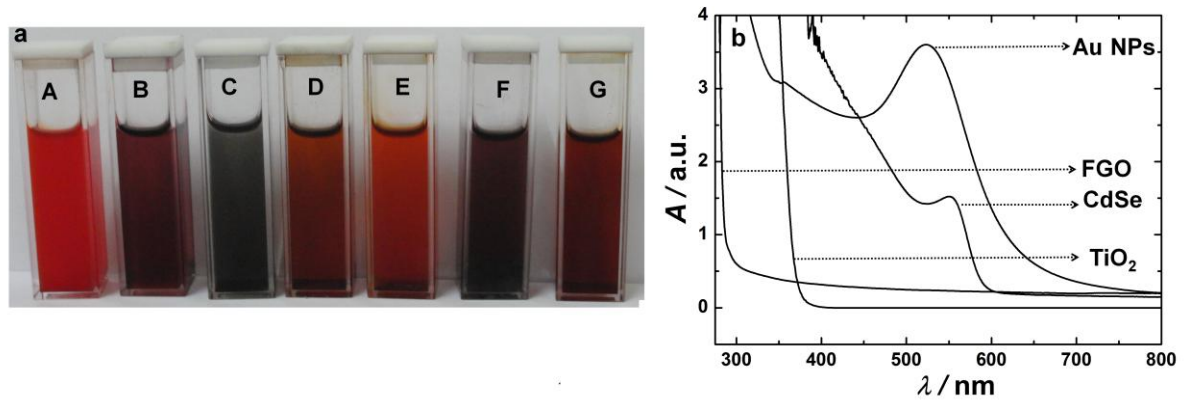


Figure 3.4:(a) Digital photographs of solutions of (A) CdSe QDs, (B) Au NPs, (C) FGO nanosheets, (D) CdSe QDs + Au NPs, (E) CdSe + FGO nanosheets, (F) FGO nanosheets + Au NPs and (G) CdSe + Au NPs + FGO nanosheets, (from left to right) and (b) Absorbance *versus* wavelength plots of colloids of neat Au NPs, neat FGO nanosheets and neat CdSe QDs. Absorption spectrum of TiO₂ film is generated from the response in the diffuse reflectance mode.

Band gaps were determined from Tauc plots, wherein, absorption coefficient varies as a function of frequency, according to

$$\alpha h\nu \propto (h\nu - E_g)^n \quad (1)$$

In (1), $h\nu$ is the photon energy and E_g is the band gap, and $n = 2$, for indirect transitions, as in TiO₂ and $n = 1/2$ for direct transitions, as in CdSe. The absorption coefficient was determined from the absorption plots using the relation:

$$\alpha = 1/d \{A(\lambda)\} \quad (2)$$

In (2), d is the thickness / path length of the film / solution and A is the absorbance. Band gaps of TiO_2 and CdSe were 3.2 and 2.02 eV respectively, obtained from the intercepts of Tauc plots.

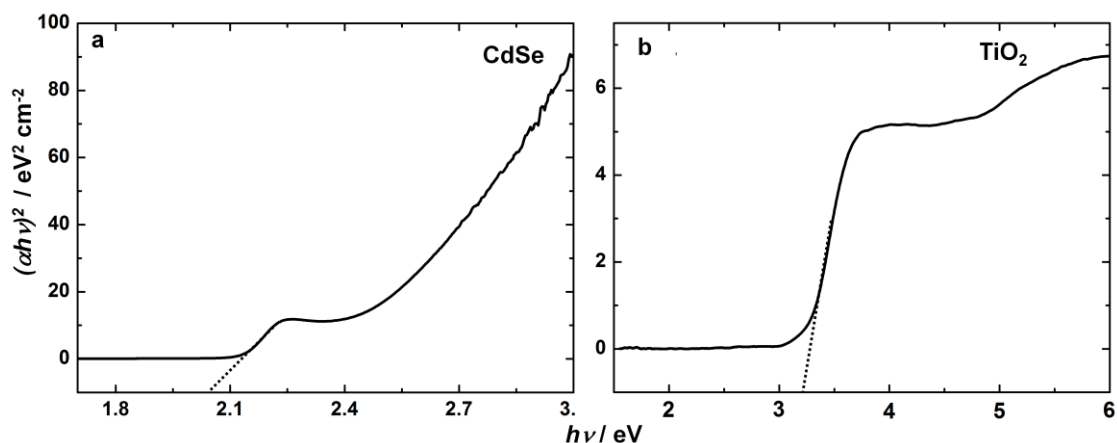


Figure 3.5: Main edge absorption spectra plotted as (a) $(\alpha h\nu)^2$ and (b) $(\alpha h\nu)^{1/2}$ vs. photon energy ($h\nu$) for CdSe QDs and TiO_2 respectively.

To comprehend the charge transfer dynamics in the composite ($\text{TiO}_2/\text{CdSe}/\text{FGO}/\text{Au}$), we examined the interplay of the individual components, in terms of fluorescence quenching effects. The band edge emission peak of CdSe QDs is found to lie in the range of 500 – 700 nm, depending upon the size of the dot.^[6,7] The neat CdSe QD dispersion showed an intense emission peak at 570 nm (**Figure 3.6a**). Evidence for charge transfer from CdSe QDs to Au NPs was obtained by following the fluorescence quenching of the CdSe QDs with increasing Au concentration. CdSe QDs strength was fixed at 3 mM, to which a 4 mM Au NP dispersion was added in small aliquots, whilst maintaining the total volume at a fixed value. The progressive decay of the emission of CdSe QDs, with increasing content of Au NPs, is an indicator of the transfer of photogenerated electrons from the CB of the donor (CdSe QDs), to the empty electronic states of the Au NPs. A red shift is also observed, at high Au concentrations, which may be due to some complex formation between Au and CdSe. We found at a volume ratio of 1:2 (CdSe QDs : Au NPs), the fluorescence of QDs almost reduced

to negligible values, as can be gauged from the inset of **Figure 3.6a** suggesting an efficient charge transfer.

To investigate further, the effect of FGO nanosheets on the emission of CdSe QDs was studied (**Figure 3.6b**). It has been demonstrated in the past, that functionalized graphene shows a fairly intense blue emission, typically in the range of 350 – 450 nm.^[8] This emission, in all likelihood, arises from the emitting centers on RGO surfaces, that primarily include the oxygen containing species, like epoxy, carbonyl and hydroxyl groups, for even though, here we employed an IL to exfoliate graphite, the possibility having oxygen moieties flanked to the graphene nanosheets in the final product (FGO) cannot be ruled out. The IL interacts with the GO nanosheets vis-à-vis (a) π - π and (b) electrostatic interactions, and therefore, these defect sites can act as emissive sites and give rise to the emission at ~500 nm, as observed for a pure suspension of FGO (**Figure 3.6b**). The luminescence peak of neat CdSe QDs, observed at 570 nm, quenches dramatically, upon addition of FGO, for upon introduction of only 50 μ L of FGO suspension to CdSe, the CdSe emission intensity reduces to ~38% of its original value. This is an indicator of rapid charge transfer from CdSe QDs to the Fermi level of FGO.

Neat Au NPs do not show any emission in the visible range (inset of **Figure 3.6a**), and therefore, we observed a quenching of the PL peak of neat FGO nanosheets' suspension (0.11 mg per mL of toluene), when a 4 mM Au NP dispersion was introduced to the same (**Figure 3.6c**). The diminishing intensity of FGO's emission peak with increasing Au NP content, again hints at electron propagation from FGO nanosheets to Au NPs. Metal nanoparticles are known to behave as electron sinks, and when brought in contact with a semiconductor like FGO nanosheets, the Au NPs act as electron acceptors. As our composite is made of TiO₂/CdSe/FGO/Au, and since neat CdSe QDs show a strong emission at 570 nm, we studied

the effect of a dispersion of a fixed composition, comprising FGO nanosheets (0.11 mg in 1 mL of toluene) and 4 mM Au NPs mixed in a 1:1 v/v ratio, on the PL peak of CdSe QDs (Figure 3.6d).

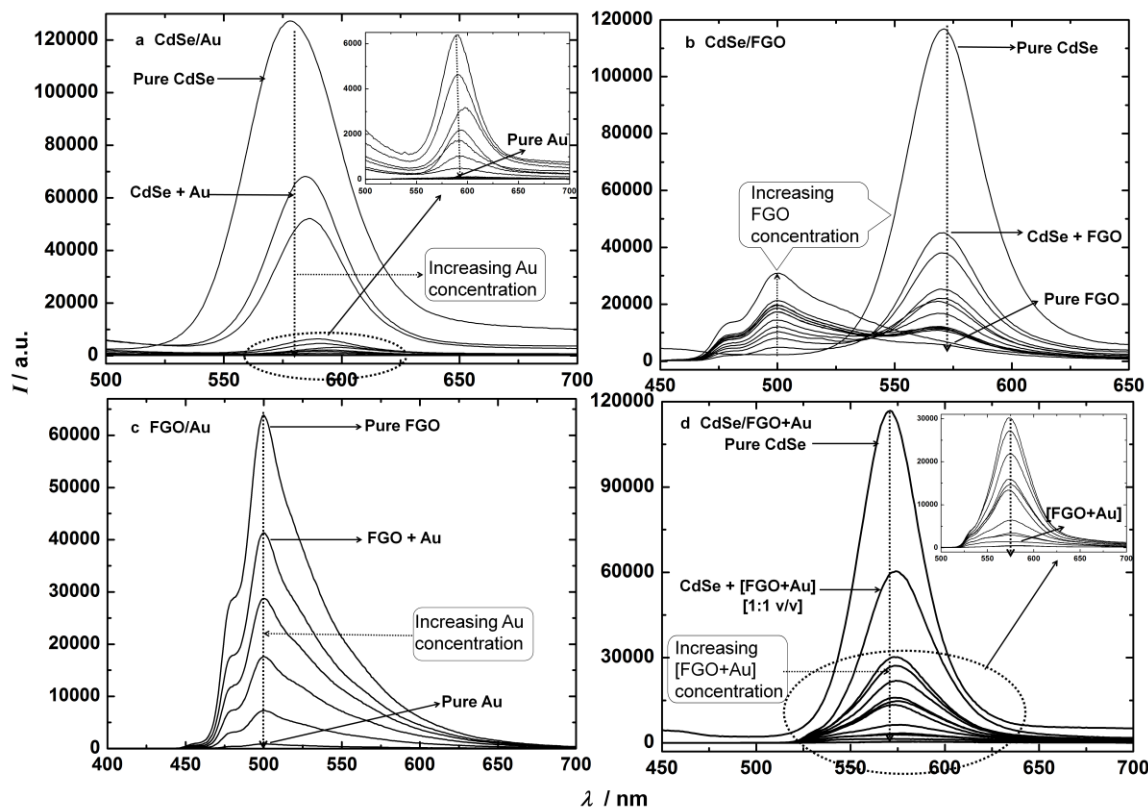


Figure 3.6: PL spectra of colloids: (a) CdSe QDs + Au NPs, (b) CdSe QDs + FGO nanosheets, (c) FGO nanosheets + Au NPs and (d) CdSe QDs + [Au NPs + FGO nanosheets (1:1 v/v)] measured with λ_{ex} fixed at 370 nm. Initial colloid strengths: CdSe QDs: 3 mM, Au NPs: 4 mM and FGO nanosheets: 0.11 mg per mL; all in toluene. The total volume of pure colloids was fixed at 3000 μ L, and aliquots of Au NPs or FGO nanosheets or [Au NPs + FGO nanosheets (1:1 v/v)] were added in steps of 50 μ L, and progressive fluorescence decay of CdSe QDs was measured in (a,b and d) and of FGO nanosheets in (c).

As anticipated, the intensity of the PL peak of neat CdSe QDs drops, with increasing concentration of this dispersion. It is evident that the photogenerated charge is transferred from CdSe QDs to the dispersion. Unlike the CdSe QDs/FGO nanosheet suspensions, where the emission due to FGO nanosheets tends to predominate at high FGO levels, here, we

observed only a weak emission ascribable to FGO at ~525 nm (inset of **Figure 3.6d**), which gains intensity at the expense of the CdSe QD emission. However, this emission due to FGO nanosheets remains rather weak, even at a fairly high content of the binary dispersion (Au NPs + FGO nanosheets : CdSe QDs ~ 2:1 v/v), owing to the fact that in the binary mixture, the non-emissive Au NPs override the contribution of FGO nanosheets.

3.3.4 Emission decay analyses

To unambiguously ascertain that the interaction between the constituents of the following three systems: (i) CdSe and FGO, (ii) CdSe and Au and (iii) CdSe, FGO and Au, is truly responsible for the emission quenching of excited CdSe, then the phenomena should be time-resolvable by following emission decay. We measured the emission decay profiles of the following films: TiO₂/CdSe, TiO₂/CdSe/FGO, TiO₂/CdSe/Au and TiO₂/CdSe/FGO/Au films and the corresponding plots are shown in **Figure 3.7**. Since FGO when incorporated in TiO₂ matrix, and utilized in film form, did not yield any reasonable fluorescence, probably due to a low content of active emissive sites, the measurements were confined to CdSe emission decay. The fluorescence decay is bi-exponential, in all cases, and it was analyzed using equation (3) and the average lifetimes were estimated using equation (4), where τ_i and A_i are time constants and amplitudes respectively, of the individual decay components.

$$f(t) = A_1 e^{-t/\tau_1} + A_2 e^{-t/\tau_2} \quad (3)$$

$$\langle \tau \rangle = \frac{\sum_i A_i \tau_i}{\sum_i A_i} \quad (4)$$

The average life time values are shown in **Table 3.1**. While the fast component of fluorescence decay profile, was found to decrease slightly on going from TiO₂/CdSe/FGO (0.37 ns) to TiO₂/CdSe/FGO/Au (0.29 ns) or TiO₂/CdSe/Au (0.27 ns), the slow component showed the reverse behavior. The longer lasting component had a lifetime of 16.02 ns for TiO₂/CdSe/FGO, 14.86 ns for TiO₂/CdSe/Au and it decreased to 12.42 ns for the

TiO₂/CdSe/FGO/Au composite. Upon band gap excitation, charge separation in CdSe QDs is followed by electron–hole recombination, to yield emission. For the film of TiO₂/CdSe, without FGO or Au, the fast component in particular, compared to any of the composite with FGO nanosheets and/or Au NPs, was characterized by a much longer lifetime, greater by an order of magnitude, with a value of 1.62 ns, indicating that Au or FGO promote electron transfer. When CdSe QDs are molecularly linked to TiO₂ surface, electron transfer from CdSe to TiO₂ occurs, and this process is driven by the differential in the CB edges of the two. However, an enhanced decay rate is achieved, when FGO nanosheets or Au NPs are an integral part of the film, as dictated by a more negative CB position of FGO or Au, with respect to the vacuum level. Here, we deduced an average lifetime of TiO₂/CdSe/Au emission to be 7.87 ns, and on replacing Au with FGO, the lifetime increased to 8.68 ns, for the composite TiO₂/CdSe/FGO, indicating that charge transfer from CdSe to Au via TiO₂, is faster than the transfer from CdSe to TiO₂ to FGO. Since the average lifetime for the TiO₂/CdSe/FGO/Au composite of 6.76 ns, was the lowest, among all, it is a clear indicator of the fact that charge transfer is more efficient and rapid for the ternary combination of CdSe QDs, FGO nanosheets and Au NPs, tethered to TiO₂ rather than in the binary systems of CdSe QDs and Au NPs and CdSe QDs and FGO nanosheets flanked to TiO₂ support.

Table 3.1: Kinetic parameters of emission decay analysis of photoanode electrode films (measured at $\lambda_{\text{ex}} = 370$ nm and $\lambda_{\text{em}} = 550$ nm) deduced from bi-exponential fits.^a

Electrode description	χ^2	τ_1 (ns)	τ_2 (ns)	A_1	A_2	$\langle\tau\rangle$ (ns)
TiO ₂ /CdSe	1.225	1.62	12.72	30.23	69.77	9.36
TiO ₂ /CdSe/FGO	0.988	0.37	16.02	46.88	53.12	8.68
TiO ₂ /CdSe/Au	0.971	0.27	14.86	47.95	52.05	7.87
TiO ₂ /CdSe/FGO/Au	0.991	0.29	12.42	44.64	53.36	6.76

FGO	1.202	2.03	17.02	48.36	51.64	9.77
FGO/Au	1.256	2.23	5.38	63.94	36.96	4.86

^aA is the relative amplitude of each lifetime, τ_1 and τ_2 are the fast and slow components of fluorescence lifetime and χ^2 represents the quality of fit.

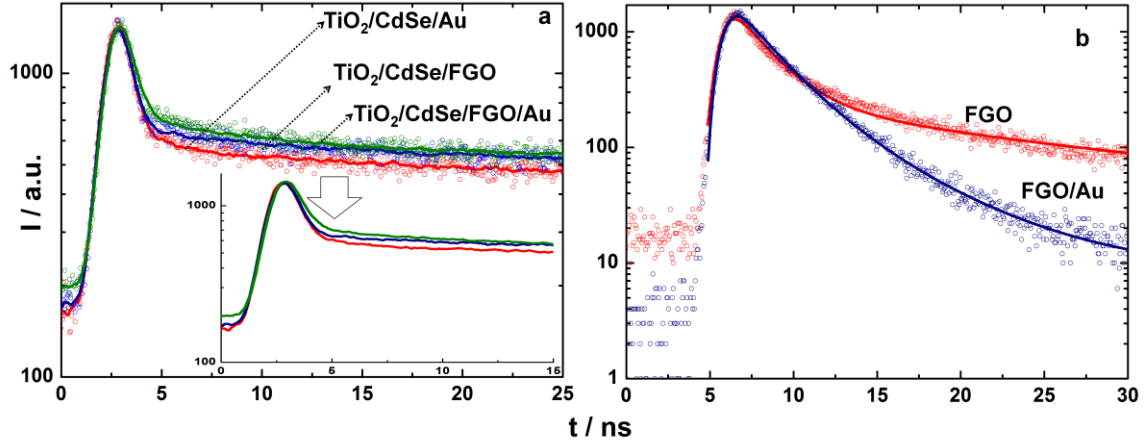


Figure 3.7: Time resolved fluorescence decay profiles of (a) $\text{TiO}_2/\text{CdSe}/\text{Au}$, $\text{TiO}_2/\text{CdSe}/\text{FGO}$ and $\text{TiO}_2/\text{CdSe}/\text{FGO}/\text{Au}$ composite films and (b) a dispersion of FGO nanosheets and [FGO nanosheets + Au NPs] in toluene. Excitation for (a) and (b) were fixed at 370 nm and emission profiles were monitored for (a) and (b) at 570 and 500 nm respectively. The solid lines represent the best fits obtained by deconvolution, assuming bi-exponential decay.

The rate of electron transfer was obtained from the expressions:

$$k_{\text{et}} = 1/\langle\tau\rangle (\text{TiO}_2/\text{CdSe}/\text{FGO}/\text{Au}) - 1/\langle\tau\rangle (\text{TiO}_2/\text{CdSe}/\text{FGO}) \quad (5)$$

or
$$k_{\text{et}} = 1/\langle\tau\rangle (\text{TiO}_2/\text{CdSe}/\text{FGO}/\text{Au}) - 1/\langle\tau\rangle (\text{TiO}_2/\text{CdSe}/\text{Au}) \quad (6)$$

The apparent electron transfer rate (k_{et}) is deduced to be $3.3 \times 10^7 \text{ s}^{-1}$ and $2.1 \times 10^7 \text{ s}^{-1}$ from equations (5) and (6) respectively, and since the two values are close, it is a reasonably good estimate. Our values also agree well with reported values for CdSe linked to TiO_2 , typically varying between 10^7 to 10^{10} s^{-1} , depending on the QD size.^[9] The average lifetime of neat FGO nanosheets' emission is 9.772 ns and it decreased to 4.859 ns, when Au NPs are

added to FGO nanosheets. The reduction in lifetime by almost half of its original value, confirms the fast charge transfer from FGO nanosheets to Au NPs.

$$k_{\text{et}} = 1/\langle\tau\rangle (\text{FGO/Au NPs}) - 1/\langle\tau\rangle (\text{FGO}) \quad (7)$$

The rate constant of $10.35 \times 10^7 \text{ s}^{-1}$ in the FGO/Au NPs system, is in principle, higher than that observed for TiO₂/CdSe/FGO/Au composite, but nevertheless, it validates the electron transfer mechanism proposed through **Figure 3.8**.

3.3.5 Energetics

The energy band diagram, illustrating the electron transfer pathway in the composite, dictated by the relative positions of CB levels of the individual components, and the redox potential of the S_n²⁻/S²⁻ electrolyte, is shown in **Figure 3.8**. The CB level of CdSe QDs with dimensions in the range of 3.5 to 4.0 nm lies at 3.9 eV, and it tends to be more negative with respect to the CB of TiO₂, on the NHE scale. Subsequent to illumination, the photogenerated electrons in CdSe QDs are transferred to the CB minimum of the TiO₂ (4.2 eV). It can be seen that the offset of 0.22 eV between the CB minimum of TiO₂ and the work function of FGO (4.42 eV) is sufficient for charge separation, and since TiO₂ nanoparticles are in direct contact with FGO nanosheets, as was seen in the HRTEM images, the flow of excited electrons to FGO is facile.^[10] Furthermore, graphene oxide sheets are known to function effectively as electron conduction supports, as they store as well as shuttle electrons.^[11] Since here, we obtained a fairly homogeneous distribution of TiO₂, Au NPs and CdSe QDs on the FGO nanosheets, the proposed electron transfer process is feasible. Au NPs, especially, when brought in contact with a semiconductor, upon Fermi level equilibration, tend to act as electron acceptors and can serve as electron sinks. The work function of neat Au lies at ~5.1 eV,^[12] but upon coming in contact with the TiO₂/CdSe/FGO, the apparent Fermi level (E_F[']) is expected to be less negative with reference to vacuum, and as we achieved higher

photocurrent in this quaternary system. Therefore upon Fermi level equilibration and illumination, as Au NPs tend to store electrons near the CB edge of the semiconductor, E_F' should in principle lie between the work function of the conducting surface (SnO₂:F) and FGO, as shown in **Figure 3.8**. The energetics of the TiO₂/CdSe/FGO/Au composite system enables Au NPs, to form a conduction bridge between FGO nanosheets and the current collector (FTO), thus allowing the passage of electrons to the external circuit. Since we found ample support, from microscopy results, for TiO₂/CdSe and Au NPs to be tethered to FGO nanosheets; FGO nanosheets therefore behave as scaffolds for the threesome, and this provides credence to the claim that electron transport to the external circuit, has to occur through FGO nanosheets. Such a stepwise electron propagation process, therefore accounts for the higher photocurrents and photovoltage achieved in this quaternary composite, in contrast to TiO₂/CdSe/FGO or TiO₂/CdSe/Au. Although the exact roles of FGO nanosheets and Au NPs are not very clear, but it is apparent that both work in synergy, and in particular, their intrinsic ability to conduct electrons improves charge separation.

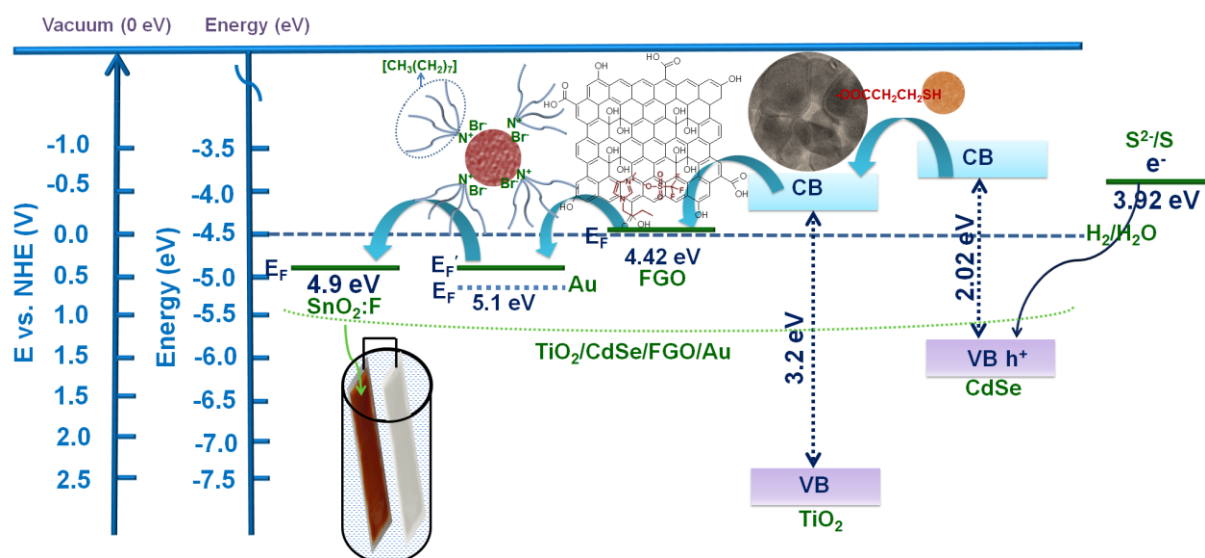


Figure 3.8: Schematic showing the energy band diagram of TiO₂/CdSe/FGO/Au composite and possible mode of electron transfer. Cartoon on left hand side displays the cell with the digital photograph of TiO₂/CdSe/FGO/Au composite film as the photoanode.

3.3.6 C-AFM studies

C-AFM was employed for evaluating the nanoscale transport properties of the TiO₂/CdSe/FGO/Au composite, as it enables a correlation between the topographical features of the film with its ability to conduct electrons across the cross-section. Surface areas of the order of 100 μm² and 1 μm² were scanned (**Figure 3.9a'** and **b'**), and the nanoscale I-V characteristics were measured, at fifteen different points on the corresponding current images, in point contact mode. The corresponding current cross sections obtained along the lines in the current images are shown in **Figure 3.9a** and **b**; since the profiles do show continuous spikes, fairly high currents are retained across the cross-section. The I-V curves shown in **Figure 3.9a''** and **b''** are the resultant scans, obtained after averaging fifteen scans in each image. When the composite film is poised to a positive bias, excited electrons in the composite are attracted to the positive bias, such that there is a continuous supply of available levels in the composite, in the vicinity of the contact, for other electrons to occupy. These electrons diffuse towards the point contact and therefore the current is high. Under negative bias, electrons are injected into the available acceptor levels in the CB of the composite, they create a barrier, and hinder further electron flow. As a consequence, currents are low. At low field strengths, in the -5 V to +5 V regime (top inset of **Figure 3.9a''**) and between +2.5 V to +7 V (inset of **Figure 3.9b''**), the current and voltage are related by Ohm's law, as

$$J = q\mu nV/d \quad (8)$$

where q is the charge, μ is the electron mobility, n is the free charge carrier density, V is the applied bias and d is the sample thickness. The average nanoscale photoconductivity was deduced to be 0.031 S cm⁻¹, indicating the highly conducting nature of the film, and the presence of uniformly distributed conducting domains in the composite. It is obvious from both **Figure 3.9a''** and **b''**, that at low fields, when carriers are introduced, the Fermi level tends to shift towards CB, carriers are trapped in the shallow traps and their contribution to

current is minimal. At high fields, however, the Fermi level reaches the trap level, and current shows a sharp increase, since all new carriers introduced can reach the CB and current rises which is consistent with the change in slope. The defect sites in CdSe QDS act as traps. At high fields, the concentration of injected carriers exceeds the concentration of carriers produced by band gap excitation, and so the injected carriers are free and therefore mobile, others are mainly intrinsic, trapped and rendered immobile. Interestingly, we found that the high field I-V data gave a good fit to Dawber's diffusion model for electron conduction.^[13]

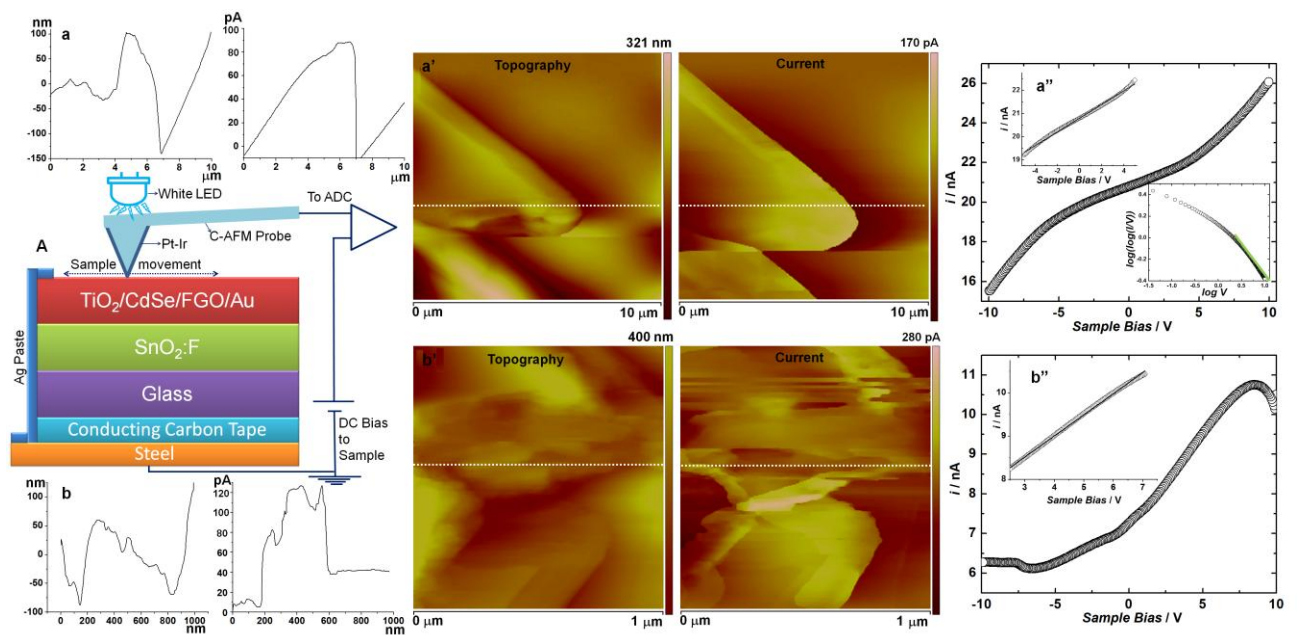


Figure 3.9: (A) is a schematic of the configuration employed for C-AFM measurements. Representative current and topography images of $\text{TiO}_2/\text{CdSe}/\text{FGO}/\text{Au}$ composite film {a' (scanned area: $100 \mu\text{m}^2$) and b' (scanned area: $1 \mu\text{m}^2$)}, corresponding section images of topography and current, taken along the dotted lines are shown in a and b, a'' and b'' are point contact I-V curves averaged over fifteen scans from fifteen points on the current images shown in a and b. Top inset of a'' shows the linear fit between -5 to $+5$ V and bottom inset of a'' shows the $\log(\log(I/V))$ versus $\log V$ response. Inset of b'' shows the ohmic dependence between $+2.5$ and $+7$ V.

The equation approximates to $\log(I/V) = \text{constant} \times V^2$; which implies a slope of 2 for a $\log(\log(I/V))$ versus $\log V$ plot. Experimentally, we achieved a slope of 1.95 in the high

potential region for this plot (bottom inset of **Figure 3.9a**) indicating an agreement with Dawber's equation. Both photoconductivity and I-V characteristics, show that electrons are accepted and transported via the TiO₂/CdSe/FGO/Au network, from the C-AFM probe tip to FTO, thereby reiterating that the organization of the nano-moieties in the composite is conducive for facile electron conduction.

3.3.7 Photoelectrochemistry of cells

Photovoltage generation (on-off cycles) for photoelectrochemical cells, based on composite films, as the photoanode, a platinum sheet as counter electrode and an aqueous 0.1 M Na₂S solution as electrolyte, are shown in **Figure 3.10A**. The plots were recorded under a step time of 100 s, when no current was applied to the cells. Upon illumination, the composite film TiO₂/CdSe/FGO/Au based cell showed a five fold enhancement in photovoltage in comparison to the cell based on TiO₂/CdSe film. The maximum photovoltage registered for the composite based cell is ~700 mV in contrast to a value of 150 mV observed for the TiO₂/CdSe cell. The composites: TiO₂/CdSe/Au and TiO₂/CdSe/FGO showed intermediate values of photovoltage, 590 mV and 400 mV respectively. Photovoltage is higher in the TiO₂/CdSe/Au and TiO₂/CdSe/FGO composites, as compared to the TiO₂/CdSe cell. Since photovoltage is largely governed by the position of CB minimum or Fermi level, it is obvious that it moves to more negative potentials with respect to NHE, in the composites based on FGO nanosheets and / or Au NPs, in comparison to TiO₂/CdSe. The net Fermi level is known to move to more negative potentials, due to charge distribution between the two (in the present case: FGO/Au and TiO₂).

Previously a photovoltage of 700 mV was obtained for a graphene/CdS QD cell, in contrast to a value close to 600 mV for a single walled carbon nanotube/CdS QD cell.^[14] Authors^[14] attributed the same to the capability of graphene nanosheets to allow a better distribution of QDs combined with a lower E_F difference between the sensitizer and the

acceptor. The photocurrent on-off cycles recorded with respect to the zero external bias, are shown in **Figure 3.10B**. Here, the effect of FGO nanosheets and Au NPs is rather pronounced, as the TiO₂/CdSe/FGO/Au composite based cell, acquires a maximum current of 400 μA , followed by TiO₂/CdSe/Au and TiO₂/CdSe/FGO composite based cells, which show photocurrents of 70 and 10 μA respectively. For graphene/CdS QDs, a photocurrent of $\sim 1.5 \text{ mA cm}^{-2}$ was achieved^[14] and for a CdSe/TiO₂ system, a photocurrent density of the same order was observed, however, for a less than unit square of illuminated electrode area.^[6] Here, more than the absolute magnitude, the photocurrent produced by TiO₂/CdSe/FGO/Au is almost 6 times the value of TiO₂/CdSe/Au, again ratifying the effective role of FGO nanosheets in separating photogenerated electron-hole pairs and transferring the electrons to the electrode surface.

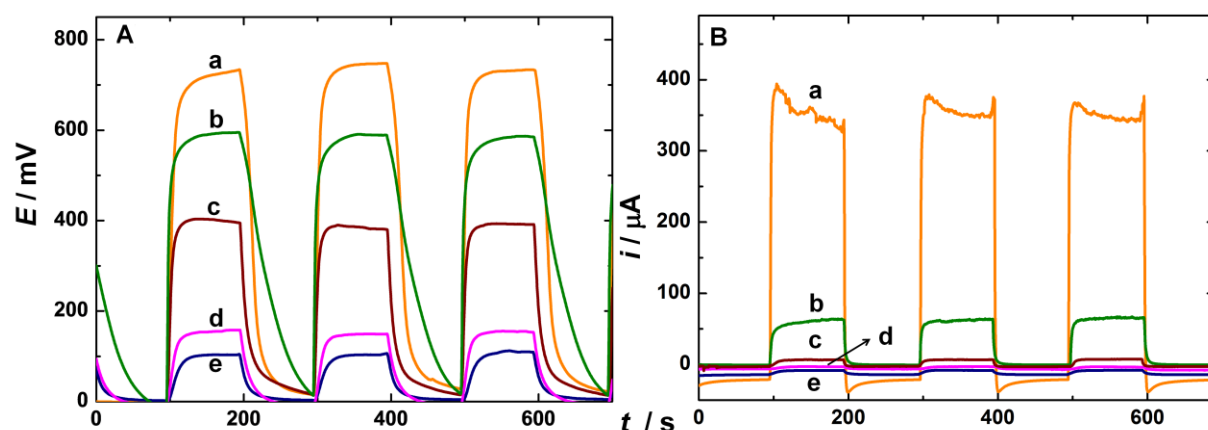


Figure 3.10: (A) Photovoltage and (B) photocurrent on-off cycles for QDSSCs based on (a) TiO₂/CdSe/FGO/Au, (b) TiO₂/CdSe/Au, (c) TiO₂/CdSe/FGO, (d) TiO₂/CdSe, and (e) TiO₂ films as photoanodes. Counter electrode: Pt, electrolyte: aqueous 0.1 M Na₂S, under illumination at $\lambda > 300 \text{ nm}$ and input power of 30 mW cm^{-2} . Measurements were performed under zero applied current or bias.

The photoelectrochemical response of the different photoanodes by employing Pt as the counter electrode and 0.1M Na₂S as the electrolyte is shown in **Table 3.2**. TiO₂/CdSe/FGO/Au has registered a J_{SC} of 3.7mA whereas a V_{OC} of 661mV. Overall

efficiency of $\sim 1\%$ has registered. In the absence of FGO the $\text{TiO}_2/\text{CdSe}/\text{Au}$ based photoanode showed a decreased J_{SC} of $3.1 \text{ mA}/\text{cm}^{-2}$ V_{OC} also has decreased ~ 1.13 times, whereas the average efficiency of 0.7% . In the composite: $\text{TiO}_2/\text{CdSe}/\text{FGO}/\text{Au}$, the superior performance is mainly due to the efficient charge separation and the increased charge separation is due to a significantly lowered rate of charge recombination, as (i) photogenerated electrons are rapidly scavenged by FGO, which has the capacity to store electrons and (ii) also by the ability of Au nanoparticles to quickly convey them to the current collector.

The photoaction spectra of the two cells, capable of producing highest photocurrents are compared in **Figure 3.11b**. The photocurrents were much higher for the $\text{TiO}_2/\text{CdSe}/\text{FGO}/\text{Au}$ composite based cell in the photopic region as compared to that shown by the $\text{TiO}_2/\text{CdSe}/\text{Au}$ cell, indicating the cumulative effect of FGO nanosheets and Au NPs in improving the current response. The IPCE of $\text{TiO}_2/\text{CdSe}/\text{FGO}/\text{Au}$ is 4.5 times more than that of $\text{TiO}_2/\text{CdSe}/\text{Au}$, indicating that graphene nanostructures facilitate charge movement. $\text{TiO}_2/\text{CdSe}/\text{FGO}/\text{Au}$ showed a maximum IPCE of 33% at 500 nm , whereas the $\text{TiO}_2/\text{CdSe}/\text{Au}$ composite registered a maximum IPCE of 21% at the same wavelength. For a system of Au/TiO_2 sensitized with CdSe QDs, a maximum IPCE slightly less than 25% was registered as opposed to a value of about 6% obtained for CdSe/ TiO_2 system,^[15] and the value was less than 2.5% in the visible region for both films. For a CdSe(ZnS)- Au/TiO_2 system, an IPCE greater than 20% was achieved at $\lambda < 400 \text{ nm}$.^[16] However, an IPCE in the range of $15\text{--}20\%$ was retained upto 550 nm . For a system of CdS QDs sensitized onto graphene an IPCE of $\sim 16\%$ was obtained at 350 nm ,^[14] authors demonstrated the superiority of graphene nanostructures for generating higher photocurrents in QD based photoanodes, as compared to single walled carbon nanotubes. It is evident that the combination of FGO nanosheets and Au

NPs provides a less resistive conduction pathway, through the coating and thus enhances the photoelectrochemical activity.

Table 3.2: Solar cell parameters of cells ($\lambda > 300$ nm, 0.1 M Na_2S aqueous electrolyte, cell area: 1 cm^2 , under 1 sun illumination (100 mW cm^{-2})) with the listed photoanodes. In both cases, Pt was used as the counter electrode.

Sample	Voc (mV)	Jsc (mA cm^{-2})	FF	η (%)
$\text{TiO}_2/\text{CdSe}/\text{FGO}/\text{Au}$	661	3.7	38	0.98
$\text{TiO}_2/\text{CdSe}/\text{Au}$	584	3.1	35	0.7

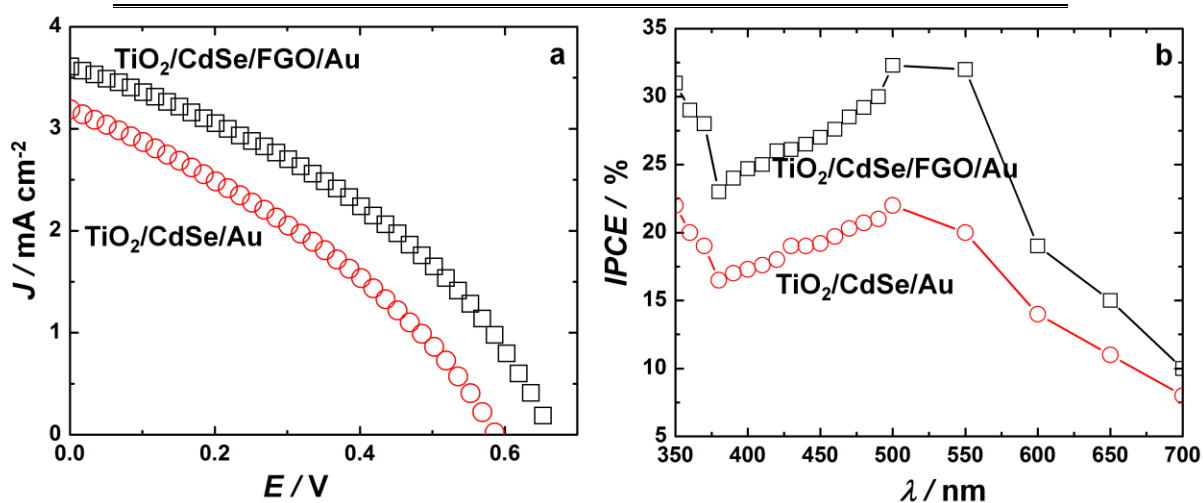


Figure 3.11: (a) J-V characteristics and (b) IPCE spectra of $\text{TiO}_2/\text{CdSe}/\text{FGO}/\text{Au}$ (\square) and $\text{TiO}_2/\text{CdSe}/\text{Au}$ (\circ) based QDSSCs. In both cases counter electrode was Pt, and the electrolyte was aqueous 0.1 M Na_2S .

3.4 Summary

QDSSCs based on $\text{TiO}_2/\text{CdSe}/\text{FGO}/\text{Au}$ composites showed dramatically enhanced photovoltage and photocurrents as compared to $\text{TiO}_2/\text{CdSe}/\text{FGO}$ and $\text{TiO}_2/\text{CdSe}/\text{Au}$ composites. The successful anchoring of CdSe QDs, Au NPs and TiO_2 onto FGO nanosheets was confirmed from HRTEM. Progressive quenching of CdSe emission by Au NPs or FGO nanosheets and the time resolved fluorescence decay experiments provided evidences for rapid and facile electron transfer, in a step-wise manner, from CdSe QDs to TiO_2 to FGO to

Au NPs in the composite, as a higher rate constant was achieved in the TiO₂/CdSe/FGO/Au, in comparison to TiO₂/CdSe/FGO and TiO₂/CdSe/Au. C-AFM also showed the presence of well-connected conducting domains in the composite, and a high average photoconductivity of 0.031 S cm⁻¹ on the nanoscale, thus indicating the homogeneity of the deposit. Combining FGO nanosheets with Au NPs yields an assembly most conducive for fast electron injection rate; it enables the formation of QDSSCs capable of producing a photovoltage 100 mV greater, and photocurrent nearly 6 times higher than that of a TiO₂/CdSe/Au based cell. An IPCE of 33% achieved for the composite confirms that the integration of electron conduit materials like FGO nanosheets and Au NPs, allows efficient electron transport, probably by the virtue of high quality interfaces generated between the four components. This method provides a convenient way to achieve a fairly uniform distribution of the electron conducting (FGO nanosheets and Au NPs) and the photoactive (CdSe QDs linked to TiO₂) materials for only such interpenetrating networks can account for the high photocurrent registered herein. Such an architecture of donor-acceptor assembly, as fabricated here, also offers the benefit of an offset between the levels of different moieties, optimal for rapid electron injection and minimal electron-hole recombination.

3.5 References

- [1] S. Ruhle, M. Shalom, A. Zaban, *ChemPhysChem* **11** (2010) 2290-2304.
- [2] Y- L. Lee, B- M. Huang, H-T. Chien, *Chem. Mater.* **20** (2008) 6903-6905.
- [3] I. Mora-Sero, S. Gimenez, F. Fabregat-Santiago, R. Gomez, Q. Shen, T. Toyoda, J. Bisquert, *Acc. Chem. Res.* **42** (2009) 1848-1857.
- [4] Z. A. Peng, X. Peng, *J. Am. Chem. Soc.* **124** (2002) 3343-3353.
- [5] M. Brust, M. Walker, D. Bethell, D. J. Schiffrin, R. Whyman, *J. Chem. Soc. Chem. Comm.* (1994) 801-802.
- [6] P. V. Kamat, *J. Phys. Chem. C* **112** (2008) 18737-18753.
- [7] J. H. Bang, P. V. Kamat, *ACS Nano* **3** (2009) 1467-1476.
- [8] J. Lu, J- X. Yang, J. Wang, A. Lim, S. Wang, K. P. Loh, *ACS Nano* **3** (2009) 2367-2375.
- [9] I. Robel, M. Kuno, P. V. Kamat, *J. Am. Chem. Soc.* **129** (2007) 4136-4137.
- [10] Y- B. Tang, C- S. Lee, J. Xu, Z- T. Liu, Z- H. Chen, Z. He, Y- L. Cao, G. Yuan, H. Song, L. Chen, L. Luo, H- M. Cheng, W- J. Zhang, I. Bello, S- T. Lee, *ACS Nano* **4** (2010) 3482-3488.

- [11] I. V. Lightcap, T. H. Kosel, P. V. Kamat, *Nano Lett.* **10** (2010) 577-583.
- [12] R. Costi, G. Cohen, A. Salant, E. Rabani, U. Banin, *Nano Lett.* **9** (2009) 2031-2039.
- [13] D. Morrison, P. Zubko, D. J. Jung, J. F. Scott, P. Baxter, M. M. Saad, R. M. Bowman, J. M. Gregg, *Appl. Phys. Lett.* **86** (2005) 152903-152906.
- [14] C. X. Guo, H. B. Yang, Z. M. Sheng, Z. S. Lu, Q. L. Song, C. M. Li, *Angew. Chem. Int. Ltd* **49** (2010) 3014-3017.
- [15] L. Liu, G. Wang, Y. Li, Y. Li, J. Z. Zhang, *Nano Res* **4** (2011) 249-258.
- [16] M-H. Jung, M. G. Kang, *J. Mater. Chem.* **21** (2011) 2694-2700.

Chapter 4

Impact of C₆₀ nanowhiskers on the photovoltaic performance of a CdS based QDSSC

4.1 Introduction

As described in **Chapter 1**, QDSSCs have attained significant scientific attention, due to their band gap tunability and cost effectiveness. The early pioneers, mainly worked on CdS based QDs and various carbon nanostructures. The use of fullerene based organized morphologies, when assembled onto the electrode surface is a critical step towards designing high quality architectures for better performing photovoltaic devices.

In this chapter, C₆₀ nanowhiskers were synthesized by liquid-liquid interfacial precipitation,^[1] and this ensemble was tethered to the conducting substrate by electrophoresis. Assembling a CdS QD layer onto the C₆₀ nanowhiskers layer, was effected by repeated SILAR cycles. The SILAR method offers two major advantages over the conventional capped QDs.^[2] The absence of a capping agent or linker molecules establishes a direct contact between the QDs and carbon nanostructures. Secondly, the clumping of nanoparticles is also reduced which implies that quantum confinement effects are enhanced.^[3] C-AFM and KPFM probes were used to gain an insight into conductivity and local work function of the CdS/C₆₀ (NW) assembly at a nanometer scale spatial resolution and these results were linked to the QDSSC properties. Such a study provided a direct visualization of conducting/less conducting domains and enabled us to figure out the availability of percolation pathways for unhindered electron propagation. QDSSCs based on CdS/C₆₀ (NW) were fabricated with a MWCNT/PDDA (multiwalled carbon nanotubes/ Poly-(dimethyldiallylammonium chloride)) film as the counter electrode and performances were compared with neat CdS and CdS/C₆₀ based electrodes. The benefit of using MWCNT/PDDA film as counter electrode was

demonstrated by comparing their photoelectrochemistry with Pt electrodes. MWCNT/PDDA films were grown by a facile layer by layer (LbL) assembly technique. Although CNTs have been used in the past as counter electrodes in QDSSCs,^[4] but such a configuration, as reported herein, was not attempted before. These studies can have profound implications in the design of high efficiency QDSSCs.

4.2 Experimental

4.2.1 C₆₀ nanowhiskers and C₆₀ based films

C₆₀ nanowhiskers were prepared by a liquid-liquid interfacial precipitation method according to a procedure reported by Minato et al.^[1] Briefly, a saturated solution of C₆₀ was prepared in toluene by dissolving 0.1 g in 25 mL of toluene and followed by ultrasonication for 2 minutes. 5 mL of the toluene saturated with C₆₀ was placed in a glass vial and 5 mL of isopropyl alcohol was gently added. The vial was preserved undisturbed at 10 °C for one week and brown colored precipitates of C₆₀ nanowhiskers were obtained. The solution was ultrasonicated for ten minutes and used directly for the electrophoretic deposition of C₆₀ nanowhiskers on FTO coated glass substrates in a two electrode cell with a Pt sheet as counter electrode by applying a fixed potential of 50 V for 60 s. The color of the brown solution faded with time, owing to the deposition of the nanowhiskers onto the substrate. The resulting uniform brown colored films were rinsed in toluene to remove any physisorbed species and dried in air. A deep purple suspension of C₆₀ was prepared by ultrasonating 20 mg of C₆₀ in 5 mL of toluene for 2 minutes. This suspension was mixed with 5 mL of acetonitrile. The same procedure as mentioned above, was employed to cast films of neat C₆₀ by electrophoresis.

4.2.2 CdS sensitized electrodes

CdS QDs were deposited on the electrophoretically fabricated films of (i) C₆₀ nanowhiskers and (ii) neat C₆₀ using the SILAR method. The C₆₀ nanowhiskers' film was successively

immersed in four different beakers for about 30 s immersion time, in each solution. The first dipping solution was composed of aqueous 0.1 M Cd(CH₃COO)₂ which, was followed by an ultrapure water rinse to remove excess of acetate. The film was then submerged in aqueous 0.1 M Na₂S, and again followed by a water rinse to remove the superfluous sulfide. The immersion cycle was iteratively repeated ten times. The resulting films were brownish-yellow and are referred to as CdS/C₆₀ (NW) electrodes and were stored in air. In an exactly similar manner, neat CdS electrodes were fabricated by SILAR on blank FTO coated substrates and CdS/C₆₀ electrodes were prepared by coating CdS using SILAR on the pre-fabricated C₆₀ films.

4.2.3 MWCNT/PDDA electrode by LbL assembly

Functionalization of MWCNTs was accomplished by dispersing 2.5 g of MWCNTs in a mixture of HNO₃ and H₂SO₄ (1:3 by volume). The resulting suspension was sonicated for 20 minutes and refluxed at 80 °C for 6 hours. The black residue was washed with copious amounts of deionized water till the supernatant liquid acquired neutral pH and dried in an oven at 60 °C for 48 hours. The polyanion suspension was prepared by dispersing 0.1 wt % of functionalized MWCNTs in deionized water by ultrasonication for fifteen minutes. The polycation solution was prepared by dissolving 0.25 wt % of PDDA in deionized water. The FTO coated substrates were exposed to the polycation solution for 5 minutes, rinsed for 4 min in two Milli-Q water baths, dried in air and then exposed to the polyanion solution for 5 minutes and again rinsed and dried. This cycle was repeated to obtain five layer pairs. The ensuing black colored thin film assembly is referred to as a MWCNT/PDDA electrode.

4.3 Results and discussion

4.3.1 Optical microscopy analysis

In the liquid-liquid interfacial precipitation technique,^[1] isopropanol is carefully introduced on to the surface of a saturated solution of C₆₀ in toluene, as a consequence thin

fibrous structures or C_{60} nanowhiskers grow in solution and the first evidence for the successful formation of C_{60} nanowhiskers is presented in the optical microscopy images shown in **Figure 4.1b** and **c**. The images show homogeneously distributed mingling C_{60} nanowhiskers with outside diameters ranging from approximately 100 nm to many microns and lengths of about a few microns. The color variations for the nanowhiskers (red, yellow, green and brown) are due to the different diameters. The nanowhiskers are clean, with hardly any traces of carbon particles. The whiskers are believed to nucleate at the interface between the layered solvents. The complete growth of nanowhiskers occurs over a span of several days, as isopropanol gradually permeates into the fullerene rich phase enhancing its hydrophilicity. In stark contrast to the whiskers, the optical microscope image of neat C_{60} (**Figure 4.1a**) shows clusters of C_{60} molecules lumped together in the form of irregular shapes in different regions. The CdS/ C_{60} electrode surface shows an undulating surface with no distinctive feature (**Figure 4.1d**). The CdS/ C_{60} (NW) electrode shows the C_{60} nanowhiskers interspersed with neat CdS (**Figure 4.1e**), the bright yellow regions arise from CdS, which is also corroborated from the image of neat CdS shown in the corresponding inset. The image of MWCNT/PDDA shows randomly distributed tubular shapes of different dimensions, embedded in a diaphanous layer, probably arising from PDDA (**Figure 4.1f**).

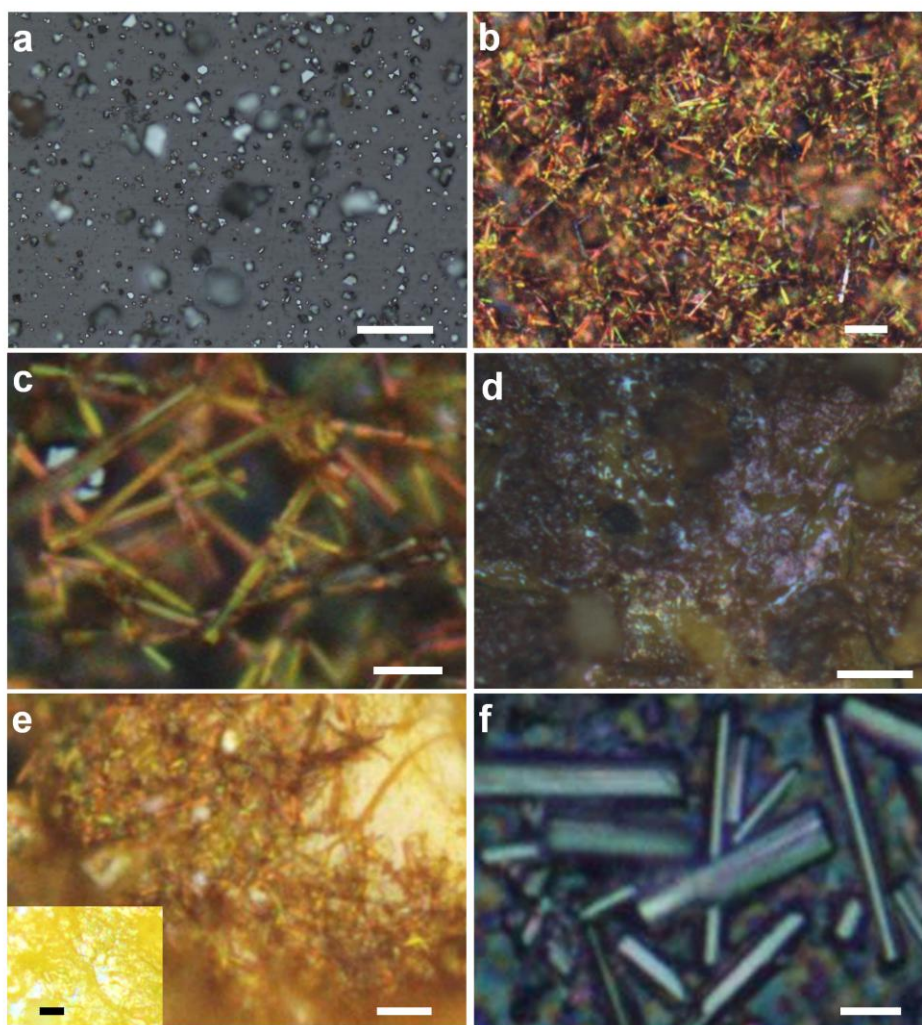


Figure 4.1: Optical micrographs of (a) neat C_{60} (scale bar = 50 μm), (b) C_{60} nanowhiskers (at low magnification, scale bar = 20 μm), (c) enlarged view of the tubular C_{60} nanowhiskers (scale bar = 5 μm), (d) CdS/ C_{60} electrode (scale bar = 50 μm), (e) CdS/ C_{60} (NW) electrode showing the nanowhiskers embedded in CdS (scale bar = 5 μm) and (f) MWCNT/PPDA electrode (scale bar = 20 μm). Inset of (e) displays the neat CdS film grown by SILAR technique (scale bar = 5 μm).

4.3.2 TEM analysis

The TEM images further confirm the formation of several micron length long C_{60} NW (Figure 4.2a and b).

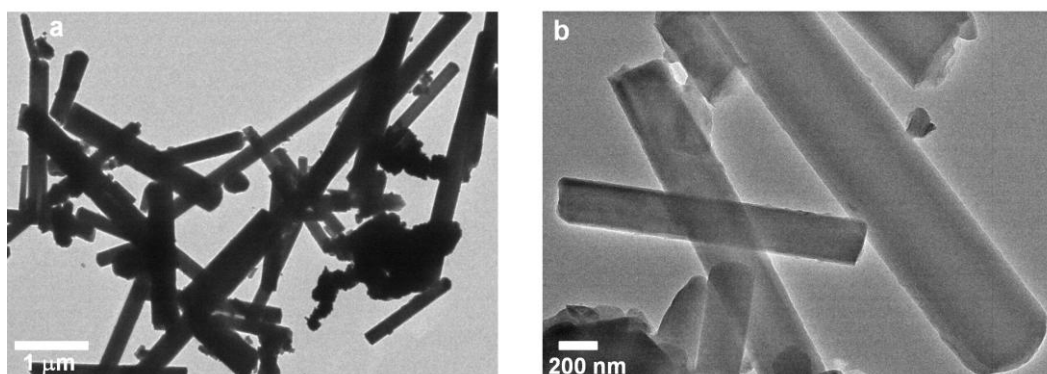


Figure 4.2: TEM images of C_{60} NWs of different magnifications in (a) and (b)

4.3.3 Structural analysis of nanowhiskers

Raman spectra of neat C_{60} and C_{60} nanowhiskers measured in the $100\text{--}2000\text{ cm}^{-1}$ wavenumber range are shown in **Figure 4.3**. Neat C_{60} showed Raman lines at 270, 494, 1461 and 1561 cm^{-1} ascribable to $H_g(1)$, $A_g(1)$, $A_g(2)$ and $H_g(8)$ modes which are in concurrence with the assignments made previously for pristine C_{60} molecules.^[5] The pentagonal pinch mode or the $A_g(2)$ mode at 1461 cm^{-1} in C_{60} is touted to be of paramount significance, as it is highly sensitive to intermolecular interactions.^[6] It was observed in an earlier report, that this peak downshifts to 1459 cm^{-1} in nanowhiskers, owing to the *in-situ* polymerization of C_{60} molecules induced by laser irradiation, during the Raman measurement.^[7] In the present study, the 1461 cm^{-1} mode was found to acquire a highly asymmetric shape as compared to the symmetric peak observed for this mode in neat C_{60} . The difference in $A_g(2)$ peak profiles is perceptible in **Figure 4.3b**. On deconvoluting the $A_g(2)$ mode of the C_{60} (NW) sample, using a non-linear iterative least squares Gaussian fitting procedure, four components at 1451 , 1455 , 1461 and 1466 cm^{-1} were obtained (**Figure 4.3c**). The two low wavenumber components are attributed to the formation of C_{60} oligomers and dimers. Since the Raman active surface modes, namely, $H_g(7)$, $A_g(2)$, and $H_g(8)$ are most susceptible to chemical changes,^[6] the 1466 cm^{-1} component is illustrative of surface interactions of C_{60} molecules with a different solvating environment (ongoing from toluene to isopropanol). Another visible difference was observed for the 270 cm^{-1} mode, which splits into two peaks, in the

nanowhiskers (inset of **Figure 4.3a**). The high degree of crystallinity retained in C_{60} (NW) is responsible for the peak split.

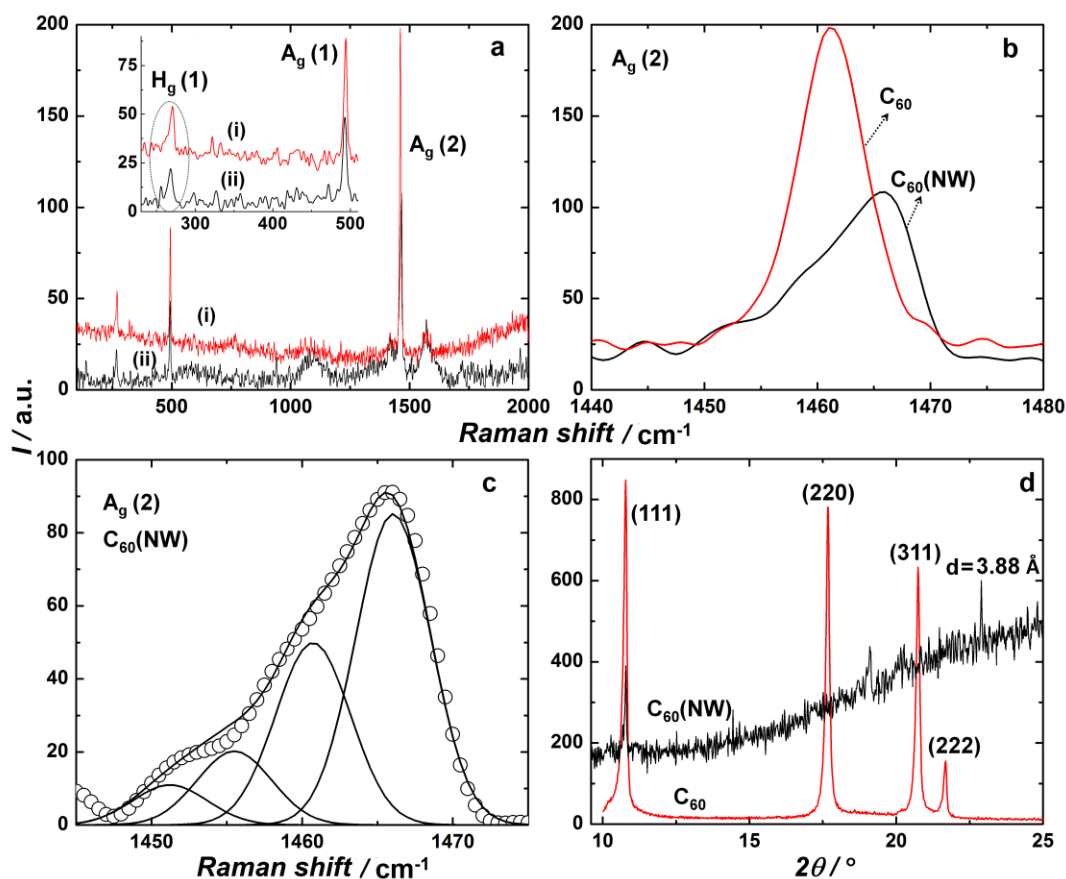


Figure 4.3: Raman spectra of (a) C_{60} (i) and C_{60} (NW) (ii) in the 100 – 2000 cm^{-1} wavenumber range, (b) illustrates the $A_g(2)$ mode variation ongoing from C_{60} to C_{60} (NW) and (c) deconvoluted $A_g(2)$ mode in C_{60} (NW). Inset of (a) is an enlarged view of the low wavenumber region. (d) X-ray diffractograms of neat C_{60} and C_{60} (NW); the hkl values are shown in parentheses.

To confirm the crystalline nature of C_{60} (NW), XRD pattern of neat C_{60} was compared with that of C_{60} (NW) and the patterns are displayed in **Figure 4.3d**. Neat C_{60} shows well-resolved peaks at $d = 8.22, 5.03, 4.27$ and 4.12 \AA corresponding to the (111), (220), (311) and (222) crystallographic planes of face centered cubic (fcc) lattice of C_{60} as per file number: 20-1323 from the JCPDS library of spectra. However, C_{60} (NW) only show three lines corresponding to (111) and (220) reflections. One additional line at $d = 3.88 \text{ \AA}$ is also

observed which probably arises from some intermediate lattice spacing. However, XRD confirms that the fcc structure of C₆₀ is retained, albeit a preferred orientation along the (220) plane, for this peak is most intense in C₆₀ (NW). Higher 2θ peaks were not registered in the C₆₀ (NW) sample, and therefore the comparison was restricted only upto 25°.

4.3.4 Fluorescence quenching and lifetime

Figure 4.4 shows the emission spectra of neat CdS, CdS/C₆₀ and CdS/C₆₀ (NW) electrodes, measured at an excitation wavelength of 350 nm. The intensity of the broad PL peak observed at ~ 553 nm in neat CdS, attributable to band edge emission,^[8] is quenched on introducing pristine C₆₀ or C₆₀ (NW) to CdS QDs. The extent of luminescence quenching is higher for C₆₀ nanowhiskers as compared to C₆₀, thus providing indirect evidence for a more effective charge transfer from the CB edge of CdS to the Fermi level of C₆₀ nanowhiskers. In order to confirm the deactivation pathway of the electron via transfer from neat CdS to C₆₀ (NW) in CdS/C₆₀ (NW) electrode and from neat CdS to C₆₀ in CdS/C₆₀ electrode, the fluorescence lifetime spectra were acquired by monitoring emission at 553 nm. The fluorescence decay profiles accurately fit to a tri-exponential decay function as described in equation (1). The residual plots revealed that single or bi-exponential functions were insufficient to model the data and much lower χ^2 were attained with tri-exponential kinetics.

$$I = A_1 \exp(-t/\tau_1) + A_2 \exp(-t/\tau_2) + A_3 \exp(-t/\tau_3) \quad (1)$$

In equation (1): I is the normalized emission intensity, t is the time after LED excitation, A₁, A₂ and A₃ are the amplitude coefficients and τ_1 , τ_2 and τ_3 are the decay time constants. The results of the fitting are summarized in **Table 4.1**.

The fast decay component had a short lifetime, in case of the CdS/C₆₀ NW (0.01 ns), whereas this short lived component for neat CdS had a lifetime of 0.11 ns. Furthermore, since the average decay time was also deduced to be the shortest for the CdS/C₆₀ (NW) electrode in comparison with neat CdS, we can infer that electron transfer from the excited state of CdS to

C_{60} (NW) is the dominant deactivation pathway in CdS/ C_{60} (NW) electrode, for had it been only due to band edge recombination, then neat CdS would have shown either the shortest or a comparable lifetime. Here, since average lifetime is longest for the neat CdS electrode, that C_{60} or C_{60} (NW) facilitates electron transport is apparent. Since, almost a 17-fold increment was observed for the fast decay component in neat CdS as opposed to CdS/ C_{60} (NW), the excited state electron transfer is the prominent quenching mechanism in the electrode. In the CdS/ C_{60} and CdS/ C_{60} (NW), the two long lived components (τ_2 and τ_3) probably arise from the CdS QDs which are not in direct contact with C_{60} or C_{60} nanowhiskers. In this scenario, the electron propagation time is increased which, results in the longer decay times.

The short lived component (τ_2) among τ_2 and τ_3 , in CdS/ C_{60} and CdS/ C_{60} (NW) electrodes is therefore ascribed to the electron injection process from CdS QDs which are directly anchored on the surface of C_{60} clusters or C_{60} nanowhiskers. The most likely mechanism for fast decay depopulation process involving photogenerated carriers in neat CdS can be associated to hole trapping.^[9] In CdS/ C_{60} (NW) and CdS/ C_{60} electrodes, quenching due to band edge recombination in CdS competes with the emission quenching of CdS, induced by fast electron transfer from CdS to C_{60} or C_{60} (NW). Factors which dictate the rate of electron transfer or emission decay include: (i) interparticle contact between the quencher and emitter, (ii) crystal or grain size of the QD relative to that of the carbon nano-moiety and (iii) the energetics i.e., the gradients between the CB edge of CdS and C_{60} or C_{60} (NW).

Table 4.1: Kinetic parameters of emission decay analysis of photoanode electrode films (measured at $\lambda_{ex} = 370$ nm and $\lambda_{em} = 553$ nm) deduced from tri-exponential fits.^a

Electrode Description	χ^2	τ_1 (ns)	τ_2 (ns)	τ_3 (ns)	A_1	A_2	A_3	$\langle \tau \rangle$ (ns)
CdS	1.0452	0.11	1.73	8.95	44.47	33.74	21.78	2.57
CdS/ C_{60}	1.2145	0.01	1.48	8.86	88.24	1.62	10.14	0.93

CdS/C ₆₀ (NW)	1.0141	0.01	1.62	12.3	94.02	2.39	3.59	0.49
--------------------------	--------	------	------	------	-------	------	------	------

^aA is the relative amplitude of each lifetime, τ_1, τ_2 and τ_3 are the components of fluorescence lifetime and χ^2 denotes the fit quality.

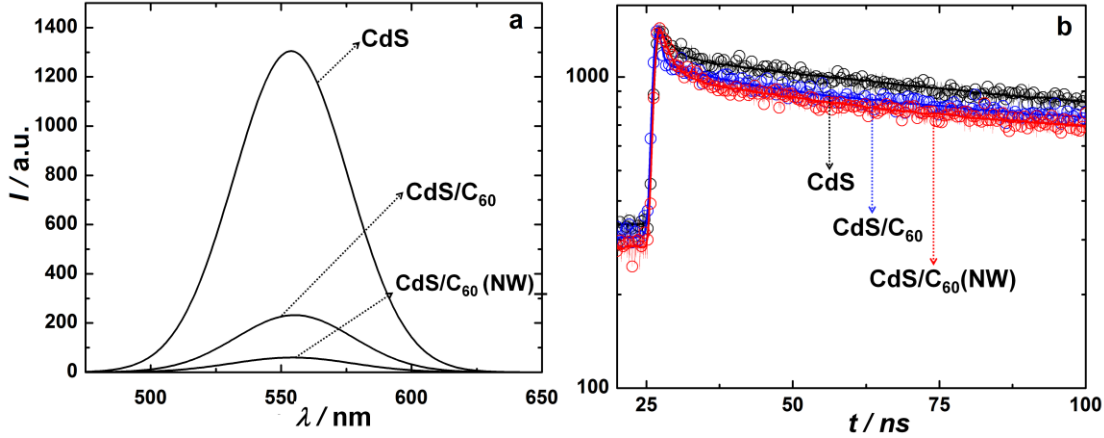


Figure 4.4: (a) Emission spectra of neat CdS, CdS/C₆₀, and CdS/C₆₀ (NW) electrodes ($\lambda_{\text{ex}} = 350$ nm, for all three samples). (b) Time resolved fluorescence decay traces of neat CdS, CdS/C₆₀ and CdS/C₆₀ (NW) electrodes. Excitation wavelength was fixed at 370 nm and emission profiles were obtained at 553 nm. The solid lines represent the best fits obtained by deconvolution, by assuming a tri-exponential decay.

The CB of CdS is poised at ~ 4.3 eV,^[10] while here the experimentally determined Fermi level (E_F') of C₆₀ (NW) lies at 4.66 eV and for C₆₀, it is positioned at 4.42 eV. Electron transfer from the CB of CdS to pristine C₆₀ or C₆₀ nanowhiskers is therefore thermodynamically favorable. In CdS/C₆₀ (NW), the energy barrier to be surmounted by the electron from CdS to reach C₆₀ (NW) is slightly larger (0.36 eV) as compared to the difference between CdS and C₆₀ (0.12 eV). It has been observed in the past that when energy levels of the donor and acceptor are too close, as in CdS and single walled nanotubes (SWNTs), the electron transfer was less favored than the transfer from CdS to graphene (wherein the latter two had an appreciable gradient).^[11] The nanowhiskers morphology of the C₆₀ assemblies allows a better interfacial contact between CdS QDs and C₆₀ (NW) thus enabling fastest electron transfer and as a consequence emission decay is fastest in this electrode among the three electrodes: CdS, CdS/C₆₀ and CdS/C₆₀ (NW). It is possible to

extract the rate constant of electron transfer (K_{et}) from the reduced emission lifetimes of CdS/C₆₀ (NW) or CdS/C₆₀ relative to the neat CdS electrode. Since electron transfer from CdS to C₆₀ (NW) or C₆₀ is the only additional quenching mechanism in CdS/C₆₀ and CdS/C₆₀ (NW) electrodes respectively with respect to that in neat CdS, the K_{et} values can be deduced from the following expression.

$$K_{et} = 1/\langle\tau\rangle(\text{CdS/C}_{60} \text{ (NW)}) \text{ or } 1/\langle\tau\rangle(\text{CdS/C}_{60}) - 1/\langle\tau\rangle(\text{CdS}) \quad (2)$$

τ is the average lifetime for emission decay. For a CdS-TiO₂ system, K_{et} of about 10^{11} s^{-1} has been reported [12] and in another report K_{et} of $\sim 4 \times 10^6 \text{ s}^{-1}$ was obtained for CdS-TiO₂. [13] The injection of higher lying electrons from CdS CB to the C₆₀ or C₆₀ (NW) is responsible for the majority of total quenching in CdS/C₆₀ and CdS/C₆₀ (NW) as K_{et} is 6.88×10^8 and $1.67 \times 10^9 \text{ s}^{-1}$ for the two electrodes respectively. These values also show that C₆₀ (NW) are more useful for improving the rate of electron transfer as compared to pristine C₆₀.

4.3.5 C-AFM and surface potential analysis

To establish the superior ability of C₆₀ (NW) relative to pristine C₆₀ for promoting electron transport, C-AFM was used to compare the nanoscale electron transport capabilities of neat CdS, CdS/C₆₀ and CdS/C₆₀ (NW) electrodes. The local current maps and the corresponding surface topography images of CdS, CdS/C₆₀ and CdS/C₆₀ (NW) are shown in **Figure 4.5**. The maximum current registered for the CdS/C₆₀ electrode is $\sim 2.1 \text{ nA}$ (**Figure 4.5a**). From the image, it is apparent that domains of high currents are small and few in number and they seem to be embedded in a low current matrix. The surface topography of CdS/C₆₀ (NW) shows a relatively smooth texture, and corresponding current image reveals that high current domains co-exist with insulating domains. The high current region can be ascribed to C₆₀ or C₆₀ nanowhiskers in CdS/ C₆₀ and CdS/C₆₀ (NW) electrodes respectively. The insulating dominant (the darker regions) arise from CdS QDs or CdS QDs coated on C₆₀ or C₆₀ nanowhiskers. In comparison to CdS/C₆₀, the CdS/C₆₀ (NW) electrode showed a

maximum current of ~30 nA, which is almost fifteen times greater than what could be achieved with the pristine assembly of molecular fullerene. The neat CdS film showed a granular topography and the current map reveals a maximum current of 50 pA. The electron conducting ability of QDs is enhanced when they are flanked by either C₆₀ or C₆₀ nanowhiskers. Prior to saturation, for all the three electrodes, a quasi-linear dependence is observed, indicative of ohmic currents, and the average electrical conductivity (σ) was deduced from equation (3).

$$\sigma = (i/V) (l/A) \quad (3)$$

In equation (3), i/V represents the slope of the straight line portion, l is the depth of the sample and A is the geometric tip area (πr^2) that contacts with the sample. The CdS/C₆₀ (NW) electrode showed the highest averaged nanoscale electrical conductivity of 95.7 S cm⁻¹, closely followed by the CdS/C₆₀ electrode. The pristine film of CdS QDs was poorly conducting with a conductivity of only 1.18 S cm⁻¹. That the CdS/C₆₀ (NW) electrode is capable of carrying more currents than CdS/C₆₀ or neat CdS is obvious.

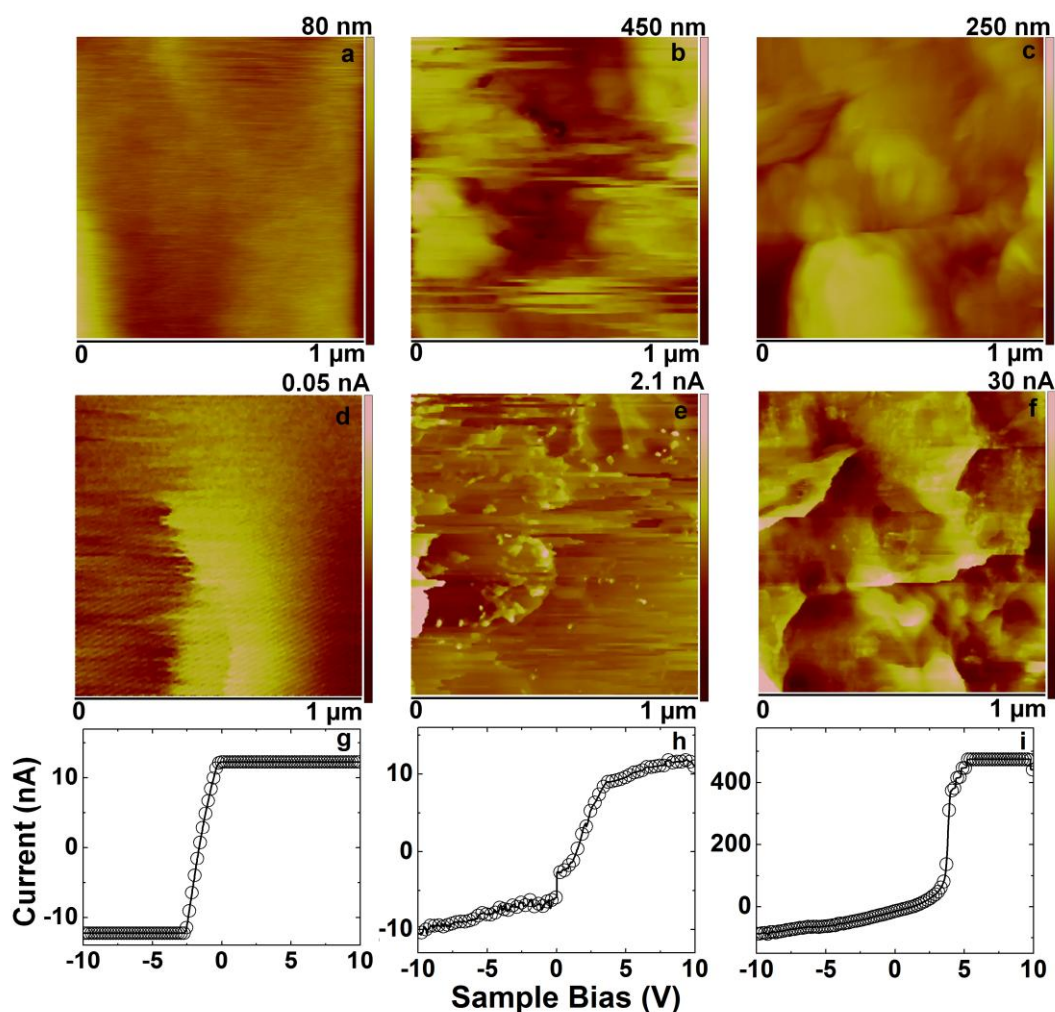


Figure 4.5: Concurrent topography (a,b,c) and current (d,e,f) images of neat CdS, CdS/C₆₀, and CdS/C₆₀ (NW) electrodes recorded over a scanned area of 1 $\mu\text{m} \times 1 \mu\text{m}$. Resultant I-V curves obtained after averaging 15 I-V curves recorded at 15 equidistant spots (on each current image shown in d,e and f) are shown in the panels (g-i) corresponding to (g) neat CdS, (h) CdS/C₆₀, and (i) CdS/C₆₀ (NW) electrodes.

The force gradient technique employs a lift height approach in which the cantilever first measures topography and then retraces the same line at a certain lift height to measure only the electrostatic interaction, which manifests itself at a shift in the resonant frequency of the tip. The topography and the surface potential images of neat CdS, C₆₀ and C₆₀ (NW) films are shown in **Figure 4.6**. The surface potential images are consistent with the topography. Only the images of the C₆₀ (NW) sample (**Figure 4.6c** and **c'**) show uniformly distributed elongated shapes, dissimilar from the images of the neat CdS or C₆₀ samples, which reveal

blobs of irregular shapes (**Figure 4.6a, a', b and b'**). The brighter regions have higher potential and the darker domains are low potential zones. The work function here can be approximated to the position of the Fermi level (E_F') for all the three samples. The E_F' was calculated using $E_F' = \phi_{\text{sample}} = \phi_{\text{tip}} (4.9 \text{ eV}) - (\text{SP})$, where SP is the magnitude of surface potential, obtained from the SP images. The Fermi level for CdS QD film deduced from a V_{CPD} of 340 mV is 4.56 eV. Similarly, work functions of C_{60} and C_{60} (NW) electrodes are 4.42 and 4.66 eV. The position of Fermi level of neat fullerene is at $\sim 4.3 \text{ eV}$, as per literature^[14] which concurs with the value observed herein. The optical band gap of CdS, determined from the Tauc plot is 2.4 eV. Relative to neat fullerene, the E_F' shifts to a more negative potential (*versus* NHE) for the C_{60} (NW) electrode. Since the difference between the E_F' value ($\sim 0.36 \text{ eV}$) of the neat CdS and C_{60} (NW) is greater than the gap between the E_F' values ($\sim 0.12 \text{ eV}$) of neat CdS and C_{60} , a larger gradient imparts a larger impetus for electron transfer to C_{60} (NW) in contrast to C_{60} . A similar effect was previously observed for CdS sensitized SWCNT and graphene electrodes, wherein the larger difference between the CB level of CdS and graphene as compared to the difference between CdS and SWCNTs, bestowed a greater driving force for electron injection in the graphene based electrode and higher photocurrents were realized therein.^[11]

The energy band diagram illustrating these subtle differences in E_F' positions of the individual components are shown in **Figure 4.7**. Electron transfer occurs from CdS QDs to C_{60} (NW) or C_{60} and subsequently to the current collecting electrode. The gradient in the energy levels as in the CdS/ C_{60} (NW) electrode are more favorable for facile electron transfer and transport and as a consequence, higher photocurrents were obtained by the CdS/ C_{60} (NW). We are cognizant of the fact that these values are dependent on method of preparation and therefore relative comparisons are justified.

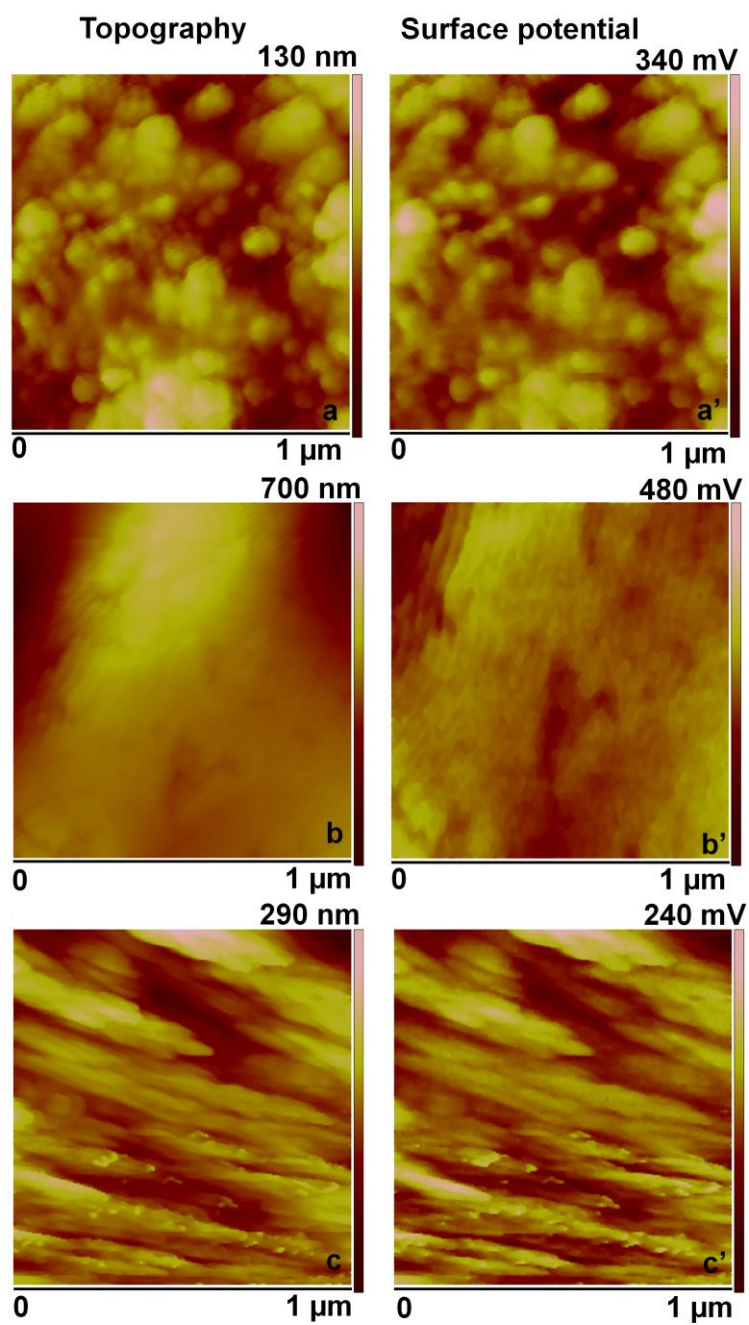


Figure 4.6: Topography and surface potential maps of (a,a'): neat CdS, (b,b'): pristine C₆₀, and (c,c'): C₆₀ (NW) electrodes recorded over a scanned area of 1 μm × 1 μm.

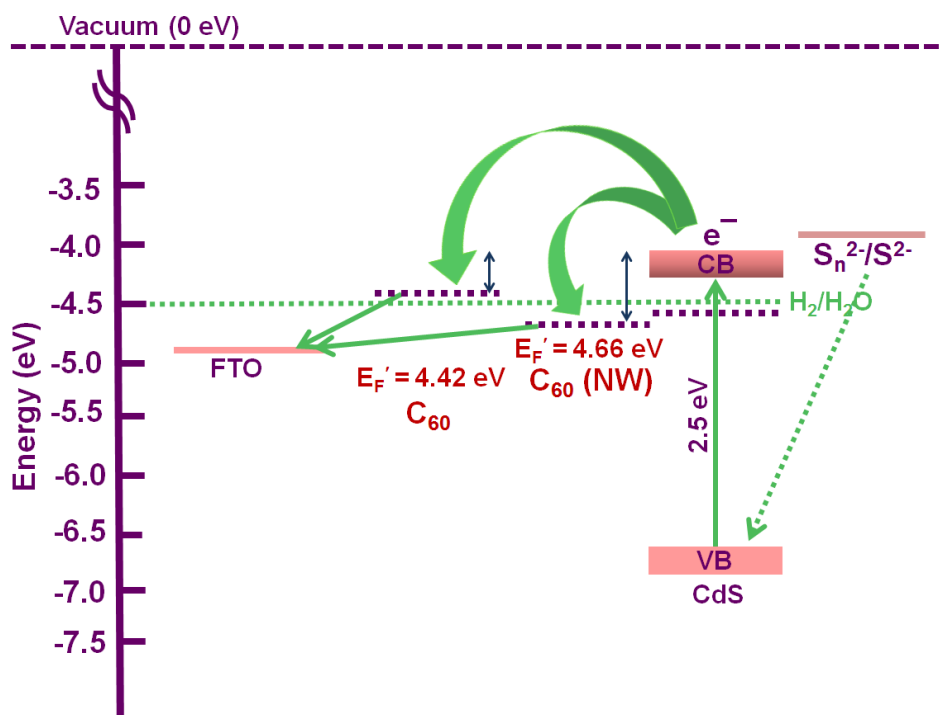


Figure 4.7: Energy band diagram showing the transfer of electrons from the CB of CdS to E_F' (Fermi level position deduced experimentally from the surface potential map in **Figure 4.6**) of C_{60} in CdS/ C_{60} or to C_{60} (NW) as in CdS/ C_{60} (NW).

4.3.6 Photoelectrochemistry of QDSSCs

The photoelectrochemical response of CdS/ C_{60} , CdS/ C_{60} (NW) and neat CdS electrodes with (a) MWCNT/PDDA and (b) Pt as the counter electrodes in 0.1 M are shown in **Figure 4.8**. Upon illumination, a J_{SC} of $600 \mu A cm^{-2}$ was registered for the CdS/ C_{60} (NW) electrode in contrast to values of ~ 300 and $200 \mu A cm^{-2}$ observed for the CdS/ C_{60} and neat CdS electrodes. The higher value of J_{SC} attained for the CdS/ C_{60} (NW) electrode indicates that the nanowhisker morphology is conducive for fast electron transport. When Pt was used as the counter electrode, J_{SC} was only half of what could be achieved with MWCNT/PDDA electrode as the auxiliary cathode. J_{SC} is only $300 \mu A cm^{-2}$ for the CdS/ C_{60} (NW) electrode and even lower for the other two electrodes, implying that the rate of reduction of S^{2-} species at Pt electrode is sluggish, whereas it is much faster when MWCNT/PDDA is employed as the counter electrode. In an earlier report,^[15] decomposition of Pt due to poisoning by S_n^{2-}/S^{2-}

based redox electrolyte was shown to have a deleterious effect on the photovoltaic performance of the devices. A V_{OC} of ~610 mV was attained for the CdS/ C_{60} (NW) cell, closely followed by 585 and 570 mV for CdS/ C_{60} and neat CdS based cells when MWCNT/PDDA was utilized as the counter electrode indicating that V_{OC} is somewhat independent of the anode microstructure, and it is simply the difference between the Fermi level of C_{60} and E^0 of S_n^{2-}/S^{2-} couple. On using Pt as the counter electrode, not much difference was observed in the value of V_{OC} which is natural for V_{OC} is largely governed by donor level of the sensitizer and the acceptor level of the carbon nanostructure in the anode. Superior performance in presence of C_{60} NW reaffirmed the ability of the C_{60} nanowhiskers to shuttle electrons more efficiently as compared to pristine C_{60} .

The higher effective surface area of the nanowhiskers tends to come to the fore by allowing adsorption of a greater proportion of CdS quantum dots which increases the overall electron collection capacity of the photoanode. Although the C_{60} nanowhiskers are assembled in a random haphazard manner, nevertheless, since the whiskers are one dimensional, electrical transport is possible in a localized manner. Uni-dimensional architectures have been shown to improve cell currents, for such structures offer longer diffusion length in comparison to nanoparticles and therefore electron lifetimes increase which favorably impacts the photocurrent response. The number of grain boundaries that the electrons encounter during their transport to the current collecting contact are much greater in the CdS/ C_{60} electrode and the trapping of electrons in the defect sites or trap sites in the sensitizer itself (as in neat CdS) are the reason for lowered photocurrents of these cells. Neat CdS is also devoid of driving force for electron injection, namely, the gradient between Fermi levels and therefore photocurrents are low. J_{SC} and V_{OC} of $150 \mu A cm^{-2}$ and 250 mV were achieved previously for a $SnO_2/CdSe/C_{60}$ system,^[16] and in yet another study for a graphene/CdS system, these values were 1.03 mA and 680 mV.^[11] Since our values for the CdS/ C_{60} (NW)-

MWCNT/PDDA cell are comparable, it is apparent that the nanowhiskers play a significant role in amplifying the photoactivity of semiconducting QDs.

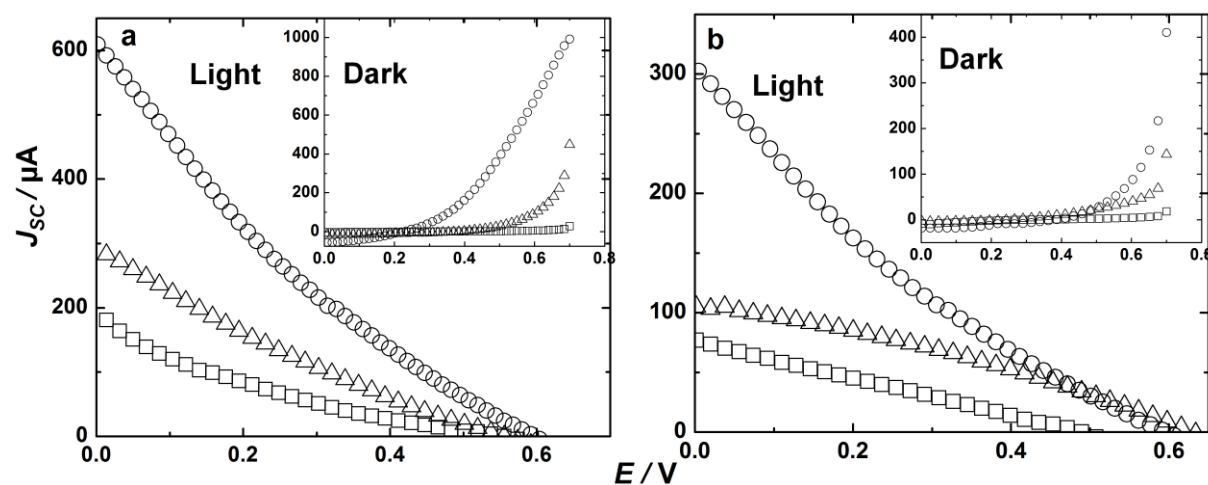


Figure 4.8: (a) J-V characteristics of QDSSCs based on CdS/C₆₀ (NW) (○), CdS/C₆₀ (△), and neat CdS (□) electrodes as the photoanodes with (a) MWCNT/PDDA film as the counter electrode and (b) Pt as the counter electrode; recorded at $\lambda > 300$ nm, under 100 mW cm^{-2} illumination. Insets of (a) and (b) show the corresponding dark currents. All measurements were performed in aqueous 0.1 M Na₂S.

IPCE *versus* wavelength spectra of the three cells with (i) CdS, (ii) CdS/C₆₀ and (iii) CdS/C₆₀ (NW) as working electrodes and each with MWCNT/PDDA film as the counter electrode are shown in **Figure 4.9**. A highest IPCE of 22% was registered for the CdS/C₆₀ (NW)-MWCNT/PDDA cell at 370 nm, which was followed by an IPCE of 12% for the CdS/C₆₀-MWCNT/PDDA cell. IPCE was ~19% for the CdS/C₆₀ (NW)-MWCNT/PDDA cell at a visible wavelength of 400 nm. As anticipated, among the three cells, the CdS-MWCNT/PDDA cell showed the least value for IPCE maximum (10%). The IPCE of CdS/C₆₀ (NW)-MWCNT/PDDA cell is nearly 2 times larger than that of CdS/C₆₀-MWCNT/PDDA cell which clearly shows that electron transfer and transport is rendered more efficient by the C₆₀ nanowhiskers. The highest IPCE value observed for the CdS/C₆₀ (NW)-MWCNT/PDDA cell is superior to a maximum value of 16% reported previously for a CdS/Graphene electrode.^[11] In yet another report on a CdSe/C₆₀ device, the IPCE maximum

was observed to be 8%. Our values are comparable or slightly superior to IPCE values reported for similar QD based cells devoid of an oxide support. Photoaction spectra were also recorded for these three photo-active electrodes with Pt as the counter electrode and these spectra are shown **Figure 4.9b**. The highest IPCE was again observed for the CdS/C₆₀ (NW)-Pt cell (12%) and this value was only 3% for the CdS-Pt cell. The advantage of MWCNT/PDDA electrode as compared to Pt as a counter electrode is also directly reflected in the IPCE values.

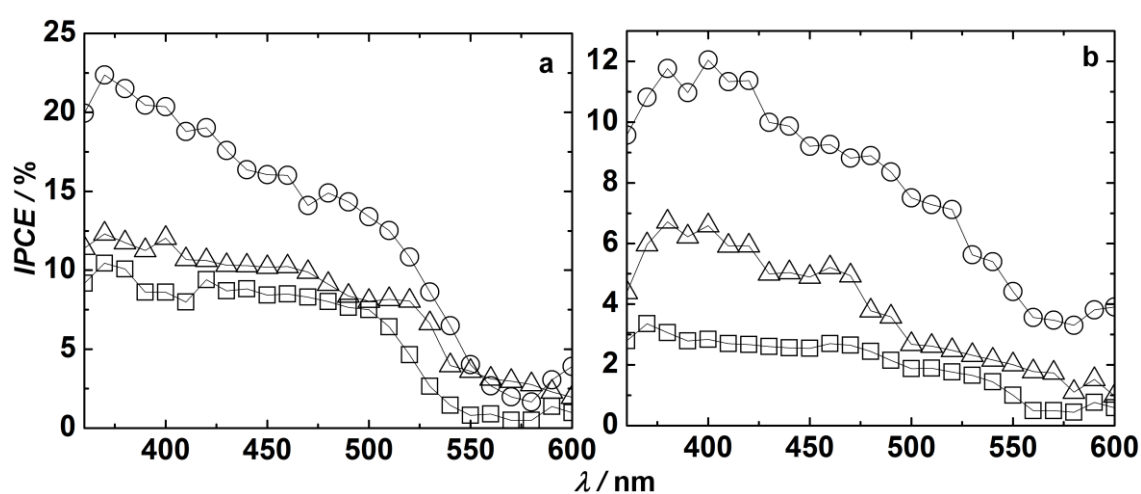


Figure 4.9: IPCE measurements of three QDSSCs based on CdS/C₆₀ (NW) (○), CdS/C₆₀ (△), and neat CdS (□) electrodes as the photoanodes with (a) MWCNT/PDDA film and (b) Pt as the counter electrode and aqueous 0.1 M Na₂S as the electrolyte, in each cell.

4.3.7 Electrochemical impedance spectroscopy of QDSSCs

Impedance spectroscopy was performed on QDSSCs based on the CdS/C₆₀ (NW) electrode in two configurations, one with Pt as the counter electrode and the other with MWCNT/PDDA film as the counter electrode (**Figure 4.10**). The electrolyte in both cells was aqueous 0.1 M Na₂S. The objective was to determine the effect of the counter electrode species (Pt or MWCNT/PDDA) on the rate of electron transfer from the counter electrode to the oxidized species of the electrolyte. The faster the charge transfer at the counter electrode, the more effective would be the cell in producing higher photovoltage. Simultaneously, the rate of back-electron transfer from photoanode (CdS/C₆₀ (NW)) should be minimized as it

will enable a larger build-up of electron density in the CB, which again amplifies photovoltage. For both cells, the Nyquist plot was composed of two semi-circles; the high frequency one (R_1C_1) is related to the charge transfer impedance at the Pt or MWCNT/PDDA / S_n^{2-}/S^{2-} interface and the semicircle at intermediate frequencies (R_2C_2) is ascribed to the CdS/ C_{60} (NW) / S_n^{2-}/S^{2-} interface. The fitted parameters are provided in **Table 4.2**.

In addition to the two semicircles, is a skewed resistive response, which is observed in the low frequency regime. This distorted behavior arises due to diffusion effects. Both charge transfer resistances R_1 and R_2 are lower and the electrochemical capacitances C_1 and C_2 are higher for the MWCNT/PDDA based cell, in comparison to the Pt based cell. That R_1 is higher and C_1 is lower for the Pt based cell indicates that the quality of electrical contact between MWCNT/PDDA and S_n^{2-}/S^{2-} is superior which enables facile charge transfer and an enhanced propensity of this electrode towards double-layer charging. τ_d corresponds to the time taken by the electron in the CB of the photoactive anode to recombine with the oxidized species (S_n^{2-} in the present case) of the electrolyte. The electron recombination time was found to be 9 and 12 ms for the cells based on Pt and MWCNT/PDDA electrodes respectively. τ_d was obtained from the middle frequency peak in the Bode plots ($\tau_d = 1/2\pi f$); the slight shift of this peak to higher frequency in the Pt based cell relative to the MWCNT/PDDA cell, also ratifies the shorter recombination time deduced for the Pt based cell.

The electron lifetime was longer for the MWCNT/PDDA cell, which accounts for the higher V_{OC} achieved for this cell. Researchers in the past have observed electron recombination times of the order of 24 ms and 19.2 ms in Z907 based and JK2 based DSSCs.^[17] The skewed portion in both curves, emanates from the sluggish diffusion of holes through the electrolyte cross-section. The difference in the diffusional rates is reflected in the Bode plots; the larger amplitude of absolute impedance ($|Z|$) in the low frequency domain,

observed for the Pt based cell, as compared to the MWCNT/PDDA based cell, reveals a faster rate for hole diffusion in the latter. It is noteworthy that R_2 is larger than the corresponding R_1 , for a given cell, and this difference is more pronounced for the Pt based cell. In all likelihood, some electrons are lost by irreversibly reacting with the electrolyte at the Pt / S_n^{2-}/S^{2-} interface in the Pt based cell. For had it not been so, then the two middle semicircles corresponding to Pt and MWCNT/PDDA based cells would have superimposed on one another, while keeping in view that the CdS/ C_{60} (NW) / S_n^{2-}/S^{2-} interface is common to both cells. How the MWCNT/PDDA electrode is more efficient in transferring electrons is difficult to explain at this juncture. Nonetheless, but these results confirm that the MWCNT/PDDA electrode is an attractive, less expensive, and a more efficient substitute for Pt electrode in QDSSCs.

Table 4.2: EIS results for CdS/ C_{60} (NW)-MWCNT/PDDA and CdS/ C_{60} (NW)-Pt cells, obtained by fitting the experimental data in the model shown in **Figure 4.10a**.

Sample	R_1 ($\Omega \text{ cm}^{-2}$)	R_2 ($\Omega \text{ cm}^{-2}$)	R_3 ($\Omega \text{ cm}^{-2}$)	C_1 (F cm^{-2})	C_2 (F cm^{-2})	C_3 (F cm^{-2})
CdS/ C_{60} (NW)- MWCNT/PDDA	68.30	345.50	483.41	0.199×10^{-6}	24.99×10^{-6}	0.0127
CdS/ C_{60} (NW)-Pt	104.16	408.22	519.2	0.176×10^{-6}	83.39×10^{-6}	0.00574

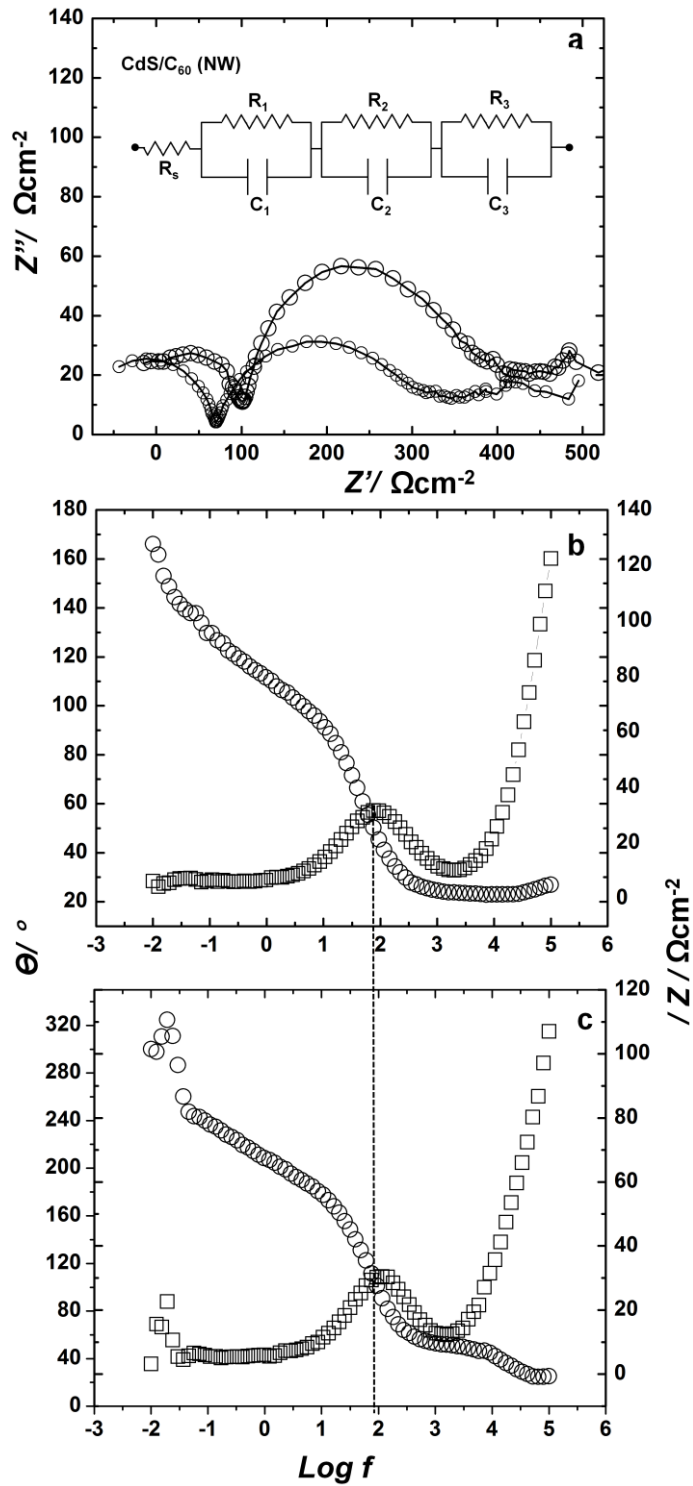


Figure 4.10: (a) Nyquist plots recorded under an ac amplitude of 10 mV for cells based on CdS/C₆₀ (NW) electrode with MWCNT/PDDA and Pt as the counter electrode under an open circuit bias of +0.550 V. Bode plots of (b) CdS/C₆₀ (NW) - MWCNT/PDDA cell and (c) CdS/C₆₀ (NW) - Pt cell: Phase angle (○) and modulus of impedance (□) versus log

frequency. Inset of (a) shows the Randles equivalent circuit used for fitting the experimental data and the solid lines in (a) represent the fits.

4.4 Summary

QDSSCs based on a CdS/C₆₀ (NW) electrode as the photoanode and a MWCNT/PDDA electrode as the counter electrode were constructed. The advantage of C₆₀ nanowhiskers owing to a higher effective surface area was realized in terms of superior photocurrents, photovoltage and IPCE values. Faster electron transfer from the CB of CdS to C₆₀ nanowhiskers were observed in the form of largest fluorescence lifetime reduction, as compared to neat CdS and CdS/C₆₀ electrodes. The overall performance of the QDSSC was improved by replacing Pt with MWCNT/PDDA as the counter electrode. The role of MWCNT/PDDA electrode in facilitating electron transport was confirmed from the lowered charge transfer and diffusional resistance and suppression of the photoelectron capture by the electrolyte in contrast to the cell with Pt as counter electrode. The increased electronic conductivity of the CdS/C₆₀ (NW) electrode and the capacity of this electrode to carry larger currents were demonstrated by C-AFM which complemented the photo-response relative to CdS or CdS/C₆₀ electrodes. By using KPFM, it was shown, that the altered position of the Fermi level in C₆₀ nanowhiskers, with respect to that of neat C₆₀ provides an extra stimulus for electron injection in the CdS/C₆₀ (NW) electrode. Facile fabrication of C₆₀ nanowhiskers based electrodes and the improved performance of the QDSSC relative to conventional C₆₀ based systems, cumulatively demonstrate that such an assembly can be easily extrapolated to a variety of QDs and significant improvements in QDSSC performances can be realized.

4.5 References

- [1] J-I. Minato, K. Miyazawa, *Carbon* **43** (2005) 2837-2841.
- [2] M. A. Hossain, J. R. Jennings, Z. Y. Koh, Q. Wang, *ACS Nano* **5** (2011) 3172-3181.
- [3] P. V. Kamat, *J. Phys. Chem. C* **112** (2008) 18737-18753.
- [4] Z. Yang, C-Y. Chen, C-W. Liu, H-T. Chang, *Chem. Comm.* **46** (2010) 5485-5487.
- [5] H. Kuzmany, R. Pfeiffer, M. Hulman, C. Kramberger, *Philos. Trans. R. Soc. London, Ser. A* **362** (2004) 2375-2406.

- [6] M. C. Martin, D. Koller, A. Rosenberg, C. Kendziora, L. Mihaly, *Phys Rev. B* **51** (1995) 3210-3213.
- [7] M. Tachibana, K. Kobayashi, T. Uchida, K. Kojima, M. Tanimura, K. Miyazawa, *Chem. Phys. Lett.* **374** (2003) 279-285.
- [8] Z.A. Peng, X. G. Peng, *J. Am. Chem. Soc.* **124** (2002) 3343-3353.
- [9] V. I. Klimov, *J. Phys. Chem. B* **104** (2000) 6112-6123.
- [10] C-F. Chi, H-W. Cho, H. Teng, C-Y. Chuang, Y-M. Chang, Y-J. Hsu, Y-L. Lee. *Appl. Phys. Lett.* **98** (2011) 12101-12103.
- [11] C. X. Guo, H. B. Yang, Z. M. Sheng, Z. S. Lu, Q. L. Song, C. M. Li, *Angew. Chem.* **49** (2010) 3014-3017.
- [12] J. L. Blackburn, D.C. Selmarten, A. J. Nozik, *J. Phys. Chem. B* **107** (2003) 14154-14157.
- [13] R. S. Dibbell, D. F. Watson, *J. Phys. Chem. C* **113** (2009) 3139-3149.
- [14] P. V. Kamat, M. Haria, S. Hotchandani, *J. Phys. Chem. B* **108** (2004) 5166-5170.
- [15] Y-L. Lee, C-H. Chang, *J. Power Sources* **185** (2008) 584-588.
- [16] P. Brown, P. V. Kamat, *J. Am. Chem. Soc.* **130** (2008) 8890-8891.
- [17] D. Kuang, P. Walter, F. Nüesch, S. Kim, J. Ko, P. Comte, S. M. Zakeeruddin, M. K. Nazeeruddin, M. Gratzel, *Langmuir* **23** (2007) 10906-10909.

Chapter 5

Effect of FRET and carbon dots on light harvesting capability of CdS QDs based photoanode

5.1 Introduction

In **Chapters 3** and **4**, the effect of carbon nanostructures on QDSSC performance was studied. While carbon nanostructures improve the electron transport performance of the photoanode, they are unable to utilize the solar spectrum efficiently. The inefficient usage of the solar spectrum remains a challenge.

FRET or Forster resonance energy transfer permits a wider spectral coverage, relaxes the stringent design requirement of aligned energy levels of photoanode components for electron transfer by cascade mechanism and thus provides exciting opportunities for designing a whole range of unexplored donor-acceptor architectures that can be easily translated into improved efficiency solar cells. The development of FRET based cells is very much in infancy, and characterization is even more so, owing to the practical difficulties in (i) distinguishing the charge transfer process from the energy transfer process in a solar cell, (ii) visualizing the actual donor-acceptor distances in the cell, and (iii) in correlating the solar cell performance with the charge/energy transfer dynamics.

As an attempt to bridge these lacunae in FRET enabled QDSSCs, and also to realize better performance, in this chapter, the synthesis and characterization of a heretofore unreported assembly employing ZnS/CdS/ZnS QDs as donors and copper phthalocyanine (CuPc) as acceptors, coupled with carbon-dots (C-dots) as the electron transport support is presented. C-dots have recently spurred a lot of active research interest, as they offer an attractive combination of several unique properties like size-dependent luminescence due to carbon structure quantum confinement effects, excellent redox properties and large electronic conductivities.^[1,2] This was the first time they were used in a solar cell. CuPc was chosen as

the acceptor, due to its high extinction coefficient in the red region, low cost and high miscibility in the liquid or polymeric electrolyte. In this assembly, we demonstrated how excited CdS QDs transfer their excitation to the CuPc molecules by FRET, and how the CuPc molecules undergo charge separation, indirectly by a photon to which they were otherwise insensitive to, thus improving charge separation in the donor. The energy transfer efficiency was quantified and the enhanced performance of the FRET enabled QDSSCs was correlated to the charge/energy transfer dynamics. Quasi solid-state FRET enabled cells were demonstrated, and this can have an enormous impact on practical solar cell applications.

5.2 Experimental

5.2.1 Synthesis of C-dots

C-dots were synthesized by a hydrothermal technique using a procedure reported by Sun et al.^[3] Glucose (4 g) was dissolved in water (40 mL) to form a clear solution, which was placed in a 40-mL teflon-sealed autoclave and maintained at 160–180 °C for 12 h. The black products were isolated by centrifugation, cleaned by three cycles of centrifugation, washing and re-dispersion in water and in alcohol, and oven-dried at 80 °C for ~4 h. The precipitate was dispersed in ultra-pure water (50 mL) and it was sonicated for 30 minutes and the resulting deep brown colloidal dispersion of C-dots was directly used for electrophoretic deposition.

5.2.2 Fabrication of the photoanode

A single layer of ZnS was deposited by SILAR method over a bare FTO as described in **Chapter 4**. For ZnS, Zn(NO₃)₂ (0.5M) and Na₂S (0.5 M) aqueous solution were used as the precursors. Over the ZnS layer, 5 layers of CdS were deposited by SILAR method, by employing Cd(NO₃)₂ and Na₂S as the precursors. Finally the ZnS monolayers were deposited over CdS and which ensconce the CdS QD layers, and serve as protective layers and prevent CdS quenching by sulfide ion electrolyte. The C-dots were electrophoretically deposited from

the C-dot suspension by using the FTO/ZnS/CdS/ZnS assembly as the working electrode and a Pt sheet as the counter electrode and by applying a potential of 30 V for 2 minutes. The color of the brown solution faded upon impregnation of the dark brown colored C-dot layers on the photoactive electrode. The resulting assembly was labeled as FTO/ZnS/CdS/ZnS/C-dot and this multilayered coating on FTO was rinsed in ultra-pure water, dried and stored in air.

5.2.3 Preparation of the MWCNT electrode

Functionalization of MWCNTs was accomplished by dispersing MWCNTs (2.5 g) in a mixture of HNO₃ and H₂SO₄ (1:3 by volume). The resulting suspension was sonicated for 20 minutes and refluxed at 80 °C for 6 hours. The black residue was washed with copious amounts of ultra-pure water till the supernatant liquid acquired neutral pH and dried in an oven at 60 °C for 48 hours. The dried black product (functionalized MWCNTs, 1 mg) were suspended in ultra-pure water (3 mL) by ultrasonication for fifteen minutes. The homogeneous MWCNT suspension was spin-coated on a FTO coated glass substrate at 1000 rpm for 30 s and the layer was annealed at 100 °C for 1 h in a vacuum oven, to yield a transparent black electrode.

5.2.4 Preparation of the gel electrolyte

A gel polymeric electrolyte was prepared according to a method reported in literature.^[4] Acrylamide (0.1 g) was dissolved in ultra-pure water (0.9 mL) and bis-acrylamide was added as the linker molecule (1.5 wt. % with respect to the monomer's weight). The mixture was degassed for 10 minutes and then ammonium persulfate (0.4 wt. % with respect to the monomer's weight) was added as the initiator to the precursor solution. The clear colorless formulation was heated at 70 °C for 1 h to yield a viscous gel. Water was expunged from the hydrogel by heating and it was continuously heated at 80 °C until a constant weight was achieved for the (dried) xerogel. The xerogel was soaked in an aqueous solution of Na₂S (0.1

M) for 12 h to allow for the swelling of the polymer matrix with electrolyte. The electrolyte was thus obtained in the form of a free standing, colorless, transparent polymeric gel.

The copper phthalocyanine (CuPc) based gel polymeric electrolyte was also prepared using the same above-mentioned procedure, except for a variation in the last step, wherein the xerogel was soaked in a CuPc (0.03 mM) and Na₂S (0.1 M) solution and the final product was a turquoise blue colored transparent gel. The gel electrolytes with and without CuPc were stored in vacuum desiccators.

Quasi solid-state devices were constructed by applying an acrylic spacer on the counter electrode film, and creating a cavity of about 1 cm × 1 cm and the free standing gel (with or without CuPc) was cut to size using a scalpel blade and inserted in the cavity. The photoanode coating (active coating facing inwards) was affixed on the electrolyte/counter electrode assembly using binder clips. The four edges of the cell were sealed using an epoxy sealant.

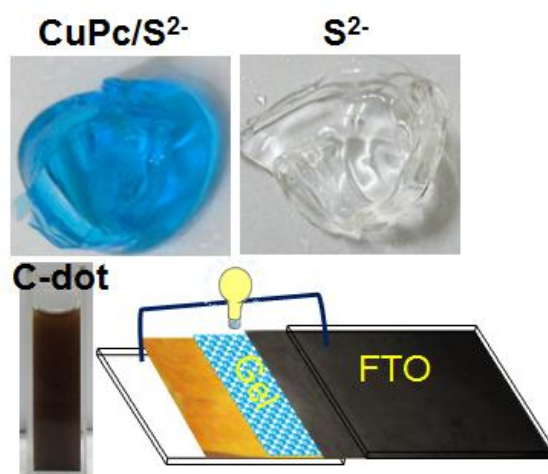


Figure 5.1: Digital photographs of the polymeric gel with and without CuPc, C-dot suspension and the device configuration (showing CdS and MWCNT electrodes).

5.3 Results and discussion

5.3.1 Energetics and donor-acceptor distances by HRTEM

The configuration of the ZnS/CdS/ZnS/C-dot photoanode is shown in a schematic (**Figure 5.2**). In the assembly of ZnS/CdS/ZnS/C-dot/CuPc, C-dots are expected to improve electron transport, so the electronic conductivity of C-dot is a relevant parameter. The conductivity of C-dots, was estimated to be 0.156 S cm^{-1} at ambient temperature by an ac impedance method, and the position of LUMO was deduced to be $\sim 0 \text{ V}$ (*versus* NHE) from a CV measurement (**Figure 5.4**). The confinement of the photoactive CdS layer between two ZnS layers, prevents direct charge injection from the conduction band of CdS QDs to C-dots as the CB of the layer in-between, i.e., ZnS is poised at 1.8 V *versus* NHE, which is 1 V (*versus* NHE), more negative with respect to the CB of CdS. Direct excited electron transfer from CdS QDs to the CuPc molecules (which are dissolved in the electrolyte) is inhibited not only by the surrounding ZnS layer, but also by the unfavorable alignment of the CB, as the LUMO of CuPc is positioned at 0.9 V (*versus* NHE) and is more negative with respect to CdS QDs. The only pathway available for the photogenerated electron deactivation in CdS QDs is therefore FRET, whereby the CdS QDs transfer their excitation energy non-radiatively to the acceptor CuPc molecules.

The CuPc molecules are dissolved in the aqueous sulfide electrolyte thereby ensuring a direct contact between the acceptor molecules with the donor layer of surface bound ZnS/CdS/ZnS QDs. CuPc then undergoes excitation and charge transfer occurs from the LUMO of CuPc to the Fermi level of C-dot (located at $\sim 0 \text{ V}$ *versus* NHE) and the electron is then channeled to the current collector, through the C-dot layer flanked to the conducting electrode. Another stimulus that favors energy transfer to be the dominant interactive mechanism between CdS and CuPc in the ZnS/CdS/ZnS/C-dot/CuPc assembly, involves the positions of CBs of CdS and CuPc relative to the Fermi level of C-dot. The larger difference

of 0.9 V (*versus* NHE) between the CB of CuPc and C-dots as opposed to 0.8 V (*versus* NHE) observed as the difference between CB of CdS and C-dots, provides an extra driving force for a preferred charge transfer between CuPc and C-dots over that between CdS QDs and C-dots.

A similar charge injection was achieved from the excited Ru-dye acceptor molecules (excited by energy transfer from CdSe QDs) to the current collector, *via* two physically separate layers of amorphous and nanocrystalline TiO₂, in a TiO₂/ZnS/CdS/CdSe/TiO₂/Ru-dye assembly.^[5] We also address the possibility of hole transfer from CuPc to C-dots in contributing to improved photocurrent.

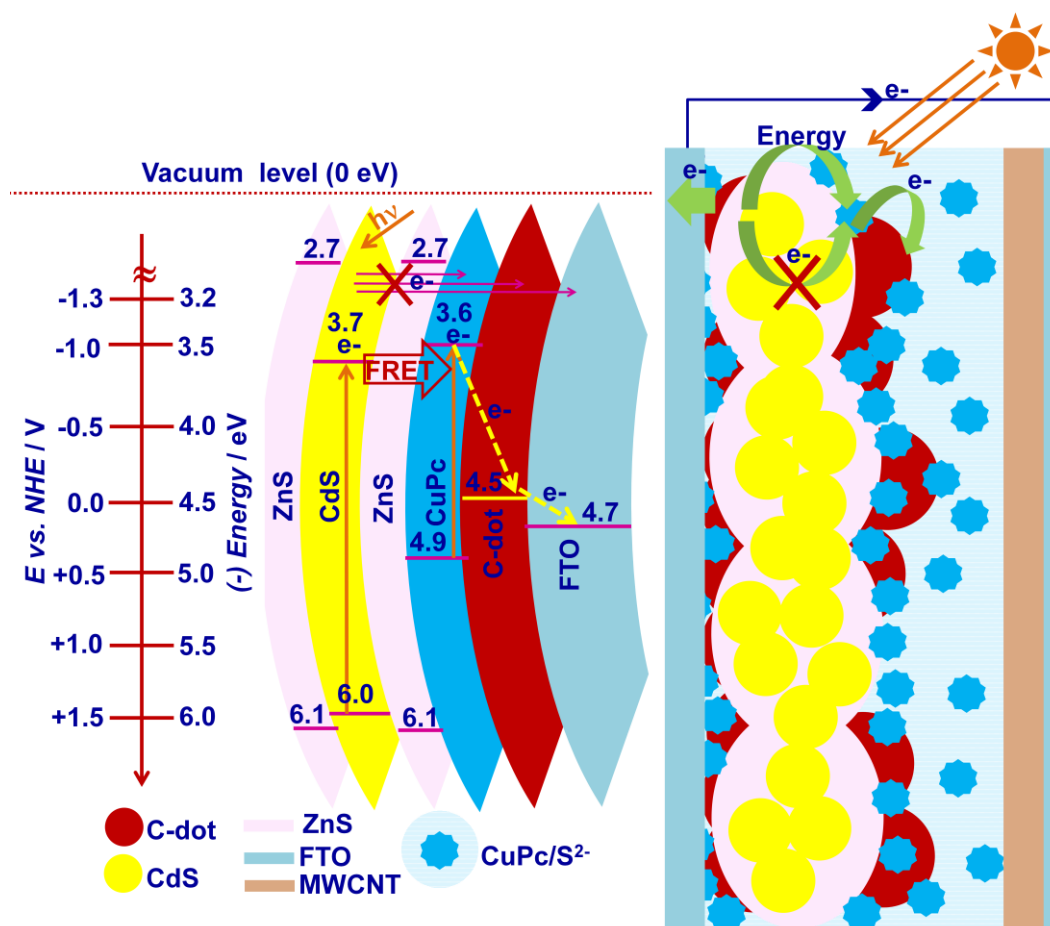


Figure 5.2: (a) Energy band diagram of a ZnS/CdS/ZnS/C-dot/CuPc cell showing possible modes for energy and electron transfer and (b) schematic of a ZnS/CdS/ZnS/C-dot/CuPc/S²⁻/MWCNT cell.

The HRTEM micrograph of ZnS/CdS/ZnS quantum dots (**Figure 5.3a**) shows the dots to have diameters in the range of 3.5 to 6.5 nm. The CdS QDs are crystalline as can be perceived from the oriented lattice fringes constituting the dots; the fringe separations are 0.33 nm and 0.21 nm, which match with interplanar 'd' spacings of 3.36 and 2.06 Å, oriented along the (111) and (220) planes of face-centered cubic structure of CdS, in concurrence with powder diffraction file (PDF) number 652887. Since the dots appear to be embedded in an amorphous phase, it is evident, that the ZnS monolayers surrounding the CdS QDs are amorphous. The successful formation of C-dot was confirmed by HRTEM. The HRTEM image of C-dots (**Figure 5.3b**), shows the C-dot to have an almost spherical geometrical shape, and composed of a hexagonal arrangement of carbon atoms. The diameter of the C-dot was estimated to be 16 nm. An enlarged view of the lattice-scale image of the dot (inset of **Figure 5.3b**) shows a clear formation of a hexagon by carbon atoms, and the interplanar spacing was deduced to be 0.34 nm, which is consistent with the (002) diffraction plane of sp^2 graphitic carbon (PDF: 75-1621). The Raman spectrum of C-dots (**Figure 5.4c**), also revealed the D band at 1345 cm^{-1} , re-affirming the hexagonal arrangement of carbon atoms, stacked in an ABAB manner. The HRTEM image of the ZnS/CdS/ZnS/C-dot/CuPc co-assembly, shows overlapping lattice fringes arising from all the three components indicating that the CdS QDs, C-dots and CuPc molecules are intimately connected at the nanoscale; but the fact that this co-assembly is not completely crystalline can be gauged from the region on the micrograph which shows a glazy contrast characteristic of an amorphous phase, which could be from ZnS (**Figure 5.3c**). Lattice fringes corresponding to the (220) plane of CdS ($d = 0.21\text{ nm}$) could be identified in the composite. In **Figure 5.3d** and **e**, lattice planes separated by an interplanar spacing of 0.32 nm arise from the (520) plane of the α -phase of tetragonal CuPc and this cluster of fringes was observed to be flanked by lattice fringes from CdS QDs. The blown-up view of the fringes from CdS QDs showed them to be separated by

0.17 nm and 0.12 nm which match with the orientations of the (311) and (422) planes of fcc-CdS (panels adjoining **Figure 5.3d** and **e**).

We observed that while some CdS nanocrystals flank the CuPc crystallites, such that there is almost no physical separation between them, some CdS QDs were found to lie at distances less than 10 nm, with respect to a CuPc crystallite. The separations between the donor (CdS) and the acceptor (CuPc) have been shown by dotted lines in **Figure 5.3d** and **e**. The average distance between a well-defined CuPc crystallite and CdS crystallite is about 4.9 nm, which concurs well with the calculated Forster radius (R_o , the distance at which the energy transfer efficiency is 50 % between the donor and the acceptor)^[6] of 4.25 nm, that has been deduced from overlap integral, in the later section. The donor and acceptor are within the Forster radius of this donor-acceptor system. **Figure 5.3e** also reveals the presence of C-dots, as distinctive lattice planes in a hexagonal arrangement could be observed; an enlarged view is presented as an inset, which conforms with the (100) plane of graphitic carbon. These topologies clearly reveal the lattice planes of C-dots to be juxtaposed with those of ZnS/CdS/ZnS QDs and CuPc nanocrystals, thus illustrating that the C-dots are in direct contact with CuPc molecules at the nanolevel, and therefore charge transfer between C-dots and CuPc is possible.

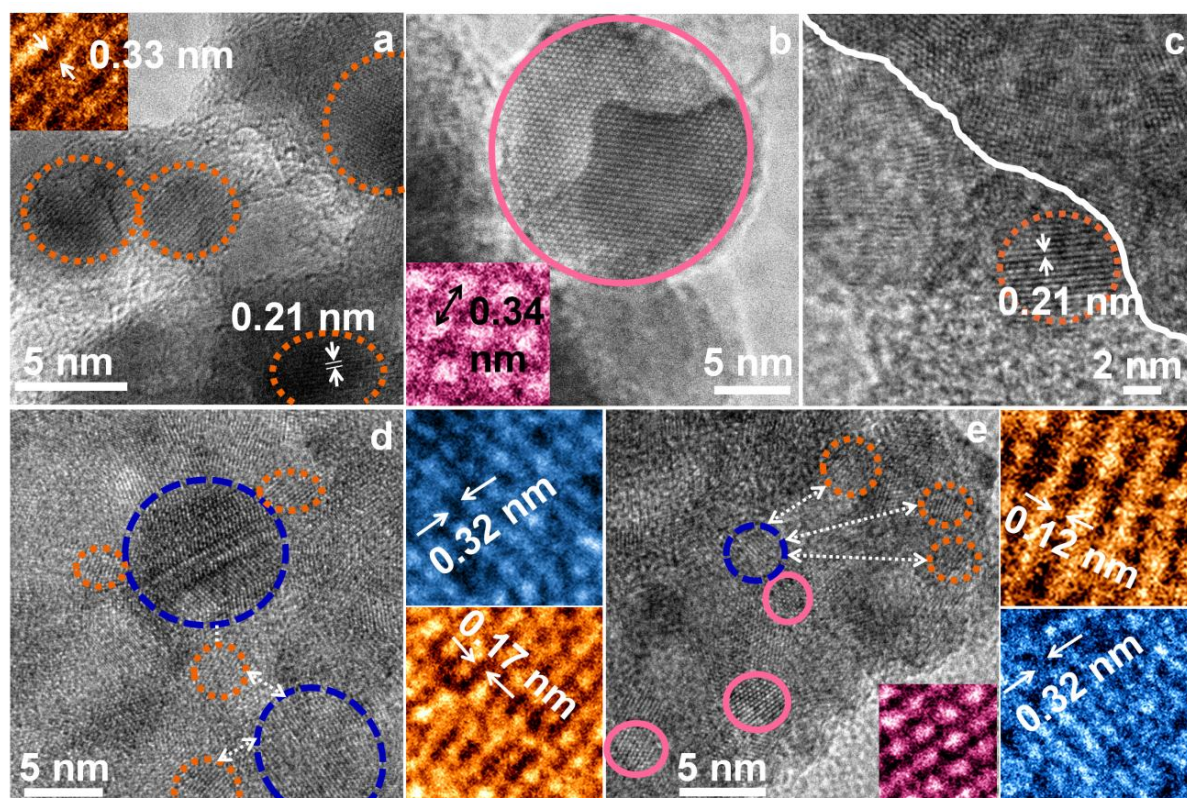


Figure 5.3: HRTEM images of (a) ZnS/CdS/ZnS QDs, inset shows a CdS QD oriented along the (111) plane, (b) C-dots, inset shows the hexagonal arrangement of graphitic carbon atoms oriented along the (002) plane, (c) overlapping lattice fringes co-exist with an amorphous phase in a CdS/C-dot/CuPc co-assembly, (d) and (e) different regions from the CdS/C-dot/CuPc co-assembly showing the inter-crystallite distances between acceptor (CuPc) and donor (CdS QDs) molecules. Panels adjoining (d) and (e) show the enlarged views of interplanar spacings in CdS and CuPc. Inset of (e) is a lattice-scale image corresponding to C-dot.

5.3.2 Characterization of C-dots

The CV plot of C-dots with Pt electrodes and recorded at a sweep rate of 20 mV s^{-1} is shown in **Figure 5.4b**. In the anodic sweep of the voltammogram, no distinct oxidation peak was observed, but in the reverse sweep, a broad reduction peak is observed at a potential (E_R) of -0.197 V (*versus* Ag/Ag^+). The potential of the reference electrode (Ag/Ag^+) was $+0.197 \text{ V}$ (*versus* NHE). The reduction potential (*versus* NHE) corresponds to the LUMO of the electroactive material. Therefore, the reduction potential of C-dots (*versus* NHE) will be: $E_R = (-0.197 + 0.197) \text{ V} = 0 \text{ V}$. 0 V (*versus* NHE) corresponds to 4.5 eV (w.r.t. vacuum level).

The LUMO of C-dots was therefore fixed at 4.5 eV in the energy band diagram shown in **Figure 5.2**. The Raman spectrum of the C-dots in **Figure 5.4 c** shows a G band at 1570 cm^{-1} and the 2D band was observed at 2650 cm^{-1} .

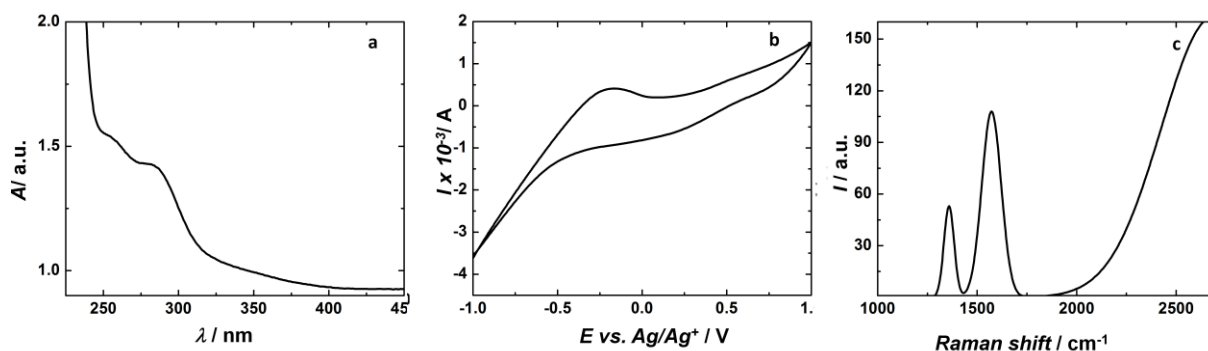


Figure 5.4: (a) Absorption spectrum of the C-dots dispersed in the deionized water, (b) CV of the C-dot solution with two Pt rods as the electrodes and $\text{Ag}/\text{AgCl}/\text{KCl}$ as reference electrode and (c) Raman spectrum of an electrophoretically deposited C-dot film obtained at a laser excitation wavelength of 532 nm.

5.3.3 SEM of MWCNTs

SEM image of MWCNTs electrode shows the presence of coiled, compactly packed network of MWCNTs. They are uniformly coated over the substrate but show no particular orientation.



Figure 5.5: SEM image of MWCNTs.

5.3.4 Fluorescence and lifetime studies

The overlap between the absorption spectrum of the acceptor and the emission spectrum of the donor, one of the primary conditions for FRET, is shown in **Figure 5.6**. While the ZnS/CdS/ZnS QD assembly was chosen as the donor due to its intense photoluminescence, the CuPc molecules were used as the acceptor dye, owing to their large extinction coefficient of $16375 \text{ mol dm}^{-3} \text{ cm}^{-1}$ at 613 nm. **Figure 5.6a** shows that the absorption of CuPc is encompassed within the luminescence of CdS QDs, particularly in the 525-625 nm wavelength span. To confirm that FRET is indeed the dominant mode for excited electron decay in the ZnS/CdS/ZnS/C-dot/CuPc configuration, the quenching of CdS fluorescence by CuPc was followed (**Figure 5.6b**) by introducing the ZnS/CdS/ZnS electrode to a CuPc solution. The fluorescence quenching measurements were performed on solid samples (such as ZnS/CdS/ZnS) coated on FTO/Glass substrates; in case of CuPc based samples, the sample/FTO/Glass was kept in a quartz cuvette filled with the aqueous CuPc solution. For fluorescence quenching and lifetime measurements, λ_{ex} was fixed at 370 nm and for lifetime, the emission decay was monitored at $\lambda_{\text{em}} = 530 \text{ nm}$. The band edge emission peak of CdS QDs generally lies in the range of 500-570 nm depending upon its size.^[7]

In the present study, the ZnS/CdS/ZnS film showed a band edge emission with a maximum at 530 nm. The PL peak intensity of this electrode diminishes with increasing concentration of CuPc. The fluorescence peak intensity of the CdS QDs quenched by ~2.5 times, upon exposure to a 0.03 mM CuPc solution. This quenching can only be a consequence of energy transfer from CdS QDs to CuPc, as excited electron transfer is energetically impossible and the ZnS layer also provides a barrier. However, to illustrate the role of ZnS in preventing excited electron transfer from CdS QDs to C-dots, the fluorescence quenching of CdS QDs was followed with and without the ZnS layers (**Figure 5.6c**). The ZnS/CdS/ZnS assembly shows an emission peak at 530 nm and neat C-dots also show a band

edge emission peak at 416 nm. The PL response of the ZnS/CdS/ZnS/C-dot assembly shows twin peaks at 416 and 530 nm, with an insignificant change in intensities, relative to their independent responses. This clearly shows that the ZnS layer entrapped between the C-dots and CdS QDs, prevents charge transfer from CdS to C-dots. The PL spectrum of a C-dot/CdS assembly (devoid of ZnS) is also shown, wherein, while the C-dot fluorescence remains almost unaltered (in comparison to neat C-dots), CdS luminescence intensity is quenched by 1.7 times, indicating that in the absence of the ZnS layer, the photoexcited electrons are transferred from CdS QDs to the Fermi level of C-dots. 0.03 mM CuPc was fixed as the strength for optimum energy transfer, on the basis of IPCE efficiency values, which are discussed later.

To reaffirm the interactive energy transfer dynamics operative between excited CdS QDs and CuPc molecules, the fluorescence lifetime spectra were recorded by monitoring emission of the FTO/ZnS/CdS/ZnS assembly at 530 nm (**Figure 5.6d**). The fluorescence data reliably fitted to a bi-exponential decay function expressed in (1).

$$I = A_1 \exp(-t/\tau_1) + A_2 \exp(-t/\tau_2) \quad (1)$$

I is the normalized emission intensity, t is the time after LED excitation, A_1 , A_2 are the amplitude coefficients and τ_1 , τ_2 are the decay time constants. The results of the fitting are summarized in **Table 5.1**.

The average lifetime for the excited electron is 15.91 ns for the FTO/ZnS/CdS/ZnS assembly, which is ascribed to the electron-hole recombination in CdS QDs, as the ZnS layers provide energy barriers for charge injection to FTO. To confirm this, we recorded the average electron lifetime for a FTO/CdS electrode. It was 12.83 ns, which is shorter than the lifetime for excited electron decay in CdS layers enwrapped by ZnS, thus proving that excited electron injection into FTO from CdS QDs which are in contact with the current collector is

faster than recombination. The energy relay from CdS QDs to CuPc was confirmed from the excited electron lifetime of the FTO/ZnS/CdS/ZnS/CuPc assembly, which was 9.35 ns. This average lifetime cannot be ascribed to band edge recombination in CdS QDs, as it is much shorter than that observed for FTO/ZnS/CdS/ZnS assembly. Since photogenerated electron transfer from CdS to CuPc is ruled out owing to unfavorable energy level offsets and the interceptor ZnS layer, excitation energy transfer through FRET to CuPc is the only possible mode for excited electron decay. Energy transfer by the exchange of virtual photon is a kinetically faster process than excited electron transfer from CuPc to FTO, and therefore, the short-lived component of 1.01 ns originates predominantly from energy transfer to CuPc and the long-lived component of 12.13 ns arises from either electron transfer from CuPc to FTO or band edge recombination in CuPc. The excited electron lifetime in the assembly prepared herein for optimum energy harvesting by FRET, i.e., the FTO/ZnS/CdS/ZnS/C-dot/CuPc assembly showed the shortest average excited electron lifetime of 8.65 ns, which ratifies the role of C-dots as excellent electron conduits, for promoting charge transfer and transport. Of the two time constants, τ_1 and τ_2 , the fast decay component of 0.84 ns is attributed to excitation energy transfer from CdS to CuPc and the slow decay component of 12.20 ns is attributed to charge transfer from CuPc to C-dots. In both the latter systems, with or without C-dots, the energy transfer process is almost twelve times faster than the charge transfer/recombination processes. To also rule out the possibility of direct charge injection from CdS to C-dots, apart from energy transfer from CdS to CuPc followed by electron transfer from CuPc to C-dot, the positions of CBs of CuPc and C-dot also favor hole transfer.

Table 5.1: Kinetic parameters of emission decay analysis of photoanode films (measured at $\lambda_{\text{ex}} = 370$ nm and $\lambda_{\text{em}} = 530$ nm) deduced from bi-exponential fits.^a

Electrode description	χ^2	τ_1 (ns)	τ_2 (ns)	A_1	A_2	$\langle\tau\rangle$ (ns)
^b ZnS/CdS/ZnS/C-dot/CuPc	1.092	0.84	12.23	31.22	68.78	8.67

^b ZnS/CdS/ZnS/CuPc	1.032	1.01	12.13	24.91	75.09	9.49
FTO/CdS	1.029	1.77	14.85	15.21	84.79	12.83
ZnS/CdS/ZnS	1.081	2.01	21.08	27.05	72.95	15.91

^bThe electrode was exposed to a solution of 0.03 mM CuPc during the measurements, to mimic the situation in a solar cell.

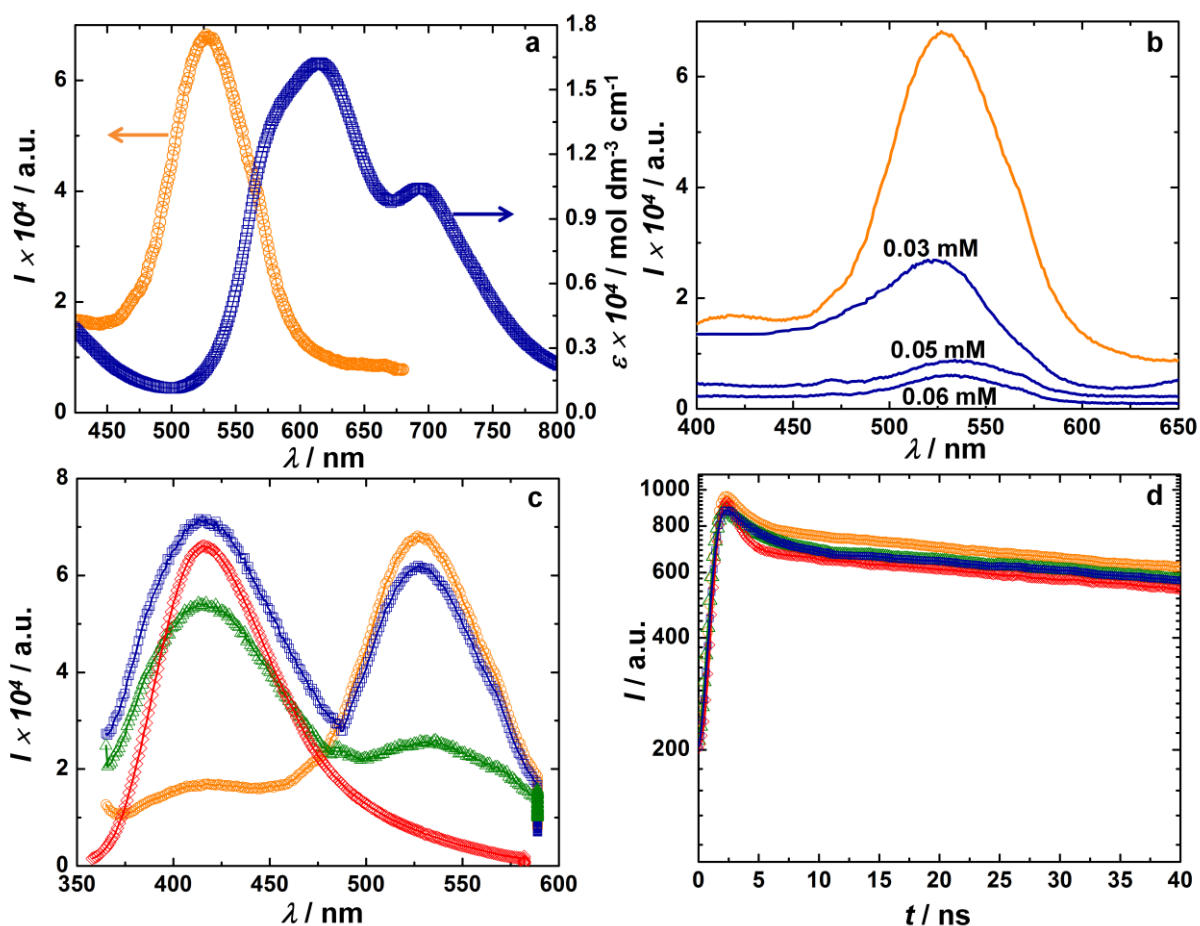


Figure 5.6: (a) Absorption spectrum (\square) of CuPc solution and the emission spectrum (\circ) of the ZnS/CdS/ZnS electrode ($\lambda_{\text{ex}} = 370$ nm), (b) quenching of emission profile of the ZnS/CdS/ZnS electrode upon exposure to different concentrations of CuPc solutions: 0.03, 0.05 and 0.06 mM ($\lambda_{\text{ex}} = 370$ nm), (c) emission spectra of ZnS/CdS/ZnS (\circ), C-dot (\diamond), CdS/C-dot (\triangle) and ZnS/CdS/ZnS/C-dot (\square) electrodes ($\lambda_{\text{ex}} = 370$ nm) and (d) time resolved fluorescence decay traces of ZnS/CdS/ZnS (\circ), CdS (\triangle), ZnS/CdS/ZnS/CuPc (\square) and ZnS/CdS/ZnS/C-dot/CuPc (\diamond) electrodes with $\lambda_{\text{ex}} = 370$ nm and with $\lambda_{\text{em}} = 530$ nm.

Indirect experimental evidences suggestive of the possibility of hole transfer from CuPc to C-dot include (a) the p-type semiconducting nature of C-dots (ascertained by a Mott-Schottky plot, shown in **Figure 5.7a**) and fluorescence quenching and electron lifetime

reduction of C-dots upon addition of CuPc (**Figure 5.7b**). Although hole transfer from CdS QDs to CuPc is energetically feasible but unlike the C-dots/CuPc system, here the CdS QDs are physically separated from CuPc by a ZnS layer. For both electron and hole transfer, the two components should be in direct contact with each other. Since the ZnS layer in between acts as a physical barrier, direct hole transfer from CdS QDs to CuPc is not possible.

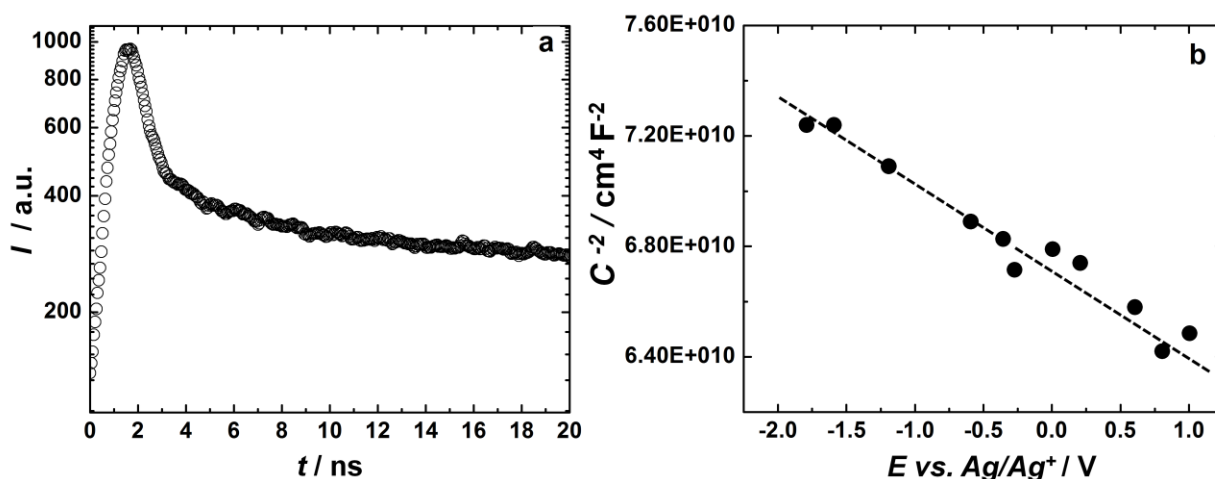


Figure 5.7: (a) PL decay trace of ZnS/CdS/ZnS/C-dot ($\lambda_{\text{ex}} = 370$ nm and $\lambda_{\text{em}} = 530$ nm). (b) Mott-Schottky plot of a C-dot dispersion in water by employing two platinum rods as electrodes.

The average lifetime of ZnS/CdS/ZnS/C-dots system at $\lambda_{\text{em}} = 530$ nm and $\lambda_{\text{ex}} = 370$ nm was 16 ns which is almost equivalent to the average lifetime of the ZnS/CdS/ZnS system ($\langle \tau \rangle = 15.9$ ns), indicating that C-dots do not contribute significantly to the decay response of the ZnS/CdS/ZnS/C-dots/CuPc system (at $\lambda_{\text{em}} = 530$ nm). The p-type semiconducting behavior of C-dots was ascertained by recording a Mott-Schottky plot of the C-dot suspension with Pt rods as working and counter electrodes and Ag/Ag⁺ as the reference electrode; at a constant frequency of 1000 Hz, over a dc potential range of -2 to $+1$ V. The negative slope of the $1/C^2$ versus potential indicates a p-type conduction behavior, thus suggesting that C-dots are capable of conducting holes.

5.3.5 Forster radius calculation

FRET involves resonance energy transfer of excitons generated in the surface bound donor (CdS QDs) to the acceptor (CuPc) molecules, spatially confined to the electrode surface via the electrochemical mediator. FRET rate (K_{ET}) should be fast for efficient energy transfer and it can be calculated from the equation provided below.

$$K_{ET}(r) = 1/\tau_D(R_0/r)^6 \quad (2)$$

In equation (2), τ_D is the excited state life time of the donor (CdS QDs) in the absence of the acceptor (CuPc) and R_0 is the Forster radius, which has been calculated from expression (3).

$$R_0^6 = 9000\ln(10)k^2Q_DJ/128\pi^5n^4N_A \quad (3)$$

In equation (3), Q_D is the fluorescence quantum yield of the donor in the absence of the acceptor, k^2 is the dipole orientation factor and the magnitude of k^2 is assumed to be $2/3$,^[6] N_A is the Avogadro's number and n is the refractive index of the medium. Q_D , the donor quantum yield of CdS QDs, has a value of 0.28. It was calculated by employing Rhodamine 101 as the standard, from absorption and fluorescence studies. The quantum yield for the donor ZnS/CdS/ZnS was determined by measuring the fluorescence and absorption of the donor at different concentrations at an excitation wavelength of 370 nm, and by comparing the same by measuring the fluorescence and absorption of a standard/reference Rhodamine 101. In this experiment, Rhodamine 101 was dissolved in ethanol as a standard with a known quantum yield of 100%.

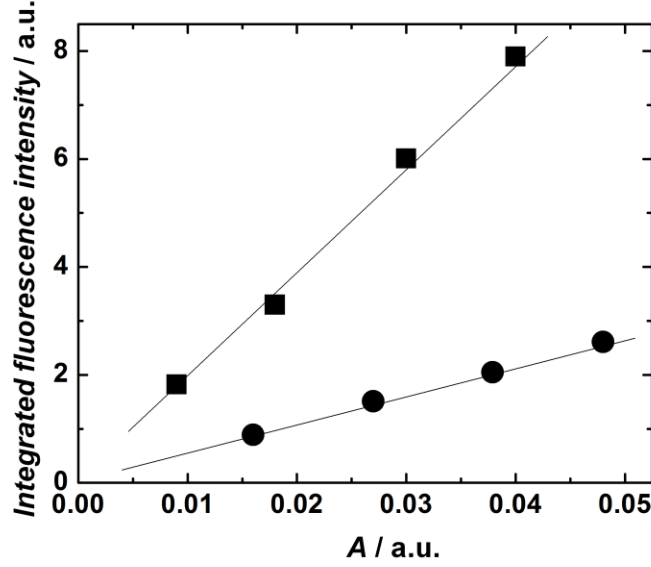


Figure 5.8: Integrated fluorescence intensity *versus* absorbance of donor: ZnS/CdS/ZnS QDs (●) and reference: Rhodamine 101 (■). The excitation wavelength was fixed at 370 nm for ZnS/CdS/ZnS and 367 nm for Rhodamine 101.

$$\phi_X = \phi_{ST} (\text{Grad}_X / \text{Grad}_{ST}) (\eta_{ST}^2 / \eta_X^2) \quad (4)$$

In equation (4), X and ST denote the test (or donor, ZnS/CdS/ZnS) and the standard or reference (Rhodamine 101) samples. ϕ , Grad and η respectively denote the quantum yield, slope of the integrated fluorescence intensity *versus* absorbance plots and the refractive index of the solvent. By substituting the experimental values in equation (4), equation (5) is obtained. For fluorescence or absorbance measurements, Rhodamine 101 was dissolved in ethanol and ZnS/CdS/ZnS was scratched out from the substrate and dispersed in the water.

$$\phi_X = 100 \times (54/187) (1.33^2 / 1.36^2) \quad (5)$$

From equation (5), the quantum yield for ZnS/CdS/ZnS was calculated to be 0.28. This value was used for calculating Forster radius. The following equation was used for determination of Forster radius.

An aqueous solution of 0.03 mM CuPc and 0.1 M Na₂S was the electrolyte and the refractive index (n) was ~1.38. From spectrophotometric data, J, the spectral overlap integral was calculated from the following expression.

$$J = \int_0^{\infty} F_D(\lambda) \varepsilon_A(\lambda) \lambda^4 d\lambda \quad (6)$$

F_D is the donor fluorescence intensity normalized to unit area (arbitrary units) and ε_A is the extinction coefficient of the acceptor (in $M^{-1} \text{ cm}^{-1}$). The spectral integral (J) for the CdS/CuPc system was deduced to be $\sim 3.08 \times 10^{-14}$ and the resulting Forster radius (R_o) is 4.25 nm. Forster radius for FRET based photoanodes containing zinc phthalocyanine (donor) with Ru 505 or black dye or N719 dye (as acceptor) were deduced to be 0.98, 4.1 and 3.2 nm respectively, in the past.^[8] Since the acceptable separation for effective dipole-dipole interaction is 1-10 nm,^[9] our value of $R_o = 4.25$ nm, should permit efficient energy transfer from CdS QDs to the CuPc molecules. To quantify energy transfer rate, the apparent rate constant of excited electron was calculated from the average lifetime analysis by employing the following equation.

$$K_{et} = 1/\langle \tau \rangle (\text{ZnS/CdS/ZnS/CuPc}) - 1/\langle \tau \rangle (\text{ZnS/CdS/ZnS}) \quad (7)$$

Equation (7) yields the energy transfer rate from ZnS/CdS/ZnS QDs to CuPc, enabled by the preceding excitation in ZnS/CdS/ZnS QDs. The rate constant for energy transfer for ZnS/CdS/ZnS QDs to CuPc molecules is $4.3 \times 10^7 \text{ s}^{-1}$, which is close to the values obtained in previous reports based on FRET.

$$E = 1 - \tau_{DA}/\tau_D \quad (8)$$

For the ZnS/CdS/ZnS/CuPc system, the energy transfer from ZnS/CdS/ZnS to CuPc occurs with an efficiency of $\sim 40\%$, which is again close to energy transfer efficiencies reported in the past for FRET based DSSCs.^[5]

$$r^6 = [R_o^6(1-E)]/E \quad (9)$$

From detailed HRTEM analyses, the average actual distance between the donor

(ZnS/CdS/ZnS) and the acceptor (CuPc) was found to be 4.9 nm and the donor-acceptor distance calculated from equation (3) is 4.54 nm. On increasing the CdS-CuPc distance, by increasing the number of ZnS layers, the separation between the CdS and CuPc increased to more than 10 nm, which is outside the FRET range, and therefore only one layer of ZnS was applied in between.

5.3.6 Performance of solid-state FRET cells

To ratify that FRET was indeed the dominant mechanism for excited electron deactivation in the ZnS/CdS/ZnS/C-dot/CuPc assembly, quasi solid-state solar cells were constructed with this assembly as the photoanode (all except CuPc), acid functionalized MWCNTs as the counter electrode and a poly(acrylamide) based gel electrolyte containing 0.1 M Na₂S and 0.03 mM CuPc as the electrolyte (shown in **Figure 5.1**). The conductivity of the gel with CuPc was 13 mS cm⁻¹ and without CuPc, it was 19 mS cm⁻¹. Since the two values are close, it is apparent that CuPc does not alter the conduction capability of the sulfide gel. The IPCE response is extremely poor for the cell devoid of the acceptor CuPc, as the ZnS monolayers encapsulate the CdS QDs and prevent direct charge injection to FTO. This cell showed a dismal IPCE of 3% at 380 nm, matching with the absorption spectrum of the CdS QDs and thus proving that ZnS monolayers inhibit excited electron transfer in the FTO/ZnS/CdS/ZnS assembly. However, the IPCE of the cell based on the FTO/ZnS/CdS/ZnS assembly as the photoanode, and S²⁻ gel with CuPc as the electrolyte, was significantly higher, with a maximum photo-response of 12% at 420 nm. The cell showed an enhanced IPCE in the 380 to 575 nm wavelength range, which commensurates with the absorption of the donor i.e., CdS QDs in the same range.

Since the IPCE of the donor-acceptor cell with CuPc is 4 times higher than the IPCE of the cell without CuPc, it is evident that the energy relay between CdS QDs and CuPc molecules is more efficient for generating excitons, than the photo-induced charge separation

process (as observed from the lower IPCE of the CdS cell, without CuPc). The increased IPCE response in the 575-650 nm range observed for the FTO/ZnS/CdS/ZnS-CuPc cell as compared to FTO/ZnS/CdS/ZnS cell, is attributed to the absorption of the acceptor (CuPc) in this range. We find that the donor-acceptor assembly system showed an increase in the external quantum yield or IPCE in the entire spectral regime, and more so, in the blue region of 370 to 500 nm. This increment originates from FRET interaction between CdS QDs and CuPc. Electrons in the VB of CdS excite by absorbing the blue part of the solar spectrum and these excited electrons transfer resonance energy to the acceptor CuPc molecules. The combined response arising from (i) the absorption of CdS in the blue region and better charge separation induced therein by FRET, and (ii) from the excitation of the CuPc in the red region indirectly by a photon, to which it was otherwise impervious to, results in a broader usage of the visible spectrum.

Various concentrations of the CuPc were also attempted, but at high concentrations, quantum yield decreased due to concentration quenching (**Figure 5.9b**). From the IPCE analysis, the concentration of the CuPc was fixed at 0.03 mM. On including conductive C-dots in the FRET-enabled assembly of FTO/ZnS/CdS/ZnS/C-dots with CuPc in the electrolyte, the IPCE increases in the entire 350-650 nm wavelength range, with a maximum of about 20% at 400 nm, exemplifying the efficiency of C-dots in channeling charge to the current collector, as opposed to the direct transfer from the LUMO of CuPc to the current collector itself. This value is 1.9 times higher than that of the cell without C-dots; a similar degree of improvement was registered in the entire spectral region.

In the past, Buhbut et al., reported a maximum IPCE of about 10 % achieved in the blue region for a FRET enabled cell, with CdS/CdSe/ZnS QDs as the donor and a squaraine dye as the acceptor.^[5] More importantly, authors demonstrated the full coverage of solar spectrum, for a cell with the donor-acceptor architecture. In the present assembly, CdS QDs are

separated from C-dots by the ZnS monolayers and therefore direct charge injection either into FTO or C-dots is prevented. Photogenerated electrons in CdS, can transfer only their excitation to the CuPc molecules via FRET, and the indirectly excited electrons in CuPc cascade into the Fermi level of C-dots, poised at 4.5 eV (*versus vacuum*), and the C-dots shuttle the electrons to FTO.

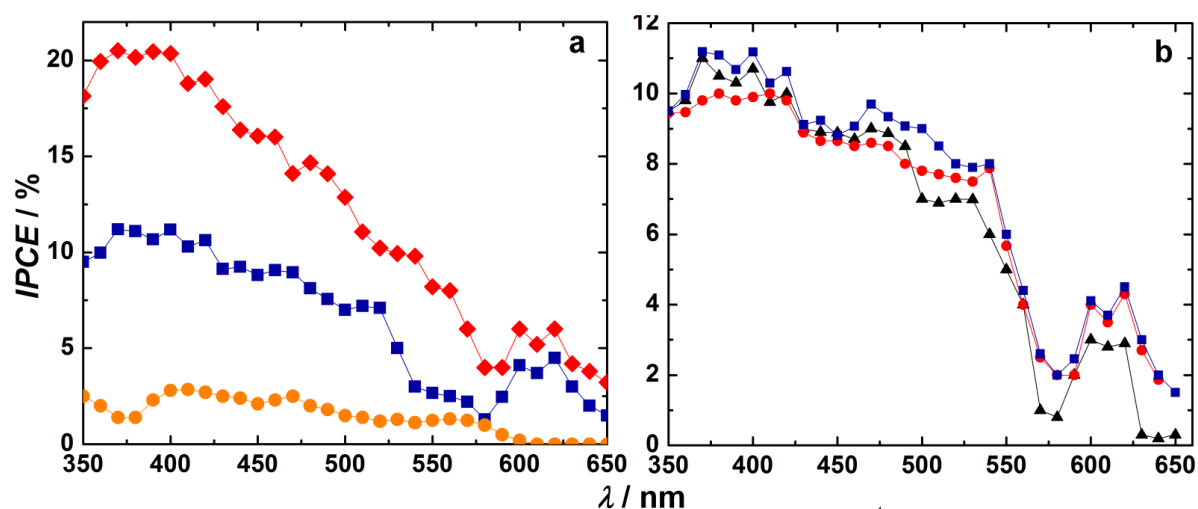


Figure 5.9: IPCE spectra of quasi solid-state solar cells with the following photoanodes: (a) ZnS/CdS/ZnS (●), ZnS/CdS/ZnS/CuPc (■) and ZnS/CdS/ZnS/C-dot/CuPc (◆) and (b) ZnS/CdS/ZnS/CuPc in contact with gel electrolytes with varying CuPc concentrations of 0.02 (▲), 0.03 (■) and 0.05 (●) mM. A poly(acrylamide) gel containing 0.1 M Na₂S was employed as the electrolyte (with or without 0.03 mM CuPc, unless mentioned otherwise) and MWCNT/FTO was used as a counter electrode. The working electrode area was fixed at 1 cm².

The high electronic conductivity of C-dots, the nanoscale proximity between C-dots and CuPc (as observed from HRTEM) and the favorable energy level offsets between the LUMO of CuPc and the Fermi level of C-dots are the driving factors for the more efficient photoconversion capability of the FTO/ZnS/CdS/ZnS/C-dot electrode exposed to CuPc in the electrolyte. Here, C-dots, play the role akin to graphene or carbon nanotubes do in QDSSCs, they increase overall photocurrents, by promoting charge transfer and transport.^[10,11] The IPCE in the blue region (energy transfer regime) is however higher than the IPCE in the red

region (due to direct electron injection) for all cells. This is due to the fact that the free CuPc molecules in the electrolyte gel do not contribute much to photocurrent; the absorption of ZnS/CdS/ZnS is greater than the absorption of ZnS/CdS/ZnS with CuPc/Na₂S-polymer gel in the 350-525 nm range.

The J-V characteristics of quasi solid-state cells with different photoanode architectures are shown in **Figure 5.10** and the cell parameters are summarized in **Table 5.2**. The hole transport layer was a sulfide ion based polymeric gel electrolyte and the counter electrode was a thin layer of acid functionalized MWCNTs deposited on FTO coated glass. The V_{oc} observed for the FTO/ZnS/CdS/ZnS based cell (without CuPc in the electrolyte) was 419 mV whereas for the FTO/ZnS/CdS/ZnS based cell with CuPc in electrolyte, V_{oc} was 512 mV, about ~1.2 times higher than that of the cell without CuPc. The J_{sc} values are 1.128 and 0.295 mA cm⁻² for the cells with and without CuPc respectively. The increase in the J_{sc} by four-fold times, ongoing from a neat CdS cell to a FRET enabled cell (encompassing a donor (CdS) - acceptor (CuPc) architecture) is a clear indicator of the fact that FRET is a powerful mechanism for improving charge separation and as a consequence, better current generation.

In previous reports, wherein CuPc was employed as the light sensitive dye, the photocurrent densities were of the order of 100 $\mu\text{A cm}^{-2}$; [12] although these values are lower than that achieved for cells with conventional N719 or JK2 dyes, but low cost and ease of incorporation of CuPc are two advantages. The overall PCE also increased 5.25 times by incorporating CuPc in the electrolyte. The current collection capability of the electrode is enhanced considerably, upon including C-dots in the photoanode assembly. It is a well-established fact, that incorporation of carbon nanostructures in QD based photoanodes generally leads to significantly increased currents, as electron- hole recombination is prevented due to faster electron transfer to the carbon moiety (relative to the inorganic transparent electrode).

In an earlier report, photocurrent increased by 1.73 times, when a CdSe based electrode was enriched with reduced graphene.^[13] The ZnS/CdS/ZnS/C-dot/CuPc cell showed a J_{sc} of 1.7 mA cm^{-2} which, is ~ 1.5 times higher than that of the cell with the exactly same configuration sans the C-dots and a large V_{oc} of 564 mV, was also observed. Cells with an aqueous liquid electrolyte containing Na_2S and CuPc (photoanode: ZnS/CdS/ZnS/C-dot) were also constructed, and it was found that the performance of the cell with the polymeric gel was comparable to that of the liquid based cell (**Figure 5.10**). A solid-state cell with high performance attributes is very much desirable for practical applications. The ZnS/CdS/ZnS/C-dot/CuPc/ Na_2S /MWCNT solid-state cell showed a PCE of 0.34%, which was 7.75 times higher in comparison to the same cell with only the donor.

In another study, Etgar et al., observed that when a tailored squaraine dye was used as the acceptor and CdSe as the donor, the resulting FRET enabled cell showed an efficiency of 1.48% whereas the acceptor alone cell showed an efficiency of 0.79%.^[14] The J-V characteristics of control cells with either only donor (CdS) or only acceptor (CuPc) are shown in **Figure 5.11**. The role of FRET in improving solar cell performance was also confirmed from the poor performance of the sole component cells.

Table 5.2: Solar cell parameters of QDSSCs ($\lambda > 300 \text{ nm}$, $0.1 \text{ M Na}_2\text{S}$ aqueous poly(acrylamide) based gel electrolyte with or without 0.03 mM CuPc , cell area: 1 cm^2 , under 1 sun illumination (100 mW cm^{-2})) with the listed photoanodes; all cells with MWCNT/FTO as the counter electrode.

Electrode configuration	V_{oc} (mV)	J_{sc} (mA cm^{-2})	FF	Efficiency (%)
ZnS/CdS/ZnS	419	0.295	39	0.04
ZnS/CdS/ZnS/CuPc	512	1.128	37	0.21
ZnS/CdS/ZnS/C-dot/CuPc	564	1.70	36	0.34
ZnS/CdS/ZnS/C-dot/CuPc	605	1.88	31	0.35

(liquid electrolyte)

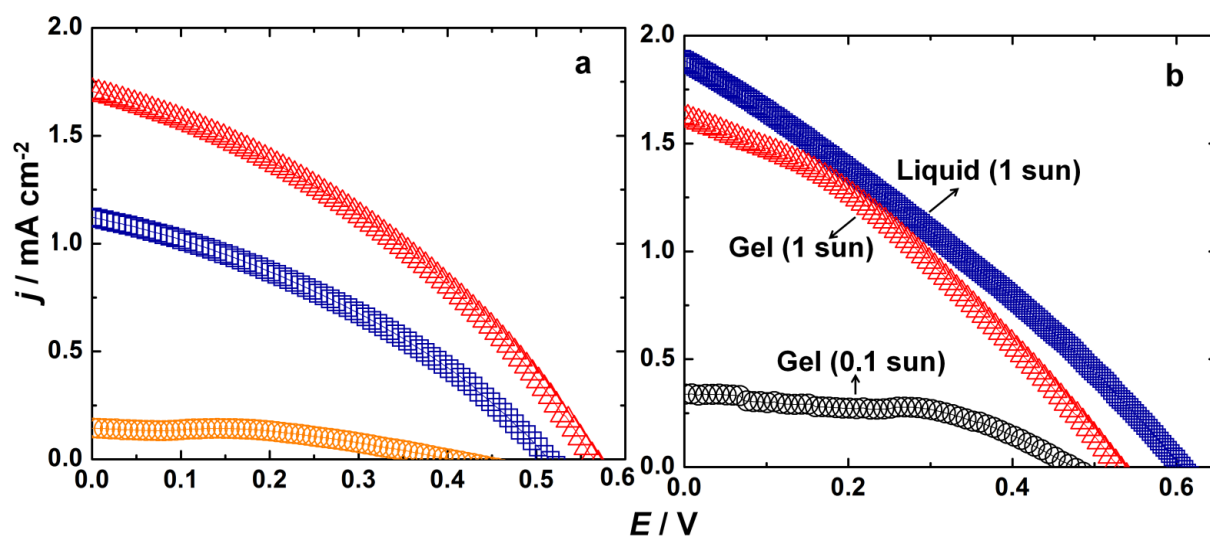


Figure 5.10: J-V characteristics of quasi solid-state QDSSCs with the following photoanode architectures: (a) ZnS/CdS/ZnS/C-dot/CuPc (Δ), ZnS/CdS/ZnS/CuPc (\square) and CdS/C-dot/CuPc (\circ) under 1 sun illumination and (b) ZnS/CdS/ZnS/C-dot/CuPc (liquid state cell) (\square), ZnS/CdS/ZnS/C-dot/CuPc (Δ) under 1 sun illumination and ZnS/CdS/ZnS/C-dot/CuPc (\circ), under 0.1 sun illumination. A poly(acrylamide) gel containing 0.1 M Na₂S was employed as the electrolyte unless mentioned otherwise and MWCNT/FTO was used as a counter electrode and $\lambda > 300$ nm. 0.03 mM CuPc was dissolved in the gel or liquid electrolyte; it was not tethered to the photoanode. The working electrode area was fixed at 1 cm⁻².

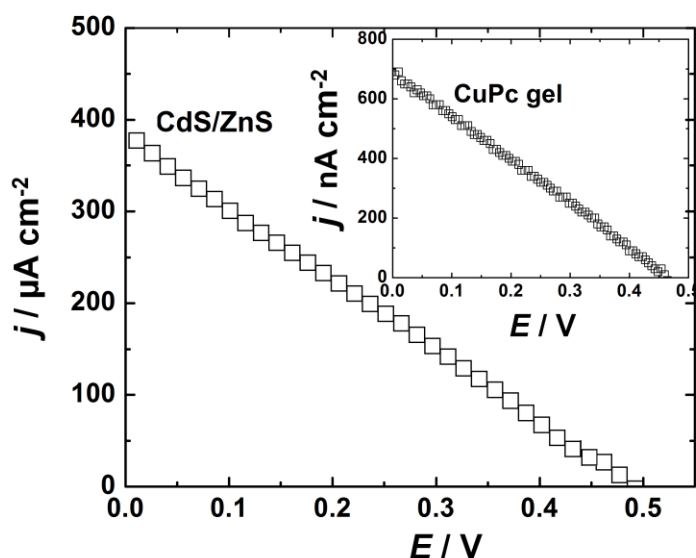


Figure 5.11: J-V characteristics of control cells with either donor or acceptor as photoanodes: FTO/CdS/ZnS/Na₂S gel/MWCNT and FTO/CuPc gel/MWCNT cell is shown in the inset.

5.3.7 EIS analysis

To unambiguously determine the role of C-dots in improving current collection and retarding excited electron (indirectly excited in CuPc)-hole recombination, electrochemical impedance spectroscopy was performed for the following solid-state cells: ZnS/CdS/ZnS/C-dot/CuPc/Na₂S/MWCNT and ZnS/CdS/ZnS/CuPc/Na₂S/MWCNT (**Figure 5.12**). For these two cells, the Nyquist plot comprises of one incomplete and one semicircle. In the high frequency domain, the point of intersection of the first unfinished semicircle with the abscissa corresponds to the charge transfer resistance at MWCNT/CuPc/Na₂S interface. The resistance corresponding to the point at which the second semicircle intersects the Z' axis, arises from the photoanode/electrolyte interface. The low frequency response originates from the diffusion of ions away from the photoanode surface.

The Bode plots of the cells (phase angle *versus* frequency) are shown as insets in **Figure 5.12**. From the Bode plot of the donor only cell, a recombination lifetime was calculated using the equation ($\tau_d = 1/2\pi f$); where the f is the middle frequency peak in the Bode plot (**Figure 5.12**). Recombination time (τ_d) is defined as the time taken by the excited state electron in the photoanode to recombine with the oxidized species of the electrolyte. This recombination time for the FRET enabled cell with the electrode having the donor-acceptor architecture of CdS and CuPc was 1.113 ms. A longer recombination time of 1.675 ms was observed for the cell with the ZnS/CdS/ZnS/C-dot/CuPc electrode capable of both FRET and fast electron transfer (due to C-dots). The role of C-dots in allowing rapid charge transfer and transport to the current collector or FTO is evident. The longer electron lifetime can also be correlated to the higher open circuit potential observed for this cell, as V_{OC} is

difference in the LUMO of CuPc (in all CuPc based cells) or CB of CdS (in all cells without CuPc) and the redox potential of the S_n^{2-}/S^{2-} electrolyte.

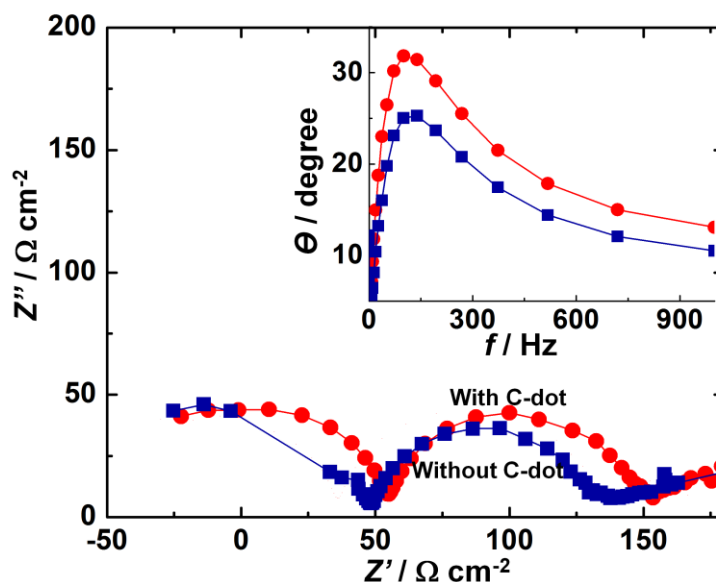


Figure 5.12: Nyquist plots recorded under an ac amplitude of 10 mV and a zero dc bias for quasi solid-state solar cells based on photoanodes of ZnS/CdS/ZnS/CuPc (■) and ZnS/CdS/ZnS/C-dot/CuPc (●). A 0.1 M Na₂S based poly(acrylamide) gel served as the electrolyte and a MWCNT/FTO assembly as the counter electrode. CuPc was dissolved in 0.03 mM strength in the gel. Inset shows the corresponding Bode plots (phase angle *versus* frequency).

5.4 Summary

A FRET enabled solar cell, with a ZnS/CdS/ZnS QD assembly flanked to the current collector as the donor, unattached CuPc molecules incorporated in a sulfide ion based gel polymeric electrolyte as acceptors and C-dots tethered electrophoretically to the electrode as electron conduits was implemented. Time resolved luminescence measurements ratified the excited electron deactivation in CdS (encapsulated within ZnS monolayers that serve as energy barriers to direct charge injection) occurs predominantly via energy transfer to CuPc molecules. This was augmented by the fact that the calculated Forster radius matched with the actual separation between CdS and CuPc, and the energy transfer efficiency was 40%. The IPCE performance is improved in nearly the entire visible spectrum for the FRET

enabled cell: ZnS/CdS/ZnS/C-dot/CuPc/S²⁻/MWCNT, relative to the donor only cell: ZnS/CdS/ZnS/S²⁻/MWCNT, due to increased charge separation induced by fast energy transfer to CuPc in the 400-550 nm range corresponding to the donor's absorption, simultaneously accompanied by increased IPCE in the red region (550-650 nm), attributed to the acceptor's absorption. The red photon to current conversion was possible only in the presence of the donor. The impact of C-dots in promoting charge transfer and transport from CuPc to the current collector was reflected in enhanced IPCE, longer electron-oxidized electrolyte species recombination time and higher charge transfer rate achieved for the cells with C-dots compared to the cells without C-dots. The broader spectral utilization, the faster energy transfer rate (as opposed to charge transfer rate) demonstrated in a FRET enabled quasi solid-state solar cell, offers ample opportunities to apply affordable blue/green absorbing donor QDs with red/near infrared absorbing chromophores to similar cells, without the need to drive charge transfer by a cascade mechanism via aligned donors and acceptors.

5.5 References

- [1] Q-L. Zhao, Z-L. Zhang, B-H. Huang, J. Peng, M. Zhang, D-W. Pang, *Chem. Commun.* 2008, 5116-5118.
- [2] P-C. Hsu, Z-Y. Shih, C-H. Lee, H-T. Chang, *Green Chem.* **14** (2012) 917-920.
- [3] X. Sun, Y. Li, *Angew. Chem. Int. Ed.* **43** (2004) 597-601.
- [4] Z. Yu, Q. Zhang, D. Qin, Y. Luo, D. Li, Q. Shen, T. Toyoda, Q. Meng, *Electrochem. Commun.* **12** (2010) 1776-1779.
- [5] S. Buhbut, S. Itzhakov, E. Tauber, M. Shalom, I. Hod, T. Geiger, Y. Garini, D. Oron, A. Zaban, *ACS Nano* **4** (2010) 1293-1298.
- [6] Th. Forster, *Discuss. Faraday Soc.* **27** (1959) 7-17.
- [7] S. Karan, B. Mallik, *J. Phys. Chem. C* **111** (2007) 16734-16741.
- [8] K. Shankar, X. Feng, C. A. Grimes, *ACS Nano* **3** (2009) 788-794.
- [9] J. I. Basham, G. K. Mor, C. A. Grimes, *ACS Nano* **4** (2010) 1253-1258.
- [10] C. X. Guo, H. B. Yang, Z. M. Sheng, Z. S. Lu, Q. L. Song, C. M. Li, *Angew. Chem. Int. Ed.* **49** (2010) 3014-3017.
- [11] B. Farrow, P. V. Kamat, *J. Am. Chem. Soc.* **131** (2009) 11124-11131.
- [12] G. D. Sharma, R. Kumar, S. K. Sharma and M.S. Roy, *Solar Energy Mat Solar Cells.* **90** (2006) 933-942.
- [13] I. V. Lightcap, P. V. Kamat, *J. Am. Chem. Soc.* **134** (2012) 7109-7116.
- [14] L. Etgar, J. Park, C. Barolo, V. Lesnyak, S. K. Panda, P. Quagliotto, S. G. Hickey, Md. K. Nazeeruddin, A. Eychmuller, G. Viscardi, M. Gratzel, *RSC Adv.* **2** (2012) 2748-2752.

Chapter 6

FRET from a Lucifer yellow dye to CdS/CdSe QDs leads to enhanced solar cell performance

6.1 Introduction

In the recent past, FRET has emerged as a very powerful solution as it addresses the primary concern of poor spectral coverage, minimizes the excessive QD quenching by the electrolyte and bypasses the inflexible design requirement of aligned energy levels for the photoanode components.^[1-3] In the previous chapter, electrode tethered QDs as donors and CuPc dissolved in electrolyte as acceptors, were used. In this chapter, the roles of QDs and dye molecules were swapped.

An energy relay donor dye, namely Lucifer yellow (LY), which, to date, had hardly ever been used in a QDSSC, was used. Lucifer yellow has a substantially high molar extinction coefficient ($11194 \text{ M}^{-1} \text{ cm}^{-1}$) and a broad spectral bandwidth ($\Delta\lambda = 110 \text{ nm}$) in the visible region. CdS/CdSe QDs were used as acceptors. The highly luminescent donor (LY) chromophores were unattached to the donor and were dissolved in the electrolyte. In this new design, the LY molecules absorb the high energy photons, undergo excitation and transfer their excitation to the TiO_2 bound CdS/CdSe acceptor QDs. The QDs were disabled from accepting electrons by direct charge injection from LY by means of a wide band gap ZnS interlayer between the $\text{TiO}_2/\text{CdS}/\text{CdSe}$ layers and the electrolyte. A poly(3,4-ethylenedioxythiophene) or PEDOT microfibers' enriched sulfide gel was used as the electrolyte. Earlier, PEDOT films with the conventional granular structure, have been used as iodine/iodide free hole transport layers in in DSSCs.^[4-6] A FRET enabled QDSSC with following configuration was fabricated: $\text{TiO}_2/\text{CdS}/\text{CdSe}/\text{LY}-\text{PEDOT}-\text{S}^{2-}\text{gel}/\text{MWCNT}$. Mechanistic insights in terms of kinetics of energy and electron transfer in this cell which is

capable of complementary light absorption and how effectively this assembly overcomes issues of fast electron recombination and produces photocurrents which are considerably enhanced in comparison to cells with only donor or only acceptor, are provided in this chapter.

6.2 Experimental

6.2.1 Fabrication of photoanode

TiO₂ nanoparticles were prepared by a sol-gel method by dissolving 10 mL of titanium isopropoxide in 40 mL of isopropanol. This mixture was added drop-wise to a solution containing 10 mL of water and 10 mL of isopropanol. The pH of the resulting turbid solution was maintained at 3 with hydrochloric acid and it transformed into a yellow colored translucent gel in 5-10 minutes. The gel was heated at 105 °C for 1 h and upon evaporation of the solvents, a yellow solid was obtained which was calcined at 500 °C for six hours in a furnace in air and a white TiO₂ powder with an anatase crystalline structure was obtained

Na₂SO₃ (0.5 g) and selenium metal powder (0.05 g) were dissolved in ultrapure water (30 mL) and refluxed for 1 h at 80 °C. After 1 h, the black color of selenium disappeared and a clear colorless solution was obtained; an indicator of the formation of sodium selenosulfite. The solution was filtered and the filtrate was used for preparing the CdSe QD shell.

TiO₂ films were deposited over FTO coated glass substrates by using doctor blade technique from a dispersion of 3 g of TiO₂ nanopowder in 15 mL of ethanol. The resulting white colored opaque film was annealed at 450 °C for 3 h. CdS QDs were deposited by chemical bath deposition (CBD) as explained in **Chapter 4**. Three layers of CdS QDs were deposited over TiO₂/FTO. FTO/TiO₂/CdS electrode was immersed in an aqueous solution of Cd(NO₃)₂ (0.5 M) for 5 minutes, rinsed in ultrapure water and dried. The resulting electrode was immersed in an aqueous Na₂SeSO₃ (0.8 M) solution at 50 °C for 1 h, rinsed and dried. Two iterations of this dip-rinse-drying in the cadmium and selenium precursors yielded a two

overlayers of CdSe QDs. The resulting FTO/TiO₂/CdS/CdSe film was dipped in a Zn(NO₃)₂ (0.5 M) solution for 5 minutes and rinsed in ultrapure water and dried, followed by a Na₂S (0.5 M) solution dip, ultra-pure water rinse and drying steps. A ZnS overlayer was obtained which serves as a protective barrier and prevents the decomposition of CdS/CdSe QDs in presence of the sodium sulfide electrolyte. The FTO/TiO₂/CdS/CdSe/ZnS electrode was used as the photoanode in QDSSCs.

6.2.2. Synthesis of PEDOT microfibers

PEDOT microfibers were prepared by using a previously reported surfactant assisted method.^[7] A reverse micro-emulsion was first synthesized by dissolving dioctyl sulfosuccinate sodium salt (AOT, 19.12 mmol) in 70 mL of n-hexane. A solution of FeCl₃ (10 mmol) in 1 mL of water was added to the AOT solution. The resulting orange colored solution was magnetically stirred at 25 °C for 5 minutes and EDOT monomer (3.52 mmol) was added. After 3 h of gentle stirring, a blue colored precipitate of PEDOT microfibers was obtained. The deep blue precipitate was filtered and washed with methanol and acetonitrile and dried at 80 °C in vacuum for 12 h.

6.2.3 Synthesis of gel electrolyte

A gel polymeric electrolyte was prepared according to a method reported in literature,^[8] which was described briefly in Chapter 5. For preparing the PEDOT microfiber enriched gel, PEDOT microfibers (2 mg) were introduced into the solution alongwith ammonium persulfate and the solution was sonicated for 10 minutes prior to the heating step. The xerogel (either with or without PEDOT microfibers) was soaked in an aqueous solution of Na₂S (0.1 M) for 12 h and the xerogel transformed into a transparent gel upon uptake of the S²⁻ solution. The electrolyte is a self-supporting, transparent gel; colorless when only S²⁻ ions were present and blue in color when both PEDOT microfibers and S²⁻ ions are present. The donor or LY dye based gel polymeric electrolyte was synthesized by employing the same

above-mentioned procedure, except for a variation in the last step, wherein the xerogel was soaked in an aqueous yellow colored LY dye (1.5 mg mL^{-1}) and Na_2S (0.1 M) solution such that eventually a transparent yellow colored gel was obtained (without PEDOT microfibers) and the gel was blue (with PEDOT microfibers). Quasi solid-state QDSSC was fabricated as described in the previous chapter. MWCNTs were employed as counter electrode. Synthesis and fabrication of CE was described in **Chapter 5**.

6.3 Results and discussion

6.3.1 Characterization of TiO_2

The d-values observed for synthesized TiO_2 powder, match well with the body centered tetragonal crystal structure of TiO_2 (anatase) in accordance with the PDF file number 894921. The HRTEM lattice scale image of TiO_2 is shown (**Figure 6.1b**). The interplanar separation is observed to be 0.36 nm which, agrees well with the d-spacing of 0.351 nm corresponding to the $\langle 101 \rangle$ reflection of the anatase phase. This result is in line with the XRD pattern wherein, the most intense peak also corresponds to the $\langle 101 \rangle$ plane.

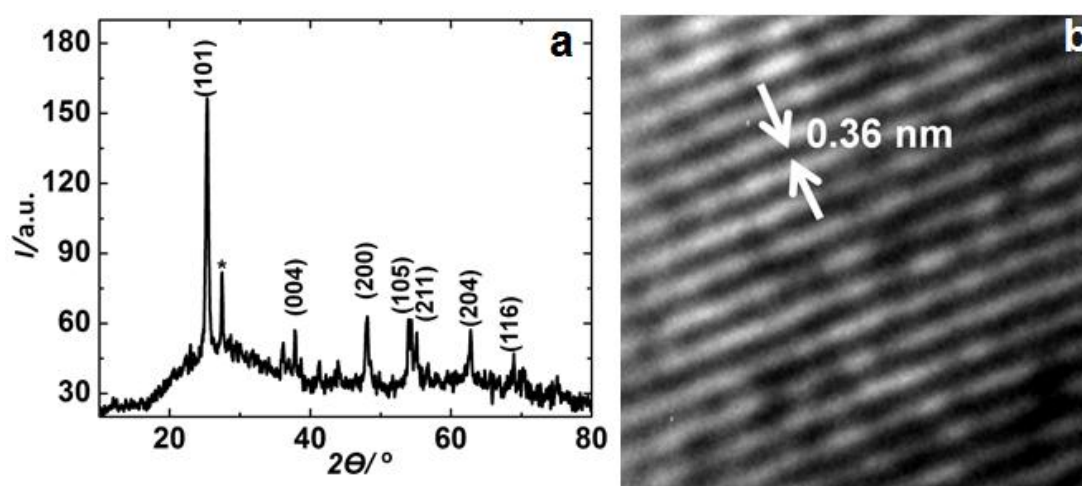


Figure 6.1: (a) X-ray diffractogram of TiO_2 nanoparticles, the hkl values are expressed within parentheses and (b) Lattice scale image of TiO_2 .

6.3.2 HRTEM analyses

The CdS layers were porous and therefore permitted the percolation of $\text{Cd}(\text{NO}_3)_2$ salt solution and its adsorption directly onto the CdS QDs. Further on exposure to the Na_2SeSO_3 solution, CdSe QDs are formed *in-situ* around the CdS QDs, thus mimicking core/shell architectures of CdS/CdSe QDs. Since, no organic linkers or capping agents were used, intimate nanoscale contact could be achieved between the two QDs. The low magnification TEM image of CdS/CdSe QDs showed the QDs to be aggregated and distinctive grain boundaries were not perceptible (panel A in **Figure 6.2a**). However, the HRTEM image of the CdS/CdSe QDs showed the lattice fringes from the core (CdS) to be encapsulated by fringes from the shell (CdSe) (**Figure 6.2b**). The image contrast in panel B clearly distinguished the lighter CdS core from the darker CdSe shell. Panels C and D reveal the enlarged views of lattice scale images extracted from **Figure 6.2b**, and the fringe separation was observed to be 0.33 nm in C and it concurs well with an interplanar separation of 0.34 nm corresponding to the $\langle 111 \rangle$ plane of the fcc lattice of CdS (PDF: 65287). Similarly, the interplanar spacing was observed to be 0.30 nm in D, which matches with the $\langle 200 \rangle$ orientation of the fcc structure of CdSe (PDF: 882346). Several images of CdS/CdSe QDs from different regions of the same sample were recorded, and the images were always composed of criss-cross fringes indicating that the samples were crystalline.

However, the lattice scale image of CdS/CdSe QDs with a monolayer of ZnS followed by an overlayer of LY dye (**Figure 6.2c**) revealed the co-existence of amorphous domains (encircled by solid lines) with crystalline regions (encircled by dashed lines). Since none of the images obtained for CdS/CdSe QDs revealed the presence of any amorphous structures, these amorphous domains are attributed to the LY dye and the crystalline domains to CdS/CdSe QDs. Therefore, the separation between the amorphous and crystalline domains can be treated as the actual distance between the LY donor dye and the CdS/CdSe acceptor

QDs. It is evident from the figure, that the separation never exceeds 5 nm, which is in fact close to the Forster radius (determined spectroscopically later). Since this value is within the realm of FRET distance (1-10 nm), it was concluded that FRET is possible from the LY dye to the CdS/CdSe QD system.

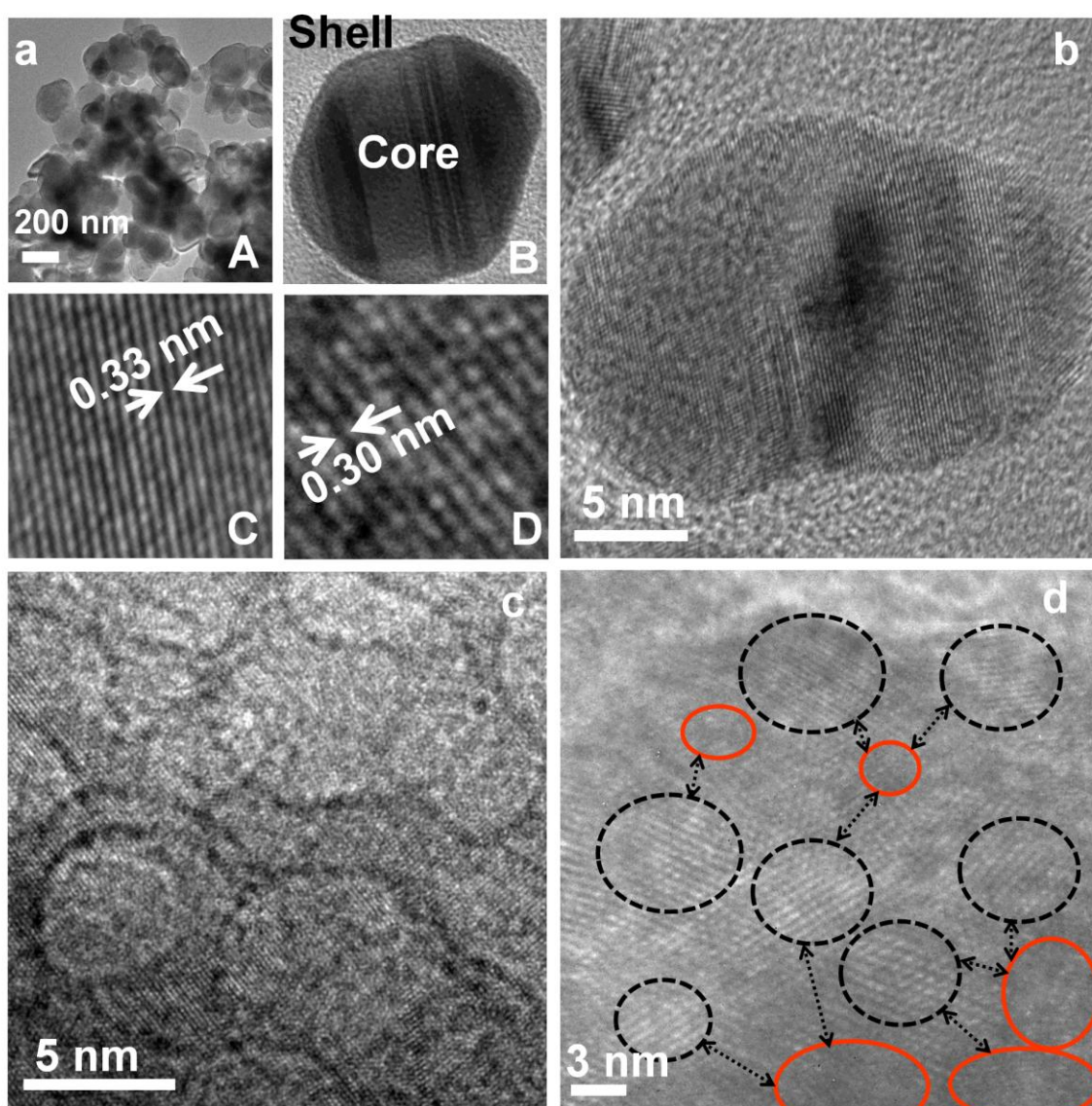


Figure 6.2: HRTEM images of (a) (A) aggregated CdS/CdSe QDs, (B) image contrast distinguishes the core from the shell, (C) enlarged views of interplanar separations that prevail in CdS core QDs and (D) CdSe shell, (b) a lattice scale image of core/shell CdS/CdSe QDs and (c) lattice scale image of the CdS/CdSe QDs with an LY dye overlayer, where the crystalline QDs and the dye are encircled in dashed (----) and solid (—) ellipses respectively.

6.3.3 Energetics of the FRET cell

The CdS/CdSe QDs were deposited by CBD technique on a TiO₂ coated transparent conducting electrode. The LY dye was dissolved in the aqueous sulfide ion electrolyte and functioned as donor or the energy relay dye. The QDs tethered to the TiO₂ electrode functioned as acceptors. The CB of CdS and CdSe lie at -1.0 V and -1.2 V (*versus* NHE) respectively and these positions are 0.589 and 0.789 V more negative relative to the CB edge of the donor and the LY dye, is poised at -0.411 V (*versus* NHE) (the latter position determined from the cyclic voltammogram of the pristine LY dye, **Figure 6.4b**). The energy band offsets between LY and the CdS/CdSe QDs render electron injection upon photo-excitation from the CB of LY dye to the CB of CdS/CdSe QDs thermodynamically unfavorable (**Figure 6.3**). Further, a monolayer of ZnS was deposited over the CdS/CdSe QDs, and since the CB of ZnS lies at -1.6 V (*versus* NHE), it acts as a barrier and prevents direct charge injection from the donor (in the electrolyte) to the CdS/CdSe QDs or titania electrode. As a consequence, the only available pathway for the photo-excited electron deactivation in the LY dye is via FRET, whereby it transfers the excitation energy non-radiatively to the CdS/CdSe QDs. Electrons in the VBs of CdS/CdSe QDs are promoted to their corresponding CBs and then transferred to the CB of TiO₂ by cascade and subsequently to the current collector.

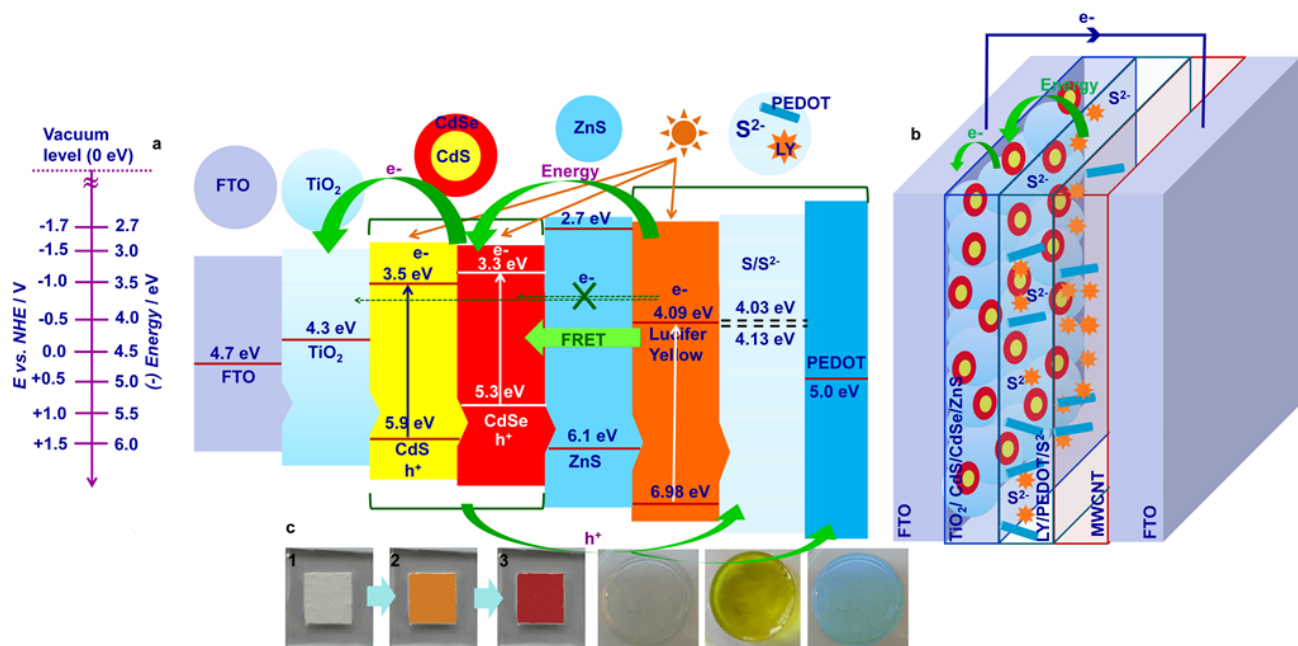


Figure 6.3: (a) Energy levels of a $\text{TiO}_2/\text{CdS}/\text{CdSe}/\text{ZnS-LY}/\text{PEDOT}/\text{S}^{2-}$ assembly, illustrating possible modes for energy, electron and hole transfer, (b) schematic of a $\text{TiO}_2/\text{CdS}/\text{CdSe}/\text{ZnS-LY}/\text{PEDOT}/\text{S}^{2-}$ -MWCNT cell and (c) From left to right, (1) TiO_2 , (2) TiO_2/CdS , (3) $\text{TiO}_2/\text{CdS}/\text{CdSe}/\text{ZnS}$ electrodes and the S^{2-} gel, LY dye/ S^{2-} gel and the LY/PEDOT microfibers/ S^{2-} gel.

6.3.4 Structure and CV of LY dye

The reduction potential of the LY dye is at ~ -0.608 V from **Figure 6.4b**. The potential of the reference electrode is $+0.197$ V. Therefore, $E_{\text{Red}} (\text{versus NHE}) = -0.608 - (+0.197)$ V $= -0.411$ V. The reduction potential of -0.411 V (*versus* NHE) corresponds to the CB position of 4.08 eV for the LY dye. The band gap of LY dye obtained from the optical absorption spectrum is 2.88 eV. Therefore the position of VB is 6.96 eV ($E_g = E_{\text{VB}} - E_{\text{CB}}$).

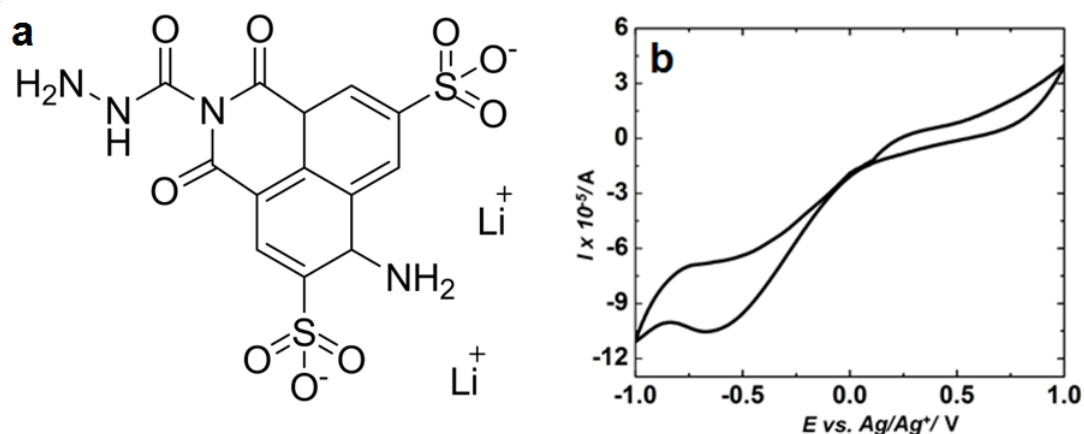


Figure 6.4: (a) Structure of LY dye and (b) cyclic voltammogram of an aqueous solution of a LY dye with two Pt rods as the working and counter electrodes and Ag/AgCl/KCl as a reference electrode.

6.3.5 Emission analysis

The choice of LY as the donor, was based on its extremely large photoluminescence quantum efficiency and a strong and narrow, high energy absorption spectrum with a λ_{max} at 430 nm and spanning between 365 to 475 nm. The absorption and luminescence of the LY dye are shown in **Figure 6.5 a**. The LY dye shows a band edge emission peak at 533 nm upon excitation at 430 nm. **Figure 6.5 b** reveals that the broad absorption the CdS/CdSe QDs spanning from 507 to 586 nm is almost completely encompassed within the emission profile of the LY dye which lies between 475 to 650 nm. Such a heavy overlap of the absorption and emission spectra of the donor and acceptor makes FRET a viable phenomenon in this cell architecture. Since FRET involves the transfer of donor excitation to the neighboring acceptor molecules in a non-radiative fashion, other pertinent evidences for FRET include luminescence quenching of the donor in presence of the acceptor and lifetime decrement.

The strong emission of the LY (with λ_{em} at 533 nm) was quenched drastically upon introducing the TiO₂/CdS/CdSe/ZnS film in the aqueous LY dye solution (**Figure 6.5c**). The film was composed of 3 layers of CdS, 1 layer of CdSe and 1 layer of ZnS. The emission intensity of LY was quenched by ~ 4.9 times of its original value. Upon employing a QD

film with more layers of CdSe (CdS:3, CdSe:2 and ZnS:1), the emission intensity was quenched by ~100 times. This composition was used for further studies. Another indirect evidence for FRET was observed by monitoring the emission of ZnS/CdSe/CdS (donor QDs tethered to TiO₂ film) in the presence of LY dye, by exciting with a different wavelength ($\lambda_{\text{ex}} = 370$ nm). The pristine ZnS/CdSe/CdS QDs did not show any emission peak when excited at 430 nm, which was the excitation wavelength of the LY dye.

The emission spectra of a TiO₂/CdS/CdSe/ZnS film alone and the same film in a LY solution, with $\lambda_{\text{ex}} = 370$ nm, is shown in **Figure 6.5d**. The band edge emission peak for pristine CdSe/CdS QDs (acceptor in the absence of donor) is observed at 603 nm, and in the presence of the donor, the LY dye, the intensity of this peak is amplified by 1.5 fold times, indicative of an interactive energy transfer from the LY dye to the CdS/CdSe QDs. The emission spectrum of the TiO₂/CdS/CdSe/ZnS–LY system (obtained at an excitation wavelength of 370 nm) comprises of two components, which were deconvoluted. The emission peak at 530 nm corresponds to LY dye's emission and the peak at 603 nm corresponds to the emission of CdS/CdSe QDs increased by the LY dye. A similar enhancement in the emission peak intensity of the acceptor (squaraine dye) was achieved in the presence of CdSe donor QDs and authors correlated the increment in acceptor's emission to efficient energy transfer from CdSe to squaraine dye in their FRET cell.^[9] FRET induces an increased charge separation in the acceptor, as the LY dye absorbs the photons which pristine CdS/CdSe QDs are insensitive to and transfers its excitation to the CdS/CdSe QDs. The emission enhancement observed for CdS/CdSe QDs is solely by energy transfer.

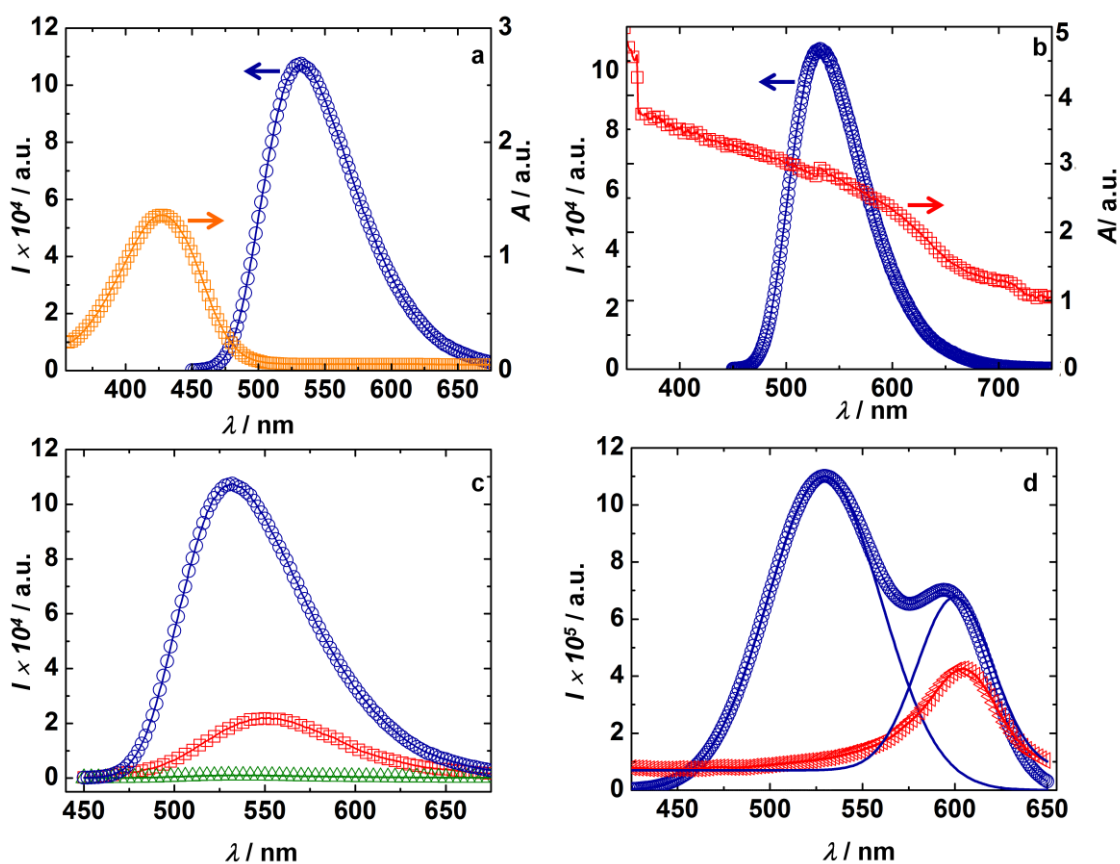


Figure 6.5: (a) Absorption (\square) and fluorescence (\circ) spectra of the LY donor dye (1.5 mg mL^{-1} , $\lambda_{\text{ex}} = 430 \text{ nm}$), (b) overlap of absorption (\square) of the acceptor: $\text{TiO}_2/\text{CdS}/\text{CdSe}/\text{ZnS}$ electrode and and emission (\circ) of the donor (LY dye) (at $\lambda_{\text{ex}} = 430 \text{ nm}$) respectively, (c) fluorescence quenching of LY dye (\circ) in the presence of $\text{TiO}_2/\text{CdS}/\text{CdSe}/\text{ZnS}$ electrode, with 3:1 (\square) and 3:2 (\triangle) layers of CdS:CdSe QDs ($\lambda_{\text{ex}} = 430 \text{ nm}$), (d) emission of pristine $\text{TiO}_2/\text{CdS}/\text{CdSe}/\text{ZnS}$ electrode composed of 3:2 layers of CdS:CdSe QDs (\triangle) and for the same electrode in the presence of 1.5 mg mL^{-1} LY dye (\circ) ($\lambda_{\text{ex}} = 370 \text{ nm}$). The symbol (\circ) represents the raw data in (d), and the solid lines represent the deconvoluted fits. ZnS, in all experiments, was deposited as a monolayer.

6.3.6 Time-resolved emission decay

To confirm that sequential energy transfer from LY to the CdS/CdSe QDs followed by electron transfer to TiO_2 will be the dominant processes when employed in a solar cell, fluorescence lifetimes for different assemblies were measured and these decay profiles are shown in **Figure 6.6**. All the time resolved fluorescence decay signals in this study were

fitted to a bi exponential function, except the LY dye. The dye exhibited a single exponential decay. In equation (1), I is the normalized emission intensity, t is the time after LED excitation, A_1 , A_2 are the amplitude coefficients and τ_1 , τ_2 are the decay time constants. The results of the fitting are collated in **Table 6.1**. The average lifetime of the transient electron was determined by using equation (1).

$$I = A_1 \exp(-t/\tau_1) + A_2 \exp(-t/\tau_2) \quad (1)$$

$$\langle \tau \rangle = \frac{\sum_i (A_i \tau_i)}{\sum_i A_i} \quad (2)$$

The pristine LY dye showed an excited electron lifetime of 5.07 ns, obtained at an excitation wavelength of 450 nm which concurs well with a previously reported lifetime of 5 ns for the same dye.^[10] Upon incorporation of a TiO₂/CdS/CdSe/ZnS film in the LY dye solution, the average lifetime of the photo-generated electron in the CB of the LY dye reduced to 3.02 ns, at the same excitation wavelength. The decreased lifetime is a clear indicator of energy transfer. Since energy transfer rate is faster than charge transfer and band-edge recombination rates, the fast decay component of 0.19 ns is ascribed to energy transfer from the LY dye to the CdS/CdSe QDs. The slow decay component of 3.77 ns is assigned to the band-edge recombination in LY dye. The rate constant (K_{ET}) of energy transfer was deduced from the lifetime analysis and it is $5.29 \times 10^9 \text{ s}^{-1}$. It must be recalled that direct electron injection from LY to CdS/CdSe QDs is inhibited by the ZnS energy barrier layer and also by the unfavorable CB positions. Electron transfer from the LY dye to TiO₂ is inhibited by the CdS/CdSe QDs which pose as a physical barrier. As a consequence, excited electron decay mode is by FRET, and to confirm that electrons in CdS/CdSe QDs, excited by absorption of indirect photons are injected into TiO₂, the average lifetime of pristine TiO₂/CdS/CdSe/ZnS electrode was measured at an excitation wavelength of 370 nm and it was found to be 5.83 ns. The short lived component of 3.92 ns was attributed to direct electron injection from CdS/CdSe QDs into TiO₂ or FTO and the long lived component of

15.60 ns was attributed to electron-hole recombination in the QDs. The average electron lifetime in the same assembly, when measured in the presence of the LY dye solution, at the same excitation wavelength of CdS/CdSe QDs (i.e., 370 nm) increased to 7.39 ns from 5.03 ns. This increase in the acceptor's lifetime in the presence of donor matches with the increment in emission of the acceptor in the presence of donor. Electron excitation in CdS/CdSe QDs by indirect photon absorption of the donor LY dye will be slower than excitation by direct photon absorption (as observed in the absence of LY dye). In the presence of the donor, two processes occur, one is electron transfer to TiO₂, by direct photon absorption and the second one is ascribed to electron injection from CdS/CdSe QDs to TiO₂ after excitation energy transfer from the LY dye to the QDs. In a previous work, Etgar et.al, also reported the increase in lifetime of the acceptor squaraine dye in presence of CdSe QD i.e., the donor moiety, which matches with our observation.^[9] Fast and efficient energy transfer from the LY dye to the CdS/CdSe QDs ensues in simultaneous decrease in the lifetime of LY dye donor molecules in presence of the CdS/CdSe QD acceptors and increase in lifetime of the QD acceptors in presence of the dye donors. Since the excitation wavelengths which lead to distinctive emission spectra are different for both donor and acceptor, lifetime analysis could be done separately.

Table 6.1: Kinetic parameters of emission decay analysis for different systems deduced from bi-exponential fits.^a

System composition	λ_{ex} (nm)	λ_{em} (nm)	χ^2	τ_1 (ns)	τ_2 (ns)	A ₁	A ₂	$\langle\tau\rangle$ (ns)
LY dye – TiO ₂ /CdS/CdSe/ZnS	450	530	0.911	0.19	3.77	19.92	80.08	3.02
TiO ₂ /CdS/CdSe/ZnS – LY dye	370	603	1.034	0.31	19.29	62.66	37.34	7.39
TiO ₂ /CdS/CdSe/ZnS	370	603	1.000	3.92	15.60	83.33	16.67	5.83
TiO ₂ /CdS/CdSe/ZnS – PEDOT	370	603	1.067	0.26	5.43	7.94	92.06	5.03

^aA is the relative amplitude of each lifetime, τ_1 and τ_2 are the components of fluorescence lifetime and χ^2 denotes the fit quality. The LY dye and PEDOT were dissolved in water and the TiO₂/CdS/CdSe/ZnS assembly was a solid electrode.

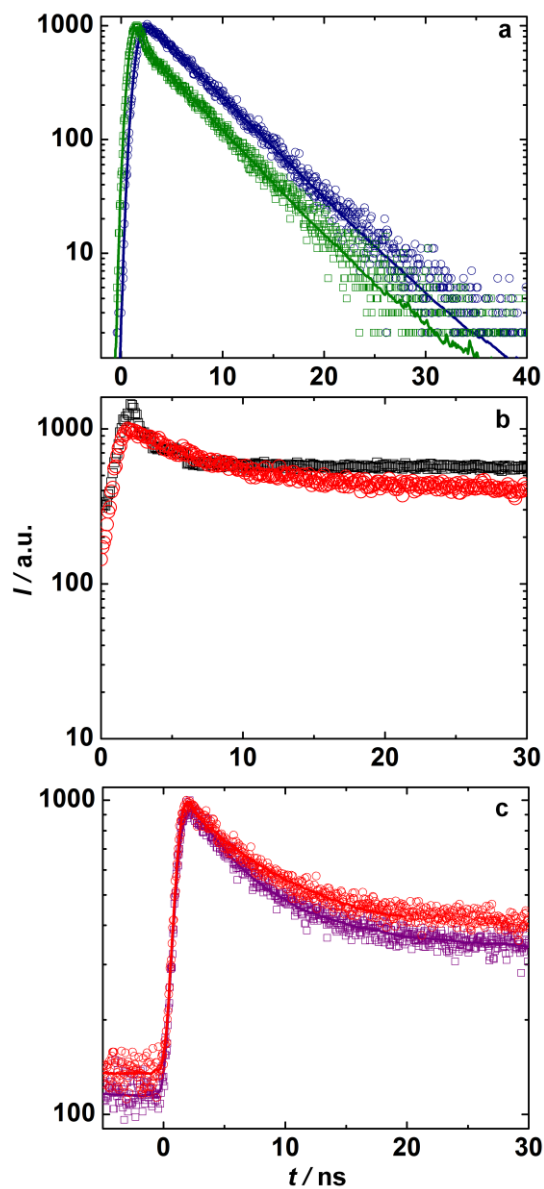


Figure 6.6: Time resolved fluorescence decay traces of (a) Lucifer yellow dye alone (1.5 mg mL^{-1}) (O) and in the presence of TiO₂/CdS/CdSe/ZnS electrode (□) with 3:2 layers of CdS:CdSe QDs ($\lambda_{\text{ex}} = 450 \text{ nm}$ and $\lambda_{\text{em}} = 530 \text{ nm}$), (b) CdS/CdSe/ZnS electrode with 3:2 layers of CdS:CdSe QDs, measured at the excitation and emission wavelength of QDs ($\lambda_{\text{ex}} = 370 \text{ nm}$ and $\lambda_{\text{em}} = 600 \text{ nm}$) alone (O) and in the presence of the 1.5 mg mL^{-1} LY dye solution (□) and (c) sole TiO₂ CdS/CdSe/ZnS electrode with 3:2 layers of CdS:CdSe QDs (O) and in the presence of an aqueous solution of PEDOT microfibers (□) ($\lambda_{\text{ex}} = 370 \text{ nm}$ and $\lambda_{\text{em}} = 603 \text{ nm}$).

6.3.7 Electrolyte modification

In addition to using FRET to maximize spectral coverage for the solar cell fabricated herein, the sulfide ion electrolyte was also modified by dispersing hole-conducting PEDOT microfibers in the gel. In the past, Fukuri et al., successfully demonstrated the enhanced performance of a DSSC by replacing the iodine/tri-iodide electrolyte with a PEDOT based hole transport polymeric film.^[8] To affirm that the PEDOT microfibers ameliorate the hole-scavenging capability of the sulfide ion electrolyte in a solar cell, the emission and decay profiles for the TiO₂/CdS/CdSe/ZnS electrode in the presence of an aqueous solution of PEDOT microfibers ($\lambda_{\text{ex}} = 370$ nm and $\lambda_{\text{em}} = 600$ nm) were measured (**Figure 6.6 c**). One criterion for hole transfer is that the CB level for the hole provider should be more positive (*versus* NHE) in comparison to the hole acceptor. The redox potential of S_n²⁻/S²⁻ couple lies at -0.47 V (*versus* NHE) and the work function of PEDOT is poised at $+0.5$ V.^[11] Since these positions are more negative relative to the VB levels of $+1.4$ and $+0.8$ V (*versus* NHE) of CdS and CdSe QDs in the quasi-core/shell structures, hole propagation from the QDs to PEDOT microfibers and S²⁻ is feasible. The band-edge emission of CdS/CdSe QDs at 603 nm is quenched by 1.3 times in the presence of PEDOT microfibers, indicating that holes are transported from the valence bands of CdS/CdSe QDs to the PEDOT microfibers and the contribution of PEDOT microfibers was ascertained from lifetime data. Here, the CdS/CdSe QDs showed an excited state life time of 5.83 ns. This lifetime reduced to 5.03 ns in the aqueous solution of PEDOT microfibers, indicating that holes are transported from the VB of CdS/CdSe QDs more efficiently to the PEDOT microfibers.



6.3.8 Forster radius and energy transfer rate

Forster radius (R_o), mainly depends upon the PL quantum yield of the donor (the LY dye, herein), the extent of overlap between the emission of the donor (the LY dye) and the absorption of the acceptor (the CdS/CdSe QDs). R_o was calculated from the equation provided below.^[12]

$$R_o^6 = 9000 \ln(10) k^2 Q_D J / 128 \pi^5 n^4 N_A \quad (5)$$

In equation (5), Q_D is the fluorescence quantum yield of the donor in the absence of the acceptor, and it was determined to 0.3 which was experimentally calculated by employing Rhodamine 6G as the standard. k^2 is the dipole orientation factor and the magnitude was assumed to be $2/3$,^[13] N_A is the Avogadro's number and n is the refractive index of the medium. All parameters, except k^2 in equations 5, 6 and 7 were determined experimentally. An aqueous solution of the LY dye and 0.1 M Na_2S were employed as the medium and the refractive index was ~ 1.38 from reflection measurements. J , the spectral overlap integral was calculated from the following expression.

$$J = \int_0^\infty F_D(\lambda) \epsilon_A(\lambda) \lambda^4 d\lambda \quad (6)$$

F_D is the donor fluorescence intensity normalized to unit area (in arbitrary units) and ϵ_A is the extinction coefficient of the acceptor ($66815 \text{ M}^{-1} \text{ cm}^{-1}$). The spectral integral (J) for the LY/CdS/CdSe system was deduced to be $\sim 4.83 \times 10^{15}$ and the resulting Forster radius (R_o) was 5.29 nm. Since this value of R_o falls within the limits of acceptable distance for effective FRET interaction, energy transfer is viable from the LY dye to the CdS/CdSe QDs.

FRET rate (K_{ET}) for energy transfer was calculated from the equation provided below.

$$K_{ET}(r) = 1/\tau_D (R_o/r)^6 \quad (7)$$

In equation (7), τ_D is the excited state lifetime of the donor (LY dye) in the absence of the acceptor (CdS/CdSe QDs). Higher the FRET rate, faster will be the energy transfer from the LY dye to the CdS/CdSe QDs. The rate constant for the energy transfer from LY to CdS/CdSe QD is $5.29 \times 10^9 \text{ s}^{-1}$. Efficiency of the energy transfer, E was calculated from the

fluorescence lifetime of the donor in presence and absence of the acceptor by using the following equation.

$$E = 1 - \tau_{DA}/\tau_D \quad (8)$$

The LY dye showed an energy transfer efficiency of ~ 40% to CdS/CdSe QDs. Buhbut and coworkers reported an energy transfer efficiency of 44% for tunneling energy from a CdS/CdSe/ZnS QD assembly to a symmetrical squaraine dye.^[13]

6.3.9 Conduction via PEDOT microfibers

The SEM image of PEDOT microfibers is shown in **Figure 6.7a**. The image showed the microfibers to be bundled together, with lengths varying between 1 and 1.5 μm . These elongated fibrillar shapes are interconnected, which is advantageous, as charges can propagate unhindered across the electrolyte through the interlinked fibers, subsequent to the photo-excitation of the photoanode and reduction of PEDOT at the cathode. This reduced neutral polymer can diffuse through the sulfide ion electrolyte and undergo oxidation at the anode and thus re-generate the electron in the VB of the acceptor (or CdS/CdSe QDs). Since a decrease in the electron lifetime in CdS/CdSe QDs, was observed in the presence of PEDOT microfibers, it is obvious that PEDOT contributes to improving the overall charge transport capability of the electrolyte. The electronic conductivity of PEDOT microfibers was found to be 0.5 S cm^{-1} from I-V measurement, which agrees well with a reported value of 0.1 S cm^{-1} for PEDOT doped with poly(styrene sulfonate) or PSS.^[14] The hole transport capability of PEDOT galvanizes electron regeneration in the QDs. The work function of PEDOT is thermodynamically favorable for accepting holes from the VBs of CdS and CdSe QDs, after excitation. The possibility of hole transfer from LY to S^{2-} or PEDOT is ruled out, since the holes created upon photo-excitation of the donor cease to exist after excitation transfer to the acceptor (CdS/CdSe QDs).

The CV plots of an aqueous 0.1 M Na₂S solution and for the same solution with PEDOT microfibers dispersed therein, were recorded between two Pt electrodes and an Ag/AgCl/KCl electrode as reference (**Figure 6.7 b**). The CV plot of the pristine S²⁻ electrolyte shows a broad oxidation peak at +0.59 V (or E_{red} = -0.59 V *versus* Ag/Ag⁺) which corresponds to -0.393 V (*versus* NHE). This oxidation peak shifts to more positive potentials, in the presence of PEDOT microfibers and it is observed at +0.67 V (*versus* Ag/Ag⁺) which corresponds to -0.473 V (E_{red} *versus* NHE). On the energy scale, pristine S²⁻, is therefore poised at 4.107 eV and in the presence of PEDOT, this level shifts to 4.027 eV. The change in the redox potential of S²⁻ impacts the V_{OC} of the QDSSC. The V_{OC} of the cell is the difference between the CB of TiO₂ and the redox potential of the electrolyte. For cells containing PEDOT, such as TiO₂/CdS/CdSe/ZnS-LY/PEDOT/S²⁻-MWCNT, the V_{OC} was found to be 716 mV and for the same cell without PEDOT, the V_{OC} was higher; it was 721 mV. While the CB position of TiO₂ remains unchanged, the shift in the redox potential of S²⁻ to more negative potentials (*versus* NHE), in the presence of PEDOT, is responsible for the observed slight lowering of V_{OC} in the cell with PEDOT microfibers dispersed in the electrolyte.

The Nyquist plots (Z'' *versus* Z') for a 0.1 M Na₂S solution, and for a 0.1 M Na₂S/PEDOT microfiber solution recorded between two Pt electrodes are shown in **Figure 6.7 c**. The high frequency regions of the Z'' *versus* Z' curves reveal an incomplete arc in both cases and the point of intersection of the first arc with the real component of impedance is 34 Ω for the S²⁻ electrolyte and 38 Ω for the PEDOT/S²⁻ electrolyte. This value is a measure of the bulk resistance offered by the electrolyte. In the low frequency domain, the behavior of the cell with PEDOT/S²⁻ solution is resistive whereas the response is capacitive for the cell with pristine S²⁻ solution. The impedance data was fitted in a RCR circuit with solution resistance (R_s), charge transfer resistance (R_{CT}) and double layer capacitance (C_{dl}) as the circuit

components. R_{CT} for charge transfer at the Pt/PEDOT/S²⁻ solution interface was found to be 5.2 times lesser than that of the Pt/S²⁻ interface, indicating that PEDOT microfibers improve the charge conduction capability the S²⁻ solution. The benefit of this improved conduction ability was clearly reflected in the increased photocurrent produced by the cell with PEDOT relative to the one without PEDOT, as J_{SC} enhanced by 1.08 times by incorporation of PEDOT in the sulfide electrolyte.

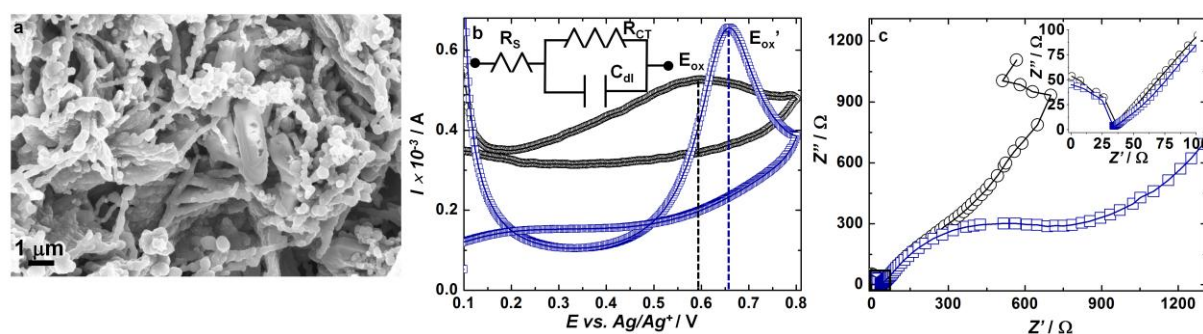


Figure 6.7: (a) SEM micrograph of PEDOT microfibers, (b) cyclic voltammograms of a PEDOT microfibers/S²⁻ solution (□) and a sole S²⁻ solution (○), measured between two Pt electrodes, at a scan rate of 10 mV s⁻¹ and (c) Nyquist plots of a PEDOT microfibers/S²⁻ solution (○) and a sole S²⁻ solution (□), measured between two Pt electrodes, over a frequency range of 10⁶ to 10² Hz and under an ac signal of 10 mV. Inset of (b) is the equivalent circuit used for fitting the data in (c) and inset of (c) is a magnified view of the high frequency region.

6.3.10 Solar cell performance

To quantify the effect of FRET on the solar cell performance metrics, quasi solid state QDSSCs were constructed with the following configuration: FTO/TiO₂/CdS/CdSe/ZnS as the photoanode, S²⁻ based polyacrylamide gel (enriched with or without PEDOT microfibers) as the electrolyte with the LY dye dissolved therein and functionalized multiwalled carbon nanotubes (MWCNTs) deposited on FTO coated glass as the counter electrode. The gel was composed of 0.1 M Na₂S and 1.5 mg mL⁻¹ of the LY dye. IPCE performances of the cells are shown in the **Figure 6.8**. The acceptor (CdS/CdSe QDs) alone cell (TiO₂/CdS/CdSe/ZnS–S²⁻–MWCNT) shows a maximum IPCE of 30% at 530 nm, which matches with the absorption

spectrum of the CdS/CdSe/ZnS QD film. While the LY dye absorbs strongly at 430 nm but this donor alone cell ($\text{TiO}_2\text{-LY/S}^{2-}\text{-MWCNT}$) yielded a very poor maximum IPCE value of 0.009% (at 530 nm). The reason for the dismal performance of the donor (LY dye) only cell is probably inefficient charge transfer to TiO_2 upon excitation. However, when the donor-acceptor architecture was used in the QDSSC: $\text{TiO}_2/\text{CdS}/\text{CdSe}/\text{ZnS}\text{-LY/S}^{2-}\text{-MWCNT}$, a substantial increase in the IPCE response was attained in the entire spectral region of 350 – 650 nm, with a maximum IPCE of 53 % at 530 nm. This increment affirms the effectiveness of FRET (vis-à-vis energy transfer from the dye to the QDs) in greatly enhancing the performance of this QDSSC. In this FRET enabled QDSSC, in addition to the electrons generated by the direct absorption of photons by the CdS/CdSe QDs, more electrons-hole pairs are produced by indirect absorption of photons in the same QD assembly upon energy transfer from the LY dye.

Sarkar et al., reported an increased photocurrent for a ZnO/Dye/CdTe assembly compared to the acceptor alone device in the entire spectral region due to additional photo generated charge carriers from N719 dye.^[15] Similarly Buhbut et al., reported a maximum IPCE of about 10% achieved in the blue region for a FRET enabled cell, with CdS/CdSe/ZnS QDs as the donor and a squaraine dye as the acceptor.^[13] The donor concentration in the electrolyte was optimized on the basis of maximum IPCE, for the QDSSCs based on the following assembly $\text{TiO}_2/\text{CdS}/\text{CdSe}/\text{ZnS}\text{-LY/S}^{2-}\text{-MWCNT}$. Whilst maintaining all other components at fixed compositions, only the LY dye concentration in the electrolyte was varied from 0.5 to 2 mg mL⁻¹ successively in small steps and the IPCE of the cell was measured at each step (**Figure 6.8a**). From the IPCE response, the optimum concentration of the donor or the LY dye was fixed at 1.5 mg mL⁻¹, as IPCE is 53% at this concentration and it decreases to 46% at higher donor content. At high donor concentrations, the quantum yield of the donor decreases due to concentration quenching. The CBs of CdS and CdSe lie at 3.5

and 3.3 eV and the LUMO of the LY dye lies at ~ 4.09 eV. Since the LUMO of the LY dye lies below the CB of the QDs, the injection of excited electrons from the LUMO of dye to the QDs is energetically impossible. The only plausible mechanism which is operative in this donor-acceptor cell and manifests in enhanced photovoltaic response is energy transfer.

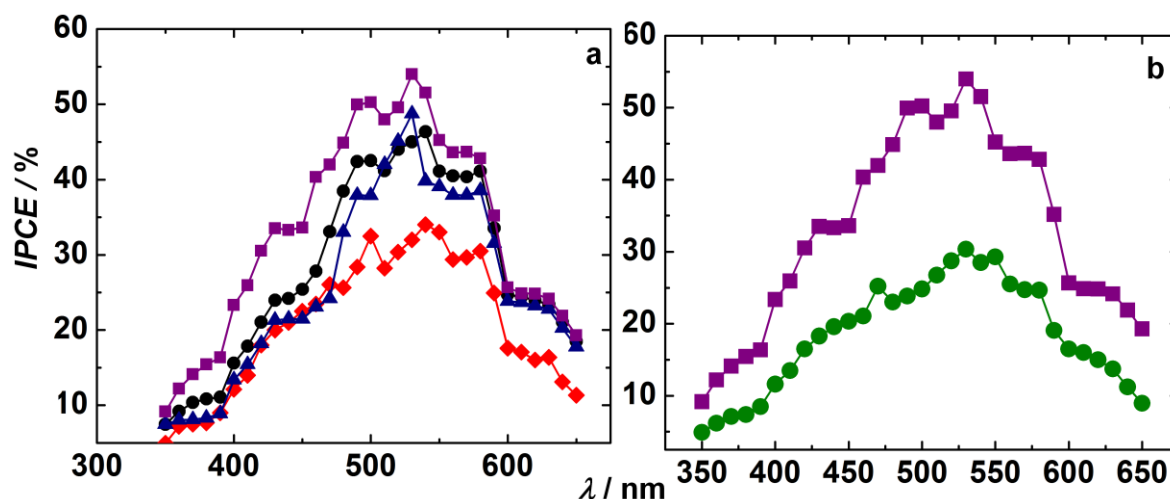


Figure 6.8: IPCE spectra of quasi solid-state QDSSCs: (a) the $\text{TiO}_2/\text{CdS}/\text{CdSe}/\text{ZnS-LY}/\text{S}^{2-}$ cell with 0.5 (\blacklozenge), 1 (\blacktriangle), 1.5 (\blacksquare) and 2 (\bullet) mg mL^{-1} Lucifer yellow dye, (b) the donor-acceptor $\text{TiO}_2/\text{CdS}/\text{CdSe}/\text{ZnS-LY}/\text{S}^{2-}$ cell with optimized 1.5 mg mL^{-1} LY dye concentration (\blacksquare), the acceptor only $\text{TiO}_2/\text{CdS}/\text{CdSe}/\text{ZnS-S}^{2-}$ (\bullet) cell. A poly(acrylamide) gel containing 0.1 M Na_2S was employed as the electrolyte and a MWCNT/FTO assembly was used as a counter electrode. PEDOT and LY dye in the gels were 2 and 1.5 mg mL^{-1} respectively.

The J-V characteristics of quasi-solid state QDSSCs with different electrolyte compositions were measured and the cell parameters are summarized in **Table 6.2**. The acceptor alone cell ($\text{TiO}_2/\text{CdS}/\text{CdSe}/\text{ZnS-S}^{2-}$ -MWCNT) produced a V_{oc} of 657 mV whereas the donor-acceptor cell ($\text{TiO}_2/\text{CdS}/\text{CdSe}/\text{ZnS-LY}/\text{S}^{2-}$ -MWCNT) showed a V_{oc} of 721 mV which was ~ 1.09 times higher than that of the acceptor alone cell. This implies that either the redox potential of the electrolyte or the Fermi level of the working electrode shifts in presence of the LY. J_{sc} values for acceptor only and the donor-acceptor cells were 7.63 and 7.79 mA cm^{-2} respectively. J_{sc} increased by 1.02 times when the acceptor alone cell is replaced by a donor-acceptor cell. While the overall PCE (η) for the acceptor alone cell was

1.5%, the FRET enabled donor-acceptor based QDSSC showed an efficiency of 1.79%. The improved efficiency also highlights the benefit of FRET.

Previously Chakrapani et al., showed that in the presence of the Se metal in the S^{2-} ion electrolyte, the oxidation potential of the sulfide varies.^[16] The oxidation potential of the redox electrolyte was observed to decrease with increase in concentration of the Se which, authors reasoned was responsible for a decrease in V_{oc} , even though they observed a concomitant increase in current density and the overall current conversion efficiency.^[16] Similarly in presence of the PEDOT microfibers, the oxidation potential of the S^{2-} electrolyte gel shifts compared to the blank S^{2-} electrolyte (**Figure 6.9b**). Therefore, the ensuing acceptor only QDSSC with the following configuration: $TiO_2/CdS/CdSe/ZnS-PEDOT/S^{2-}-MWCNT$ showed a slightly lowered V_{oc} in comparison to cell with same configuration devoid of PEDOT microfibers. The cell with PEDOT microfibers showed a V_{oc} of 617 mV compared to 657 mV for the cell without PEDOT. But J_{sc} and η were higher for the cell with PEDOT microfibers and η was 1.6%. For the FRET enabled QDSSC with PEDOT microfibers: $TiO_2/CdS/CdSe/ZnS-LY/PEDOT/S^{2-}-MWCNT$, while the V_{oc} decreased by 1.01 times, but the overall PCE increased from 1.79 to 1.94% in comparison to the same cell without PEDOT microfibers. Improvements of the order of 6.66 and 8.4% in efficiency were registered for the acceptor only cell and the donor-acceptor cells with PEDOT microfibers relative to the same cells without the PEDOT microfibers. The ability of PEDOT microfibers to effectively transport holes, in combination with the S^{2-} ions was clearly reflected in the enhanced photocurrent and efficiency response. QDSSCs were also attempted by replacing the aqueous S^{2-} electrolyte completely with a PEDOT microfiber/water suspension or in the form of a drop-cast film on the photoanode, but no appreciable photocurrents were obtained, possibly owing to the poor quality of the photoanode/hole transport layer interface and

therefore only the combination of PEDOT microfibers and S^{2-} was employed for harnessing the hole/electron conducting capability of PEDOT.

Table 6.2: Solar cell parameters of QDSSCs ($\lambda > 300$ nm, 0.1 M Na_2S aqueous poly(acrylamide) based gel electrolyte with or without 1.5 mg mL^{-1} LY and with and without PEDOT, cell area: 1 cm^2 , under 1 sun illumination (100 mW cm^{-2}) with the listed photoanodes; all cells with MWCNT/FTO as the counter electrode.

Electrode configuration	V_{OC} (mV)	J_{SC} (mA cm^{-2})	FF	Efficiency (%)
$TiO_2/CdS/CdSe/ZnS$	657	7.63	30	1.5
$TiO_2/CdS/CdSe/ZnS/LY$ Dye	721	7.79	32	1.79
$TiO_2/CdS/CdSe/ZnS/PEDOT$	617	8.07	32	1.6
$TiO_2/CdS/CdSe/ZnS/LY/PEDOT$	716	8.2	33	1.94

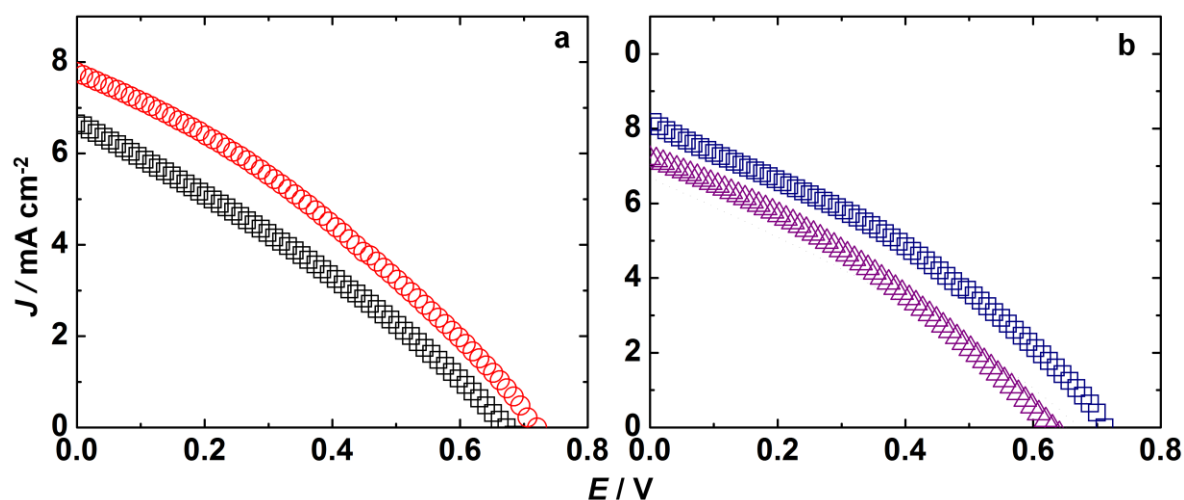


Figure 6.9: J-V characteristics of quasi solid-state QDSSCs with the following photoanode architectures: (a) donor-acceptor $TiO_2/CdS/CdSe/ZnS-LY/S^{2-}$ (\circ) and acceptor only $TiO_2/CdS/CdSe/ZnS-S^{2-}$ (\square) cells and (b) donor-acceptor: $TiO_2/CdS/CdSe/ZnS-LY/PEDOT/S^{2-}$ (\square) and acceptor only $TiO_2/CdS/CdSe/ZnS-PEDOT/S^{2-}$ (\triangle) cells. All experiments were performed under 1 sun illumination and at $\lambda > 300$ nm; a poly(acrylamide) gel containing 0.1 M Na_2S was employed as the electrolyte and a MWCNT/FTO assembly was used as a counter electrode. Concentrations of PEDOT and LY dye in the gels were 2 and 1.5 mg mL^{-1} respectively.

6.3.11 EIS studies

To reaffirm the role of PEDOT, in improving the hole transport capability of the S^{2-} electrolyte, the EIS spectra of the following two cells: $TiO_2/CdS/CdSe/ZnS-PEDOT/S^{2-}-MWCNT$ and $TiO_2/CdS/CdSe/ZnS-S^{2-}-MWCNT$ were recorded (**Figure 6.10a**). Both plots consist of one incomplete and one distorted semicircle, the first semicircle can be assigned to a parallel combination of the resistance and capacitance at the counter electrode/electrolyte interface, whereas the second semicircle originates from similar circuit elements operative at the photoanode/electrolyte interface. Since the span of the two plots is almost similar, it is apparent that the charge transfer resistances at the two interfaces are unaffected by the presence of PEDOT in the electrolyte. The Bode phase diagrams corresponding to the two cells are shown in the inset. Electron (in the CB of TiO_2) -hole (in S^{2-} or PEDOT) recombination time (τ_d) was calculated from the $|Z|$ versus \log (frequency) plots, by using the following equation.

$$\tau_d = 1/2\pi f \quad (9)$$

The middle frequency peak position slightly shifts to higher frequency (inset of **Figure 6.10a**), revealing a decrease in the electron recombination time from 2.76 to 1.45 ms ongoing from the cell with S^{2-} and PEDOT to the one with S^{2-} alone. The increase in the electron-hole recombination time in the presence of PEDOT indicates fast hole transport from the QDs to PEDOT and as a consequence more efficient charge separation. To investigate the effect of LY dye on recombination time, the Nyquist plots for the cells with and without the donor dye were recorded. Both plots comprise two skewed semicircles, but for the donor-acceptor cell, the impedance at low frequencies is noticeably larger than that observed for the acceptor only cell. From the corresponding Bode plots, the electron-hole recombination time in the acceptor only cell ($TiO_2/CdS/CdSe/ZnS-S^{2-}-MWCNT$) was calculated to be 2 ms and it was

0.96 ms for the donor-acceptor cell ($\text{TiO}_2/\text{CdS}/\text{CdSe}/\text{ZnS}-\text{LY}/\text{S}^{2-}-\text{MWCNT}$), indicating that the donor inhibits electron-hole recombination.

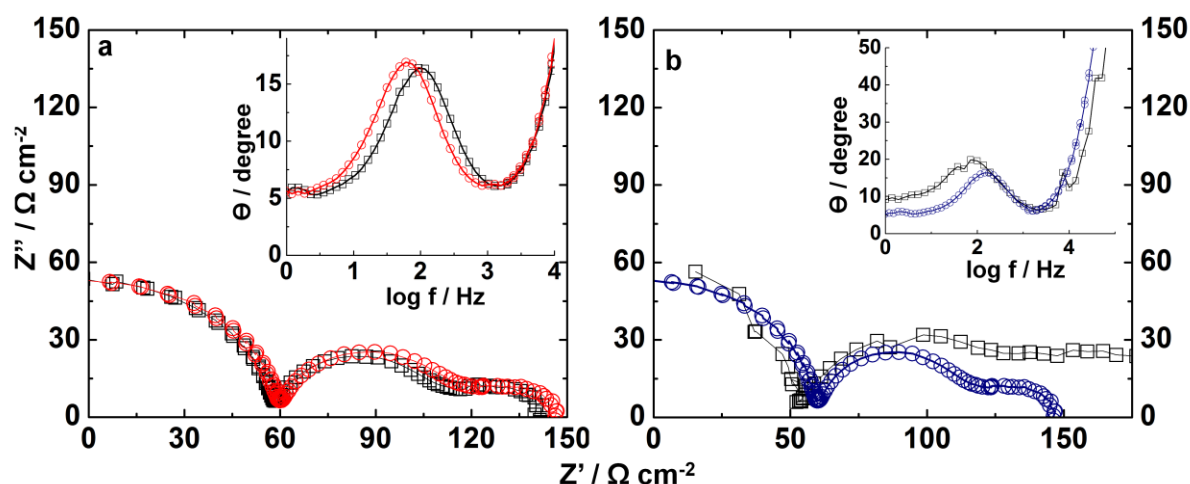


Figure 6.10: Nyquist plots recorded under an ac amplitude of 10 mV and a zero dc bias for quasi solid-state QDSSCs (a) with PEDOT: $\text{TiO}_2/\text{CdS}/\text{CdSe}/\text{ZnS}-\text{PEDOT}/\text{S}^{2-}$ (O) and without PEDOT: $\text{TiO}_2/\text{CdS}/\text{CdSe}/\text{ZnS}-\text{S}^{2-}$ (\square), (b) donor-acceptor QDSSCs: $\text{TiO}_2/\text{CdS}/\text{CdSe}/\text{ZnS}-\text{LY}/\text{S}^{2-}$ (\square) and acceptor only QDSSCs: $\text{TiO}_2/\text{CdS}/\text{CdSe}/\text{ZnS}-\text{S}^{2-}$ (O). A 0.1 M Na_2S based poly(acrylamide) gel served as the electrolyte and a MWCNT/FTO assembly as the counter electrode. LY dye and PEDOT microfiber concentrations were 1.5 and 2 mg mL^{-1} in the gel. Inset shows the corresponding Bode plots (phase angle *versus* frequency).

6.4 Summary

FRET was demonstrated in a QDSSC based on a donor-acceptor architecture with unattached LY dye molecules as donors and CdS/CdSe QDs anchored to titania as acceptors, wherein upon illumination facile excitation transfer occurs from the LY dye to CdS/CdSe QDs, which is followed by rapid charge injection from QDs to TiO_2 . The energy and electron transfer processes were mechanistically discerned by fluorescence quenching of the LY dye in the presence of CdS/CdSe/ZnS QDs, by decreased electron lifetime of the dye in the presence of the QDs and also from the increments in the QD's emission and lifetime in the presence of the LY dye. The Forster radius (or the CdS/CdSe/ZnS QD – LY dye separation) was estimated to be 5.29 nm and the energy and electron transfer rates were deduced to be

5.29×10^9 and $3.2 \times 10^9 \text{ s}^{-1}$. The synergy between the QDs and dye molecules was evidenced from the remarkably enhanced IPCE of 53% achieved by the cell encompassing a combination of tethered CdS/CdSe QDs and unattached LY dye molecules as opposed to the dismal performances of the acceptor only (30%) and donor only (0.009%) cells. The performance of the FRET enabled cell was further augmented by the incorporation of PEDOT microfibers in the sulfide ion electrolyte. PEDOT microfibers improve the hole transport ability of the S^{2-} gel which was evidenced from the decreased lifetime of CdS/CdSe QDs in the presence of PEDOT. The overall PCE of the quasi solid state FRET enabled QDSSC with the following configuration: $\text{TiO}_2/\text{CdS}/\text{CdSe}/\text{ZnS-LY}/\text{PEDOT}/\text{S}^{2-}\text{-MWCNT}$ increased by 1.94% in comparison with sole acceptor cell. The performance metrics, in particular, the greatly enhanced IPCE in the visible region spanning from 400 to 650 nm, for the cell containing an unconventional luminescent donor, namely Lucifer yellow, open up opportunities to deploy this relatively less used dye as an efficient energy relay dye in diverse types of solar cells.

6.5 References

- [1] H. Choi, P. K. Santra, P. V. Kamat, *ACS Nano* **6** (2012) 5718-5726.
- [2] G. K. Mor, J. Basham, M. Paulose, S. Kim, O. K. Varghese, A. Vaish, S. Yoriya, C. A. Grimes, *Nano Lett.* **10** (2010) 2387-2394.
- [3] J. I. Basham, G. K. Mor, C. A. Grimes, *ACS Nano* **2010**, 4, 1253-1258.
- [4] Y. Saito, T. Azechi, T. Kitamura, Y. Hasegawa, Y. Wada, S. Yanagida, *Coord.Chem. Rev.* **248** (2004) 1469-1478.
- [5] U. Kim, Y-E. Sung, J-B. Xia, M. Lira-Cantu, N. Masaki, S. Yanagida, *J. Photochem. Photobiol. A* **193** (2008) 77-80.
- [6] N. Fukuri, N. Masaki, T. Kitamura, Y. Wada, S. Yanagida, *J. Phys. Chem. B* **110** (2006) 25251-25258.
- [7] X. Zhang, J-S. Lee, G. S. Lee, D-K. Cha, M. J. Kim, D. J. Yang, S. K. Manohar, *Macromolecules* **39** (2006) 470-472.
- [8] Z. Yu, Q. Zhang, D. Qin, Y. Luo, D. Li, Q. Shen, T. Toyoda, Q. Meng, *Electrochem. Commun.* **12** (2010) 1776-1779.
- [9] L. Etgar, J. Park, C. Barolo, V. Lesnyak, S. K. Panda, S. Quagliotto, G. Hickey, Md. K. Nazeeruddin, A. Eychmuller, G. Viscardi, M. Gratzel, *RSC Adv.* **2** (2012) 2748-2752.
- [10] C. J. D. Grauw, H.C. Gerritsen, *Appl. Spectrosc.* **55** (2001) 670-678.

- [11] F. Huang, L. Hou, H. Wu, X. Wang, H. Shen, W. Cao, W. Yang, Y. Cao, *J. Am. Chem. Soc.* **126** (2004) 9845-9853.
- [12] J. R. Lakowicz, *Principles of Fluorescence Spectroscopy, 2nd ed.*; Kluwer Academic/Plenum Publishers: New York, (1999).
- [13] S. Buhbut, S. Itzhakov, E. Tauber, M. Shalom, I. Hod, T. Geiger, Y. Garini, D. Oron, A. Zaban, *ACS Nano* **4** (2010) 1293-1298.
- [14] B. Lee, V. Seshadri, G. A. Sotzing, *Langmuir* **21** (2005) 10797-10802.
- [15] S. Sarkar, A. Makhal, K. Lakshman, T. Bora, J. Dutta, S. K. Pal, *J. Phys. Chem. C* **116** (2012) 14248-14256.
- [16] V. Chakrapani, D. Baker, P. V. Kamat, *J. Am. Chem. Soc.* **133** (2011) 9607-9615.

Chapter 7

A plasmonic solar cell integrated with a carbon nanotubes supercapacitor in a single device: Unifying energy conversion and storage

7.1 Introduction

In the previous chapters, carbon nanostructures and FRET were used to improve PCEs in QDSSCs. Taking this further, yet another very effective strategy of integrating plasmonics with QDSSCs, is explored in this chapter. A hitherto unreported photoanode architecture of TiO₂/CdS/Au (fibers) was employed as the exciton generator, and dual function- acid functionalized MWCNTs were employed as the counter electrode for the QDSSC and also as one of the electrodes for a symmetrical supercapacitor in the form of a Janus type electrode, thus yielding a three electrode integrated photovoltaic supercapacitor. The photocurrent produced by the plasmonic QDSSC upon irradiation was channelized to the symmetrical MWCNT supercapacitor. The role of Au plasmons in improving the solar cell performance of the TiO₂/CdS photoanode was determined by absorbance, fluorescence quenching, lifetime analyses and solar cell parameters. The supercapacitor performance was evaluated from photo-charging-discharging behavior, cycling stability and cyclic voltammetry. The ease and economy of fabrication coupled with the twin functions of energy conversion and storage opens up opportunities to combine different photoactive and ion storage materials for creating solar-powered supercapacitors, as they rely only on the sun's munificence and literally do away with the need for any other external electrical stimulus.

7.2 Experimental

7.2.1 Preparation of Au fibers

Au nanofibers were synthesized according to the reported literature procedure.^[1] Initial gold seed particle solution was prepared by first mixing 20 mL of sodium citrate (0.025 M)

and 0.2 mL of HAuCl_4 (0.00025 M) aqueous solutions. An ice cold aqueous solution containing NaBH_4 (0.01 M) and sodium citrate (0.025 M) was prepared in another beaker. 0.6 mL of the NaBH_4 /sodium citrate solution was added to the Au salt/sodium citrate solution while stirring. Immediately an orange red colored seed solution was formed and it was stored at low temperature for further use. Growth solutions were prepared by mixing 15 mL of CTAB (0.2 M) and 15 mL of HAuCl_4 (0.0005 M) aqueous solutions. It was distributed in two vials labeled as A and B and a beaker labeled as C. The growth solutions were distributed in such a way that A and B contained 2.25 mL each and C contained 22.5 mL. Aliquots of 12.5 μL of an aqueous solution of ascorbic acid (0.1 M) were added to A and B, whereas to C, 125 μL of ascorbic acid (0.1 M) solution and 100 μL of concentrated nitric acid was also added. A volume of 200 μL of the initial gold seed solution was added to the vial A and stirred for 5 seconds. Then 200 μL of A were transferred to vial B and the mixture was stirred for 5 seconds. Finally, 200 μL of the solution from B was added to beaker C and stirred for 5 seconds. The resulting solution in C was left undisturbed at room temperature for 12 h. Gold fibers precipitated and settled at the bottom of beaker C. The supernatant liquid was decanted and discarded and the gold fibers were washed with deionized water and stored in deionized water.

7.2.2 Fabrication of photoanode

Titanium dioxide nanoparticles were prepared by a sol-gel method which was described in **Chapter 6**. TiO_2 films were deposited over FTO coated glass substrates by using doctor blade technique from a dispersion of 3 g of TiO_2 nanopowder in 15 mL of ethanol. The resulting white colored opaque film was annealed at 450 °C for 3 h. CdS QDs were deposited on the TiO_2 layer by SILAR technique (5 cycles) as described in **Chapter 4**. A layer of Au fibers was applied over the TiO_2/CdS electrode, by exploiting the affinity that Au has for the sulfur in CdS. A suspension of Au fibers (1 mg) in 1 mL of ultrapure water was sonicated for

5 min and then spin coated over TiO₂/CdS at 1000 rpm for 30 s and dried at room temperature in air.

7.2.3 Fabrication of MWCNT electrodes

A MWCNT electrode was prepared as described in **Chapter 5** and employed as the counter electrode for the QDSSC. Silver paste was applied uniformly over the back (glass) side of this electrode and dried at 60 °C and a silver-grey colored homogeneous solid film of Ag was obtained. Over the Ag surface of the MWCNT/FTO/glass/Ag electrode, the MWCNT dispersion was again spin coated and treated as mentioned above to yield the MWCNT/FTO/glass/Ag /MWCNT electrode. This coated substrate was utilized as the counter electrode for the QDSSC and also as one of the electrodes of the supercapacitor. A simple MWCNT/FTO/glass electrode was used as the second electrode of the supercapacitor. Cell configurations and connections are discussed in detail in the latter section.

7.2.4 Synthesis of electrolytes and cells

A polymeric gel electrolyte for the QDSSC was prepared as described in **Chapter 5**. Hydrogel was obtained which was used for the solar cell part of the photo-supercapacitor. The gel electrolyte for the supercapacitor part of this dual function cell was synthesized by dissolving 12 wt.% of PMMA in a solution of lithium triflate (0.2 M) in propylene carbonate, by continuous stirring and heating at 65 °C for 1 h. A transparent homogeneous gel of LiCF₃SO₃/PC/PMMA was obtained which, was stored in a vacuum. An adhesive acrylic spacer, 0.64 mm thick and 2 mm wide was applied along the four edges of the TiO₂/CdS/Au coated plate. The cavity thus created by the spacer running continuously along the perimeter of the photoanode was filled with the self-supporting poly(acrylamide)/S²⁻-hydrogel, by simply cutting it to size using a scalpel blade and inserting it in the cavity with forceps. The MWCNT/FTO/glass/Ag/MWCNT electrode was firmly pressed onto this assembly of TiO₂/CdS/Au/hydrogel with the MWCNT/FTO side facing the hydrogel. The acrylic spacer

was again applied along the four sides of the MWCNT/FTO/glass/Ag/MWCNT electrode on the Ag/MWCNT side. The cavity created by the spacer was filled with the $\text{LiCF}_3\text{SO}_3/\text{PC}/\text{PMMA}$ gel using a glass rod, and this assembly was left undisturbed in a vacuum oven to remove the entrapped bubbles in the gel. The assembly of $\text{TiO}_2/\text{CdS}/\text{Au}/\text{hydrogel}/\text{MWCNT}/\text{FTO}/\text{glass}/\text{Ag}/\text{MWCNT}/\text{LiCF}_3\text{SO}_3/\text{PC}/\text{PMMA}$ was then affixed onto the MWCNT/FTO/glass assembly, with the Li^+ gel facing the MWCNT/FTO surface. The quasi-solid state photo-supercapacitor device had the following composition: $\text{TiO}_2/\text{CdS}/\text{Au}/\text{hydrogel}/\text{MWCNT}/\text{FTO}/\text{glass}/\text{Ag}/\text{MWCNT}/\text{Li}^+\text{gel}/\text{MWCNT}/\text{FTO}$. Two electrode solar cells without the supercapacitor part were also fabricated using the same procedures as above, with the following configuration: $\text{TiO}_2/\text{CdS}/\text{Au}/\text{hydrogel}/\text{MWCNT}/\text{FTO}/\text{glass}$.

7.3 Results and discussion

7.3.1 HRTEM analysis

The electron microscopy images of Au fibers and a $\text{TiO}_2/\text{CdS}/\text{Au}$ film were shown in **Figure 7.1**. **Figure 7.1a** and **b** show the SEM images of Au fibers and the fibers are typically several tens of micrometers long and they have bent, looped and curled morphologies. The TEM image of Au micro-fibers shows them to be composed of distinctive curved and bent nanoscale fibers, a few microns long and 100 to 250 nm wide (**Figure 7.1c**). The HRTEM image extracted from one such Au nano-fiber (**Figure 7.1d**) shows the fiber to be highly crystalline with a fringe separation of 0.24 nm which corresponds to the 111 plane of a face centered cubic (fcc) lattice of Au (PDF: 652870). The crystal fringes are ordered perpendicular to the growth direction of 111 lattice spacing. The corresponding selected area electron diffraction (SAED) pattern could also be indexed to the 111 zone axis (**Figure 7.1e**). Since crisscross fringes were observed in the right hand region of **Figure 7.1d**, it is apparent that the Au fibers are polycrystalline. The low magnification TEM image of a $\text{TiO}_2/\text{CdS}/\text{Au}$

film shows the film to be composed of a framework of irregular shaped particles and elongated fiber like shapes, with indistinguishable grain boundaries, thus indicating a good mixing of CdS, TiO₂ and Au fibers (**Figure 7.1f**). A HRTEM image shown in **Figure 7.1g** taken from the TiO₂/CdS/Au film shows overlapping and juxtaposed lattice fringes from CdS QDs, TiO₂ and Au. The well-defined plane facet with a region marked as A' in **Figure 7.1g** probably originates from the tip of an Au nano-fiber. An enlarged view of A' is displayed in panel A, and the inter-fringe spacing is 0.24 nm (which stems from the 111 plane of fcc Au) thus confirming that the crystalline structure of Au fibers is retained in the TiO₂/CdS/Au film. Blown-up views of regions labeled as B' and C' in **Figure 7.1g** are shown in panels B and C and the inter-fringe distances are 0.17 and 0.35 nm which correspond to the 222 plane of CdS with a fcc structure (PDF: 652887) and the 101 plane of TiO₂ with a body centered tetragonal crystal structure (PDF: 894921) respectively.

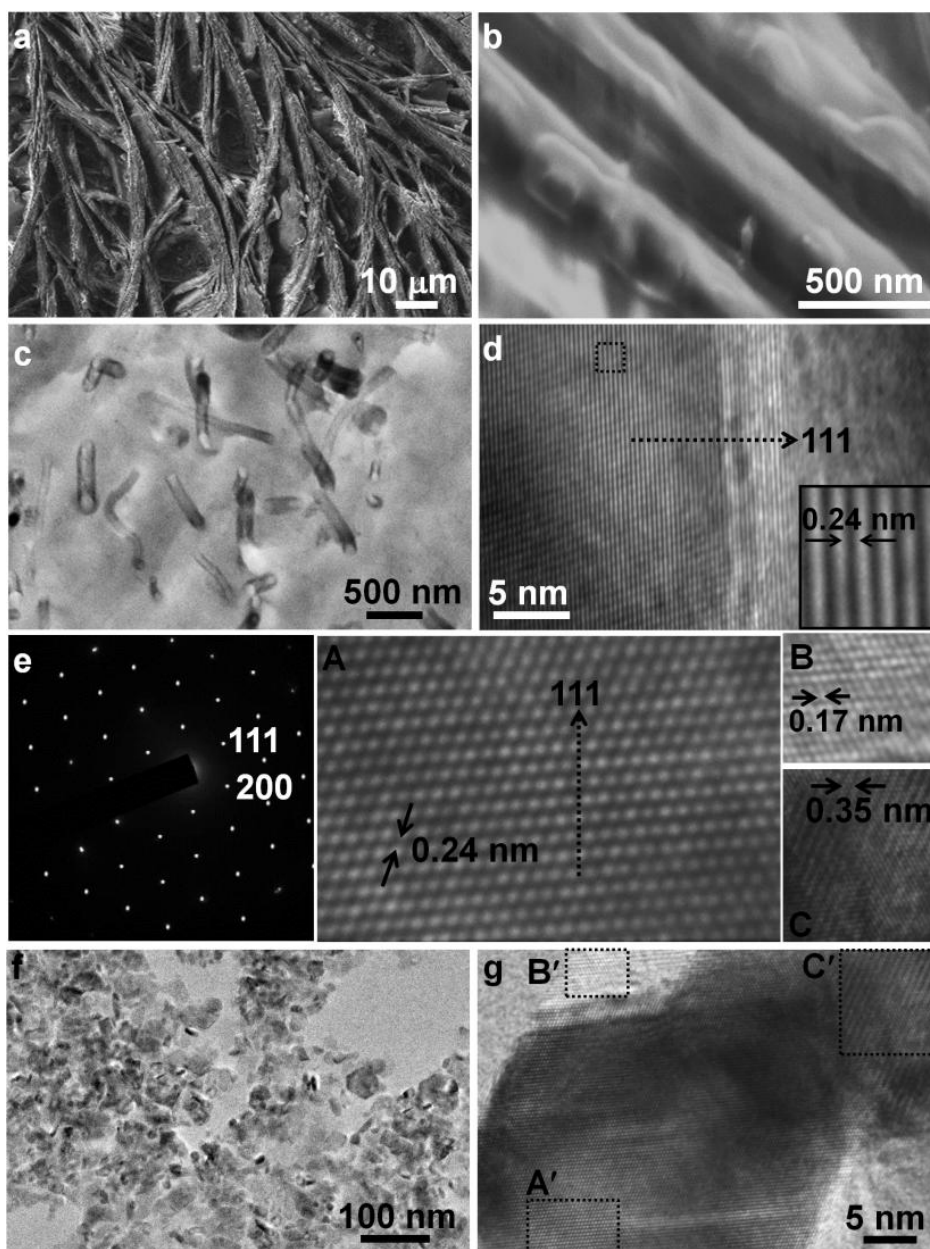


Figure 7.1: (a and b) SEM images of Au fibers, (c) TEM image of Au nano-fibers, (d) lattice scale image of an Au nano-fiber, (e) SAED pattern of an Au nano-fiber, (f) TEM and (g) HRTEM images of a TiO₂/CdS/Au film. Regions marked as A', B' and C' in (g) have been enlarged in panels A, B and C respectively. The dotted arrows in (d) and A are growth directions.

7.3.2 Optical characterization

Figure 7.2a shows the absorption spectra of the films of interest. The TiO₂/CdS film shows a broad absorption in the 400-500 nm wavelength regime, which is characteristic of

band gap excitation in CdS QDs. Upon incorporation of Au fibers in the TiO₂/CdS film, the resulting TiO₂/CdS/Au film shows an increase in absorption in the same wavelength region which surprisingly does not coincide with the $\lambda_{\text{SPR(max)}}$ of Au fibers. The Au fiber colloid shows a distinct absorption peak at 530 nm (**Figure 7.2b**) corresponding to surface plasmon resonance ($\lambda_{\text{SPR(max)}}$), typical of metal nanoparticles.^[2] The absorption increment is effected either by scattering of light by Au plasmons, which increase the optical path length of light within the film matrix and enhance the CdS QD's absorption or by the near field coupling between the surface plasmon polaritons and the excited state of the dots.^[3]

Figure 7.2b shows the variation in intensity and position of the plasmonic absorption peak of Au fibers, as a function of irradiation time in the presence of a TiO₂/CdS film. A TiO₂/CdS film was immersed in the Au fiber colloid and this system was exposed to light radiation with $\lambda > 350$ nm for different intervals of time and the absorption of the system was measured intermittently. The absorption of TiO₂/CdS was eliminated by using this film as a reference. The system prior to irradiation shows only the surface plasmonic peak of Au fibers at 530 nm. After irradiating the system for 2 min, the intensity of the $\lambda_{\text{SPR(max)}}$ of Au fibers increased by 2.67 times. Upon exposure of the CdS QD film/Au colloid to light, the excited electrons in the conduction band of CdS are transferred to Au fibers, for metal nanoparticles are known to serve as excellent electron sinks,^[4] thus increasing the plasmonic absorption of Au. The intensity of the $\lambda_{\text{SPR(max)}}$ increases and broadens and it also blue-shifts by 4 nm upon irradiation. The blue shift occurs due to an increase in electron density in the metal nanoclusters which causes an increase in their frequency,^[5] effected by electron transfer from excited CdS QDs. To indubitably establish that both processes (i) charge transfer from CdS QDs to Au fibers and (ii) increase in CdS absorption by Au plasmons occur concomitantly, the absorption of Au fibers was monitored as a function of increasing CdS QD concentration. The concentration of Au colloid was fixed at 1mg mL⁻¹, and the CdS QD film with 1, 2, 3, 4

and 5 layers grown by SILAR were introduced in the solution successively and the absorption of the system was measured. With increase in CdS thickness or concentration, the overall absorption intensity of the CdS/Au system enhanced, and this also accompanied by a blue-shift of the $\lambda_{\text{SPR(max)}}$ of Au fibers by 4 nm (**Figure 7.2c**). The increase and shift in the Au plasmonic absorption are induced by increasing electron density in Au nanoparticles (transferred from the CB of CdS), as a function of increasing CdS thickness.

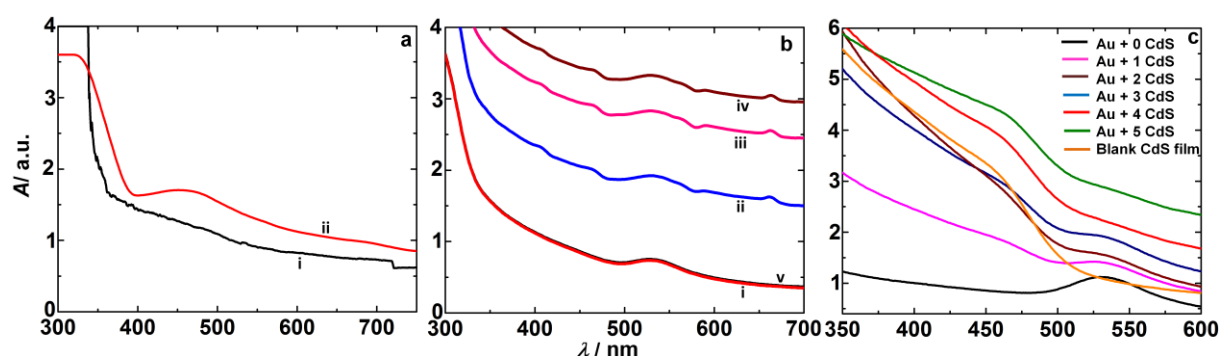


Figure 7.2: (a) Absorption spectra of a (i) TiO₂/CdS and (ii) a TiO₂/CdS/Au film, (b) absorption spectra of a TiO₂/CdS/Au film after (i) 0 (ii) 2 (iii) 4 (iv) 6 min of white LED irradiation, spectra was recorded after stopping the irradiation, (v) after 30 min after stopping the irradiation, and (c) absorption spectra of the Au colloid with various concentrations of CdS QDs.

7.3.3. Emission and lifetime studies

Emission studies on the TiO₂/CdS/Au assembly further affirmed the charge transfer operative between CdS and Au fibers. The TiO₂/CdS film showed a peak with $\lambda_{\text{em(max)}}$ at 550 nm corresponding to the band edge emission of CdS QDs,^[6] when the film was excited at $\lambda_{\text{ex}} = 370$ nm. After integrating the TiO₂/CdS film with Au fibers, by immersion in an Au colloid of 0.5 mg mL⁻¹ strength, the emission intensity of CdS QDs quenched by ~2.45 times due to the charge transfer in the TiO₂/CdS/Au film. Since a maximum quenching by 69 % was achieved when the CdS QDs were exposed to an Au colloid of 1mg mL⁻¹ strength, this concentration of Au fibers was fixed for solar cell application.

The emission decay analyses of the pristine TiO₂/CdS film and a TiO₂/CdS/Au film (the latter derived by bringing in contact a TiO₂/CdS film with Au colloid of optimized concentration of 1mg mL⁻¹) are shown in **Figure 7.3a**. The excited state lifetimes were measured at an emission wavelength of 550 nm with $\lambda_{\text{ex}} = 370$ nm (**Figure 7.3b**). The fluorescence data was fitted to a bi-exponential decay function as shown through equation 2.

$$I = A_1 \exp(-t/\tau_1) + A_2 \exp(-t/\tau_2) \quad (2)$$

In equation (2), I is the normalized emission intensity, t is the time after light emitting diode (LED) excitation, A₁ and A₂ are the amplitude coefficients and τ_1 and τ_2 are the decay time constants. The average lifetimes were calculated by using the following equation and the fitted parameters are summarized in **Table 7.1**.

$$\langle \tau \rangle = \frac{\sum A_i \tau_i^2}{\sum A_i \tau_i} \quad (3)$$

The TiO₂/CdS film showed an average life time of 11.94 ns, wherein the slow decay component of 12.75 ns is due to band edge recombination and the fast decay component of 1.85 ns can be attributed to the charger transfer from CdS QDs to the CB of the TiO₂ or to the current collector, which is an energetically permissible mechanism.

Table 7.1: Kinetic parameters of emission decay analysis of photoanode films (measured at $\lambda_{\text{ex}} = 370$ nm and $\lambda_{\text{em}} = 550$ nm) deduced from bi-exponential fits.^a

Electrode description	χ^2	τ_1 (ns)	τ_2 (ns)	A ₁	A ₂	$\langle \tau \rangle$ (ns)
TiO ₂ /CdS	0.977	1.85	12.75	32.19	67.81	11.94
TiO ₂ /CdS/Au fiber	1.115	1.22	8.93	21.07	78.93	8.66

^a A₁ and A₂ are the relative amplitudes of each lifetime, τ_1 and τ_2 are the components of fluorescence lifetime and χ^2 denotes the fit quality.

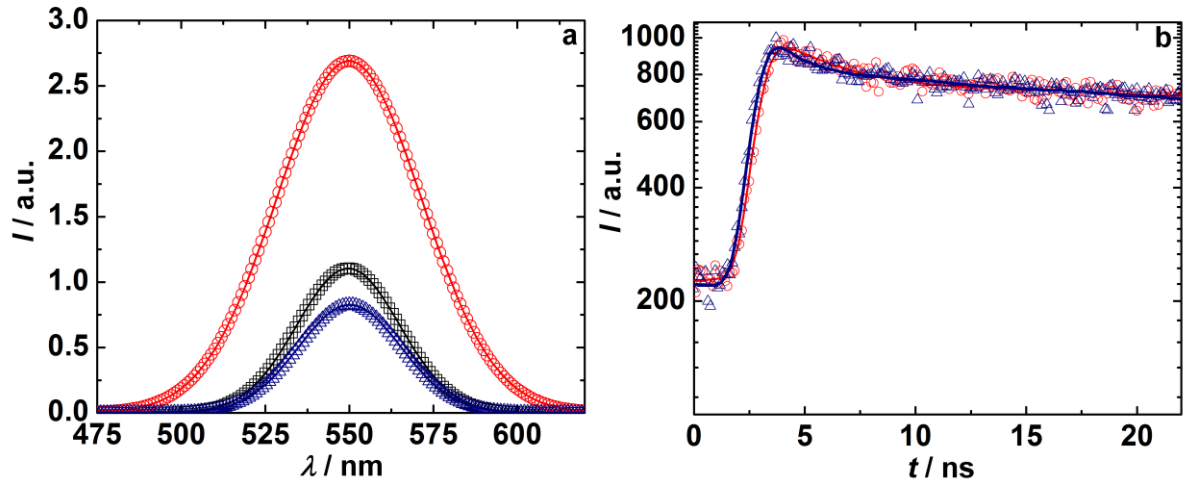


Figure 7.3: (a) Emission spectra of a TiO₂/CdS film (○), a TiO₂/CdS/Au film at a lower concentration of Au (□) and TiO₂/CdS/ at a higher concentration of Au (△) ($\lambda_{\text{ex}} = 370$ nm) and (b) time resolved fluorescence decay analysis of a TiO₂/CdS (○) and a TiO₂/CdS/Au film (△) with $\lambda_{\text{ex}} = 370$ nm and $\lambda_{\text{em}} = 550$ nm.

The CB position of the CdS is aligned at 3.8 eV and the CB position of TiO₂ is lower by 0.5 eV and the position of FTO/Glass is at 4.7 eV. The TiO₂/CdS/Au film showed an average lifetime of 8.66 ns. The Fermi level of Au fibers is poised at 5.1 eV. The decrease in the excited state lifetime indicates the role of Au fibers as electron acceptors, as the Fermi level of Au is conducive for accepting electrons from the CB of CdS QDs. The energy band diagram of the plasmonic device is shown in **Figure 7.4a**.

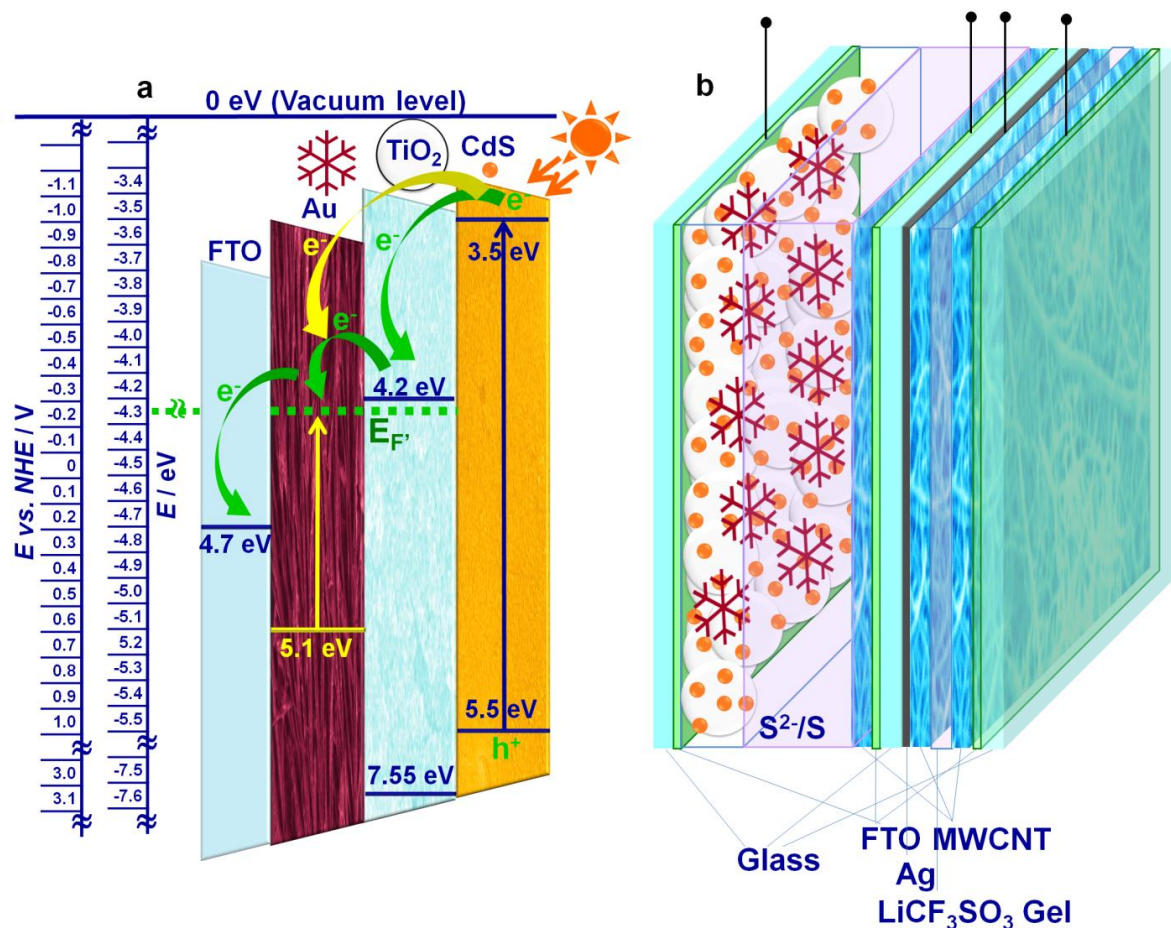


Figure 7.4: (a) Energy band diagram of a plasmonic solar cell showing the possible electron transfer modes and (b) a schematic of the solar powerd supercapacitor.

7.3.4 Photoelectrochemical response

It has been established that the surface plasmon resonance of Au fibers can increase the absorption of CdS QDs which, can effectively lead to an increment in photocurrent. The TiO₂/CdS/Au film was employed as the photoanode in a quasi solid-state QDSSC. A 0.2 M S²⁻ based poly(acrylamide) gel served as the electrolyte and a functionalized MWCNT coated FTO/Glass was used as the counter electrode.

The J-V response is shown in **Figure 7.5a**. The TiO₂/CdS/Au film showed a J_{SC} of 5.4 mA cm⁻², which was 1.26 times greater than the current produced by the conventional TiO₂/CdS electrode devoid of plasmonic Au. This enhancement is due to intense local electromagnetic field produced by the plasmonic nanoparticles, which couple light very

effectively from the far-field to the near-field of QDs. Due to this, the excitation rate in QDs increases significantly and hence the photocurrent. The TiO₂/CdS/Au assembly showed an increase not only in J_{SC} but also in V_{OC} compared to the cell with TiO₂/CdS as photoanode. The TiO₂/CdS based cell showed a V_{OC} of 651 mV, whereas the plasmonic device showed an increased voltage of 671 mV. Since the redox potential of S²⁻ is fixed, the Fermi level of TiO₂ shifts to a more negative potential (*versus* NHE) in the presence of Au fibers, due to charge transfer from TiO₂/CdS to Au. As a consequence, V_{OC} increased. A similar increment in the V_{OC} of a DSSC containing Au@TiO₂ nanoparticles was induced by the charging effect of plasmonic nanoparticles.^[5] The plasmonic cell showed an overall PCE of 2.1%, which was 1.45 times higher than that of the conventional TiO₂/CdS cell. The solar cell parameters are provided in **Table 7.2**. Some theoretical studies in the past revealed that embedding the plasmonic particles over the active layer can take advantage of both light scattering and the localized surface plasmon resonance near field.^[7]

To quantify the plasmonic effect on solar cell performance, the IPCE values of QDSSCs with TiO₂/CdS and TiO₂/CdS/Au as photoanodes were measured (**Figure 7.5b**). In comparison, the TiO₂/CdS/Au film showed an increased IPCE across 350 to 600 nm, compared to TiO₂/CdS. The TiO₂/CdS film showed a highest IPCE of 32% at 400 nm and the TiO₂/CdS/Au film showed a maximum IPCE of 38% at the same wavelength. Previously, a DSSC with a TiO₂/N719 electrode showed a maximum IPCE of 80% at 550 nm whereas in the presence of Au nanoparticles encapsulated with SiO₂, an increased IPCE of 85% was obtained at the same wavelength.^[5] In another study, the IPCE of a DSSC increased from 60 to 76% at 530 nm due to the plasmonic effect of Ag@SiO₂.^[8]

The photocurrents *versus* time transients for the two cells (with and without plasmonic electrodes) are shown in **Figure 7.5c**. The photocurrent generated by both cells is fast, nearly saturated, and reproducible during repetitive on/off cycles of visible light illumination. The plasmonic QDSSC with TiO₂/CdS/Au as photoanode produced an I_{SC} of 1 mA, and it's non-

plasmonic analogue: TiO₂/CdS of an equivalent area, generated an I_{SC} of 0.7 mA upon illumination. These values were reproducibly obtained upon excitation under an input power of 20 mW cm⁻², λ > 300 nm.

Table 7.2: Solar cell parameters of QDSSCs with the listed photoanodes. Cells contained a 0.2 M S²⁻ poly (acrylamide) gel electrolyte and MWCNTs as the counter electrode (under 1 sun illumination, λ > 300nm).

Electrode configuration	V _{OC} (mV)	J _{SC} (mA cm ⁻²)	FF	Efficiency (%)
TiO ₂ /CdS	651	4.3	52	1.46
TiO ₂ /CdS/Au	677	5.4	56	2.1

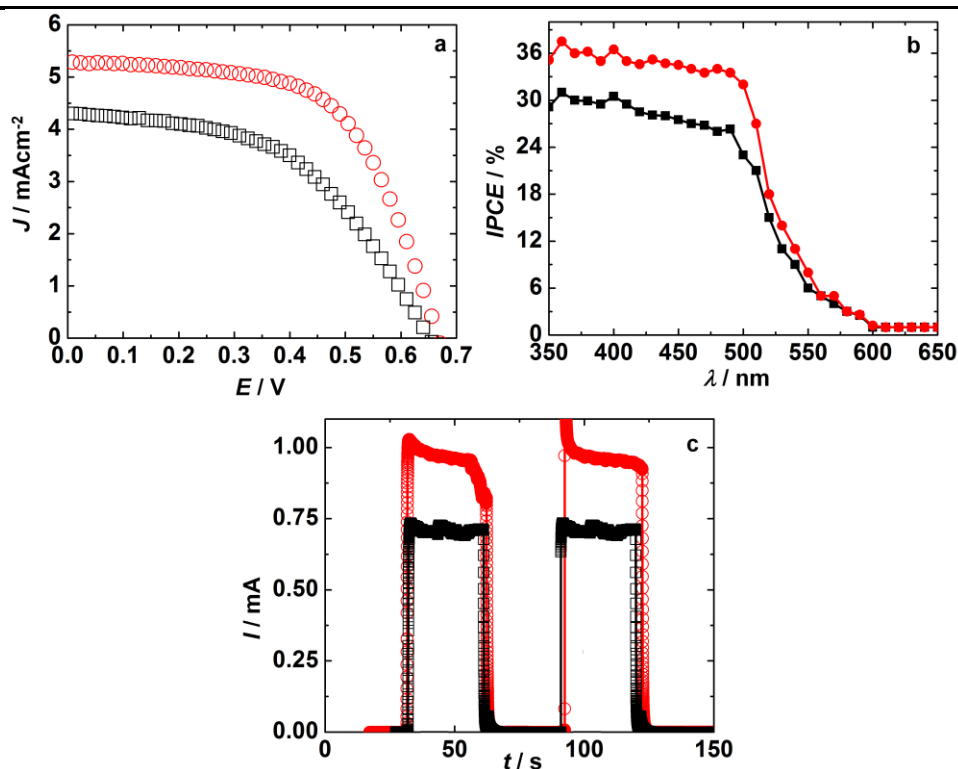


Figure 7.5: (a) J-V characteristics of the cell with TiO₂/CdS (□) and TiO₂/CdS/Au (○) electrodes under 1 sun illumination (λ > 300 nm, 100 mW cm⁻², AM 1.5), (b) IPCE spectra with the following photoanodes: TiO₂/CdS (■) and TiO₂/CdS/Au (●) and (c) photocurrent on-off cycles of a cell based on TiO₂/CdS (□) and TiO₂/CdS/Au (○) as photoanodes under illumination, with λ > 300 nm and an input power of 20 mW cm⁻². In (a-c) an acrylamide polymeric gel based on S_n²⁻/S²⁻ redox couple was employed as the electrolyte and a MWCNT/FTO assembly was used as a counter electrode, Measurements in (c) were performed under zero applied current or bias.

7.3.5 Photovoltaic supercapacitor performance

A photovoltaic supercapacitor was assembled with a plasmonic photoanode; since the plasmonic QDSSC produced higher photocurrents than the non-plasmonic cell. A schematic illustrating the descriptions, positioning of the electrodes and the sequence of photo-activated phenomena in the photo-supercapacitor is shown in **Figure 7.4b**. A schematic showing the cell configuration and working is displayed in **Figure 7.6a**. Cells with the following configuration were constructed: $\text{TiO}_2/\text{CdS}/\text{Au}$ as photoanode labeled as I, $\text{MWCNT}/\text{FTO}/\text{Glass}/\text{Ag}/\text{MWCNTs}$ as the Janus type electrode in-between labeled as II, wherein the MWCNTs flanked to FTO worked as the counter electrode for the QDSSC part (A in **Figure 7.6a**) and the MWCNTs attached to an Ag layer served as one of the two electrodes for the supercapacitor (B in **Figure 7.6a**). The middle electrode (II) is a single physical entity, but it consisted of two separate electrode surfaces, which were classified as A and B in **Figure 7.6a**. The non-conducting glass surface was made conductive by applying a uniform thin layer of silver paste over it and a thin layer of MWCNTs was drop-casted over the Ag surface. The third electrode assembled parallelly with respect to the above-described two electrodes was $\text{MWCNT}/\text{FTO}/\text{Glass}$ (labeled as III), which was used as the second electrode for the electrical double layer supercapacitor. The first two electrodes (I and II) of the QDSSC part were separated by a 0.2 M S^{2-} poly(acrylamide) gel, and the second (II) and the third electrode (III) were separated from each other by a gel electrolyte containing 0.1 M lithium triflate pre-dissolved in propylene carbonate and then immobilized in $15 \text{ wt } \%$ PMMA. Thus, an overall assembly comprising of a plasmonic or non-plasmonic QDSSC (electrodes: I and A of II) unified with a symmetric supercapacitor composed of functionalized MWCNTs (electrodes: B of II and III) was achieved and this was utilized for photovoltaic supercapacitor application. Upon shining light on this photo-supercapacitor cell (**Figure 7.6b**), the photo-generated electrons in the photoanode were directed to flow from

the working electrode of the solar cell to the supercapacitor part, via the external circuit, thus charging the supercapacitor, without the aid of any external power supply. In a previous report, Chen et al., fabricated a photo-supercapacitor, wherein the supercapacitor electrodes were PEDOT based and the solar cell was a traditional DSSC with N719 dye sensitized TiO₂ as the charge resource. In their work, a common Pt electrode coated with PEDOT on one side was used as the supercapacitor working electrode.^[9] Our device structure is entirely different as the counter electrode of the QDSSC (MWCNT/FTO) is electrically insulated from the working electrode of the supercapacitor part (MWCNT/Ag); only though the external circuit the two layers can be connected.

The symmetric supercapacitor electrodes (B of II and III) of the photovoltaic supercapacitor were connected to a potentiostat to measure the galvanostatic charge-discharge characteristics, and ± 0.5 V was set as the maximum charging voltage. The electrical connections made for making the measurements are shown in **Figure 7.6b**. No current was supplied to the cell from the potentiostat. In dark, the cell did not show any charge-discharge characteristics, due to zero current generation in the QDSSC part of the cell. Under visible light illumination (input power: 20 mW cm⁻², $\lambda > 300$ nm), the QDSSC part of the cell (the photoanode was TiO₂/CdS/Au) produced 1 mA current (by electron hole separation in CdS, followed by electron transfer to current collector FTO) which was channelized through the external circuit to the MWCNT/FTO/Glass electrode (labeled as III) of the symmetrical supercapacitor part of the cell. The supercapacitor part charged in 30 s from 0 to + 0.5 V and simultaneously electrons flowed from the MWCNT/Ag (labeled as B, electrode of supercapacitor) to MWCNT/FTO (labeled as A, counter electrode of QDSSC) via the external circuit; the direction of electron flow is as shown in **Figure 7.6b**. At the counter electrode, the electrolyte species is reduced, and the reduced species undergoes oxidation at the photoanode and replenishes the hole in CdS QDs, regenerates the dot, and the

same cycle of e^- - h^+ separation by illumination and subsequent steps follow. Upon swapping the electrical connections, as shown in **Figure 7.6c**, i.e., by connecting the $TiO_2/CdS/ZnS/Au$ (I) photoanode with MWCNT/Ag (B) and by connecting MWCNT/FTO (A) with MWCNT/FTO (III), the MWCNT/FTO (III) electrode discharged to 0 V, in a time span of 10 s, followed by an increase in voltage in the reverse direction till a value of -0.5 V was acquired in a time span of 37 s, which is nearly equal to time required for charging from 0 to $+0.5$ V (when the electrical connections were just the reverse). In this reverse charging cycle, electrons flow out of the MWCNT/FTO (III) supercapacitor electrode to the MWCNT/FTO (A), counter electrode of the QDSSC, and again, the CdS QDs are regenerated after electrolytic reduction and oxidation. Now, as the QDSSC continues to be illuminated, the photocurrent generated by the photoanode is directed to MWCNT/Ag (B) for charging instead of MWCNT/FTO (III), which was the case in the previous scenario and the same cycle of charging, electrolyte reduction/oxidation and CdS QD regeneration occur.

When the discharge was performed in dark (**Figure 7.6d**, by retaining the same electrical connections as shown in **Figure 7.6c**), electrons flow from the MWCNT/FTO (III) supercapacitor electrode to the QDSSC counter electrode: MWCNT/FTO (A) and the holes in CdS QDs are replenished. The discharge time from $+0.5$ to 0 V was found to be 75 s. In dark, however the photoanode produces no current and therefore the electrical double layer formation in the supercapacitor part of the cell terminates and therefore both processes: charging of MWCNT electrodes and photocurrent production come to a halt. The reason for longer discharge time in dark is the fact that self-discharge is expected to occur over a longer time span (75 s) compared to the scenario wherein, light triggered the charging of the MWCNT electrode in the opposite direction (**Figure 7.6c**), when the connections were swapped and therefore the electrode abruptly acquired 0 V in 10 s. The charge-discharge profile under light on-off and connection swap modes is shown in **Figure 7.7**.

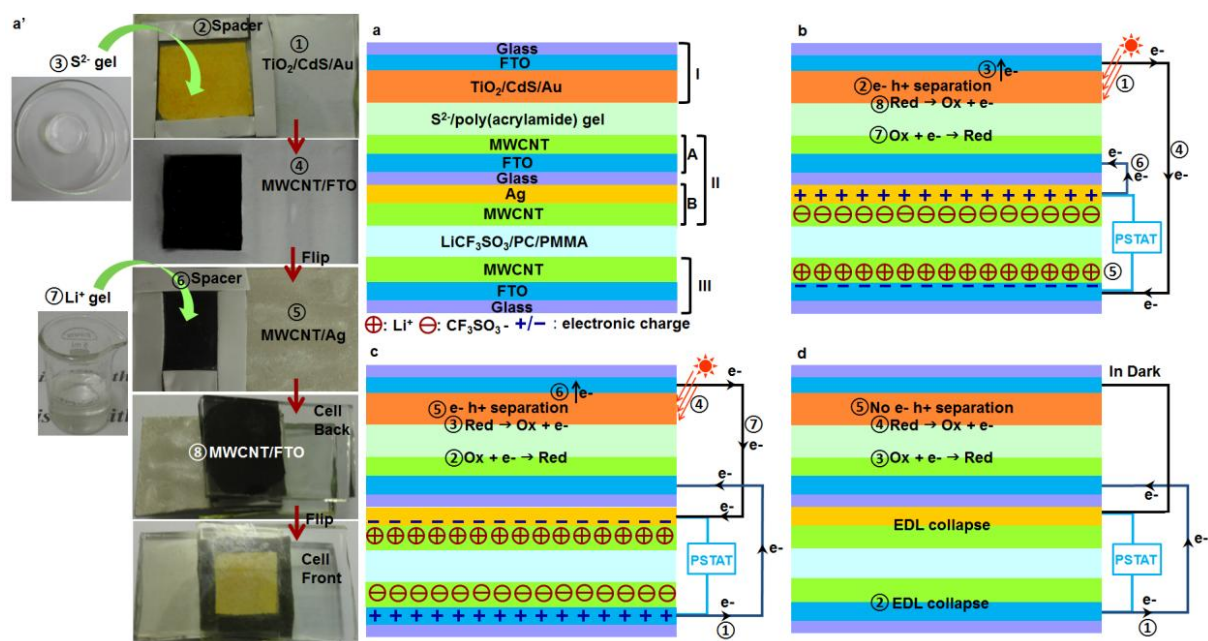


Figure 7.6: Schematics of (a) the photovoltaic supercapacitor configuration with the following electrodes: (I): $\text{TiO}_2/\text{CdS}/\text{Au}$, (II): (A) MWCNT/FTO and (B) MWCNT/Ag and (III): MWCNT/FTO , (b) sequence (1 to 8) of phenomena that lead to the charging of the supercapacitor under illumination, electrodes: I and III and electrodes: A and B of II are connected via external circuit, (c) sequence (1 to 8) of phenomena that lead to the discharging of the supercapacitor, followed by charging in the opposite direction, under illumination, electrodes: I and B of II and electrodes: A of II and III are connected via external circuit and (d) sequence (1 to 5) of phenomena that lead to discharging of the supercapacitor in dark; connections are similar to those in (c). Experiments were performed under zero bias and zero current from the potentiostat. Electrodes B of II and III were connected to the potentiostat for recording charge-discharge characteristics and cyclic voltammograms. (a') are the steps illustrating cell construction with photographs.

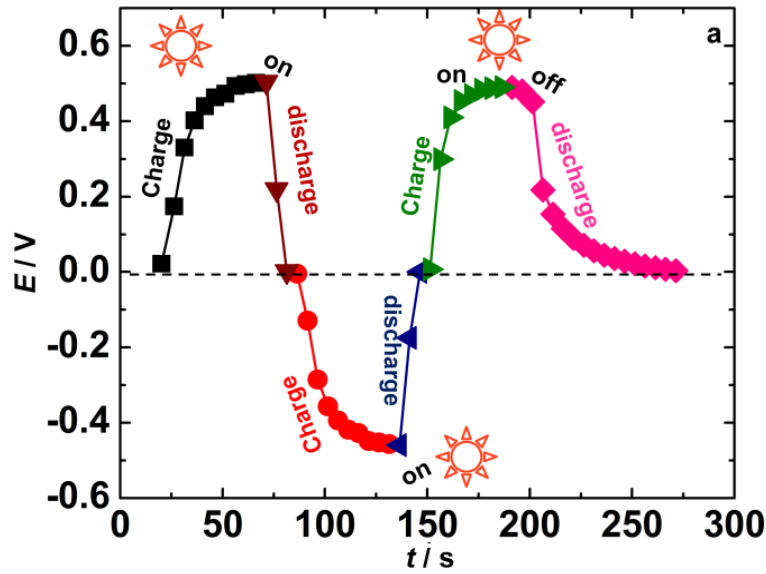


Figure 7.7: (a) Charge-discharge characteristics of the solar powered supercapacitor, under illumination (0.2 mW cm^{-2}) and in dark. In light: In the 1st charge, electrodes I and III, A and B of II are connected. In light: the 1st discharge is followed by 2nd charge and 2nd discharge and in dark: the 3rd discharge occurs; in all these, I and B of II and electrodes: A of II and III are connected.

The specific capacitance of the supercapacitor was calculated using the following equation from slope of the discharge curve.

$$C = I \times \Delta t / \Delta V \times m \quad (4)$$

In equation (4), C is the specific capacitance, I is the current applied for discharge, Δt is the time in seconds for discharge, ΔV is the voltage window and m is the mass of the active material of the working electrode. When the cell was discharged in dark, the specific capacitance was 150 F g^{-1} . To quantitatively evaluate the charge storage capacity, the specific capacitance of the symmetric supercapacitor part was determined independently from cyclic voltammetry, (**Figure 7.8b**) by only connecting the supercapacitor electrodes to the potentiostat and by using the following equation.

$$SC = (\text{integral area of the CV curve}) / \text{scan rate} \quad (5)$$

The obtained specific capacitance was 200 F g^{-1} which is comparable to the specific capacitance obtained for the same cell when powered by the plasmonic QDSSC. Previously,

Niu et al., reported a specific capacitance of 102 F g^{-1} for CNTs electrodes pre-treated with nitric acid.^[10] In yet another report on MWCNTS used as electrodes in $1 \text{ M H}_2\text{SO}_4$, a high specific capacitance of 249 F g^{-1} was achieved,^[11] which is better than most of the reported values for CNT based electrodes. The higher capacitance of the MWCNTs over single walled CNTs can be attributed to the presence of the mesopores due to the open central canal and accessible network of entangled nanotubes, which facilitates the transfer of the ions from the solution to the charged interface.^[12] But it must be noted that a direct comparison with literature values is not reasonable, for the reported values are for systems which are powered by external power sources or potentiostats, capable of delivering non-fluctuating stable currents over long periods of time, whereas here we charged the supercapacitor, using a plasmonic QDSSC.

The cycling stability of the photovoltaic supercapacitor was gauged, by measuring the charge-discharge characteristics for 25 cycles (**Figure 7.8c**). The variation of specific capacitance was reasonably small, between 150 to 102 F g^{-1} when the cell was charged (in light, input power: 20 mW cm^{-2} , $I = 1 \text{ mA}$) and discharged (in dark) 25 times. The robust and reproducible performance of the photovoltaic supercapacitor which utilizes a combination of an inexpensive plasmonic QDSSC and a MWCNT electrical double layer supercapacitor is commendable for it literally does away with the need of any external electrical power source, as it relies only on solar energy for charging a supercapacitor, which in turn can power electronic devices.

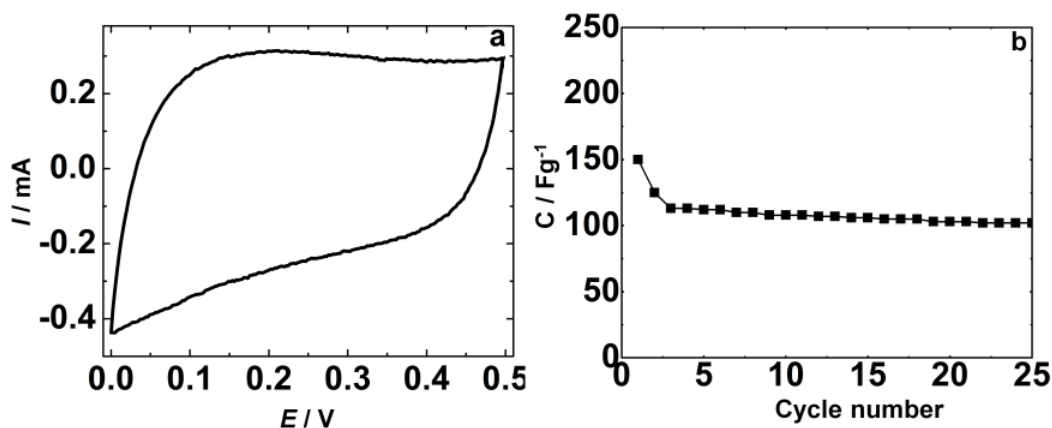


Figure 7.8: (a) Cyclic voltammogram of the MWCNT supercapacitor part containing a 0.2 M LiCF_3SO_3 /PMMA gel and (b) specific capacitance change as a function of the number of cycles under light on-off conditions.

7.3.6 EIS analysis

To evaluate the role of internal resistances in the electrodes on photovoltaic or supercapacitor performances, the electrochemical impedance data expressed as Nyquist plots (**Figure 7.9**) were recorded for the QDSSC as well as for the supercapacitor independently. The measurements were performed over a frequency range of 10^{-2} to 10^6 Hz under an ac amplitude of 10 mV. For the solar cell part, the measurement was done under a dc potential of 0 V superimposed over the ac voltage (**Figure 7.9a**). The resultant plot consists of two semicircles, a small semicircle at high frequency and a large semicircle at an intermediate frequency. The hemisphere at high frequency represents the charge transfer resistance at the counter electrode and the electrolyte interface, whereas the large semicircle is ascribed to the charge transfer resistance at the working electrode and the electrolyte interface. The charge transfer resistance for the $\text{TiO}_2/\text{CdS}/\text{Au}$ electrode is significantly less compared to the TiO_2/CdS system, which indicates that the charge separation is more efficient in the presence of the Au fibers. The plasmonic device showed a charge transfer resistance of $\sim 558 \Omega \text{ cm}^{-2}$ whereas the non-plasmonic one showed a value of $\sim 1338 \Omega \text{ cm}^{-2}$. From the optical studies it

is evident that the excited electrons of the CdS can be transferred to the Fermi level of the Au fibers. The electron hole recombination rate is retarded compared to the non-plasmonic cell.

For the supercapacitor part, impedance was performed at a dc potential of +0.45 V and the resulting spectrum consists of a small semicircle and a Warburg diffusion line. The semicircle at the high frequency region represents the resistive nature of the supercapacitor. The semicircle has two intersections on the real axis. The first intersection of the semicircle represents the ohmic resistance of the bulk electrolyte solution. The diameter of the semicircle represents the charge transfer resistance which is $\sim 5.8 \Omega \text{ cm}^{-2}$. Such a low value of resistance indicates that the MWCNTs will be highly receptive to ingress of both electrolyte ions and electrons from the external circuit. The Warburg element at lower frequency represents the ion diffusion into the bulk of the electrode through pores.^[12] Since the Warburg line almost makes a 90° angle, the behavior is capacitive, rather than resistive, which is generally observed in EDLCs.

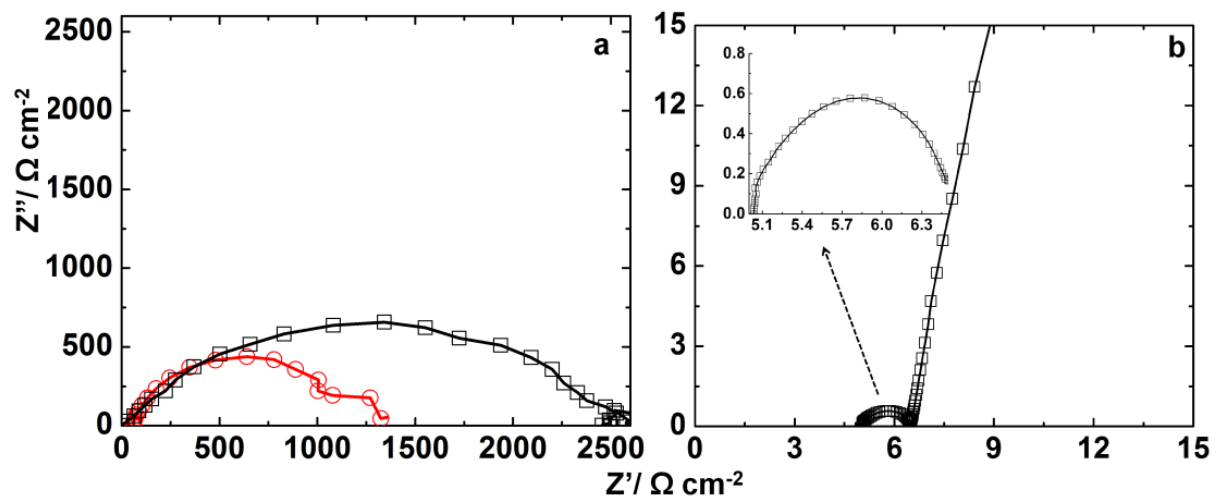


Figure 7.9: Nyquist plots recorded under an ac amplitude of 10 mV for (a) photoanodes based on TiO_2/CdS (\square) and $\text{TiO}_2/\text{CdS}/\text{Au}$ (\circ) and (b) the MWCNT supercapacitor part at a dc potential of +0.45 V.

7.4 Summary

In this chapter a novel design for a solar powered supercapacitor was demonstrated by combining a plasmonic QDSSC which provided the electrical stimulus for charging a contiguously linked MWCNT based supercapacitor. A Janus type electrode composed of MWCNTs on either side, wherein one surface served as the counter electrode for the QDSSC and the other as the supercapacitor electrode was constructed and assembled into a photo-supercapacitor for the first time. A plasmonic photoanode with Au fibers embedded in a TiO₂/CdS assembly was used for powering the supercapacitor part. Plasmonic effects and the electron conducting capability of Au fibers translated into increased photocurrents via increased visible light absorption of CdS, enhanced IPCE and increased PCE for the TiO₂/CdS/Au cell compared to the non-plasmonic cell. The photocurrent generated by the plasmonic QDSSC part of the cell was efficiently directed to the MWCNT supercapacitor part of the cell, and a capacitance of 150 F g⁻¹ was achieved without the aid of any external electrical pulse. The solar powered supercapacitor retained 68% of its original capacitance at the end of 25 redox cycles, when operated under 0.2 sun illumination for a prolonged period of time, thus ratifying the stability of the plasmonic QDSSC part in producing invariant photocurrents under extended exposure and the supercapacitor part in enduring repeated cycling without undergoing degradation.

7.5 References

- [1] F. Kim, K. Sohn, J. Wu, J. Huang, *J. Am. Chem. Soc.* **130** (2008) 14442-14443.
- [2] M. Brust, M. Walker, D. Bethell, D. J. Schiffrin, R. Whyman, *J. Chem. Soc. Chem. Commun.* (1994) 801-802.
- [3] D. Paz-Soldan, A. Lee, S. M. Thon, M. M. Adachi, H. Dong, P. Maraghechi, M. Yuan, A. J. Labelle, S. Hoogland, K. Liu, E. Kumacheva, E. H. Sargent, *Nano Lett.* **13** (2013) 1502-1508.
- [4] A. Wood, M. Giersig, P. Mulvaney, *J. Phys. Chem. B* **105** (2001) 8810-8815.
- [5] H. Choi, W. T. Chen, P. V. Kamat, *ACS Nano* **5** (2012) 4418-4427.
- [6] Z. A. Peng, X. G. Peng, *J. Am. Chem. Soc.* **124** (2002) 3343-3353.
- [7] D. Qu, F. Liu, Y. Huang, W. Xie, Q. Xu, *Opt. Express* **19** (2011) 24795-24803.
- [8] H. Li, K. Yuan, Y. Zhang, J. Wang, *ACS Appl. Mater. Interfaces* **5** (2013) 5601-5608.
- [9] H-W. Chen, C-Y. Hsu, J-G. Chen, K-M. Lee, C-C. Wang, K-C. Huang, K-C. Ho,

J. Power Sources **195** (2010) 6225-6231.

[10] C. Niu, E. K. Sichel, R. Hoch, D. Moy, H. Tennent, *Appl. Phys. Lett.* **70** (1997) 1480-1482.

[11] H. Jiang, T. Zhao, C. Z. Li, J. Ma, *Chem. Commun.* **47** (2011) 8590-8592.

[12] H. Jiang, L. P. Yang, C. Z. Li, C. Y. Yan, P. S. Lee, J. Ma, *Energy Environ. Sci.* **4** (2011) 1813-1819.

[13] A. Burke, *J. Power Sources* **91** (2000) 37-50.

Chapter 8

Plasmonic effects of Au encapsulated carbon dots increase the efficiency of a ZnO based DSSC

8.1 Introduction

In this chapter, the use of plasmonic effect was further explored, to improve QDSSC efficiencies, and cells using Au@C-dots in the photoanode were constructed. In this chapter, ZnO, instead of TiO₂, was used as the wide gap semiconductor. ZnO is expected to improve the cell performance due to a higher electron mobility compared to titania. Herein, ZnO nanorods were prepared by a hydrothermal route and water suspendable, fluorescent Au@C-dots by facile hydrothermal methods; the latter by dehydration of glucose in the presence of an Au salt. DSSCs were constructed with ZnO nanorods as the wide-gap semiconducting support and capable of absorbing high energy photons which enabled FRET, N-719 dye as the principal sensitizer and energy acceptor and an Au@C-dots overlayer which served as a plasmonic electron conduit capable of high light absorption and rapid charge propagation. The Au@C-dots also presented an energetically favorable CB position which permitted fast charge transfer in the photoanode. An ionic liquid based iodine-iodide redox couple functioned as the electrolyte and a MWCNTs layer was used as the counter electrode. The role of Au@C-dots and the dynamics of energy transfer from ZnO nanorods to N719 dye in improving the photovoltaic performance of the DSSC were discerned by following charge/energy transfer dynamics by absorption, fluorescence quenching and lifetime measurements. The synergy between N719 dye and Au@C-dots was also realized from their independent contributions to increasing the IPCE in the 510-550 wavelength range of the visible spectrum. I-V characteristics of DSSCs with and without Au@C-dots were compared.

The use of plasmonic Au@C-dots was further explored by integrating the ZnO/N719/Au@C-dots photoanode with electrochromic MoO₃ as counter electrode for photoelectrochromic applications.

8.2 Experimental

8.2.1 Au@C-dots and photoanode fabrication

Au@C-dots were synthesized by a hydrothermal technique using a procedure reported by Sun et al.^[1] A solution of HAuCl₄ (1 mL, 0.02 M) was added to a glucose solution (40 mL, 0.5 M) with continuous stirring and a clear solution was obtained. The solution was placed in a 40-mL teflon-sealed autoclave and maintained at 160-180 °C for 4 h. The black products were isolated by centrifugation, cleaned by three cycles of centrifugation, washing and re-dispersion in water and in alcohol, and oven-dried at 80 °C for ~4 h. The precipitate was dispersed in ultra-pure water (50 mL) and it was sonicated for 30 minutes and the resulting deep brown colloidal dispersion of Au@C-dots was used.

ZnO nanorods were synthesized by a hydrothermal route. Briefly, aqueous solutions of zinc nitrate (0.1 M) and hexamine (0.1 M) were mixed and magnetically stirred for 10 minutes. The resulting clear solution was transferred to a 100 mL Teflon lined autoclave and kept at 95 °C for 2 h. The white precipitate was isolated by centrifugation and washed with copious amount of waters and ethanol and oven dried at 80 °C for 4 h.

A paste of ZnO nanorods was prepared by dispersing 1.5 g of ZnO powder in 10 mL of ethanol and sonicated for 30 min for uniform dispersion. The ZnO paste thus obtained was applied over FTO coated glass using doctor-blading. The film was initially heated at 90 °C for 30 min. and then annealed at 350 °C for 1 h. After cooling down to 80 °C, the ZnO electrode was immersed in a solution of acetonitrile and *tert*-butanol (volume ratio 1:1) containing 0.5 mM N719 dye for 2 h. The active surface area for photoanode was fixed as

0.25 cm⁻². After washing the electrode with acetonitrile to remove the superfluous dye, Au@C-dots were drop casted over this ZnO/N719 assembly. The ZnO/N719/Au@C-dots electrode was obtained upon solvent evaporation.

8.2.2 MWCNT electrode and DSSC construction

MWCNTs deposited over FTO were employed as the counter electrode. The functionalization has explained briefly in **Chapter 4**. DSSCs were constructed by affixing an adhesive acrylic spacer (640 μm thick and 3 mm wide) on the MWCNT/FTO electrode. Two ports, each of one mm width were left open and the photoanode (film side facing inwards) was affixed onto the spacer. The I₂/I⁻ electrolyte (0.03 M iodine and 0.6 M 1-methyl-3-butylimidazolium iodide in acetonitrile/ tert-butanol (85:15)) was injected into the assembly and the ports were sealed with an epoxy sealant.

8.3 Results and discussion

8.3.1 Structural features of Au@C-dots and ZnO nanorods

The survey scan illustrating the presence of various elements: C, O and Au in Au@C-dots are shown in **Figure 1a**. The deconvoluted C1s core level spectrum of Au@C-dots (**Figure 8.1b**) showed two low intensity peaks at 288.1 and 281.1 eV flanking the high intensity peak at 284.6 eV corresponding to C-C bonds. The high and low energy peaks on either side of the C-C peak originate from C-O and C-Au interaction in Au@C-dots. Since Au@C-dots were synthesized using an aqueous suspension of glucose via a hydrothermal route, the oxidation of some C-C bonds to yield C-OH or C-O-C groups is feasible which is responsible for the asymmetric structure of C1s signal. Further, the carbon encapsulating the electron rich metal (Au) is responsible for the weak signal at a higher binding energy. The Au4f spectrum revealed the Au(4f_{5/2}) and Au(4f_{7/2}) signals at 87.9 and 84.2 eV with a peak separation of 3.7 eV (**Figure 8.1c**). These values are comparable to those reported for pure elemental Au

having the Au(4f_{5/2}) and Au(4f_{7/2}) signature peaks at 87.94 and 84 eV.^[3,4] The retention of these peaks clearly illustrated the complete reduction of Au³⁺ to Au⁰ in Au@C-dots. The presence of C-O groups was also seen from the broad O1s signal seen at 531 eV (inset of **Figure 8.1a**). The density of states near the Fermi level for Au@C-dots is displayed in the VB spectrum in **Figure 8.1d**. The VB position of Au@C-dots extracted from the plot was found to be 6 eV, and this value was used for explaining the energetics of the system. The loading of Au onto C-dots, deduced from the ratio of I_{C-Au}/I_{C-C} contributions in the deconvoluted C1s spectrum of Au@C-dots was ~0.18. The value of I_(C-O)/I_(total) gave a measure of the level of oxidation of C-dots and it was found to be fairly low, approximately 0.07, indicating that the network of carbon atoms was largely preserved in Au@C-dots.

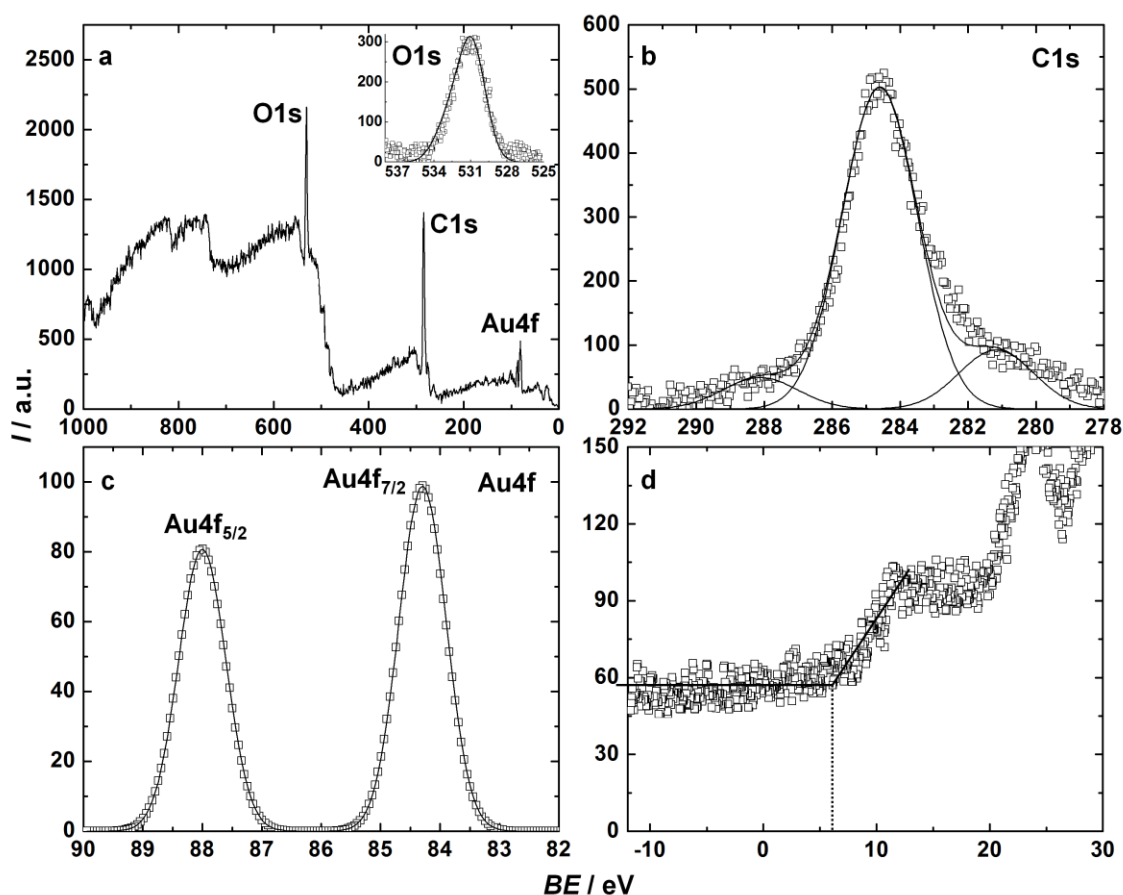


Figure 8.1: (a) XPS survey spectrum of Au@C-dots and deconvoluted core level spectra of (b) C1s, (c) Au4f and O1s (inset of (a)) and (d) VB spectrum of Au@C-dots displaying the Fermi edge.

8.3.2 SEM and TEM analysis

The low magnification SEM image of ZnO nanorods (**Figure 8.2a**) shows clumps of nanorods misaligned with respect to each other but packed in a dense crisscross manner which can enable a high dye loading. The rods have hexagonal geometrical shapes and their facets are clearly defined and they terminate with hexagonal end planes. The corresponding high magnification image (**Figure 8.2b**) shows that ZnO nanorods form a continuous network with very few void spaces. The rods have smooth surfaces and their lengths vary from 0.5 to 2 μm and their widths typically, lie between 100 to 500 nm. Some of the rods are not very long, and they appear like thick hexagonal disks. However, such a morphology with a high available surface area is most conducive for anchoring a large number of dye molecules. The TEM image of the ZnO nanorods (**Figure 8.2c**) also showed the rods to have a hexagonal end facets and rectangular side-walls. The HRTEM image of a ZnO nanorod shows the fringe spacing to be 0.28 nm (**Figure 8.2d**) which matches with the (100) plane of hexagonal ZnO (wurtzite) corresponding to $d = 0.2817$ nm as per PDF number 891937. The growth axis of the nanorod is perpendicular the fringe-spacing and is shown with a dashed arrow. The EDX plot of ZnO nanorods (**Figure 8.2e**) showed two strong signals from Zn and O and no other impurity signals were seen, thus suggesting a pure hexagonal phase ZnO formation. The atomic percentages of Zn and O are 52.5 and 47.5, the Zn:O ratio is 1.1 which is indicative of slight oxygen deficiency.

The SEM image of Au@C-dots shows the presence of quasi-spherical shapes embedded in a porous particulate network (**Figure 8.2f**); closer inspection of the network reveals the presence of many small spheres not fully developed with indistinct grain boundaries but interconnected to each other. The average diameter of the clearly visible spheres ranges between 100 to 250 nm. The EDX plot extracted from one such sphere is shown in **Figure 8.2g**. Distinct signals from C, O and Au are observed indicating that the C-dots are oxidized

and Au is present in the spheres. The TEM image of Au@C-dots shows the presence of overlapping core/shell particles (**Figure 8.2h**) and the size of the particles ranges from 130 to 250 nm, which matches with SEM observations. The enlarged view of one such core/shell shows the amorphous C-dots ensconcing crystalline Au. The observed fringe spacing is 0.2 nm (**Figure 8.2i**) which agrees with a d-spacing of 0.2039 nm corresponding to the (200) plane of Au with a fcc lattice (PDF: 652870).

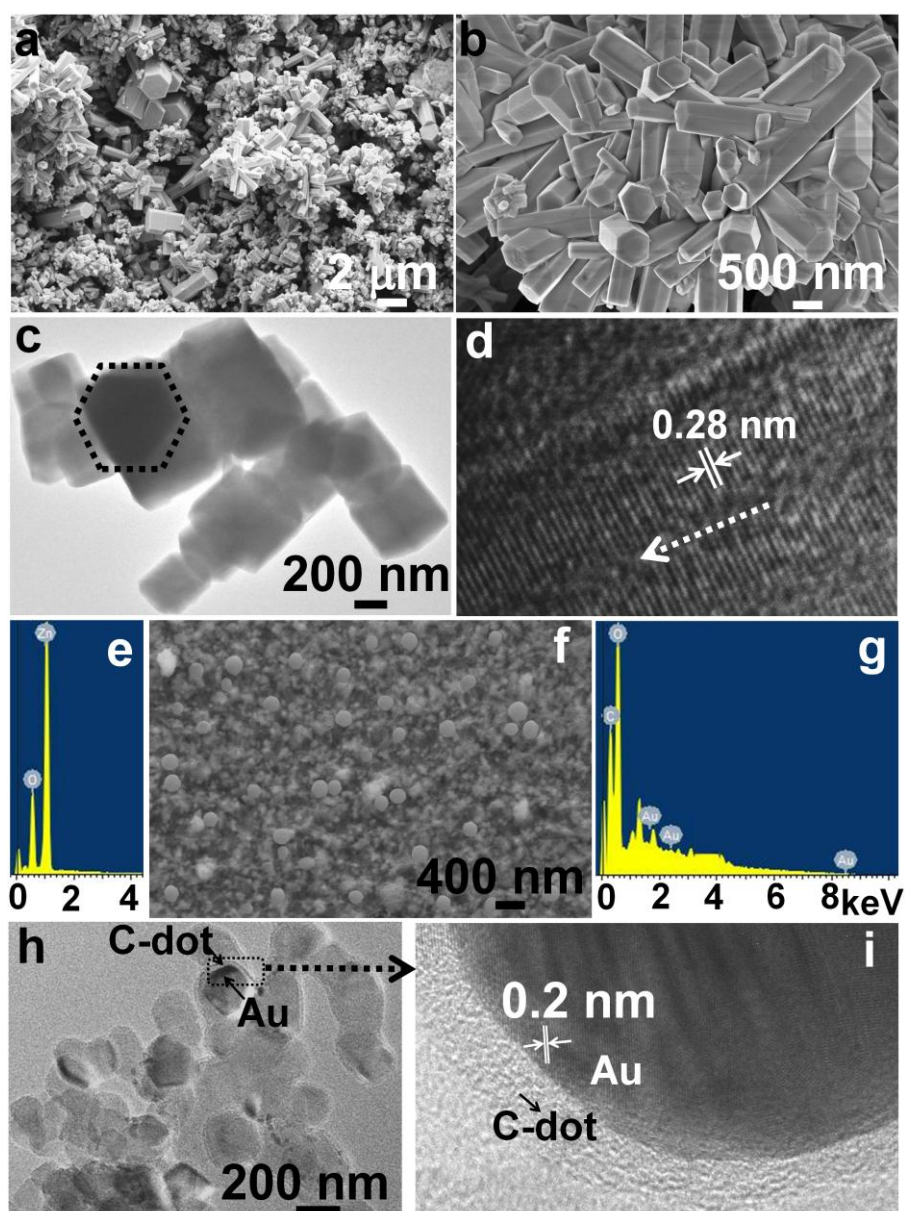


Figure 8.2: SEM images of ZnO nanorods at (a) low and (b) high magnifications, (c) TEM and (d) HRTEM images of ZnO nanorods, (e) EDX plot of ZnO nanorods, (f) SEM image, (g) EDX plot, (h) TEM image and (i) lattice scale image of Au@C-dots.

8.3.3 Structural characterizations of ZnO and Au@C-dots

The Raman spectrum of Au@C-dots reveals a graphitic structure for C-dots. The XRD pattern of ZnO nanorods (**Figure 8.3**) also confirmed the crystal structure. The observed d -values match well with the hexagonal crystal structure of ZnO in accordance with the PDF file number 891397. The Raman spectrum of Au@C-dots shows a peak at 1413 cm^{-1} which is attributed to the D band, characteristic of sp^3 hybridized carbon in C-dots.

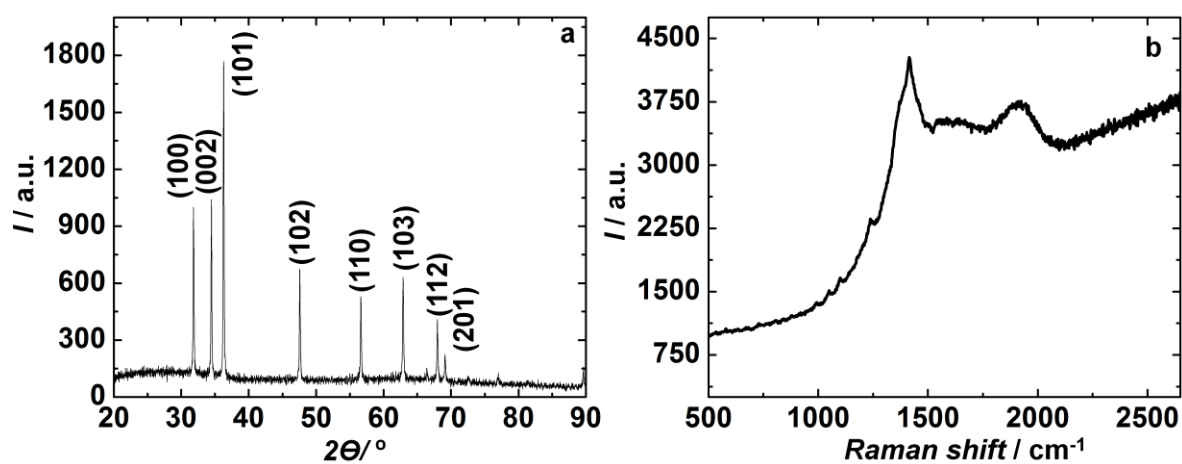


Figure 8.3 (a) XRD pattern of ZnO nanorods, the hkl values are expressed within parentheses and (b) Raman spectrum of Au@C-dots.

8.3.4 Plasmonic and interactive effects of Au@C-dots

N719 dye molecules anchored over the wide band gap ZnO nanorods were employed as the sensitizers. To further improve the solar cell performance, plasmonic Au nanoparticles encapsulated in C-dots referred to as Au@C-dots were also included in the ZnO/N719 assembly. To probe the plasmonic effect induced by Au nanoparticles, the absorption spectra of various components were recorded (**Figure 8.4c**). The aqueous solution of Au@C-dots shows a surface plasmon resonance peak at $\sim 590\text{ nm}$ (**Figure 8.4a**) which is red-shifted compared to the pristine Au nanoparticles (530 nm) prepared by borohydride reduction method reported in literature.^[4] The shift in the absorption is due to a higher refractive index imparted by the thick C-dots shells. The pristine N719 dye solution showed a λ_{max} at 530 nm

and a shoulder at 356 nm. The optical band gap deduced for the dye from the absorption edge is 1.9 eV. However, upon incorporating the dye in ZnO, the resulting film did not show the plasmonic peak possibly due to the swamping of this peak by the featureless but strong absorption of ZnO. For the ZnO/N719/Au@C-dots film, a broad absorption centered at 533 nm is observed and the intensity of this absorption increased appreciably for the ZnO/N719/Au@C-dots film compared to ZnO/N719 film. This enhancement in absorption of the N719 dye can be attributed to the plasmonic effect of Au nanoparticles. It is effected either by scattering of light by Au plasmons, which increase the optical path length of light within the film and improve the dye's absorption or by the near field coupling between the surface plasmon polariton and the excited state of the dye.^[5]

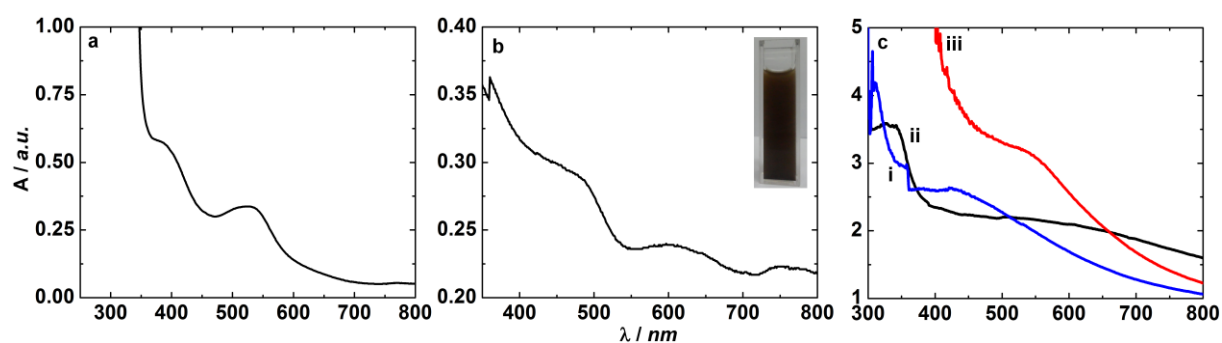


Figure 8.4: Absorption spectra of (a) N719 dye solution, (b) Au@C-dots dispersion and (c) (i) ZnO/Au@C-dots, (ii) ZnO/N719 and (iii) ZnO/N719/Au@C-dots.

8.3.5 Emission and lifetime studies

It is well known that the C-dots are highly photoluminescent materials. The fluorescence spectrum of Au@C-dots (**Figure 8.5a**) recorded at an excitation wavelength of 370 nm shows a peak at 443 nm corresponding to the band edge emission. This emission spectrum is consistent with previously synthesized C-dots by other techniques.^[6,7] To study the interaction between N719 dye and Au@C-dots, an aliquot of 100 μL of N719 dye (0.5×10^{-5} M) was added to an aqueous dispersion of Au@C-dots (1 mg mL^{-1}) and fluorescence was measured. The intensity of the emission peak increased by ~ 1.5 times for the N719 dye +

Au@C-dots solution compared to Au@C-dots. This emission increase is not a dilution effect was proved by measuring the emission spectrum of a pristine diluted Au@C-dots (0.5 mg mL⁻¹); emission decreased with dilution. The increase with dye addition is therefore indicative of charge transfer from the N719 dye to the CB of the C-dots. The energy level offsets are conducive for this charge transfer as the CB of N719 dye and Au@C-dots lie at 3.8 and 4 eV respectively. On further addition of an aliquot of the dye to Au@C-dots, the fluorescence intensity increased, and thereafter it saturates. Both C-dots and Au nanoparticles are independently known to serve as electron acceptors.^[8]

Further, the electrical conductivity of Au@C-dots was determined to be ~0.2 S cm⁻¹ at ambient temperature by an ac impedance method. The high conductivity is favorable for fast electron transfer as well as rapid charge transport and this can reduce electron hole recombination. Therefore in the ZnO/N719/Au@C-dots assembly, the excited electrons of the dye can be transferred either to the CB of ZnO nanorods which lies at 4.3 eV or to the Fermi level of the Au@C-dots (3.8 eV). Both can subsequently transfer electrons to the current collector.

To ratify that electron transfer occurs from the N719 dye molecules to Au@C-dots, the emission decay profiles were analyzed. The excited state lifetime of pristine Au@C-dots was procured at an emission wavelength of 443 nm with $\lambda_{ex} = 370$ nm (**Figure 8.5b**). The fluorescence data was fitted to a bi-exponential decay function expressed in equation 1.

$$I = A_1 \exp(-t/\tau_1) + A_2 \exp(-t/\tau_2) \quad (1)$$

In (1), I is the normalized emission intensity, t is the time after LED excitation, A₁, A₂ are the amplitude coefficients and τ_1 , τ_2 are the decay time constants. The average lifetime was calculated by using the following equation and the fitted parameters are collated in **Table 8.1**.

$$\langle \tau \rangle = \frac{\sum_i A_i \tau_i^2}{\sum_i A_i \tau_i} \quad (2)$$

The Au@C-dots aqueous solution exhibited an excited state average lifetime of 1.35 ns, which was ascribed to the electron hole recombination in C-dots. The average lifetime of a N719 dye/Au@C-dots suspension obtained at the same emission wavelength of 443 nm increased to 1.83 ns. The slow decay component was longer for pristine Au@C-dots (2.4 ns) compared to N719 dye/Au@C-dots (2.2 ns), whereas the fast decay component was shorter for pristine Au@C-dots (0.25 ns) as opposed to N719 dye/Au@C-dots (0.3 ns). In Au@C-dots, the slow component is due to surface trap states and the fast one is ascribed to the band edge recombination. In the presence of the dye, upon electron transfer to Au@C-dots, the surface trap states recombine faster while the band edge recombination takes longer time, possibly because time taken for electron transfer from the dye to surface states on Au@C-dots will be shorter than the time taken for electrons to be transferred to the CB of Au@C-dots.

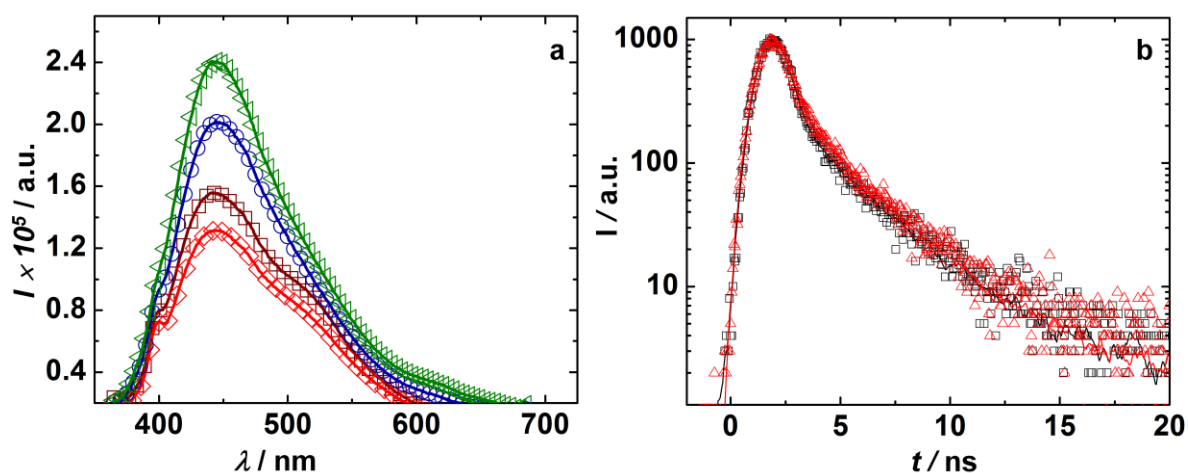


Figure 8.5: (a) Emission spectra of aqueous solutions of Au@C-dots with ($\lambda_{\text{ex}} = 370$ nm). Fluorescence of Au@C-dots (\square) and diluted Au@C-dots (\diamond) and as a function of increasing volume of 0.5×10^{-5} M N719 dye solution in undiluted Au@C-dots: 100 μL (\circ) and 200 μL (\triangle). (b) Time resolved fluorescence decay analysis of Au@C-dots aqueous solution (\square) and a dispersion of 0.5×10^{-5} M N719 dye (200 μL) and Au@C-dots solution (\triangle) with $\lambda_{\text{ex}} = 370$ nm and $\lambda_{\text{em}} = 443$ nm.

8.3.6. Energy transfer between ZnO and N719 dye

Apart from the plasmonic effect, the possibility of FRET from ZnO nanorods to the N719 dye also exists. For excitation transfer from a donor to an acceptor via FRET, certain prerequisites have to be satisfied. The emission of ZnO nanorods should overlap with the absorption of N719 dye. The luminescence spectrum of ZnO nanorods (**Figure 8.6b**) shows a peak at 551 nm at an excitation wavelength of 370 nm which is consistent with emission data of previously reported ZnO nanostructures.^[9,10] This visible light emission can be assigned to the surface defects due to oxygen vacancies. EDX data had also revealed the Zn:O stoichiometric ratio to be greater than unity, implying oxygen deficient ZnO. **Figure 8.6a** shows the overlap of the sharp emission peak of ZnO nanorods with the broad absorption of the N719 dye, the primary criterion for FRET to occur. In an earlier report on ZnO/N719, energy transfer from ZnO nanoparticles to N719 dye was observed and it also increased the overall solar cell performance.^[11] The distance between donor and acceptor was calculated by using the following equation.^[12]

$$R_o^6 = 9000 \ln(10) k^2 Q_D J / 128 \pi^5 n^4 N_A \quad (3)$$

In equation (3), Q_D is the experimentally obtained fluorescence quantum yield of the ZnO donor in the absence of the acceptor N719 dye and the obtained value was 4×10^{-3} , k^2 is the dipole orientation factor and the magnitude of k^2 was assumed to be $2/3$,^[12] N_A is the Avogadro's number and n is the refractive index of the medium, which was fixed as 1.4, determined using reflectance data. J , the spectral overlap integral was calculated from the following expression.

$$J = \int_0^\infty F_D(\lambda) \epsilon_A(\lambda) \lambda^4 d\lambda \quad (4)$$

F_D is the donor fluorescence intensity normalized to unit area (arbitrary units). ϵ_A is the extinction coefficient of the acceptor (in $M^{-1} cm^{-1}$). The spectral integral (J) for the ZnO/N719 system was deduced to be $\sim 6 \times 10^{-14}$ and the resulting Forster radius (R_o) was 1.89 nm, which validated energy transfer from ZnO to the dye. Further evidence for energy transfer

was obtained in the form of quenching of the ZnO luminescence in the presence of the N719 dye ($\lambda_{\text{ex}} = 370$ nm). The emission intensity of ZnO quenched by 2.26 times upon addition of the dye. The possibility of electron transfer from ZnO to N719 dye was ruled out as the CB of ZnO is at 4.3 eV and is 0.6 eV lower than the CB position of the N719 dye.

Lifetime time analysis also confirmed energy transfer. The time resolved fluorescence decay signals were fitted to a bi-exponential function. Pristine ZnO nanorods showed an average life time of ~ 22 ns, which matches well with a previous report on ZnO nanoparticles.^[11] Upon including the dye in the film, the ZnO/N719 film showed a decreased lifetime of 5.74 ns (**Figure 8.6c**). For pristine ZnO film, the fast decay component is attributed to electron transfer to FTO and the slow component to electron-hole recombination within the band gap states. In the ZnO/N719 film, the short lived component of 2.225 ns is ascribed to energy transfer (which is faster than electron transfer) and the long lived component of 7.54 ns arises from (i) recombination in the gap states and (ii) electron transfer from ZnO to FTO. Unlike pristine ZnO, where photoexcited electrons in the gap states are transferrable to FTO, in the presence of the dye, all of these indistinguishable electron transfer modes exist: (i) transfer of photoelectrons generated in the dye by direct excitation when impinged by light to ZnO, (ii) transfer of photoelectrons produced in the dye by absorption of virtual photons or energy from ZnO and (iii) transfer of excited electrons in ZnO to FTO which do not participate in energy transfer. The efficiency of energy transfer (E) was estimated from the lifetime analysis of the ZnO with and without N719, by using the following equation.

$$E = 1 - \tau_{\text{DA}}/\tau_{\text{D}} \quad (5)$$

ZnO showed an energy transfer efficiency of $\sim 66\%$ to N719 dye. The energy transfer rate was $4.4 \times 10^8 \text{ s}^{-1}$. It is obvious that in the ZnO/N719 assembly, energy transfer by FRET (option ii from above) is the pre-dominant mechanism. Through FRET, additional dye

molecules are excited and this can improve photocurrents and therefore, the overall solar cell performance.

Table 8.1: Kinetic parameters of emission decay analysis for different systems deduced from bi-exponential fits.^a

System composition	λ_{ex} (nm)	λ_{em} (nm)	χ^2	τ_1 (ns)	τ_2 (ns)	A_1	A_2	$\langle\tau\rangle$ (ns)
Au@C-dots	370	443	0.93	0.25	2.41	77.58	22.42	1.35
Au@C-dots/ N719	370	443	0.96	0.30	2.20	68.80	31.20	1.83
ZnO	370	550	1.10	22.93	0.19	41.79	58.21	22.63
ZnO/N719	370	550	1.12	2.23	7.54	63.94	36.96	5.74

^aA is the relative amplitude of each lifetime, τ_1 and τ_2 are the components of fluorescence lifetime and χ^2 denotes the fit quality. Au@C-dots and N719 were dissolved in water and the ZnO and ZnO/N719 assembly were solid electrodes.

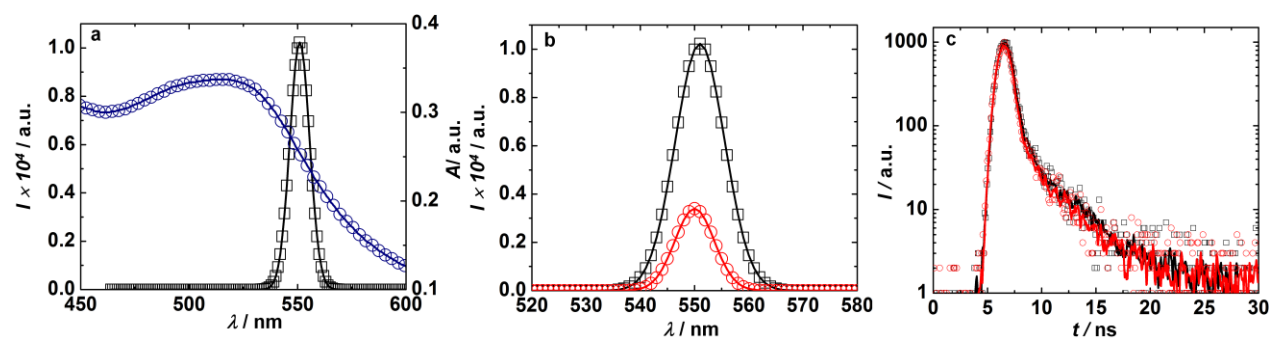


Figure 8.6: (a) Spectral overlap between the absorption of the N719 dye (\circ) and the emission of ZnO nanorods (\square) ($\lambda_{\text{ex}} = 370$ nm), (b) emission spectrum of ZnO film (\square) and the ZnO/N719 electrode (\circ) at an excitation wavelength of 370 nm and (c) emission decay profiles of ZnO (\square) and ZnO/N719 (\circ) electrodes with $\lambda_{\text{ex}} = 370$ nm and $\lambda_{\text{em}} = 550$ nm.

The electron as well as the energy transfer dynamics are shown in the **Figure 8.7**. The photocurrent generation modes that prevail in the ZnO/N719/Au@C-dots electrode are: direct transfer of photoexcited electrons in N719 to ZnO or Au@C-dots, energy transfer from ZnO gap states to N719 dye, and direct electron transfer from Au@C-dots to FTO. The dye's charge separation ability is increased by FRET and by the plasmonic effect of Au@C-dots. Energy transfer from ZnO to Au@C-dots was not possible owing to the presence of N719 intermediate layer; for FRET the donor-acceptor separation should lie within 1-10 nm.^[13]

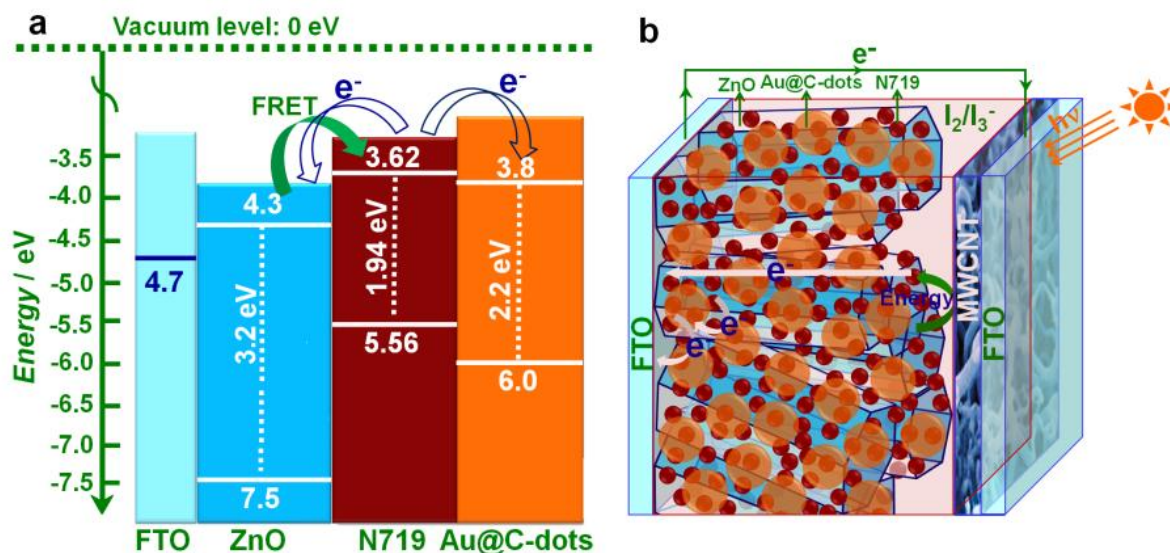


Figure 8.7: Energy level diagram of (a) the ZnO/N719/Au@C-dots photoanode and (b) electron propagation and FRET in the corresponding DSSC.

8.3.7 Plasmonic and FRET enabled DSSCs

It has been foresaid that the localized surface plasmon resonance of Au@C-dots can increase the absorption of the N719 dye and thus increase photocurrents. IPCE were determined for ZnO/N719 and ZnO/N719/Au@C-dots as photoanodes (**Figure 8.8a**). A sandwich type solar cell with an electrolyte consisting of 0.6 M 1,2-dimethyl-3-propylimidazolium iodide, 0.05 M iodine in acetonitrile and a MWCNTs on FTO/Glass as counter electrode. The spectrum of the ZnO/N719 film showed a maximum IPCE in the visible region with a value of 48% at 530 nm. The ZnO/N719/Au@C-dots electrode showed a higher quantum efficiency exclusively due to the LSPR in the wavelength range of 500-550 nm. It showed a highest IPCE value of 53% at 530 nm. In a previous report, Choi et al., observed an overall increment for IPCE in visible region due to the plasmonic effect of Au nanoparticles encapsulated with an insulating SiO₂ shell for a N719/TiO₂ based DSSC.^[14]

Here, in addition to the plasmonic enhancement of IPCE, the IPCE in the 350-450 nm wavelength range, IPCE was enhanced due to FRET, as the electrons of the dye were excited by the indirect absorption of photons due to FRET. The acceptor or dye showed increased

charge separation in the region where it absorbed upon accepting excitation energy from ZnO. From fluorescence and lifetime analysis, it was established that Au@C-dots promote electron transfer and transport. This factor too, contributes towards the increment in IPCE in the overall spectral region.

Figure 8.8b shows the J-V characteristics the cells with ZnO/N719 and ZnO/N719/Au@C-dots electrodes under one sun illumination. The solar cell parameters are summarized in **Table 8.2**. The plasmonic cell showed an enhanced efficiency compared to the non-plasmonic one. The ZnO/N719 based cell showed an overall efficiency of 3.16% whereas the ZnO/N719/Au@C-dots cell showed an overall efficiency of 4.1%. J_{SC} increased ~1.2 times and FF also enhanced for the plasmonic device compared to the non-plasmonic one. However, the V_{OC} decreased slightly for the plasmonic cell in comparison to the conventional cell. It might be due to the shift in the Fermi level of composite to less negative potentials (with respect to the NHE). The increase in the photocurrent and hence the PCE for ZnO nanorods with Au@C-dots can be thus explained on the basis of the enhanced light harvesting due to the LSPR and contribution to photocurrent by direct excitation of Au@C-dots. In an earlier study, for a ZnO nanoflower based cell, an overall efficiency of 1.6% was achieved whereas the Au loaded ZnO nanoflowers gave an improved efficiency of 2.5%.^[15] In an another study, upon incorporation of Au@SiO₂ in the TiO₂ film, the overall efficiency increased from 1.2 to 2.2%.^[16] In order to distinguish the effect of FRET on efficiency, Makhal et al., measured the efficiency for a ZnO/N719 cell in the presence and absence of the UV light. They observed that the high energy photon efficiency increased from 0.11 to 0.24%.^[11] In a similar way, in this assembly too, FRET will contribute to efficiency.

There are only a few reports on C-dots as a light sensitive material. In an earlier report on C-dots sensitized TiO₂ with I₂/I₃⁻ as electrolyte, a J_{sc} of 200 $\mu A cm^{-2}$ was obtained.^[17] The photovoltaic properties of the Au@C-dots sensitized ZnO nanorods were measured and this

cell delivered a J_{sc} of $205 \mu\text{A cm}^{-2}$ (inset of **Figure 8.8b**). These results show the potential of Au@C-dots for increasing PCE in solar cells.

Table 8.2: Solar cell parameters of cells ($\lambda > 300 \text{ nm}$), I_2/I^- based electrolyte, cell area: 0.25 cm^2 , under 1 sun illumination (100 mW cm^{-2}) with the listed photoanodes; all cells with MWCNT/FTO as the counter electrode.

Electrode configuration	V_{oc} (mV)	J_{sc} (mA cm^{-2})	FF	Efficiency (%)
Dye/ZnO	639	10	50	3.16
Dye/ZnO/Au@C-dots	610	11.6	58	4.1
ZnO/Au@C-dots	393	0.203	32	0.02

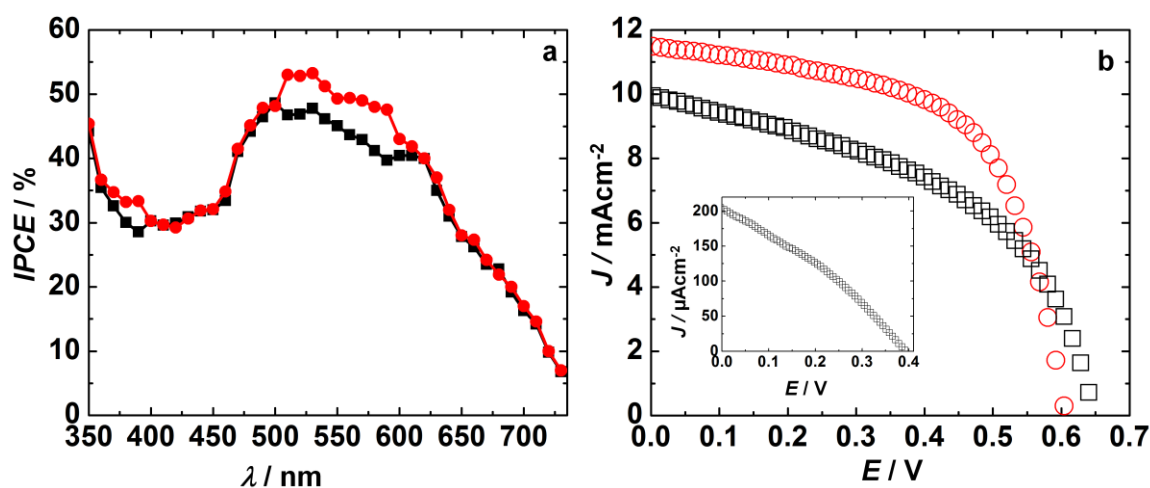


Figure 8.8: (a) IPCE spectra of DSSCs with the following photoanodes: ZnO/N719 (■) and ZnO/N719/Au@C-dots (●) and (b) J-V characteristics of cells with ZnO/N719 (□) and ZnO/N719/Au@C-dots (○) under one sun illumination ($\lambda > 300 \text{ nm}$, 100 mW cm^{-2} , AM1.5). A I_2/I^- redox couple was employed as electrolyte and a MWCNT/FTO assembly as a counter electrode. Inset of (b) is the J-V plot of ZnO/Au@C-dots (without N719) as photoanode.

8.3.8 Photoelectrochromic cells with MoO_3 as coloring counter electrode

The use of plasmonic Au@C-dots was further explored by integrating the ZnO/N719/Au@C-dot photoanode with an electrochromic MoO_3 film as the counter electrode for photoelectrochromic applications.

8.3.9 Fabrication of the MoO_3 electrode

An aqueous 0.05 M ammonium molybdate bath (pH=9) was prepared by dissolving an appropriate weight of AR grade MoO_3 powder in a few cubic centimetre of warm ammonia (NH_3) and then diluted to desired volume with double distilled water. Two FTO substrates were employed as the working as well as the counter electrode. A fixed dc potential of 1.5 V has been applied for 30 s, and MoO_2 was deposited cathodically. As deposited MoO_2 films were annealed at 450-500 °C in an ambient conditions for 1 h. Upon annealing, the pale brown film turned to a transparent film, indicating the formation of crystalline MoO_3 phase.^[18]

8.3.10 SEM analysis

The SEM image of a MoO_3 film shows an undulating morphology with wedge like shapes jutting out of a smooth surface. (**Figure 8.9**).

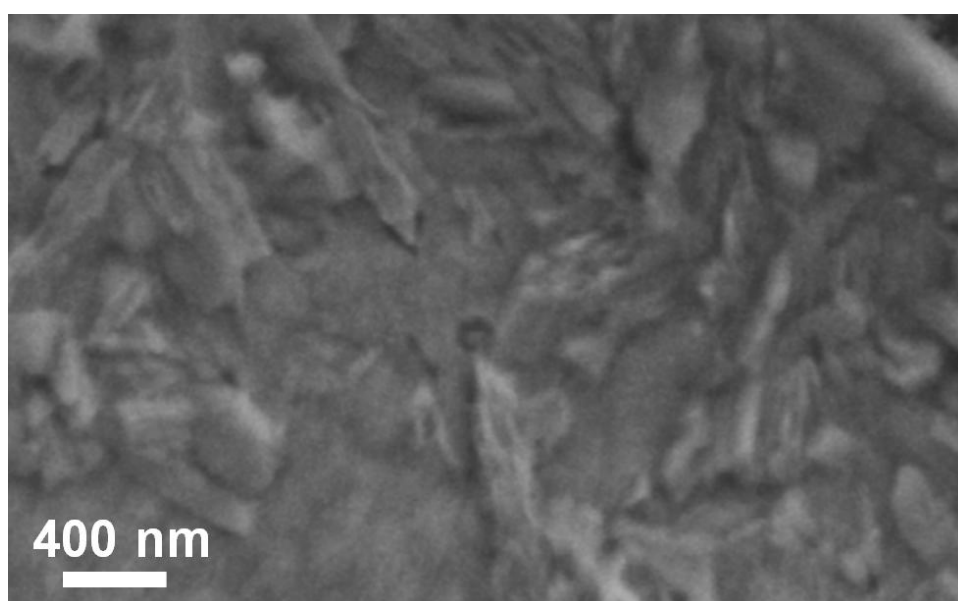


Figure 8.9 SEM image of MoO_3 film.

8.3.11 Structural characterization of MoO_3

The XRD pattern of the air annealed MoO_3 film is shown in **Figure 8.10a**. XRD analysis clearly shows the formation of the crystalline MoO_3 . The observed d-values matches well with the orthorhombic crystal structure of MoO_3 in accordance with the PDF file 35609. A Raman spectrum of crystalline MoO_3 is shown in the **Figure 8.10b**. It showed a peak at 990

cm^{-1} , which is attributed to the Mo=O asymmetric stretching of terminal oxygens. The peak at 813 cm^{-1} was due to the doubly connected bridge-oxygen Mo-O-Mo stretching modes of the doubly coordinated oxygen, caused by corner shared oxygen atoms, common to two MoO_6 octahedra.^[19]

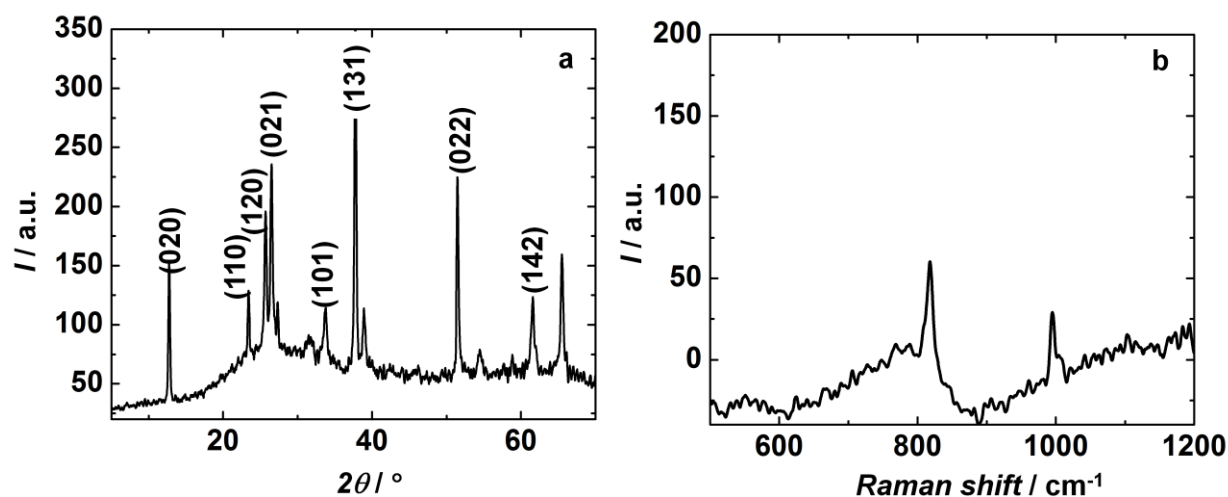


Figure 8.10 (a) XRD pattern of MoO_3 , the hkl values are represented within the parantheses and (b) Raman spectrum of MoO_3 .

8.3.12 Photoelectrochromic response

Photoelectrochemical cells were constructed with ZnO/N719/Au@C-dot as the photoanode, a transparent MoO_3 film as the counter electrode, and I_2/I^- was employed as the electrolyte. The J-V characteristics are shown in **Figure 8.11**. The measurements were done under 1 sun illumination. Upon illumination, the exciton generation takes place and finally the electrons reach at the counter electrode vis-à-vis the external circuit. As in a conventional electrochromic device, the injection of lithium ions into the electrochromic layer causes it to color. Here, it will color according to following equation.



(Transparent, Oxidized) (Blue, Reduced)

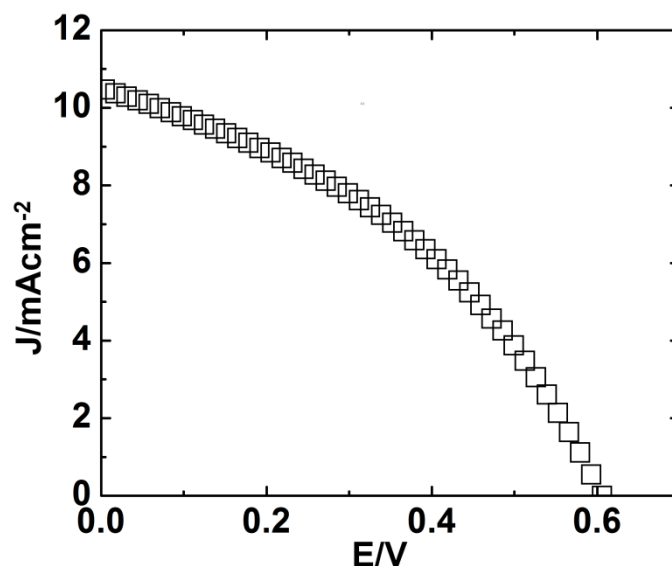


Figure 8.11: J-V characteristics of solar/photoelectrochromic cells with MoO₃ as a counter electrode under one sun illumination ($\lambda > 300$ nm, 100 mW cm^{-2} , AM1.5). A ZnO/N719/Au@C-dot assembly was used as the photoanode and I₂/I⁻ solution was employed as electrolyte.

Electrons are transferred to MoO₃ (in the oxidized state) from the external circuit and Li⁺ ions are inserted from the electrolyte for charge compensation. The reversible color change is between colorless and blue. When sunlight is blocked or in dark, the charge stored in the electrochromic layer drives the process in reverse, releasing lithium ions from the electrochromic layer and triggering it to bleach. Thus, without an external control, the photoelectrochromic device will color in sunlight and bleach in its absence. The external circuit can also be employed to control the device, disconnection of the circuit will cause the device to remain in its current state irrespective of the presence or absence of sunlight. Moreover, an external voltage can be supplied to the device to drive the device to either the bleached or colored state. A typical configuration of a photoelectrochromic device, based on ZnO/N719/Au@C-dot and MoO₃ is shown in **Figure 8.12**.

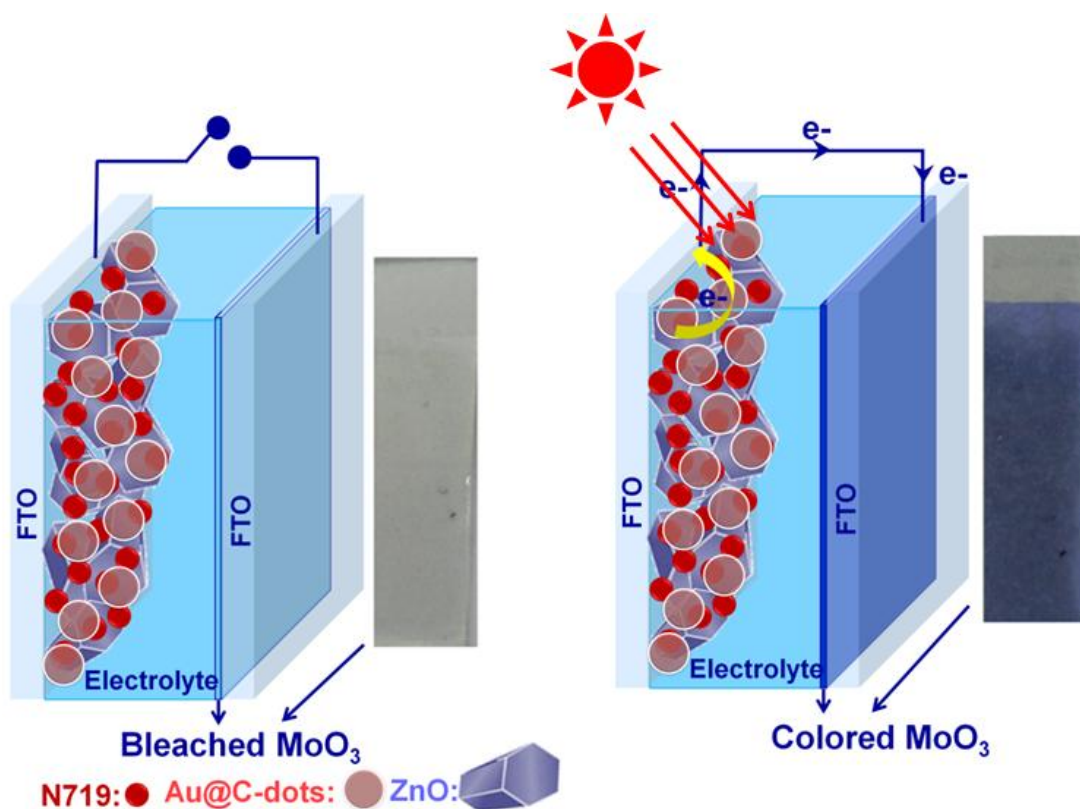


Figure 8.12 Photoelectrochromic cell configurations with MoO_3 as the coloring counter electrode, (a) show the electrochromic in bleached (colorless) state in open circuit and (b) the electrochromic in colored (blue) state under illumination under closed circuit. The photographs of the corresponding films in bleached and colored states are shown.

The transmittance *versus* wavelength curves, recorded for the MoO_3 film when used as the counter electrode with a $\text{ZnO}/\text{N719}/\text{Au@C-dot}$ photoanode, under different durations, of one sun illumination, are shown in **Figure 8.13**. The time spans for which the cell was subjected to 100 mW cm^{-2} light irradiance, were fixed at 10, 20, 30, 40, 50, 60, 70 and 80 s. No external bias was applied to the cell during the measurement. The transmittance of the film was measured at the end of each of these time intervals over the visible region. The film showed an excellent open circuit memory upon coloration by illumination (~3-4 h without color fading) and %T plots were recorded under *ex-situ* conditions. Prior to exposure to one sun, the film was oxidized and its transmittance in this bleached state was found to lie in the range of 75 to 80% in the visible and NIR region. Upon illumination, the transmittance of the

electrochromic film decreased as a function of increasing period of illumination. Transmission modulation (ΔT) is a useful parameter for determining the suitability of a given material for electrochromic application. We define modulation as $\Delta T(\lambda) = T_b(\lambda) - T_c(\lambda)$, where T_b and T_c are transmittances in the bleached (as-fabricated) and colored (upon x min exposure of 1 sun illumination, $x = 0, 10, 20, 30, 40, 50, 60, 70$ and 80 s) states respectively. Transmission modulation as a function illumination time is displayed in **Figure 8.13**. Measured ΔT was found to be $\sim 40\%$ (under 80 s- illumination w.r.t 0 s- transmittance) which is acceptable for smart window applications. These studies show that ZnO/N719/Au@C-dot/MoO₃ coloration is suitable for energy efficient electrochromic window application.

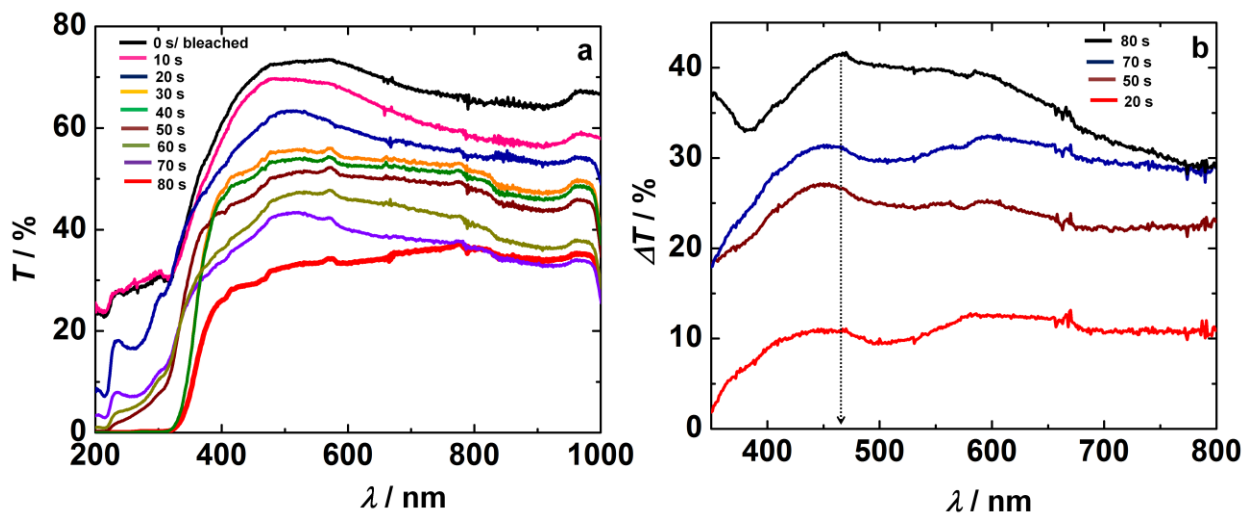


Figure 8.13: (a) Transmittance as a function of wavelength of MoO₃ as the coloring counter electrode of a photoelectrochromic cell; the %T variation was recorded for different exposure times under 1 sun illumination. (b) Transmission modulation *versus* wavelength of MoO₃; time intervals in (b) correspond to T_c values obtained by shining for the given duration, and these were used for calculating ΔT .

8.4 Summary

Au enconced by carbon dots (Au@C-dots) were integrated with a traditional ZnO/N719 photoanode configuration to improve the light harvesting efficiency of a DSSC. Au@C-dots and hexagonal faceted ZnO nanorods were synthesized by facile hydrothermal routes. The dual functions of Au@C-dots involving the plasmonic effect of Au nanoparticles which increases the light absorption capacity of N719 dye combined with the ability of C-dots to undergo appreciable charge separation upon illumination were demonstrated. ZnO/N719/Au@C-dots based electrodes were constructed and the multiple electron decay modes that prevail in this system and their implications on solar cell performance metrics were elucidated. Rapid electron transfer from N719 dye to Au@C-dots was affirmed by fluorescence and lifetime increments of Au@C-dots. Favorable energy level offsets between ZnO nanorods and N719 dye and a Forster radius of 1.89 nm enabled energy transfer from the gap states of ZnO nanorods to N719 dye with an efficiency of 66%. The plasmonic and FRET enabled DSSC with ZnO/N719/Au@C-dots as photoanode showed a PCE of 4.1%, greater than 3.16% observed for the conventional ZnO/N719 based DSSC. A photoelectrochromic cell was assembled with electrochromic MoO₃ as the counter electrode and ZnO/N719/Au@C-dot as the photoanode. Upon illumination, the photocurrent produced by the photoanode was channelized to the MoO₃ counter electrode through the external circuit and MoO₃ underwent coloration upon reduction. The reversible color change was between colorless and blue. This optical modulation attained by controlling light impinging duration showed the applicability of the ZnO/N719/Au@C-dots photoanode with MoO₃ counter electrode for photoelectrochromic window applications.

8.5 References

- [1] X. Sun, Y. Li, *Angew. Chem. Int. Ed.* **43** (2004) 597-601.
- [2] P. Zhang, T. K. Sham, *Phys. Rev. Lett.* **90** (2003) 245502-245506.
- [3] I. Tunc, S. Suzer, *J. Phys. Chem. B* **109** (2005) 7597-7600.

- [4] M. Brust, M. Walker, D. Bethell, D. J. Schiffrin, R. Whyman, *J. Chem. Soc., Chem. Commun.* (1994) 801-802.
- [5] D. Paz-Soldan, A. Lee, S. M. Thon, M. M. Adachi, H. Dong, P. Maraghechi, M. Yuan, A. J. Labelle, S. Hoogland, K. Liu, E. Kumacheva, E. H. Sargent, *Nano Lett.* **13** (2013) 1502-1508.
- [6] J. Zhou, C. Booker, R. Li, X. Zhou, T. K. Sham, X. Sun, Z. Ding, *J. Am. Chem. Soc.* **129** (2007) 744-745.
- [7] S. N. Baker, G. A. Baker, *Angew. Chem. Int. Ed.* **49** (2010) 6726-6744.
- [8] R. Narayanan, M. Deepa, A. K. Srivastava, *J. Mater. Chem. A* **1** (2013) 3907-3918.
- [9] B. Djuricic, Y. H. Leung, K. H. Tam, *Appl. Phys. Lett.* **88** (2006) 103107-103110.
- [10] X. Tang, E. S. G. Choo, L. Li, J. Ding, J. Xue, *Chem. Mater.* **22** (2010) 3383-3388.
- [11] A. Makhal, S. Sarkar, T. Bora, S. Baruah, J. Dutta, A. K. Raychaudhuri, S. K. Pal, *J. Phys. Chem. C* **114** (2010) 10390-10395.
- [12] Th. Forster, *Ann. Phys.* **437** (1948) 55-75.
- [13] S. Buhbut, S. Itzhakov, E. Tauber, M. Shalom, I. Hod, T. Geiger, Y. Garini, D. Oron, A. Zaban, *ACS Nano* **4** (2010) 1293-1298.
- [14] H. Choi, W. T. Chen, P. V. Kamat, *ACS Nano* **6** (2012) 4418-4427.
- [15] V. Dhas, S. Muduli, W. Lee, S – H. Han, S. Ogale, *Appl. Phys. Lett.* **93** (2008) 243108-243111.
- [16] S. Sarkar, A. Makhal, T. Bora, S. Baruah, J. Duttab, S. K. Pal, *Phys. Chem. Chem. Phys.* **13** (2011) 12488-12496.
- [17] X. Yan, X. Cui, B. S. Li, L. S. Li, *Nano Lett.* **10** (2010) 1869-1873.
- [18] R. S. Patil, M. D. Uplane, P. S. Patil, *Int. J. Electrochem. Sci.* **3** (2008) 259-265.
- [19] T. Siciliano, A. Tepore, E. Filippo, G. Micocci, M. Tepore, *Mater. Chem. Phys.* **114** (2009) 687-691.

Chapter 9

Summary and conclusions

The work done in this thesis focused on improving solar energy conversion efficiencies in solution processed quantum dot sensitized solar cells (QDSSCs), for they are relatively less expensive than their dye sensitized analogues and theoretically, they have the potential to acquire efficiencies above the Shockley-Queisser limit. Since photovoltaic performance parameters are closely linked to the energetics of the components of a solution processed solar cell, which in turn dictates the electron transfer dynamics, much emphasis was laid on constructing hitherto unexplored photoanode architectures and on elucidating the charge transfer and transport mechanisms in these systems by detailed fluorescence quenching, lifetime analyses and impedance studies and correlating the same to solar cell performances.

The effect of including a carbon nanostructure such as ionic liquid functionalized graphene oxide (FGO) and metal nanoparticles (Au) in facilitating electron transport in a QDSSC with TiO_2/CdSe as the photosensitive electrode was studied. A $\text{TiO}_2/\text{CdSe}/\text{FGO}/\text{Au}$ nanocomposite was prepared and the synergy between the four components was demonstrated, as the highest power conversion efficiency ($\text{PCE} = 1\%$, under 1 sun) was achieved for this assembly compared to other configurations. Taking this further, the influence of another carbon nanostructure, C_{60} nanowhiskers, on a CdS QD solar cell response was explained by comparing the charge transport dynamics of CdS/C_{60} nanowhiskers with that of an assembly encompassing conventional C_{60} clusters (i.e., CdS/C_{60}) and the advantage of the whiskers was clearly brought out. Other than the use of carbon nanostructures, another concept, Forster resonance energy transfer or FRET, was also utilized in this work to realize improved efficiencies in QDSSCs. An electrode tethered QD

assembly of ZnS/CdS/ZnS was used as the donor and copper phthalocyanine (CuPc) molecules dissolved in the electrolyte were used as acceptors. Photoluminescent and electronically conducting carbon dots or C-dots were also incorporated in this cell to enhance electron transfer and transport. Incident photon to current conversion efficiency or IPCE measurements revealed an optimal utilization of the visible spectrum, due to FRET. A quasi-solid state FRET enabled QDSSC was demonstrated. Extending this further, another FRET cell was fabricated, with reversed roles, wherein CdS/CdSe QDs served as acceptors and a Lucifer yellow dye dissolved in the electrolyte functioned as the donor. Via FRET, a superior QDSSC performance over the bulk of the visible spectrum was realized in the donor-acceptor cell, as opposed to donor or acceptor only cells. A PCE of 1.8% was obtained under 1 sun for the FRET cell. Furthermore, the hole transporting ability of the conventional S_n^{2-}/S^{2-} redox couple was also improved by use of poly(3,4-ethylenedioxythiophene) microfibers. Apart from carbon nanostructures and FRET, yet another strategy involving plasmonic effects was also used for improving solar cell responses, by integrating Au microfibers with CdS/TiO₂ electrodes. This work was further extended by combining this plasmonic photoanode with an electrical double layer capacitor based on multiwalled carbon nanotubes (MWCNTs). A new design for a solar powered supercapacitor was implemented, wherein the photocurrent generated by the plasmonic electrode was channelized to charge the MWCNT supercapacitor. The benefit of plasmonics in increasing solar cell parameters was also established by using Au encapsulated C-dots in a ZnO based DSSC and a PCE of 4.1% was achieved. Another practical application was illustrated by using electrochromic MoO₃ as a counter electrode in the ZnO/Dye/Au@C-dots based cell and photoelectrochromism was shown.

While the configurations of QDSSCs can be tailored to maximize performance, as done in this thesis, but there are some concerns which need to be addressed. Long term operational- and shelf- stabilities of these cells are major concerns, which have to be tackled

in near future, so that they can, eventually, be useful on a commercial scale. Upscaling with no loss in performance is another issue, which requires concerted scientific effort. More efforts are also required to replace the aqueous poly(sulfide) or sulfide electrolyte, with equally cheap and better performing non-aqueous and solid-state counterparts, so that “all solid-state cells” can be constructed. Research efforts, in future, should be devoted towards preparing scalable, non-toxic cells at low temperature, in air, with minimum processing steps.

Whilst maintaining that the above mentioned efforts are the need of the hour, nonetheless, these advanced solar technology solutions (e.g. QDSSCs, in terms of materials and properties, some described elaborately in this work) do show promise to offer competition to traditional silicon based cells. The work done in this thesis, unravels, not only fundamental aspects but also describes the applications of QDSSCs, and is therefore, significant, as the studies presented herein, provide valuable insights for a better understanding of how the composition of the various components of a QDSSC: the photoanode, the redox couple based electrolyte and the counter electrode and the interactions between them influence solar cell performance metrics. At the same time, these studies are also useful for the photovoltaic community, at large, as the phenomena or materials used herein can be adapted to other members of third generation photovoltaic cells, and improvements in solar power conversion efficiencies can be realized.

List of publications

List of publications included in the thesis:

- [1] **R. Narayanan**, M. Deepa, A. K. Srivastava, S. M. Shivaprasad, Efficient plasmonic dye-sensitized solar cells with fluorescent Au-encapsulated C-Dots. *ChemPhysChem* **15** (2014) 1106-1115.
- [2] **R. Narayanan**, A. Das, M. Deepa, A. K. Srivastava, Energy relay from an unconventional Yellow dye to CdS/CdSe quantum dots for superior solar cell performance. *ChemPhysChem* **14** (2013) 4010-4021.
- [3] **R. Narayanan**, M. Deepa, A. K. Srivastava, Forster resonance energy transfer and carbon dots enhance light harvesting in a solid-state quantum dot solar cell. *J. Mater. Chem. A* **1** (2013) 3907-3918.
- [4] **R. Narayanan**, B. N. Reddy, M. Deepa, Facile charge propagation in CdS quantum dot cells. *J. Phys. Chem. C* **116** (2012) 7189-7199.
- [5] **R. Narayanan**, M. Deepa, A. K. Srivastava, Nanoscale connectivity in a TiO₂ CdSe quantum dots/functionalized graphene oxide nanosheets/Au nanoparticles composite for enhanced photoelectrochemical solar cell performance. *Phys. Chem. Chem. Phys.* **14** (2012) 767-778.

Papers presented in conferences:

- [1] Forster resonance energy transfer and carbon dots enhance light harvesting in a solid-state quantum dot solar cell, **TAPSUN - 2012** held at NPL Delhi, December 5-6, 2012.
- [2] A CdS/Bi₂S₃ bilayer and a poly(3,4-ethylenedioxythiophene)/S²⁻ interface control quantum dot solar cell performance, **ICYRAM - 2012** held at Singapore, July 1-7, 2012.
- [3] Facile charge propagation in CdS quantum dots, **Research Scholar's Day** held at IIST Trivandrum, December 25-26, 2011.

